

Kinetics of OH Radical Reactions with Furan Derivatives and Related Phenomena Relevant to Low Temperature Combustion

Charlotte Ann Whelan

Submitted in accordance with the requirements for the degree of
Doctor of Philosophy

The University of Leeds
School of Chemistry

September 2019

Contributions to Published Works

Whelan, C.A., Blitz, M., Shannon, R., Onel, L., Lockhart, J., Seakins, P., Stone, D.,
Temperature and Pressure Dependent Kinetics of QOOH Decomposition and Reaction
with O₂: Experimental and Theoretical Investigations of QOOH Radicals Derived from Cl
+ (CH₃)₃COOH. *J. Phys. Chem. A.* **2019**

The candidate confirms that the work submitted is her own and that appropriate credit has been given where reference has been made to the work of others.

This copy has been supplied on the understanding that it is copyright material and that no quotation from the thesis may be published without proper acknowledgement.

The right of Charlotte Ann Whelan to be identified as Author of this work has been asserted by her in accordance with the Copyright, Designs and Patents Act 1988.

© 2019 The University of Leeds and Charlotte Ann Whelan

Acknowledgements

I am extremely grateful for the support I have received of the past four years that has made it possible for me to complete this thesis. First and foremost, I would like to express my immense gratitude to my supervisors Doctor Daniel Stone and Professor Paul Seakins for giving me the opportunity to be a part of such a fantastic research group. In particular, I wish to thank my primary supervisor, Dan, for the infinite wisdom and patience he has offered me throughout this research project, and for making the project one I enjoyed so much.

I would also like to give a special thanks to Mark for all his help in the lab, Diogo for all his advice on using Gaussian and MESMER, and to Lavinia for deriving the complex QOOH fitting equations.

I have been fortunate enough to have made some great friends during my time in Leeds, with particular thanks to Zara, Sam, David, Tom L, Tom S, Grace, Ellie, Graham, Alex and all the other Heard, Seakins and Stone research group members past and present.

My family have always been tremendous in their support of me continuing with my education and I would like to thank my parents, Judith and Mark, for their constant encouragement.

Of my friends outside of academia, I would like to thank Amy and Natasha, who politely listened to me talk about kinetics for four years even if they didn't understand what was said.

Last but not least I would like to thank my partner, Max, for his constant reassurances and always knowing the right words to say when I didn't.

Abstract

Biofuels have been proposed as a method to mitigate the effects of climate change as a result of fossil fuel combustion. Furans, a group of heterocyclic ethers, have been suggested as potential biofuels, in particular 2,5-dimethylfuran, which has a similar energy density to gasoline. In order to assess the feasibility for use as vehicle fuels, knowledge of the kinetics and reaction mechanisms occurring under combustion conditions is required.

A kinetic study of reactions relevant to low temperature combustion has been performed using laser flash photolysis-laser induced fluorescence spectroscopy. Chapters 4-6 describe a detailed experimental study of the reaction between the OH radical and furan and its alkylated derivatives over a range of temperatures (298-770 K) and pressures (4-150 Torr). Experiments were performed under pseudo-first-order conditions, using flash photolysis of H₂O₂/furan/N₂ or (CH₃)₃COOH/furan/N₂ gas mixtures with monitoring of OH radicals by laser-induced fluorescence (LIF) spectroscopy.

For the reaction of OH + furan, the room temperature rate coefficient was determined to be independent of pressure, with an average value of $k = (3.34 \pm 0.48) \times 10^{-11} \text{ cm}^3 \text{ molecule}^{-1} \text{ s}^{-1}$. Over all temperatures investigated (298-595 K) the reaction appears to be at, or close to, the high-pressure limit. Results demonstrate a negative temperature dependence over temperatures between 298 K and 595 K, with $-E_a/R = (510 \pm 71) \text{ K}$. This temperature dependence is consistent with the behaviour observed in previous studies. Results have been analysed in combination with high temperature shock tube data to provide a parameterisation of the kinetics that describes a temperature range relevant to both low and high temperature combustion.

The OH + 2-methylfuran (2-MF) room temperature rate coefficient was measured to be $k = (7.38 \pm 0.37) \times 10^{-11} \text{ cm}^3 \text{ molecule}^{-1} \text{ s}^{-1}$. Results demonstrate a negative temperature dependence for the reaction of OH + 2-MF over temperatures between 298 K and 770 K,

with $-E_a/R = (716 \pm 79)$ K, and no significant dependence on pressure over this temperature range. Results were combined with shock tube data to provide a parameterisation for use in combustion models over a wide temperature range.

For the reaction of OH + 2,5-DMF, the rate coefficient at 298 K, $k = (1.10 \pm 0.10) \times 10^{-10}$ cm³ molecule⁻¹ s⁻¹, was found to be at, or close to, the high-pressure limit over the pressure range studied. Above 298 K the OH + 2,5-DMF reaction exhibits pressure-dependent kinetics with a negative temperature dependence observed over the temperature and pressure ranges investigated. Fits to the data indicate a low-pressure limit of $k_0 = (2.80 \pm 1.60) \times 10^{-29} \exp((1930 \pm 220)/T)$ cm⁶ molecule⁻¹ s⁻¹ and a high-pressure limit of $k_\infty = (1.50 \pm 0.10) \times 10^{-11} \exp((640 \pm 20)/T)$ cm³ molecule⁻¹ s⁻¹. The high pressure limiting rate coefficients were analysed in conjunction with previous shock tube data to describe the kinetics over a wide temperature range.

For OH + 2,5-dimethylfuran (2,5-DMF), the potential energy surface of the reaction was investigated at the M06-2X/cc-pVTZ level of theory. Master equation analyses have been performed for each reaction system using the Master Equation Solver for Multi-Energy well Reactions (MESMER) to complement the results obtained experimentally. The MESMER calculations indicate that addition of OH to the furan ring is dominant under the experimental conditions of this study, with addition to the C1 site dominant for furan, to the C2 and C5 sites, approximately equally, for 2-MF, and to the C2 site for 2,5-DMF.

Chapter 8 changes focus to the kinetics of the QOOH radical. QOOH radicals are key species in autoignition, produced by internal isomerisations of RO₂ radicals, and are central to chain branching reactions in low temperature combustion. The kinetics of QOOH radical decomposition and reaction with O₂ have been determined as a function of temperature and pressure, for the first time, using observations of OH radical production and decay following H-atom abstraction from *tertiary*-butyl hydroperoxide ((CH₃)₃COOH) by Cl atoms to produce QOOH ($\cdot\text{CH}_2(\text{CH}_3)_2\text{COOH}$) radicals. The kinetics

of QOOH decomposition have been investigated as a function of temperature, in the range 251 to 298 K, and pressure, in the range 10 to 350 Torr, in helium and nitrogen bath gases, and those of the reaction between QOOH and O₂ have been investigated as a function of temperature, in the range 251 to 304 K, and pressure, in the range 10 to 100 Torr. Decomposition of the QOOH radicals was observed to display temperature and pressure dependence, with a barrier height for decomposition of (44.7 ± 4.0) kJ mol⁻¹ determined by master equation fitting to the experimental data. The rate coefficient for the reaction between QOOH and O₂ was determined to be $(5.6 \pm 1.7) \times 10^{-13}$ cm³ s⁻¹ at 298 K, with no significant dependence on pressure, and can be described by the Arrhenius parameters $A = (7.3 \pm 6.8) \times 10^{-14}$ cm³ s⁻¹ and $E_a = -(5.4 \pm 2.1)$ kJ mol⁻¹ in the temperature range 251 to 304 K.

Table of Contents

Chapter 1 Introduction	1
1.1 A Changing Atmosphere	1
1.1.1 CO ₂ and the Atmosphere.....	1
1.1.2 Fossil Fuels and Transportation	3
1.2 Combustion	5
1.2.1 Engines	5
1.2.2 Fuel Chemistry	7
1.2.3 High Temperature Combustion.....	8
1.2.4 Low Temperature Combustion	9
1.2.5 Atmospheric Implications.....	11
1.2.6 Combustion Modelling	12
1.3 Biofuels	13
1.3.1 Properties of biofuels.....	14
1.3.2 Biofuel Combustion and Emissions	15
1.3.3 First Generation Biofuels	15
1.3.4 Second Generation Biofuels	16
1.3.5 Third Generation Biofuels.....	17
1.3.6 Conversion Processes.....	17
1.4 Furans: Potential Biofuels.....	18
1.4.1 Production of Furans from Lignocellulosic Waste	18
1.5 Outline of this Thesis	20
1.6 References.....	21
Chapter 2 Gas Phase Kinetics	25
2.1 Theory of Gas Phase Kinetics	25
2.2 Temperature Dependence of Reaction Rates.....	27
2.3 Bimolecular Gas Phase Reaction Rate Theory.....	28
2.4 Unimolecular Reaction Rate Theory	34
2.5 Termolecular Reaction Rate Theory	36
2.6 Concluding Remarks	38
2.7 References.....	39

Chapter 3 Experimental Techniques	40
3.1 Kinetic Techniques	40
3.1.1 Relative Rate Method	40
3.1.2 Discharge Flow	42
3.1.3 Shock Tube	44
3.1.4 Rapid Compression Machine	45
3.1.5 Flash Photolysis	47
3.2 Analytical Techniques	48
3.2.1 Gas Chromatography	48
3.2.2 Mass Spectrometry	49
3.2.3 Absorption Spectroscopy	50
3.2.4 Resonance Fluorescence	51
3.2.5 Laser induced fluorescence	52
3.3 Details of the Apparatus and Kinetic Methods Used in This Work	54
3.3.1 Radical Generation	55
3.3.2 Radical Detection	57
3.3.3 Reaction Cells	59
3.3.4 Pressure Readings	61
3.3.5 Gas Sample Preparation	62
3.3.6 Experimental Procedure	63
3.4 Kinetic Analysis	64
3.5 References	67
Chapter 4 Kinetic Study of the OH + Furan Reaction as a Function of Temperature and Pressure	70
4.1 Background and Previous Work	70
4.1.1 Studies of OH + Furan at Low Temperature (<1000 K)	71
4.1.2 Studies of OH + Furan at High Temperature (>1000 K)	83
4.1.3 Theoretical Studies of OH + Furan	85
4.1.4 Combustion Models of Furan	86
4.2 Experimental Procedure	89
4.3 Results and Discussion	91
4.3.1 Kinetics at 298 K	91
4.3.2 OH Radical Precursors	96
4.3.3 Effects of Pressure and Temperature	97

4.4	Conclusion	107
4.5	References.....	108
Chapter 5 Kinetic Study of the OH + 2-Methylfuran Reaction as a Function of Temperature and Pressure.....		110
5.1	Background and Previous Work	110
5.1.1	Studies of OH + furan at low temperature (<1000 K)	110
5.1.2	Studies of OH + 2-MF at High Temperature (>1000 K).....	115
5.1.3	Theoretical Studies of OH + 2-MF	116
5.1.4	Combustion Models of 2-MF.....	117
5.2	Experimental Procedure.....	119
5.3	Results and Discussion	121
5.3.1	Kinetics at 298 K	121
5.3.2	Effects of Pressure and Temperature	125
5.4	Conclusion	131
5.5	References.....	132
Chapter 6 Kinetic Study of the OH + 2,5-Dimethylfuran Reaction as a Function of Temperature and Pressure.....		134
6.1	Background and Previous Work	134
6.1.1	Studies of OH + 2,5-DMF at Low Temperature (<1000 K)	135
6.1.2	Studies of OH + 2,5-DMF at High Temperatures (>1000 K)	139
6.1.3	Theoretical Studies of OH + 2,5-DMF.....	141
6.1.4	Combustion Models of 2,5-DMF	142
6.2	Experimental Procedure.....	145
6.3	Results and Discussion	147
6.3.1	Kinetics at 298 K	147
6.3.2	Effects of Pressure and Temperature	151
6.3.3	Reactivity of Furans with OH.....	162
6.4	Conclusion	163
6.5	References.....	165
Chapter 7 Interpretation of Experimental Results for OH + Furan and its Derivatives.....		168
7.1.1	Electronic Structure Calculations.....	168
7.1.2	Master Equation Calculations	169

7.2	Previous work.....	171
7.2.1	<i>ab initio</i> Calculations and Calculation of Kinetics for OH + Furan	171
7.2.2	<i>ab initio</i> Calculations and Calculation of Kinetics for OH + 2-Methylfuran	179
7.2.3	<i>ab initio</i> Calculations and Calculation of Kinetics for OH + 2,5-Dimethylfuran.....	186
7.2.4	Combustion Models	188
7.3	Computational Methods Used in This Work.....	194
7.4	Results and Discussion	197
7.4.1	<i>ab initio</i> Calculations of the OH + 2,5-DMF PES.....	197
7.4.2	Master Equation Calculations of OH + Furan.....	209
7.4.3	Master Equation Calculations of OH + 2-MF.....	205
7.4.4	Master Equation Calculations of OH + 2,5-DMF	201
7.5	Conclusion	215
7.6	References.....	217

Chapter 8 Temperature and Pressure Dependent Kinetics of QOOH Decomposition and Reaction with O₂: Experimental and Theoretical Investigations of QOOH Radicals Derived from Cl + t-BuOOH.....		219
8.1	Background and Previous Work	219
8.2	Experimental Procedure	224
8.3	Analysis.....	226
8.4	Results and Discussion	234
8.4.1	QOOH Decomposition Kinetics.....	234
8.4.2	Master Equation Analysis	241
8.4.3	Kinetics of QOOH + O ₂	248
8.5	Conclusions.....	251
8.6	References.....	252
Summary and Future Work.....		254
Appendix.....		259

List of Figures

Chapter 1

- Figure 1.1 IPCC Fifth Assessment graph to show the radiative forcing effect in $W m^{-2}$ of key radiatively active species in the atmosphere relative to pre-industrial levels of 1750.....2
- Figure 1.2 Atmospheric mixing ratios of three long-lived GHGs over 2000 years. Increases at around 1750 are attributed to anthropogenic activity during the industrial revolution. Mixing ratios are parts per million (ppm) for CO_2 and parts per billion (ppb) for N_2O and CH_43
- Figure 1.3 Schematic of a Spark-Ignition, Compression-Ignition and Homogeneous Charge Compression Ignition engine.....7
- Figure 1.4 The mechanism for low temperature oxidation of the fuel RH adapted from Zádor *et al.*.....11
- Figure 1.5 Production of 2,5-DMF and 2-MF from fructose via HMF, adapted from Dumesic *et al.* (2007)19

Chapter 2

- Figure 2.1 Potential energy surface for the reaction $A + BC$. Reproduced from reference 2.31
- Figure 2.2 Typical potential energy surfaces with a barrier to reaction products (left) and without a barrier (right).34
- Figure 2.3 Schematic diagram of the apparent first-order rate coefficient, k , as a function of $[M]$. The observed rate is second-order at low pressures and tends to a limiting first-order value at high pressures.....36

Chapter 3

- Figure 3.1 Schematic of discharge flow set up, where z is the distance between reaction initiation and detection43
- Figure 3.2 Top: shock tube setup before diaphragm is punctured. Bottom: shock tube after diaphragm is punctured showing the shock front as the high and low pressure gases meet.45
- Figure 3.3 Typical pressure traces for inert gas tests in a RCM.....46
- Figure 3.4 Typical flash photolysis decay measured by laser induced fluorescence (LFP-LIF), black points are experimental data. Red line is exponential fit to give k'47
- Figure 3.5 Schematic of absorption spectroscopy51
- Figure 3.6 Resonance fluorescence is fluorescence from a species in which the light emitted is at the same frequency as the light absorbed.....52
- Figure 3.7 Jablonski diagram showing the possible fates of an excited energy state.....53
- Figure 3.8 Schematic of the experimental set up used in this work.....55
- Figure 3.9 Principle concepts of a laser system.....56

Figure 3.10 Schematic energy level diagram showing the transitions relevant to off- and on- resonant fluorescence of the OH radical following the A – X electronic transition. Collisional energy transfer processes are presented in blue.	58
Figure 3.11 A schematic of a photomultiplier tube.	59
Figure 3.12 Reaction cell used for high temperature (298-770 K) experiments conducted in this thesis	60
Figure 3.13 Reaction cell used for low temperature (251-298 K) experiments conducted in this thesis	61
Figure 3.14 A typical calibration for an MFC (SN: 906LS002).....	62
Figure 3.15 OH fluorescence decay at [furan] = 4.06×10^{14} molecule cm^{-3} at 298 K and 50 Torr. $k' = (13885 \pm 122) \text{ s}^{-1}$ according to E3.16.....	66
Figure 3.16 Bimolecular plots for the reaction of OH + furan at 298 K at 4 Torr (black diamonds) and 95 Torr (blue diamonds) the slopes of which give $k = (3.40 \pm 0.10) \times 10^{-11} \text{ cm}^3 \text{ molecule}^{-1} \text{ s}^{-1}$ (red line) and $k = (3.30 \pm 0.10) \times 10^{-11} \text{ cm}^3 \text{ molecule}^{-1} \text{ s}^{-1}$ (green line) respectively. Note some 1σ error bars are smaller than symbols.....	67

Chapter 4

Figure 4.1 Structure of furan with numbered carbons.	70
Figure 4.2 kobs (k) vs. reactant concentration for furan (diamond), ethane (triangle) and thiophene (circle), reported by Lee and Tang	72
Figure 4.3 Plots for the experimental data for OH + furan from relative rate experiments using <i>n</i> -hexane as a reference compound from Atkinson <i>et al.</i>	74
Figure 4.4 Arrhenius plots for the reaction of OH with furan, tetrahydrothiophene (THT) and thiophene reported by Wine and Thompson	76
Figure 4.5 Relative rate plot for furan, 2-MF and 2-EF from relative rate experiments using propene as a reference compound reported by Bierbach <i>et al.</i>	78
Figure 4.6 Arrhenius plot for OH + furan from Wine and Thompson from 254-425 K and 30-150 Torr and Eble from 296-570 K and 2 to 10 bar.	81
Figure 4.7 Rate coefficient of OH + furan reported by Elwardany <i>et al.</i> between 924-1388 K. Black line is the Arrhenius fit reported by Elwardany <i>et al.</i> as $k = 1.30 \times 10^{-21} \times T^3 \exp(1866.7/T) \text{ cm}^3 \text{ molecule}^{-1} \text{ s}^{-1}$. No error for the data was provided.	84
Figure 4.8 Ring-opening products reported by Mousavipour <i>et al.</i> from the addition of OH to the C1 site in furan.....	85
Figure 4.9 Results for the production of acrolein ($\text{C}_3\text{H}_4\text{O}$) from OH addition to furan reported by Liu <i>et al.</i> from EI-MBMS experiments (black squares) compared to the model of Liu <i>et al.</i> (blue solid line) and the model by Tian <i>et al.</i> (dashed red line).....	87

Figure 4.10 Flow-rate analysis for the consumption of furan in a fuel-rich furan flame ($\phi = 1.7$) corresponding to a simulated temperature of 1135 K taken from the study by Liu <i>et al.</i>	88
Figure 4.11 Arrhenius fits (solid lines) and extrapolations (dashed lines) to Wine and Thompson (blue), Eble (red), Elwardany <i>et al.</i> (black), Tian <i>et al.</i> (green) and Liu <i>et al.</i> (brown).	89
Figure 4.12 OH fluorescence decay at $[\text{furan}] = 4.06 \times 10^{14}$ molecule cm^{-3} at 298 K and 50 Torr. $k_{\text{obs}} = (13885 \pm 122)$ s^{-1} according to E4.1.....	91
Figure 4.13 Bimolecular plots for the reaction of OH + furan at 298 K at 4 Torr (black diamonds) and 95 Torr (blue diamonds) the slopes of which give $k = (3.40 \pm 0.10) \times 10^{-11}$ cm^3 molecule $^{-1}$ s^{-1} (red line) and $k = (3.30 \pm 0.10) \times 10^{-11}$ cm^3 molecule $^{-1}$ s^{-1} (green line) respectively. Note some 1σ error bars are smaller than symbols.	92
Figure 4.14 Pressure dependence of OH + furan at 298 K.	92
Figure 4.15 Literature room temperature rate coefficients for OH + furan with results from this work	93
Figure 4.16 Effect of laser power on k for the reaction of OH + furan at $[\text{furan}] = 4.39 \times 10^{14}$ molecule cm^{-3}	95
Figure 4.17 Oxygen dependence of the reaction of OH + furan at 298 K and 50 Torr. Note some errors bar may be smaller than symbols.	96
Figure 4.18 Left: fluorescence decay of OH at 298 K where $(\text{CH}_3)_3\text{COOH}$ is thermally stable. Red dashed line shows time of photolysis. Blue arrow indicates signal produced before photolysis. Yellow arrow indicates signal produced on photolysis. Right: fluorescence decay of OH at 500 K with thermal decomposition of $(\text{CH}_3)_3\text{COOH}$	97
Figure 4.19 Arrhenius plot of this work with 95 % confidence limits. Arrhenius parameters from E4.2 are $A = (6.43 \pm 1.27) \times 10^{-12}$ cm^3 molecule $^{-1}$ s^{-1} and $-E_a/R = (510 \pm 71)$ K.	99
Figure 4.20 Arrhenius plot of this work (black diamonds), Eble (red circles) and Wine and Thompson (blue circles) where lines represent Arrhenius fits to respective data, results of which can be seen in Table 4.6.....	100
Figure 4.21 Arrhenius plot of the fit of E2 to the combined data sets of this work and Eble.....	101
Figure 4.22 Example potential energy surface showing a barrierless addition reaction between OH + furan.	102
Figure 4.23 Plot of the temperature dependent kinetics of OH + furan. Black open diamonds represent Elwardany <i>et al.</i> data for high-temperature (924-1388 K) shock tube experiments. Symbols for experiments carried out at 298 K can be found in the graph key. This work is represented by black diamonds, the black line of fit to the data according to E4.2 and the dashed blackline is the extrapolation of E4.2 to the high temperature range.....	103

Figure 4.24 The effect of temperature OH + furan. Results from this work (black solid diamonds), Wine and Thompson (blue solid circles), Eble (red circles) and Elwardany <i>et al.</i> (open black diamonds). Fit to E3 to the combined data from this work and Elwardany <i>et al.</i> (black line) and from this work, Eble and Elwardany <i>et al.</i> (red line).	104
Figure 4.25 Khaled <i>et al.</i> reported Arrhenius plot for the total rate coefficients of OH radical reactions with 1,3-butadiene, cis/trans-1,3-pentadiene and 1,4-pentadiene. Lines represent the best fit to the experimental rate coefficient	106
Figure 4.26 Comparison of the fit of E4.3 to data from this work compared to the model produced by Liu <i>et al.</i> and Tian <i>et al.</i>	107

Chapter 5

Figure 5.1 Structure of 2-Methylfuran (2-MF) with numbered carbons	110
Figure 5.2 Arrhenius plot for OH + 2-MF from Eble. From 296-566 K and averaged over 2, 5 and 10 bar.....	113
Figure 5.3 Rate coefficient of OH + 2-MF reported by Elwardany <i>et al.</i> between 890 ⁻¹ 333 K. Black line is the Arrhenius fit reported by Elwardany <i>et al.</i> as $k = 1.47 \times 10^{-10} \times T^3 \exp(-2285.7/T) \text{ cm}^3 \text{ molecule}^{-1} \text{ s}^{-1}$	115
Figure 5.4 PES of OH + 2-MF showing the addition and abstraction channels from Davis and Sarathy. Energies are in kcal mol ⁻¹ and are an average of calculations at the CBS-QB3 and G4 levels of theory.	116
Figure 5.5 Schematic of furylCH ₂ as a result of the reaction between OH + 2-MF	117
Figure 5.6 Schematic of MF-yl-2 as a result of the reaction between OH + 2-MF	117
Figure 5.7 Comparison of combustion models (key inset) with Arrhenius fits to experimental data of Eble and Elwardany <i>et al.</i>	119
Figure 5.8 OH fluorescence decay at [2-MF] = 4.04 × 10 ¹⁴ molecule cm ⁻³ at 298 K and 20 Torr. $k_{\text{obs}} = (29320 \pm 708) \text{ s}^{-1}$	121
Figure 5.9 Bimolecular plots for the reaction of OH + 2-MF at 298 K at 20 Torr (black diamonds) and 95 Torr (blue diamonds) the slopes of which give $k = (7.82 \pm 0.27) \times 10^{-11} \text{ cm}^3 \text{ molecule}^{-1} \text{ s}^{-1}$ (red line) and $k = (7.64 \pm 0.15) \times 10^{-11} \text{ cm}^3 \text{ molecule}^{-1} \text{ s}^{-1}$ (green line) respectively. Note some 1σ error bars are smaller than symbols.....	122
Figure 5.10 Pressure dependence of OH + 2-MF at 298 K.	123
Figure 5.11 Literature room temperature rate coefficients for OH + 2-MF with results from this work.....	124
Figure 5.12 Effect of laser power on k for the reaction of OH + 2-MF at 298 K and 50 Torr. Rate coefficient found to be independent of laser power ..	125
Figure 5.13 Pressure dependence on 2-MF + OH at 660 K	126

Figure 5.14 Arrhenius plot of this work (black diamonds) with Arrhenius fit to data (black line) with 95 % confidence limits. Arrhenius parameters for this work are $A = (7.17 \pm 0.16) \times 10^{-12} \text{ cm}^3 \text{ molecule}^{-1} \text{ s}^{-1}$ and $-E_a/R = (716 \pm 79) \text{ K}$	127
Figure 5.15 Arrhenius plot of this work (black diamonds) and Eble (red circles) with Arrhenius fit to data, this work (black line) and Eble (red line) with 95 % confidence limits. Arrhenius parameters for this work are $A = (7.17 \pm 0.16) \times 10^{-12} \text{ cm}^3 \text{ molecule}^{-1} \text{ s}^{-1}$ and $-E_a/R = (716 \pm 79) \text{ K}$	128
Figure 5.16 Plot of the temperature dependent kinetics of OH + 2-MF. Black open diamonds represent Elwardany <i>et al.</i> data for high-temperature (890-1333 K) shock tube experiments. Symbols for experiments carried out at 298 K can be found in the graph key. This work is represented by black diamonds, the red line of fit to the data according to E5.2 and the dashed red line is the extrapolation of E5.2 to the high temperature range.	129
Figure 5.17 The effect of temperature OH + 2-MF. Results from this work (black solid diamonds), Eble (red circles) and Elwardany <i>et al.</i> (open black diamonds). The black line represents the modified Arrhenius fit E5.3 to the combined data from this work and Elwardany <i>et al.</i> and to this work, Eble and Elwardany <i>et al.</i> with 95 % confidence limits.	130
Figure 5.18 Comparison of the fit of E5.3 to Davis and Sarathy, Tran <i>et al.</i> and Somers <i>et al.</i>	131

Chapter 6

Figure 6.1 Structure of 2,5-DMF with labelled carbon sites.....	134
Figure 6.2 Arrhenius plot for OH + 2,5-DMF from Eble. From 296-557 K and 2 to 10 bar (1520-7600 Torr). Arrhenius parameters are $A = (7.42 \pm 0.85) \times 10^{-12} \text{ cm}^3 \text{ molecule}^{-1} \text{ s}^{-1}$ and $-E_a/R = (747 \pm 44) \text{ K}$	137
Figure 6.3 Literature rate coefficients for the reaction of OH + 2,5-DMF. Elwardany <i>et al.</i> study was carried out at 1.2-1.7 atm. Bierbach <i>et al.</i> and Aschmann <i>et al.</i> studies were carried out at 760 and 735 Torr respectively.	140
Figure 4 Possible reactions after initial OH radical addition to 2,5-DMF suggested by Aschmann <i>et al.</i>	141
Figure 6.5 Comparison of combustion models (key inset) with Arrhenius fits to experimental data of Eble and Elwardany <i>et al.</i> Note the Togbe <i>et al.</i> and Cheng <i>et al.</i> studies report the same rate coefficients.	144
Figure 6.6 Observed OH fluorescence signal in the presence of excess 2,5-DMF at 298 K and 50 Torr, $[2,5\text{-DMF}] = 1.4 \times 10^{14} \text{ cm}^3 \text{ molecule}^{-1}$. Black squares experimental data, red line exponential fit E6. From E6.1, $k = (14700 \pm 130) \text{ s}^{-1}$	147

Figure 6.7 Bimolecular plots for the reaction of OH + 2,5-DMF at 298 K. Left plot is at 20 Torr, the slope of which gives $k = (1.08 \pm 0.10) \times 10^{-10} \text{ cm}^3 \text{ molecule}^{-1} \text{ s}^{-1}$ and the intercept is $(352 \pm 63) \text{ s}^{-1}$. Right plot is at 150 Torr, the slope of which gives $k = (1.07 \pm 0.10) \times 10^{-10} \text{ cm}^3 \text{ molecule}^{-1} \text{ s}^{-1}$ and the intercept is $(257 \pm 11) \text{ s}^{-1}$. Note some 1σ error bars are smaller than symbols.....	147
Figure 6.8 Effect of pressure on the rate coefficient for OH + 2,5-DMF at 298 K. Black diamonds are averages rate coefficients at each pressure. Red line shows the average of the data points. Error bars are 1σ	148
Figure 6.9 Bimolecular rate coefficients for the reaction of OH + 2,5-DMF at 410 K and 50 Torr with mesh filters applied.....	149
Figure 6.10 OH + 2,5-DMF in the presence of N ₂ and O ₂ at 635 K, 50 Torr. Orange line indicates an average value of $k = (5.37 \pm 0.47) \times 10^{-11} \text{ cm}^3 \text{ s}^{-1}$	150
Figure 6.11 Literature room temperature rate coefficients for OH + 2,5-DMF with results from this work.....	151
Figure 6.12 Effect of pressure on the rate coefficient for OH + 2,5-DMF at 410 K. Error bars are 1σ . Note some error bars are smaller than symbols.....	152
Figure 6.13 Troe (black line) and Lindemann (red line) equations fitted to data at 550 K over pressures from 20 Torr ($3.51 \times 10^{17} \text{ molecules cm}^{-3}$) to 150 Torr ($2.63 \times 10^{18} \text{ molecules cm}^{-3}$).....	153
Figure 6.14 Bimolecular rate coefficients for OH + 2,5-DMF at 298 K (■), 410 K (●), 475 K (▲), 535 K (◆), 550 K (▼), 610 K (◄) and 635 K (●) in N ₂ at pressures between 20 and 150 Torr. Solid lines show the fit to E6.2. Error bars are 1σ . Note some error bars are smaller than symbols.....	154
Figure 6.15 Plots showing the bimolecular rate coefficients for OH + 2,5-DMF at 298 K (■), 410 K (●), 475 K (▲), 535 K (◆), 550 K (▼), 610 K (◄) and 635 K (●) in N ₂ at pressures between 20 and 150 Torr. Solid lines show the fit to E6.2. Error bars are 1σ . Note some error bars are smaller than symbols.....	155
Figure 6.16 Comparison of rate coefficients determined from Troe parameterisation of data with the observed rate coefficients from experimental data. The slope was determined as 0.90 ± 0.02 and the intercept as $(3.60 \pm 0.97) \times 10^{-12} \text{ cm}^3 \text{ molecule}^{-1} \text{ s}^{-1}$	156
Figure 6.17 Arrhenius plot of this work (k_∞ , black diamonds) and Eble (red circles) with Arrhenius fit to data, this work (black line) and Eble (red line) with 95 % confidence limits. Arrhenius parameters are shown in Table 6.4.....	157
Figure 6.18 Plot for the reaction of OH + 2,5-DMF. Black squares represent Elwardany <i>et al.</i> data for high-temperature (915-1278 K) shock tube experiments, red circle represents Bierbach <i>et al.</i> at 298 K, blue triangle represents Aschmann <i>et al.</i> at 298 K, red line represents high-pressure limit rate coefficient from this work, determined from the parameterisation of E18.....	158

Figure 6.19 Rate coefficients for OH + 2,5-DMF from this work at $T = 298\text{-}635\text{ K}$ at the high-pressure limit parameterised from E6.4, Elwardany <i>et al.</i> at $T = 915\text{-}1278\text{ K}$ and $p = 1.2\text{-}1.7\text{ atm}$ and Aschmann <i>et al.</i> and Bierbach <i>et al.</i> at 298 K and atmospheric pressure. Red line shows fit to E6.6.	159
Figure 6.20 The effect of temperature OH + 2,5-DMF. Results from this work (black solid diamonds), Wine and Thompson (blue solid circles), Eble (red circles) and Elwardany <i>et al.</i> (open black diamonds). Fit to E6.6 to the combined data from this work and Elwardany <i>et al.</i> (black line) and from this work, Eble and Elwardany <i>et al.</i> (red line) and Eble and Elwardany <i>et al.</i> (blue line).....	160
Figure 6.21 Comparison of the E6.6 fit to this work and Elwardany <i>et al.</i> (black line) and the models from the literature (key inset).	162
Figure 6.1 Structures of furan (a), 2-MF (b) and 2,5-DMF (c).....	162
Figure 6.23 Plots for the reaction of OH radicals with 2-methylfuran (2-MF), 3-methylfuran (3-MF), 2,3-dimethylfuran (2,3-DMF), and 2,5-dimethylfuran (2,5-DMF), with 1,3,5-trimethylbenzene as the reference compound from Aschmann <i>et al.</i>	1630
Figure 6.24 Temperature dependence across full temperature range of OH radical reaction rate coefficients with furan (black), 2-MF (red) and 2,5-DMF (blue) from this work (diamonds), Eble (crosses) and Elwardany <i>et al.</i> (triangles). Solid lines are the double modified Arrhenius fit E6.6 to all data sets, dashed line this work and Elwardany <i>et al.</i> and dotted like Eble and Elwarday <i>et al.</i>	164

Chapter 7

Figure 7.1 Model of the Energy Grained Master Equation for an association reaction from Glowacki <i>et al.</i>	170
Figure 7.2 Pre-reactive complex along the PES of OH + furan, geometrical parameters are bond lengths in Angstroms and bond angles in degrees. Optimized at MP2/6-311G(d,p); QCISD/6-311G(d,p), (in brackets) and MP2/6-311+G(2df,2p), (in parentheses), levels of theory.	172
Figure 7.3 Schematic energy diagram the potential energy surface for the formation of the C1 and C2 adducts by the reaction of furan with hydroxyl radical from Anglada <i>et al.</i>	173
Figure 7.4 Schematic energy diagram of the potential energy surface for the ring-opening process of formation of the C1 adduct from Anglada <i>et al.</i>	174
Figure 7.5 Schematic energy diagram of the potential energy surface of OH + furan in kJ mol^{-1} at the CCSD/6-311+G(3df,2p) level of theory.	175
Figure 7.6 Comparison of the predicted rate coefficient reported by Mousavipour <i>et al.</i> and experimental rate coefficient reported in the literature for OH + furan.....	176
Figure 7.7 Potential energy diagram for reaction between OH and furan at levels of ROCBS-QB3, (RHF-UCCSD(T)-F12a/cc-pVDZ-F12), and [RHF-UCCSD(T)-F12a/cc-pVTZ-F12]......	178

Figure 7.8 Oxidation pathways of furan proposed by Yuan <i>et al.</i> based at 298 K and 760 Torr.....	179
Figure 7.9 PES for the OH + 2-MF by Zhang <i>et al.</i> Energies in kJ mol ⁻¹ at 298 K obtained at the G3MP2B3 level of theory.	181
Figure 7.10 PES of OH + 2-MF showing the addition and abstraction channels from Davis and Sarathy. Energies are in kcal mol ⁻¹ and an average of calculations at the CBS-QB3 and G4 methods.	182
Figure 7.11 Comparison of the predicted rate coefficient reported by Davis and Sarathy and experimental rate coefficient reported in the literature for OH + 2-MF.....	184
Figure 7.12 Oxidation pathways of 2-MF proposed by Yuan <i>et al.</i> based on calculations at 298 K and 760 Torr.	185
Figure 7.13 Comparison of the predicted rate coefficient reported by Simmie and Metcalfe and experimental rate coefficient reported in the literature for OH + 2,5-DMF.	187
Figure 7.14 Oxidation pathways of 2,5-DMF proposed by Yuan <i>et al.</i> based on calculations at 298 K and 750 Torr	189
Figure 7.15 Reactions for OH + 2-MF in the 2-MF oxidation kinetic model by Somers <i>et al.</i> Corresponding Arrhenius parameters can be found in Table 7.4.....	190
Figure 7.16 Arrhenius plots of the reactions of OH + furan (a) OH + 2-MF (b) and OH + 2,5-DMF (c) with the total predicted rate coefficient from combustion models. Theoretical rate coefficients employed in the models are also shown. The rate coefficients determined by the double modified Arrhenius fit to experiment work carried out in this thesis is also shown.	194
Figure 7.17 Comparison of the species energies calculated at the M06-2x/cc-pVTZ level of theory for OH + 2-MF compared to equivalent species energy calculated at the G3MP2 level of theory by Zhang <i>et al.</i> (black diamonds) and the average of CBS-QB3 and G4 methods by Davis and Sarathy (blue stars). The red line is the line of best fit with a slope of (0.95 ± 0.04) and an intercept of (7.95 ± 3.91). Grey line is a 1:1.	195
Figure 7.18 Comparison of the vibrational frequencies calculated at the M06-2x/cc-pVTZ level of theory for OH + 2-MF compared to equivalent species frequencies calculated at the CBS-QB3 and G4 level of theory by Davis and Sarathy. The red line is the line of best fit with a slope of (0.99 ± 0.001) and an intercept of (-2.22 ± 2.10). Grey line is a 1:1.	196
Figure 7.19 Potential energy surface of OH + 2,5-DMF calculated using Gaussian at the M06-2x/cc-pVTZ level of theory.	198
Figure 7.20 Schematic energy diagram of the potential energy surface of OH + furan in kJ mol ⁻¹ at the CCSD/6-311+G(3df,2p) level of theory by Mousavipour <i>et al.</i> Highlighted addition channels are those relevant temperatures below 2000 K.....	200
Figure 7.21 Ring-opening products reported by Mousavipour <i>et al.</i> from the addition of OH to the C1 site in furan.....	200

Figure 7.22 Rate coefficients for OH + furan calculated by MESMER against the observed rate coefficients from the experiment of Chapter 4. The grey line shows a 1:1 fit. The slope of the line of best fit was determined as (0.92 ± 0.06) and the intercept was determined as $(1.55 \pm 1.34) \times 10^{-12} \text{ cm}^3 \text{ molecule}^{-1} \text{ s}^{-1}$	202
Figure 7.23 Rate coefficients for OH + furan simulated in MESMER (dashed green line) and the comparison with the experimental results discussed in Chapter 4 (black diamonds).	203
Figure 7.24 Modified Arrhenius fit to MESMER simulations for OH + furan (blue line, green dashed line) and unmodified Arrhenius fit to experimental results (black line, black diamonds) with associated 95 % confidence limits.	204
Figure 7.25 Yields for addition and abstraction channels for OH + furan predicted by MESMER at temperatures from 298 to 3000 K. The blue line represents addition and the orange line represents abstraction.	205
Figure 7.26 Schematic the C2 and C5 OH addition channels from a PES at the M06-2x/cc-pVTZ level.	206
Figure 7.27 Rate coefficients for OH + 2-MF calculated by MESMER against the observed rate coefficients from the experiment discussed in Chapter 5. The grey line shows a 1:1 fit. The slope of the line of best fit was determined as 0.98 ± 0.05 and the intercept was determined as $(3.60 \pm 21.6) \times 10^{-13} \text{ cm}^3 \text{ molecule}^{-1} \text{ s}^{-1}$	207
Figure 7.28 Rate coefficients for OH + 2-MF simulated in MESMER (dashed green line) and the comparison with the experimental results of Chapter 5 (black diamonds).....	208
Figure 7.29 Modified Arrhenius fit to MESMER simulations of OH + 2-MF (blue line, green dashed line) and experimental results (black line, black diamonds) with associated 95 % confidence limits.	209
Figure 7.30 Yields for addition and abstraction channels predicted by MESMER for the reaction of OH + 2-MF at temperatures from 298 to 600 K. Blue line represents the total addition of OH to the furan ring. Orange line represents the total H atom abstraction by OH.....	210
Figure 7.31 Experimental results for OH + 2-MF from this study (solid diamonds) and shock tube experiments by Elwardany <i>et al.</i> (open diamonds). The temperature dependence of the reaction begins to turn over at ~780 K.....	210
Figure 7.32 Rate coefficients for OH + 2,5-DMF calculated by MESMER against the observed rate coefficients from the experiment of Chapter 6. The grey line shows a 1:1 fit. The slope of the line of best fit was determined as 1.09 ± 0.04 and the intercept was determined as $(6.18 \pm 2.42) \times 10^{-12} \text{ cm}^3 \text{ s}^{-1}$	212
Figure 7.33 Pressure and temperature dependent results of OH + 2,5-DMF discussed in Chapter 6 (diamonds) with MESMER simulated rate coefficients (lines)	212

Figure 7.34 Troe fits using E8.4-E8.7(solid lines) to MESMER simulations for kinetics of OH + 2,5-DMF (solid diamonds) using a barrier height of -75.5 kJ mol⁻¹ in with $\langle \Delta E \rangle_{\text{down}} = 395 \text{ cm}^{-1}$ and $A = 1.07 \times 10^{-10} \text{ molecule}^{-1} \text{ cm}^3 \text{ s}^{-1}$ 214

Figure 7.35 Yields for addition and abstraction channels predicted by MESMER for the reaction of OH + 2,5-DMF at temperatures from 298 to 2400 K. Blue line represents the addition of OH to the C2 position. Orange line represents abstraction of an H atom by OH at the C1 and C3 positions. 215

Chapter 8

Figure 8.1 Summary of QOOH chemistry involved in autoignition processes. 220

Figure 8.2 Schematic potential energy surface showing the relationship between RO₂ and QOOH. 221

Figure 8.3 PES showing the isomerization and dissociation pathways of the QOOH from adapted from Zádor *et al.* 223

Figure 8.4 Summary of the relevant chemistry occurring within the reaction system. Processes shown in grey occur only for photolysis at a wavelength of 248 nm. 227

Figure 8.5 Simulated OH time-profiles (thick lines), using the reactions and rate coefficients listed in Table 8.1 for a range of O₂ concentrations, and the fit to the simulation using Equation 8.1 (thin lines). 231

Figure 8.6 Sensitivity of fits to determine k_3 to the values for k_3 used in the model input (defined as the ratio of the value for k_3 determined by fitting Equation 1 to the output from model simulations of the temporal behaviour of OH to the corresponding value for k_3 used as input in the model). 232

Figure 8.7 Sensitivity of fits to determine K_4 to the concentration of O₂ used in the model input (defined as the ratio of the value for K_4 determined by fitting Equation 8.1 to the output from model simulations of the temporal behaviour of OH to the corresponding value for K_4 used as input in the model, where $K_4 = k_4[\text{O}_2]$). 232

Figure 8.8 Sensitivity of fits to determine k_3 (filled squares) and K_4 (open circles) to those used as inputs for the model simulations of the temporal behaviour of OH occurring as a result of reactions R8.1-R8.6 as a function of the initial concentration of (CH₃)₃COOH. The sensitivities to k_3 and K_4 are as defined in Figures 8.6 and 8.7, respectively. 233

Figure 8.9 Sensitivity of fits to determine a) k_3 (filled squares) and b) K_4 (open circles) to those used as inputs for the model simulations of the temporal behaviour of OH occurring as a result of reactions R8.1-R8.6 as a function of the rate of COCl decomposition to produce Cl + CO following photolysis of (COCl)₂ at a wavelength of 248 nm. The sensitivities to k_3 and K_4 are as defined in Figures 8.5 and 8.6, respectively. 233

Figure 8.10 Typical OH time profiles (10 Torr N ₂ , 298 K) for a range of O ₂ concentrations (0 cm ⁻³ (black); 3.15 × 10 ¹⁶ cm ⁻³ (blue); 6.68 × 10 ¹⁶ cm ⁻³ (brown); 9.07 × 10 ¹⁶ cm ⁻³ (green); 1.64 × 10 ¹⁶ cm ⁻³ (red)). The inset shows the first 100 μs in greater detail.	235
Figure 8.11 Pressure dependence of <i>k</i> ₃ from 251 – 298 K in a) He bath gas and b) N ₂ bath gas. Data reported by Zádor <i>et al.</i> for experiments at (298 ± 2) K in He bath gas are also shown (open circles).	237
Figure 8.12 Temperature dependence of <i>k</i> ₂ , the rate coefficient for reaction of Cl with (CH ₃) ₃ COOH observed in this work (black points) with Arrhenius parameterisation (solid red line).	239
Figure 8.13 Temperature dependence of <i>k</i> ₆ , the rate coefficient for reaction of OH with (CH ₃) ₃ COOH observed in this work (black points) with Arrhenius parameterisation (solid red line). The parameterisation for <i>k</i> ₆ reported by Baasandorj <i>et al.</i> is also shown (solid blue line).	240
Figure 8.14 Variation of the rate coefficient describing the loss of OH in the system (<i>k</i> ' ₆) as a function of the O ₂ concentration for experiments performed at 298 K with similar (CH ₃) ₃ COOH concentrations.	241
Figure 8.15 Pressure dependence of <i>k</i> ₃ from 251 – 298 K in a) He bath gas and b) N ₂ bath gas. The solid lines are the MESMER fits which give a barrier height to decomposition of 44.7 kJ mol ⁻¹ , with Δ <i>E</i> _{down} = 89 cm ⁻¹ in He and Δ <i>E</i> _{down} = 147 cm ⁻¹ in N ₂ . Data reported by Zádor <i>et al.</i> for experiments at (298 ± 2) K in He bath gas are also shown (open circles).	243
Figure 8.16 Pressure dependence of <i>k</i> ₃ from in He bath gas observed in this work (filled data points) and by Zádor <i>et al.</i> (open data points). Solid lines are the MESMER fits to the observations made in this work, which gave a barrier height to decomposition of 44.7 kJ mol ⁻¹ and Δ <i>E</i> _{down} = 89 cm ⁻¹ in He. Broken lines are MESMER simulations using a barrier height of 48.1 kJ mol ⁻¹ and Δ <i>E</i> _{down} = 250 cm ⁻¹ , as reported by Zádor <i>et al.</i>	244
Figure 8.17 Results for <i>k</i> ₃ at 298 K reported by Zádor <i>et al.</i> and corresponding output from MESMER for simulations (black line, barrier to decomposition of 48.1 kJ mol ⁻¹ and <Δ <i>E</i> > _{down} = 250 cm ⁻¹) and fits to the results of Zádor <i>et al.</i> (coloured lines).	245
Figure 8.18 Troe fits using Equations E8.3-E8.6 (solid lines) to MESMER simulations (filled data points) using a barrier height of 44.7 kJ mol ⁻¹ in a) He, with <Δ <i>E</i> > _{down} = 89 cm ⁻¹ and b) N ₂ , with <Δ <i>E</i> > _{down} = 147 cm ⁻¹	247
Figure 8.19 Variation in χ ² for fits fixed to of <i>k</i> ₄ for data at a) 298 K; b) 282 K; c) 274 K; d) 251 K. In each case, the minimum in the χ ² for the fit, indicating the best fit to the data, corresponds to the value of <i>k</i> ₄ determined by the unconstrained fit (shown by filled symbols).	249
Figure 8.20 Experimental results for <i>k</i> ₄ as a function of temperature (black points) with Arrhenius fit to data (red solid line), giving <i>A</i> = (7.3 ± 6.8) × 10 ⁻¹⁴ cm ³ s ⁻¹ and <i>E</i> _a = -(5.4 ± 2.1) kJ mol ⁻¹ . Confidence intervals (95 %) for the Arrhenius fit are given by the red broken lines. Also shown are the measured (blue filled circle) and calculated (blue open circle) results for <i>k</i> ₄ at room temperature reported by Zádor <i>et al.</i>	251

List of Tables

Chapter 1

Table 1.1 Properties of ignition engines: petroleum spark-ignition (SI), diesel compression-ignition (CI) and homogenous charge compression ignition (HCCI).....	6
Table 1.2 Emission scaling factors for different blends of biodiesel relative to base diesel. Emissions are hydrocarbons (HC), carbon monoxide (CO), nitrogen oxides (NO _x) and particulate matter (PM).....	14
Table 1.3 Furan derivative structures and abbreviations.....	18

Chapter 4

Table 4.1 Room temperature rate coefficients for previous studies of OH reaction with furan. DF-RF Discharge flow resonance fluorescence. CP-GC continuous photolysis gas chromatography. FP-RF flash photolysis resonance fluorescence. LFP-LIF laser flash photolysis-laser induced fluorescence. *Results from absolute measurement technique. Results obtained using the relative rate method are provided as reported and updated for current recommendations for the rate coefficients of the reference reactions.....	82
Table 4.2 Room temperature rate coefficients for the reaction of OH + furan from this work and previous studies. Results for this work are given as an average of all experiments over 298 K and errors are given as 2σ	94
Table 4.3 Bimolecular rate coefficients from the decays of OH + furan at 298 K and 50 Torr with mesh filters applied to the photolysis laser beam.	95
Table 4.4 Average rate coefficients with standard deviation at several temperatures.....	98
Table 4.5 Average rate coefficients for OH + furan at temperatures between 298 and 595 K. Individual rate coefficients can be seen in the Appendix.....	99
Table 4.6 Comparison of Arrhenius parameters for the reaction of OH + furan between this work, Eble, and Wine and Thompson	100
Table 4.7 Arrhenius parameters from the fit of E4.3 to the combined data from this work and Elwardany <i>et al.</i> and from this work, Eble and Elwardany <i>et al.</i>	105

Chapter 5

Table 5.1 Literature rate coefficients for the oxidation of 2-MF by the OH radical and for the reaction of OH with reference compounds used in the relative rate experiments. Updated rate coefficients using recent literature for those reference compounds are shown. Values for <i>trans</i> -2-butene are taken from current IUPAC recommendations. Values for 1,3,5-trimethylbenzene are the highest and lowest rate coefficients available in the current literature...	114
--	-----

Table 5.2 Room temperature rate coefficients for the reaction of OH + 2-MF from this work and previous studies. Results for this work are given as an average of all experiments over 298 K.....	124
Table 5.3 Bimolecular rate coefficients from the decays of OH + 2-MF at 298 K and 50 Torr with mesh filters applied to the photolysis laser beam.....	125
Table 5.4 Average rate coefficients for OH + MF at temperatures between 298 and 770 K, errors are 1 σ . Individual rate coefficients can be seen in the Appendix.....	126
Table 5.5 Comparison of Arrhenius parameters for the reaction of OH + 2-MF between this work and Eble.....	128
Table 5.6 Arrhenius parameters from the fit of E5.3 to the combined data from this work and Elwardany <i>et al.</i> and from this work, Eble and Elwardany <i>et al.</i>	130
Chapter 6	
Table 6.1 Comparison of the physical properties of the fuels gasoline, 2,5-DMF and ethanol.	134
Table 6.2 Literature rate coefficients for the oxidation of 2,5-DMF by the OH radical and for the reaction of OH with reference compounds used in the relative rate experiments. Updated rate coefficients using recent literature for those reference compounds are shown. Values for <i>trans</i> -2-butene are taken from current IUPAC recommendations. Values for 1,3,5-trimethylbenzene are the highest and lowest rate coefficients available in the current literature.....	138
Table 6.3 Rate coefficients for OH + 2,5-DMF at 410 K and 50 Torr with mesh filters applied to the photolysis laser beam.	149
Table 6.4 Comparison of Arrhenius parameters for the reaction of OH + 2,5-DMF between this work and Eble. Fit to the k_{∞} of this work means errors are significantly smaller than parameters and so are omitted here.	157
Table 6.5 Arrhenius parameters from the fit of E6.6 to the combined data from this work and Elwardany <i>et al.</i> and from this work, Eble and Elwardany <i>et al.</i>	160
Chapter 7	
Table 7.1 Relative energies in kJ mol ⁻¹ for the formation of the C1 and C2 adducts with their associated transition states and pre-reactive complexes for OH + furan from studies by Anglada, Mousavipour <i>et al.</i> and Yuan <i>et al.</i>	178
Table 7.2 Relative energies in kJ mol ⁻¹ for the formation of the addition products and the methyl abstraction product with associated transition states and pre-reactive complexes for OH + 2-MF from studies by Zhang <i>et al.</i> and Davis and Sarathy.....	183
Table 7.3 Arrhenius parameters reported by Davis and Sarathy for the OH + 2-MF reaction calculated using CHEMRATE.	184

Table 7.4 Arrhenius parameters for the reaction of OH + 2-MF in the 2-MF oxidation kinetic model by Somers *et al* Reaction schemes can be seen in Figure 7.15.

.....190

Chapter 8

Table 8.1 Reactions and rate coefficients adopted in simulations of OH used to demonstrate the fidelity and sensitivity of Equation 8.1 in determinations of k_3 and k_4 (unless otherwise shown as varying in Figures 8.6-8.9).

Reactions R1 and R5 are treated as instantaneous, and thus represented by non-zero initial concentrations of Cl, COCl and OH, which were approximated from the absorption cross-sections of (COCl)₂ ($3.10 \times 10^{-19} \text{ cm}^2$) and (CH₃)₃COOH ($1.99 \times 10^{-20} \text{ cm}^2$) at 248 nm, typical laser fluence ($10 - 30 \text{ mJ cm}^{-2}$) and typical experimental concentrations of (COCl)₂ and (CH₃)₃COOH ($1 \times 10^{14} \text{ cm}^{-3}$ and $1 \times 10^{15} \text{ cm}^{-3}$ respectively). The reaction channel in Cl + (CH₃)₃COOH in which H-abstraction occurs from one of the methyl groups (leading to production of a peroxy radical, RO₂) is not included in the simulations..... 230

Table 8.2 Summary of results for k_3 235

Table 8.3 Summary of results for k_2 (Cl + (CH₃)₃COOH) and k_6 (OH + (CH₃)₃COOH) as a function of temperature. 238

Table 8.4 Summary of results for k_4 250

List of Abbreviations

B3LYP	Density functional theory exchange correlation hybrid
CBS	CBS Complete basis set
cc-pVDZ	Correlation-consistent polarised double zeta basis set
cc-pVTZ	Correlation-consistent polarised triple zeta basis set
CCSD	Coupled cluster theory with singles and doubles excitations
CI	Chemical impact ionisation
CI	Compression-ignition
CP-GC	Continuous photolysis-gas chromatography
DF	Discharge flow
EI	Electron impact ionisation
ES	Electrospray ionisation
FAB	Fast atom bombardment
FI	Field ionisation
FTIR	Fourier transform infrared spectroscopy
GC	Gas chromatography
GHG	Greenhouse gas
HC	Hydrocarbons
HCCI	Homogeneous charge compression ignition
IPCC	The United Nations Intergovernmental Panel on Climate Change
IR	Infrared
IRC	Intrinsic reaction coordinate
LFP-LIF	Laser flash photolysis-laser induced fluorescence
M06-2x	M06-2x A Minnesota exchange-correlation functional for density functional theory
MALDI	Matrix-assisted laser desorption/ionisation
MESMER	Master Equation Solver for Multi-Energy well Reactions
MFCs	Mass flow controllers
MP2	Møller Plesset perturbation theory
MPWB1K	Hybrid meta density functional theory
MS	Mass spectrometry
PES	Potential energy surface
PMT	Photomultiplier tube
QCISD	Quadratic configuration interaction with singles and doubles
RCM	Rapid compression machine
RF	Resonance Fluorescence
RO	Restricted open shell
RRKM	Rice and Ramsperger, Kassel, and Marcus
SCT	Simple collision theory
SI	Spark-ignition
SIMS	Secondary ion mass spectroscopy
SSA	Steady state approximation
TOF	Time-of-flight
TST	Transition state theory
UCCSD(T)	Open shell unrestricted coupled cluster theory with singles and doubles excitations and with estimated triples contributions
UMP2	Unrestricted Møller Plesset perturbation theory
UV	Ultra-violet
VOCs	Volatile organic compounds

WHO World Health Organisation

Chapter 1 Introduction

In the last 200 years, anthropogenic emissions of trace gases have resulted in substantial changes to the composition of the Earth's atmosphere and climate. Emissions of radiatively active species, commonly known as greenhouse gases (GHGs), have significantly contributed to a rise in global temperatures and a deterioration in air quality, particularly carbon dioxide (CO₂) from fossil fuel combustion.¹ There is a significant scientific interest in biofuels and their combustion properties owing to their potential to replace fossil fuels and to satisfy growing global energy demands. Biofuels offer a solution to reduce the impact fossil fuel combustion has on the environment while maintaining energy security and potentially improving air quality.

1.1 A Changing Atmosphere

1.1.1 CO₂ and the Atmosphere

The United Nations Intergovernmental Panel on Climate Change (IPCC) released their Fifth Assessment Report (AR5) in 2014 which outlined the impact increasing concentrations of GHGs have had on the Earth's atmosphere. The IPCC summarised the effect by describing the radiative forcing power of several positive and negative radiative forcers. Radiative forcing is defined by the IPCC as the net change in the energy balance of the Earth system due to some imposed perturbation.²

Perturbation of net radiation occurs when the concentrations of radiatively active species (e.g. GHGs and aerosols) change within the atmosphere, or when the amount of solar irradiance upon Earth changes, either by a change in solar fluxes or changes in Earth's surface reflection properties. The IPCC reported radiative forcing of species relative the pre-industrial era with 1750 taken as a reference pre-industrial year and measured radiative forcing in units of W m⁻² (Figure 1.1).

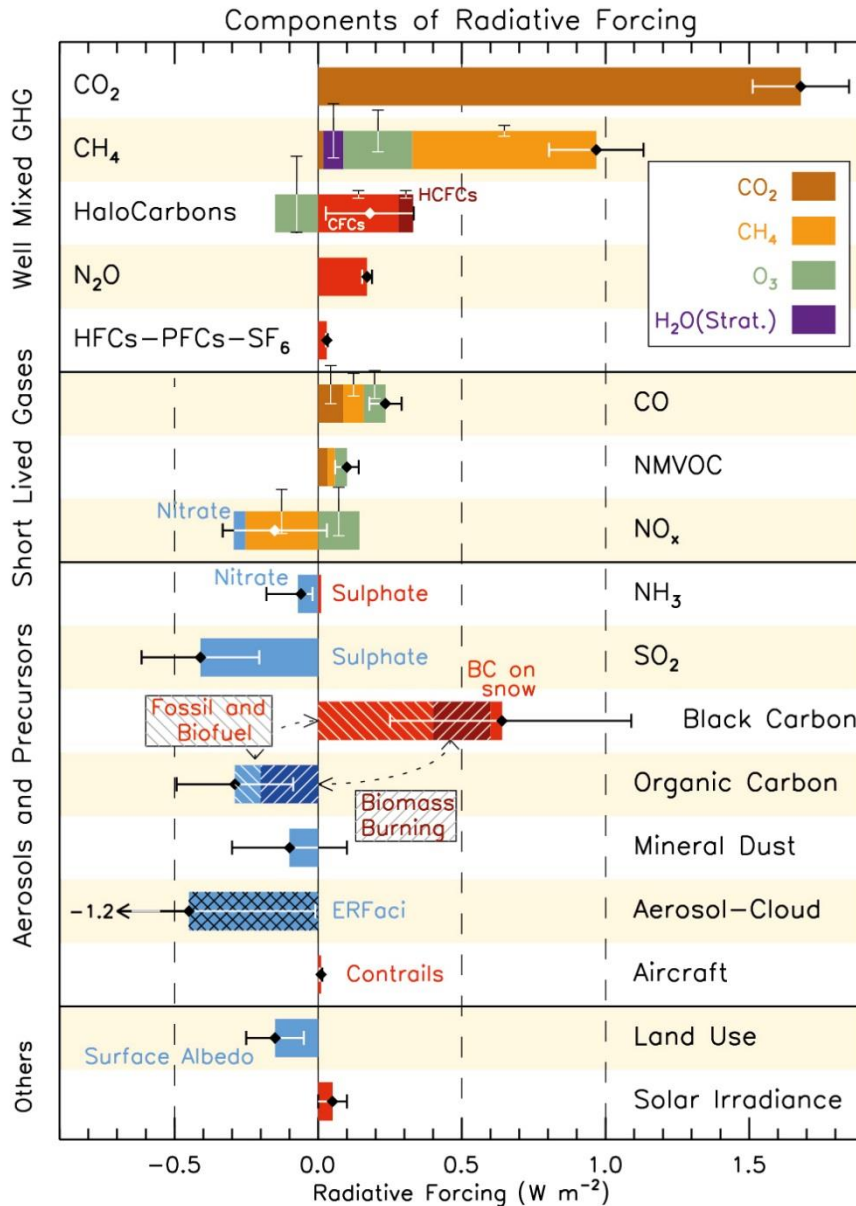


Figure 1.1 IPCC Fifth Assessment graph to show the radiative forcing effect in $W m^{-2}$ of key radiatively active species in the atmosphere relative to pre-industrial levels of 1750.³

An increase in the radiatively active species in the atmosphere has to lead changes to climate parameters and resulted in a new equilibrium state of the climate system.² Figure 1.1 shows that CO₂ has the largest radiative forcing effect; this is due to the increasing abundance of CO₂ in the atmosphere and its ability to enhance the absorption by the atmosphere of outgoing terrestrial radiation from the Earth's surface and simultaneously enhance the infrared radiation emitted at higher altitudes and colder temperatures. This is an example of positive radiative forcing and where the term

“greenhouse gas” originates, as the effects from CO₂ tends to warm the lower atmosphere and surface.⁴ Other radiatively active species, such as methane (CH₄), nitrous oxide (N₂O), ozone (O₃) and halocarbons, with increasing atmospheric concentrations as a result of anthropogenic activity also contribute to a warming climate by trapping additional radiative energy in the Earth’s atmosphere.

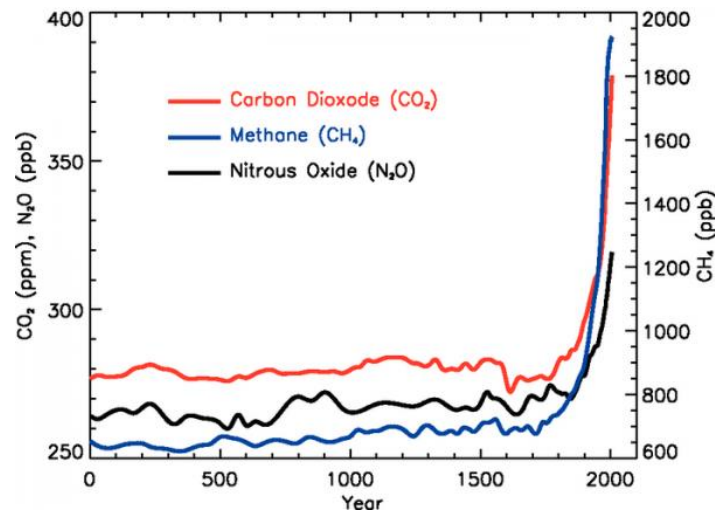


Figure 1.2 Atmospheric mixing ratios of three long-lived GHGs over 2000 years. Increases at around 1750 are attributed to anthropogenic activity during the industrial revolution. Mixing ratios are parts per million (ppm) for CO₂ and parts per billion (ppb) for N₂O and CH₄.⁵

1.1.2 Fossil Fuels and Transportation

GHGs concentrations, particularly CO₂, have increased rapidly since the start of the industrial era when mass global fossil fuel burning began (Figure 1.2). The introduction of coal burning as well as an increase in deforestation and biomass destruction has led to a significant increase in the abundance of CO₂ in the atmosphere. In the last century the introduction of vehicle use into everyday life, and consequentially the rapid growth in petroleum and diesel combustion, has led to a substantial increase in CO₂ emissions.⁵

Petrol and diesel are a mixture of complex hydrocarbons derived from refining crude oil and on combustion produce a mixture of several gases and particulate matter. As with

all combustion reactions, CO₂ and water vapour are primarily produced, as well as many other pollutants.

Nitrogen oxides such as NO and NO₂ (NO_x) are produced during engine combustion when nitrogen present in the air is oxidised, in addition to nitrogen containing compounds present in the fuels. Diesel engines produce much more NO_x gases than petroleum engines due to higher combustion temperatures. Sulphur dioxide (SO₂) is produced when diesel containing sulphur is burned during combustion and particulate matter (PM) is formed both during combustion and in the atmosphere as a result of pollutants found in exhaust fumes. Volatile organic compounds (VOCs) are released from unburned fuel and produced from incomplete combustion; petroleum releases more VOCs as it is a more volatile fuel than diesel. Incomplete fuel combustion leads to carbon monoxide (CO), especially in spark-ignition engines as they have lower combustion temperatures than diesel engines. Ozone (O₃), a tropospheric pollutant, is formed *via* photochemical reactions involving VOCs and NO_x.^{6,7}

Severe adverse health effects as a consequence of pollutants in ambient air can be detrimental to human life. In 2013, 7 million premature deaths occurred as a result of air pollution according to the World Health Organisation (WHO).⁸ Ill health caused by motor pollution can range from nausea and asthma to emphysema and lung cancer, and was recently linked to vascular dementia and Alzheimer's disease.⁹ Pollution also leads to reduced activity of the immune system and can be dangerous to those with susceptibility factors such as age, nutritional status and predisposing health conditions.^{10,11} Birth defects and serious child development delays as a result of air pollution have been seen in many cities internationally.¹²

There is pressure on governments to reduce carbon emissions and air pollution, and efforts to slow the effects of climate change and improve air quality can be seen in international legislation and treaties. The Kyoto protocol of 1997 and annual global

summits, as well as EU targets, regularly address the immediate need to reduce emissions. However, at times governments fail to negotiate terms and many targets have not been met.¹³

Biofuels have been proposed to mitigate the climate impact of fossil fuels and improve air quality. Biofuel blends are already commonplace in some countries such as Brazil¹⁴ and the EU has adopted a policy to aim to have 10% of transport fuel in every EU country come from renewable sources, such as biofuels, by 2020.¹⁵

1.2 Combustion

1.2.1 Engines

Spark-ignition (SI) petroleum and compression-ignition (CI) diesel engines are the most common internal combustion engines found in motor vehicles globally. Petroleum, commonly also known as petrol or gasoline, is employed to fuel cars using an SI engine. The combustion process is initiated by igniting a premixed air-fuel mixture using a spark from a spark plug, as shown in Figure 1.3. The reaction propagates through the mixture as a wave and the speed of combustion is determined by the rate at which heat and radicals diffuse into the gas ahead of the mixture. The timing of ignition in engines using SI depends on the position of the piston when the spark is ignited within the combustion chamber and is controlled in modern engines by an engine control unit.¹⁶ The ignition delay time in engines using SI is the time between the spark is ignited and a pressure rise within the engine.¹⁷ The temperature and pressure within the chamber vary depending on the position of the piston, temperatures can range from ~1000-2000 K and pressures can reach up to 60 bar¹⁷ (Table 1.1). Although SI engines are known as petrol or gasoline engines, they are able to operate with several other fuels such as ethanol and liquefied petroleum gas (LPG).

In contrast, diesel internal combustion engines operate by injecting diesel fuel into air compressed in the combustion chamber where temperature is elevated by the increase

in pressure, with temperatures increasing to above 2600 K.¹⁸ The pressure range of a diesel engine depends on the compression ratio exerted on the fuel mixture.¹⁷ The chemical reaction occurs at the interface where the fuel and air meet, and the rate of reaction is determined by the rate at which the fuel and air diffuse into the interface. Ignition timing in diesel engines is controlled by the compression stroke and the ignition delay is the time between the initial injection of fuel and the start of combustion, consisting of a physical delay in which the air and fuel mix, atomise and vaporise, and a chemical decay due to pre-combustion reactions.¹⁹

Diesel engines were until recently considered the most environmentally friendly of the two internal combustion engines owing to their greater efficiency, producing 116.8 g km⁻¹ of CO₂ compared with 121.7 g km⁻¹ produced by petrol engines.²⁰ However, recent studies have concluded that the elevated temperatures of diesel engines have resulted in a significant increase in NO_x emissions which are found to be dangerous to human health.

Engine	Temperature Range / K	Pressure Range / bar	Suitable Fuels
Petroleum SI	~1000-2000 ^{17,18}	~4-60 ¹⁷	Petrol, autogas, methanol, ethanol, bioethanol, hydrogen, nitromethane
Diesel CI	<2500 ¹⁸	Dependent on compression ratio	Diesel, Biodiesel
HCCI	Fuel dependent	Fuel dependent	Biofuels

Table 1.1 Properties of ignition engines: petroleum spark-ignition (SI), diesel compression-ignition (CI) and homogenous charge compression ignition (HCCI).

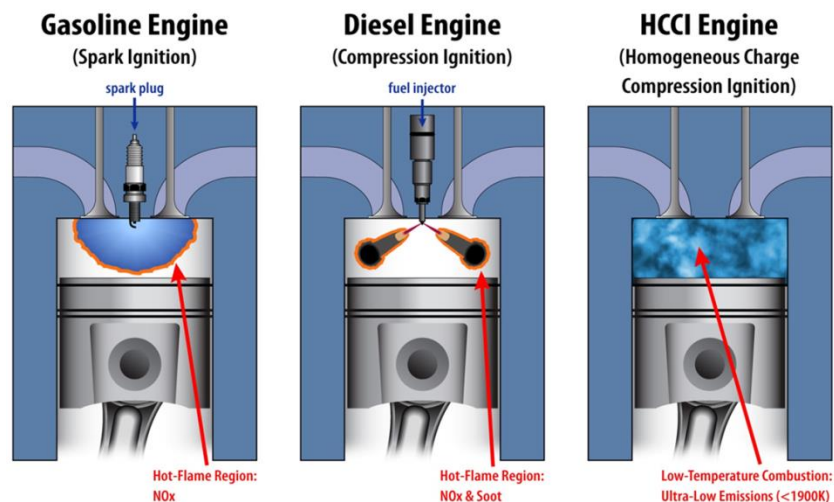


Figure 1.3 Schematic of a Spark-Ignition, Compression-Ignition and Homogeneous Charge Compression Ignition engine.²¹

Advances in technology means engines have been adapted to combine engine efficiency with low emissions compared to conventional spark-ignition or diesel engines. These advanced engines, such as in homogeneous charge compression ignition (HCCI) engines (Figure 1.3), rely on chemical kinetics in order to time ignitions.^{22,23} Fuel and air are premixed and compressed to the point of spontaneous ignition, known as autoignition. Unlike spark-ignition or diesel engines, where the timing of ignition is controlled, the ignition in HCCI engines is governed by gas phase chemistry of the primary elementary steps in fuel oxidation.²² Because the ignition delay is controlled by kinetics at low temperatures, rather than an external source, HCCI engines can operate at lower temperatures than traditional engines, reducing NO_x formation. HCCI engines can be developed to suit certain fuels, including biofuels. Employing biofuels in engines results in a net reduction in CO₂ production when compared to traditional fuels.²⁴

1.2.2 Fuel Chemistry

Fuel chemistry is critical to understanding low temperature combustion and central to the development and efficient use of biofuels.²⁵ Before any new fuel can be implemented,

combustion products, reaction kinetics and combustion mechanisms need to be known and understood.

Combustion is a process consisting of many elementary reactions. The combustion of a simple fuel, for example hydrogen, consists of over 20 elementary reactions.^{26,27} Combustion of a hydrocarbon such as diesel can have thousands of elementary reactions.²⁸ The interaction of the initiation, chain-branching, chain-propagation and termination reactions determine the whole combustion process. Initiation reactions, often involving the OH radical, are of vital importance for modelling fuel chemistry and the ignition process in particular.

Processes involved in combustion can be separated into high and low temperature regimes because of the differences in chemistry dominating the overall combustion processes at different temperatures. Temperatures above 1000 K, where traditional fuels operate, are considered high whereas low temperature combustion is said to occur below 1000 K.^{29,30}

1.2.3 High Temperature Combustion

Combustion processes can be divided into low or high temperatures regimes depending on the rate of three reactions involving hydrogen and molecular oxygen. At high temperatures, the combustion of an alkane, RH, can be initiated by an H abstraction by an OH radical (R1.1), or by thermal decomposition to produce an alkyl radical, R, and an H radical (R2), with the temperature determining which process dominates. At around 1000 K the reaction involving OH (R1) will dominate, but when the temperature is high enough to provide the amount of energy needed to break the alkyl chain of RH, R1.2 will dominate.



Recombination can occur or R can follow many reaction pathways to produce species such as alkanes, alkenes, aldehydes and ketones that can be themselves oxidised.

The H produced from the thermal decomposition of RH (R1.2) can react with oxygen to form the energised intermediate HO_2^* (R1.3). At high temperatures and low pressures HO_2^* can dissociate to the reactive hydroxyl radical, OH, and atomic oxygen, O, (R4). This is the most important branching reaction in the high temperature oxidation process. At low temperatures and higher pressures HO_2^* is quenched by the bath gas, M, and the relatively unreactive HO_2 is stabilised (R1.5), and so R1.4 becomes less significant.³¹



At high temperatures the amount of energy in the system results in R1.4 dominating and therefore the rate of combustion depends on the thermodynamics of R1.3. Above 1000 K, H, O and OH species are important chain carriers, and reactions involving these are significant as the principal route to fuel oxidation in hydrocarbon combustion.²⁹

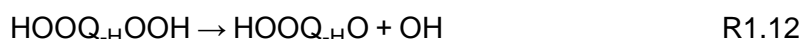
1.2.4 Low Temperature Combustion

Low temperature combustion of fuels occurs between 500 and 1000 K. At these lower temperatures it is the chemical kinetics that control the reaction rather than thermodynamics, therefore the kinetics and mechanism must be understood.³¹ Under certain conditions a fuel can spontaneously ignite, without an external source of ignition such as a spark, in a process known as autoignition. The autoignition of a fuel is dependent on pressure, temperature and oxygen concentration.

A fuel, RH, is oxidised in low temperature combustion by a radical, typically OH, to form the alkyl radical R (R1.6). R can add to oxygen to form an alkyl peroxy adduct, RO_2 (R1.7).



RO₂ can decompose to form a hydroperoxy radical, HO₂, and an alkene as seen in R8. However, HO₂ is relatively unreactive at these temperatures and so its formation effectively results in chain termination.³² The main pathway of RO₂ at these temperatures is isomerisation through an internal hydrogen abstraction to form the QOOH radical (R1.9). QOOH can decompose and cyclise to produce a cyclic ether (O-heterocycle) and a highly reactive OH radical, or form an alkene and an unreactive HO₂ radical which results again in termination. QOOH can also react with oxygen to produce O₂QOOH (R1.10), O₂QOOH can undergo isomerisation (R1.11) via an intermediate, HOOQ_{-H}OOH, to form a ketohydroperoxide, HOOQ_{-H}O, and an OH radical (R1.12). HOOQ_{-H}O is an important species as it can dissociate to produce two radicals, providing a chain branching pathway at low temperatures, such as OQ_{-H}O and OH which initiate the generation of many other radical species (R13).³²⁻³⁴



When the temperature of the system increases, the equilibrium of O₂ addition in R1.7 and R1.10 is shifted back toward the dissociation reaction, the termination reaction through R1.8 is favoured and the low temperature chain branching is quenched. This results in the rate of reaction slowing down and gives a negative temperature dependence.^{31,34,35} Figure 1.4 shows the overall mechanism for low temperature oxidation.

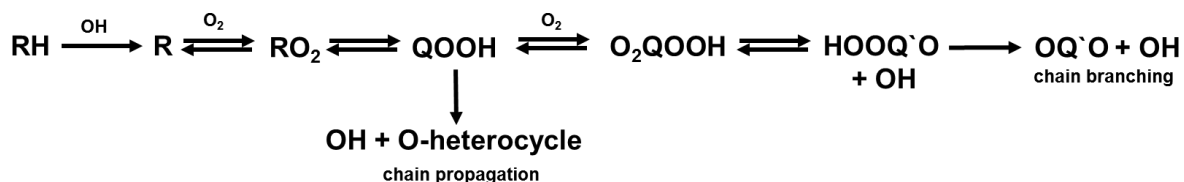
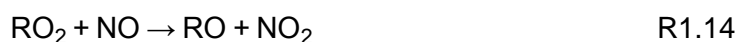


Figure 1.4 The mechanism for low temperature oxidation of the fuel RH adapted from Zádor *et al.*³²

1.2.5 Atmospheric Implications

The potential for fuels to enter the atmosphere through general use and as a result of incomplete combustion will have atmospheric implications. It is therefore vital to understand the chemistry at ambient conditions when assessing the viability of a fuel.

At ambient temperatures (~298 K) and atmospheric pressure, fuel exposed to air will form radicals through reactions with the OH radical (~10⁶ molecule cm⁻³)³⁶ (R1.6). These radicals will oxidise resulting in RO₂ radicals (R1.7). Nitric oxide (NO) emitted in exhaust fumes will react with RO₂ to form nitrogen dioxide (NO₂) (R1.14), which will be photolysed by sunlight (<400 nm), returning to NO and giving an O(³P) atom (R1.15). Tropospheric ozone (O₃) forms when O(³P) reacts with oxygen in the air (R1.16).



Tropospheric ozone is a pollutant and inhalation of ozone can cause respiratory irritation and enhance the effects of bronchitis, emphysema and asthma. Tropospheric ozone also damages vegetation and ecosystems, causing damage to plant foliage and a reduction in agricultural crop yields.³⁷

VOCs are released into the atmosphere during combustion, as well as from biogenic sources, and exist in the gas phase at ambient atmospheric temperature and pressure. VOCs are removed from the atmosphere via chemical reactions primarily with tropospheric ozone and the reactive hydroxyl and nitrate (NO₃) radical species present in the atmosphere. VOCs are also removed by wet and dry deposition and by photolysis.

For the majority of gas phase VOCs present in the troposphere, reaction with the OH radical is the dominant loss process. These reactions proceed via four reaction pathways: H-atom abstraction from C-H and O-H bonds; OH radical addition to double and triple carbon bonds; OH radical addition to aromatic rings; and OH radical interaction with N-, S-, and P- atoms.³⁸

1.2.6 Combustion Modelling

The measurement and calculation of rate coefficients for elementary reactions is of central importance in hydrocarbon oxidation and in modelling of combustion engines. Large scale use of fuels will inevitably lead to atmospheric emissions, the oxidation of which will have an impact on air quality and climate. Kinetics are also therefore of fundamental importance for the assessment of the impact of a fuel on the environment.

Combustion models describe the complex physical and chemical phenomena in combustion systems by solving differential equations describing the kinetics and transport of reactive species. Combustion models aid the design of more efficient internal combustion engines by ensuring an understanding of the fundamental physical processes occurring when a fuel combusts in a particular system. Models are capable in delivering information on many aspects of a fuel in an engine system, including induction time, species concentration, reaction rate, temperature, enthalpies, and mixture density, depending on the environment. As a result, models can provide data for the design and testing of new combustion systems where experiment is difficult or impossible. HCCI engine combustion models consist of simulation models built from chemical kinetics, as kinetics govern the ignition and therefore operation of HCCI engines.

In the literature there are examples of comprehensive detailed kinetic models for certain fuels that can operate within an HCCI engine. A detailed model attempts to describe the chemical changes of a system at the molecular level, allowing predictions of reaction pathways and trace species.³⁹ Of particular interest is the ability to predict the ignition

delay time for a fuel, since this indicates the time at which autoignition occurs following mixing of the fuel with air and is a critical parameter in the optimisation of engine conditions. Formation of pollutants, such as NO, under engine conditions is also of interest and can be predicted through detailed chemical modelling of the elementary reactions occurring in the system. Detailed combustion models have been described in the literature for a number of different fuels and biofuels, including hydrocarbon fuels, ethanol, dimethyl ether and methyl decanoate^{25,40-44}.

The basic data required for combustion models to simulate the complex chemical mechanism of even the simplest fuels potentially involves many hundreds of possible elementary reactions (section 1.2.3), however not all of these will have been investigated experimentally or theoretically. Biofuels are of increasing interest as alternatives to petroleum based fuels because they offer sustainability and reduced climatic impact. However, the development of novel biofuels is hindered by a lack of relevant detailed kinetic models. Combustion experiments are required to determine rate parameters to better define combustion mechanisms and therefore combustion models.⁴⁵

1.3 Biofuels

Biofuels are fuel alternatives produced from organic matter through biological processes and offer long-term fuel security through a renewable source. Biofuels are classified based on their methods of preparation and starting material used: either first, second or third generation. Bioalcohols and biodiesel are the most common biofuels and can be burned in conventional internal combustion engines. In comparison with diesel and petroleum based fuels, biofuels have reduced exhaust emissions to a significant degree.²⁴ For example, Table 1.2 shows the change in emission scaling factors for different blends of biodiesel relative to base diesel, with hydrocarbon (HC) emissions reducing from 0.95 for a 5 % biodiesel blend (B5) to 0.31 for a 100 % biodiesel blend (B100).

Blend	Emission			
	HC	CO	NO _x	PM
B5	0.95	0.98	1.00	0.98
B10	0.89	0.96	1.01	0.95
B15	0.84	0.94	1.01	0.93
B100	0.31	0.66	1.08	0.62

Table 1.2 Emission scaling factors for different blends of biodiesel relative to base diesel. Emissions are hydrocarbons (HC), carbon monoxide (CO), nitrogen oxides (NO_x) and particulate matter (PM).⁴⁶

The ideal biofuel would be completely CO₂ neutral, where CO₂ emitted from combustion would have been sequestered via photosynthesis during crop growth. However, this is often not the case, since the use of machinery and fertilizers during crop cultivation leads to net emissions, albeit much less than those for conventional fuels. Biofuels can be produced locally on a small scale and offer economic benefits as well as energy security and enhanced rural development.⁴⁷

1.3.1 Properties of biofuels

Biofuels are organic compounds primarily produced from biomass that, except biohydrogen, possess a functional group containing oxygen, unlike conventional fuels which consist primarily of long chain hydrocarbons.⁴⁸ The presence of oxygen increases the complexity of how the molecule will burn: alcohols, esters, carboxylic acids and ethers all have varying reaction characteristics. The oxygen content of biofuels allows for biodegradation, which is advantageous if a spillage was to occur but may be problematic in long term storage due to corrosion of steel tanks.⁴⁹ The presence of oxygen increases the polarity of a fuel, and so it is more likely to form crystals which could result in freezing at low temperatures, meaning biofuels may not be practical in colder climates.⁵⁰

1.3.2 Biofuel Combustion and Emissions

Biofuels undergo combustion with varying degrees of efficiency depending on the fuel composition. Although there is great potential to reduce atmospheric CO₂ concentrations, combustion of biofuels may result in increased atmospheric emissions of other pollutants that could have a negative effect on the environment. Bioethanol blended fuels produce increased concentrations of acetaldehyde and formaldehyde in comparison to petrol, but show decreased benzene emissions. Similarly, biodiesel can lower emissions of PM but there can also increase NO_x emissions.⁵¹

Biofuels are combustible at low temperatures in HCCI engines and therefore the radical chemistry of these fuels needs to be understood (see section 1.2.4). A thorough understanding of biofuel combustion mechanism is important if biofuels are to be employed in internal combustion engines.

1.3.3 First Generation Biofuels

First generation biofuels are produced directly from food crops such as sugar cane, corn and soybeans. First generation biofuels can be burned directly or blended with petroleum, distributed by current infrastructure and burned in existing engines. Examples of first generation fuels are bioethanol, biodiesel, vegetable oil and syngas, a synthetic fuel gas consisting of CO, CO₂ and H₂. In order to grow enough energy crops for a practical amount of fuel, large spaces of land is required, resulting in competition with food crops. This leads to rising food prices and reduced food security. The edible crops need to be replenished at least once a year, and growing them requires fertilizer and machinery which add to the carbon footprint of the biofuel. There are concerns over the environmental impact of first generation biofuels. The conversion of rainforests and grasslands to grow crops creates a biofuel carbon debt through the release of 17 to 420 times more CO₂ than the annual GHG reduction the biofuels would offer when used in place of fossil fuels, as well as disturbing ecosystems through the loss of biodiversity.⁵²

Concerns over water availability, seasonal variations and poor harvests also bring the sustainability of first generation biofuels into question.

1.3.4 Second Generation Biofuels

First generation biofuels are considered to be a short-term solution in finding alternative fuels. Second generation biofuels, also known as advanced biofuels, overcome some of the problems surrounding first generation fuels. Second generation biofuels are produced from non-edible feedstock via organic matter or perennial plants that naturally create oil and do not come into competition with food crops. Perennial plants are long-lived and therefore do not require as many fertilizers as first generation crops.⁵³ Perennials also have significant CO₂ fixing in soil, and so the overall net CO₂ contribution is lower than in first generation biofuels.⁵⁴ Second generation biofuels can also be derived from waste matter, municipal waste or waste vegetable oil and can be sourced from residue of agriculture and industry. Biomass can be directly burned for energy and electricity generation, or converted to liquid fuels using a variety of physical and chemical processes. The chemistry surrounding the conversion of biomass to biofuels has received a lot of attention from both chemical engineers as well as organic chemists as the resulting liquid can be used as fuel and as chemical feedstock in many syntheses. Some examples of second generation fuels include bioalcohols and biodiesel produced from cellulosic materials.⁵⁵

There are many advantages associated with second generation fuels. The disadvantages arise from difficulty in transforming the lignocellulosic biomass into a liquid fuel. The fibrous biomass consists of biopolymers: lignin, cellulose, and hemicellulose, which are difficult to break down and cannot be done in traditional ways such as fermentation. The plant cell wall is primarily made up of cellulose, a fibrous linear polymer held by hydrogen bonds and van der Waals forces. Hemicellulose is similar to cellulose but with the addition of branching sugars. These monosaccharides consist of pentoses

such as xylose, hexoses such as glucose, and uronic acids. Lignin is a large and complex structure of cross-linked polymers of phenolic monomers.⁵⁶

1.3.5 Third Generation Biofuels

Third generation biofuels are a relatively new class of biofuels derived from microorganisms, specifically algae. Also known as oilgae, this organism can photosynthesise thus converting CO₂ to biomass. This can be harvested and converted to biodiesel via an oil or bioalcohol through fermentation. Third generation biofuels are not the focus of this investigation and therefore will not be discussed further here.⁵⁷

1.3.6 Conversion Processes

Lignocellulosic biomass is an abundant and renewable raw material which can be converted to biofuels. The conversion of lignocelluloses to liquid fuel requires the deoxygenation and depolymerisation of the molecule. This is a difficult conversion but can be achieved through several processes, both thermochemical and biochemical. Thermochemical processes include pyrolysis, torrefaction and gasification. Pyrolysis is the thermochemical decomposition of organic biomass at high temperatures in the absence of oxygen. Liquids are formed by simultaneously depolymerising and fragmenting cellulose, hemicelluloses and lignin.⁵⁸ Torrefaction is a process similar to pyrolysis which is carried out at lower temperatures of 200-320 °C, under atmospheric pressure and in the absence of oxygen. Water within the biomass is released and the biopolymer hemicellulose breaks down. The result of torrefaction is a dry, blackened solid material.⁵⁹ Gasification is a process which forms synthetic gas, where a limited oxygen supply allows the formation of CO₂, CO and H₂. Gasification is the partial oxidation of carbonaceous fuel to convert to a gaseous product suitable to provide energy when heated.^{60,61}

Many biochemical techniques are in development, one process is fermentation with unique or genetically modified bacteria. This process is used for feedstock such as landfill gas and municipal waste.⁶²

1.4 Furans: Potential Biofuels

Furan and its alkylated derivatives, such as those shown in Table 4, have been proposed as suitable biofuels, which can be employed as fuel additives and replacements. Furans are aromatic heterocyclic ethers which can be derived from lignocellulosic biomass and municipal waste. In particular, 2,5-dimethylfuran (2,5-DMF) is of interest since it has been found to have an energy density (31.5 MJ dm^{-3}) similar to gasoline (32.2 MJ dm^{-3})⁶³. Furans can overcome some of the drawbacks associated with bioalcohols such as low energy density and water absorption from air.²⁴

Furans are emitted into the atmosphere from several sources, such as biomass burning and fossil fuel combustion.⁶⁴ They can also be formed in situ in the degradation of biogenically emitted conjugated dienes: furan is formed in the oxidation of 1,3-butadiene and 3-methylfuran is formed in the oxidation of isoprene.⁶⁵⁻⁶⁷

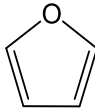
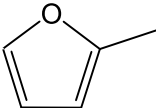
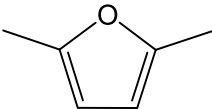
Compound	Abbreviation	Structure
furan	F	
2-methylfuran	2-MF	
2,5-dimethylfuran	2,5-DMF	

Table 1.3 Furan derivative structures and abbreviations

1.4.1 Production of Furans from Lignocellulosic Waste

There are several chemical conversion processes currently known for the conversion of hexose monosaccharide molecules found in lignocellulosic biomass into furan and its derivatives.⁶⁸⁻⁷⁰ There is already great interest in the conversion of biomass to derive

polymers and organic chemicals.⁷¹ A hexose molecule, for example fructose, can undergo several dehydration steps to remove three water molecules, resulting in 5-hydroxymethylfurfural (HMF). HMF can then be converted to the furan 2,5-DMF by hydrogenolysis steps as demonstrated by Dumesic *et al.* (2007) in Figure 1.5.⁶⁸

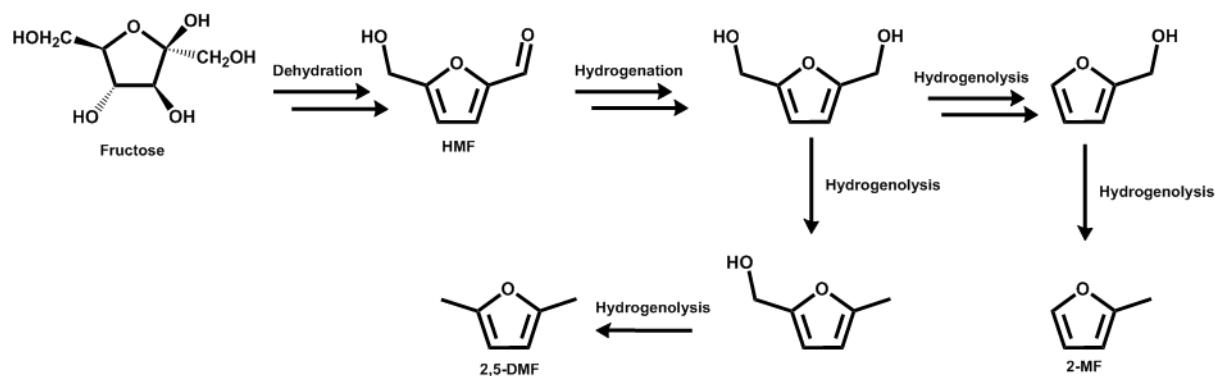


Figure 1.5 Production of 2,5-DMF and 2-MF from fructose via HMF, adapted from Dumesic *et al.* (2007)⁶⁸

Several transformation routes from hexose monosaccharides to furans are available, each offering different catalysts and conditions. Roman *et al.* (2007) reported conversion of hexose to HMF using a copper-ruthenium catalyst achieving a high yield.⁶⁸ Binder *et al.* (2009) reported a successful yield of HMF via a DMA (*N,N*-dimethylacetamide) catalyst containing LiCl.⁷¹ Alternatively, xylose may be used as a starting material to produce 2-methylfuran (2-MF) through conversion of furfural as suggested by Wang *et al.* (2014).⁶⁹

Established conversion processes, desirable fuel properties and environmental benefits have led to the proposition of furan biofuels as a replacement or additive to conventional fossil fuels. There is little in the literature on the kinetics, mechanism and products of the oxidation reaction of the furans and the impacts the furans and their combustion products have on the environment need to be further studied and understood before they can be employed as a fuel.^{24,72}

1.5 Outline of this Thesis

This thesis will describe the kinetics of low temperature oxidation mechanisms. The reaction of the hydroxyl radical, OH, with furan, 2-methylfuran and 2,5-dimethylfuran will be discussed and described both experimentally and theoretically. The chemistry of QOOH radicals derived *via* the reaction of Cl atoms with $(\text{CH}_3)_3\text{COOH}$ will also be described here, with this work detailing the first direct measurements of the temperature dependence for the kinetics of decomposition and reaction with O_2 for any QOOH species.

The experimental work described in this thesis focuses on reaction systems relevant to low temperature combustion. All reaction system involved the OH radical, which was monitored directly by laser induced fluorescence (LIF) in order to deduce the kinetics for each system.

A summary of the following chapters presented in this thesis:

Chapter 2 introduces theories of chemical reactions and kinetics.

Chapter 3 describes methods used to investigate gas phase kinetics and detect reactive species and introduces the laser flash photolysis laser induced fluorescence (LFP-LIF) technique used throughout this thesis to determine rate coefficients for bimolecular gas phase reactions. The details of the specific apparatus used throughout this thesis are provided.

Chapter 4 gives a detailed experimental study of the reaction between OH and furan ($\text{C}_4\text{H}_4\text{O}$).

Chapter 5 and 6 builds on the work presented in chapter 4 and report an experimental study of the reaction of OH with 2-methylfuran ($\text{C}_5\text{H}_6\text{O}$) and 2,5-dimethylfuran ($\text{C}_6\text{H}_8\text{O}$). Rate coefficients are determined as a function of pressure and temperature.

Chapter 7 gives a detailed theoretical analysis of the furan oxidation systems as well as a comparison between the experimental results from this work and theoretical studies in the literature.

Chapter 8 describes the decomposition of the QOOH radical to form OH in the absence and presence of O₂. OH yields are determined as a function of pressure and temperature.

The final chapter provides a summary of all experimental work presented in this thesis and its scientific significance.

1.6 References

1. Hartmann, D.L., A.M.G. Klein Tank, M. Rusticucci, L.V. Alexander, S. Brönnimann, Y. Charabi, F.J. Dentener, E.J. Dlugokencky, D.R. Easterling, A. Kaplan, B.J. Soden, P.W. Thorne, M. Wild and P.M. Zhai. 2013: *Observations: Atmosphere and Surface. In: Climate Change 2013: The Physical Science Basis. Contribution of Working Group I to the Fifth Assessment Report of the Intergovernmental Panel on Climate Change* Cambridge University Press, Cambridge, United Kingdom and New York, NY, USA, 2013.
2. IPCC, 2013: *Climate Change 2013: The Physical Science Basis. Contribution of Working Group I to the Fifth Assessment Report of the Intergovernmental Panel on Climate Change*. Cambridge University Press, Cambridge, United Kingdom and New York, NY, USA, 2014.
3. Myhre, G., D. Shindell, F.-M. Bréon, W. Collins, J. Fuglestvedt, J. Huang, D. Koch, J.-F. Lamarque, D. Lee, B. Mendoza, T. Nakajima, A. Robock, G. Stephens, T. Takemura and H. Zhang. *Anthropogenic and Natural Radiative Forcing. The Physical Science Basis. Contribution of Working Group I to the Fifth Assessment Report of the Intergovernmental Panel on Climate Change 2013*.
4. Brasseur, G., Orlando, J. And Tyndall, G. *Atmospheric Chemistry and Global Change*. New York: Oxford University Press, 1999,
5. Forster, P., V. Ramaswamy, P. Artaxo, T. Berntsen, R. Betts, D.W. Fahey, J. Haywood, J. Lean, D.C. Lowe, G. Myhre, J. Nganga, R. Prinn, G. Raga, M. Schulz and R. Van Dorland *Changes in Atmospheric Constituents and in Radiative Forcing. In: Climate Change 2007: The Physical Science Basis. Contribution of Working Group I to the Fourth Assessment Report of the Intergovernmental Panel on Climate Change*. Cambridge, United Kingdom and New York, NY, USA, 2007.
6. Faiz, A., C.S. Weaver and M.P. Walsh. *Air Pollution from Motor Vehicles: Standards and Technologies for Controlling Emissions*. World Bank, 1996, pp.xiii-xv.
7. Winther, M. Petrol passenger car emissions calculated with different emission models. *Science of The Total Environment*, 1998, **224**(1–3), pp.149-160.
8. *Economic cost of the health impact of air pollution in Europe: Clean air, health and wealth*. Copenhagen: WHO Regional Office for Europe: WHO Regional Office for Europe, 2015.
9. Moulton, P.V. and W. Yang. Air Pollution, Oxidative Stress, and Alzheimer's Disease. *Journal of Environmental and Public Health*, 2012, **2012**, p.9.

10. Kampa, M. and E. Castanas. Human health effects of air pollution. *Environmental Pollution*, 2008, **151**(2), pp.362-367.
11. Wong, G.W.K. Air pollution and health. *The Lancet Respiratory Medicine*, **2**(1), pp.8-9.
12. Radim J. Šrám, B.B., Jan Dejmek and Martin Bobak. Ambient Air Pollution and Pregnancy Outcomes: A Review of the Literature. *Environmental Health Perspectives*, 2005, **113**(4), pp.375-382.
13. Helm, D. Climate-change policy: why has so little been achieved? *Oxford Review of Economic Policy*, 2008, **24**(2), pp.211-238.
14. Lefol Nani Guarieiro, L. and A. Lefol Nani Guarieiro. Vehicle Emissions: What Will Change with Use of Biofuel? In: Z. FANG, ed. *Biofuels - Economy, Environment and Sustainability*. InTech, 2013, pp.357-386.
15. Heather D.C. Hamje, H.H., Laura Lonza, Heiko Maas, Alan Reid, Kenneth D. Rose, Tom Venderbosch. European Commission. *EU renewable energy targets in 2020: Revised analysis of scenarios for transport fuels*. Joint Research Centre – Institute for Energy and Transport Luxembourg: Publications Office of the European Union
16. Hartman, J. *How to Tune and Modify Engine Management Systems*. Motorbooks, 2004, pp.65-69.
17. Srinivasan, S. *Automotive Engines*. McGraw-Hill Education (India) Pvt Limited, 2001,
18. Dawn K. Manley, A.M., And Craig A. Taatjes. Research needs for future internal combustion engines. *Phys. Today*, 2008, **61**(11), pp.47-52.
19. Lakshminarayanan P.A., A.Y.V. *Ignition Delay in a Diesel Engine*. In: *Modelling Diesel Combustion*. [online]. Springer, Dordrecht., 2010.
20. Environment, T. *CO₂ Emissions from Cars: the Facts*. European Federation for Transport and Environment AISBL, 2018.
21. Hairuddin, A.A., A. Wandel and T.F. Yusaf. An Introduction to a Homogeneous Charge Compression Ignition Engine. *Journal of Mechanical Engineering and Sciences*, 2014, **7**, pp.1042-1052.
22. Scheer, A.M., *et al.* Low-temperature combustion chemistry of novel biofuels: resonance-stabilized QOOH in the oxidation of diethyl ketone. *Physical Chemistry Chemical Physics*, 2014, **16**(26), pp.13027-13040.
23. Taatjes, C.A., *et al.* *Advanced fuel chemistry for advanced engines*. SAND2009-6051. Sandia National Laboratories, 2009.
24. Luque, R., *et al.* Biofuels: a technological perspective. *Energy & Environmental Science*, 2008, **1**(5), pp.542-564.
25. Kohse-Höinghaus, K., *et al.* Biofuel combustion chemistry: from ethanol to biodiesel. *Angewandte Chemie International Edition*, 2010, **49**(21), pp.3572-3597.
26. Li, J., *et al.* An updated comprehensive kinetic model of hydrogen combustion. *International Journal of Chemical Kinetics*, 2004, **36**(10), pp.566-575.
27. Smirnov, N.N. and V.F. Nikitin. Modeling and simulation of hydrogen combustion in engines. *International Journal of Hydrogen Energy*, 2014, **39**(2), pp.1122-1136.
28. Warnatz, J., U. Maas and R.W. Dibble. *Combustion: Physical and Chemical Fundamentals, Modeling and Simulation, Experiments, Pollutant Formation*. Springer Berlin Heidelberg, 2013, pp.84-86.
29. Griffiths, J.F. and J.A. Barnard. *Flame and Combustion, 3rd Edition*. Taylor & Francis, 1995, pp.94-97.
30. Warnatz, J. Hydrocarbon oxidation high-temperature chemistry. *Pure and applied chemistry*, 2000, **72**(11), pp.2101-2110.
31. Straun H. Robertson, P.W.S.a.M.J.P. *Low-Temperature Combustion and Autoignition: Chapter 2: Elementary Reactions*. Elsevier Science, 1997,

32. Zádor, J., C.A. Taatjes and R.X. Fernandes. Kinetics of elementary reactions in low-temperature autoignition chemistry. *Progress in Energy and Combustion Science*, 2011, **37**(4), pp.371-421.
33. Pilling, M.J., S.H. Robertson and P.W. Seakins. Elementary radical reactions and autoignition. *Journal of the Chemical Society, Faraday Transactions*, 1995, **91**(23), pp.4179-4188.
34. Miller, J.A., M.J. Pilling and J. Troe. Unravelling combustion mechanisms through a quantitative understanding of elementary reactions. *Proceedings of the Combustion Institute*, 2005, **30**(1), pp.43-88.
35. Westbrook, C.K. Biofuels Combustion. *Annual Review of Physical Chemistry*, 2013, **64**(1), pp.201-219.
36. Stone, D., L.K. Whalley and D.E. Heard. Tropospheric OH and HO₂ radicals: field measurements and model comparisons. *Chemical Society Reviews*, 2012, **41**(19), pp.6348-6404.
37. Agency, U.S.E.P. *Ozone*. Washington, DC: Office of Air and Radiation EPA, 2003.
38. Kwok, E.S.C. and R. Atkinson. Estimation of hydroxyl radical reaction rate constants for gas-phase organic compounds using a structure-reactivity relationship: An update. *Atmospheric Environment*, 1995, **29**(14), pp.1685-1695.
39. Simmie, J.M. Detailed chemical kinetic models for the combustion of hydrocarbon fuels. *Progress in Energy and Combustion Science*, 2003, **29**(6), pp.599-634.
40. Marinov, N.M. A detailed chemical kinetic model for high temperature ethanol oxidation. *International Journal of Chemical Kinetics*, 1999, **31**(3), pp.183-220.
41. Muharam, Y. and J. Warnatz. Kinetic modelling of the oxidation of large aliphatic hydrocarbons using an automatic mechanism generation. *Physical Chemistry Chemical Physics*, 2007, **9**(31), pp.4218-4229.
42. Curran, H.J., S.L. Fischer and F.L. Dryer. The reaction kinetics of dimethyl ether. II: Low-temperature oxidation in flow reactors. *International Journal of Chemical Kinetics*, 2000, **32**(12), pp.741-759.
43. Fischer, S.L., F.L. Dryer and H.J. Curran. The reaction kinetics of dimethyl ether. I: High-temperature pyrolysis and oxidation in flow reactors. *International Journal of Chemical Kinetics*, 2000, **32**(12), pp.713-740.
44. Hoffman, S.R. and J. Abraham. A comparative study of n-heptane, methyl decanoate, and dimethyl ether combustion characteristics under homogeneous-charge compression-ignition engine conditions. *Fuel*, 2009, **88**(6), pp.1099-1108.
45. Baulch, D.L. *Low-Temperature Combustion and Autoignition: Chapter 3: Kinetic Databases*. 1997, pp.236-237.
46. Group, A.Q.E. *Road Transport Biofuels: Impact on UK Air Quality*. Department for Environment, Food and Rural Affairs; Scottish Government; Welsh Assembly Government; and Department of the Environment in Northern Ireland.
47. Dale, B.E., *et al.* Take a Closer Look: Biofuels Can Support Environmental, Economic and Social Goals. *Environmental Science & Technology*, 2014, **48**(13), pp.7200-7203.
48. Demirbas, A. Combustion Efficiency Impacts of Biofuels. *Energy Sources, Part A: Recovery, Utilization, and Environmental Effects*, 2009, **31**(7), pp.602-609.
49. Geyer, W.B. Compatibility of steel with oxygenation fuels. *In: ILTA Conference* 1996.
50. Kesieme, U., *et al.* Biofuel as an alternative shipping fuel: technological, environmental and economic assessment. *Sustainable Energy & Fuels*, 2019, **3**(4), pp.899-909.
51. Anderson, L.G. Effects of using renewable fuels on vehicle emissions. *Renewable & Sustainable Energy Reviews*, 2015, **47**, pp.162-172.

52. Fargione, J., *et al.* Land Clearing and the Biofuel Carbon Debt. *Science*, 2008, **319**(5867), pp.1235-1238.
53. Alves, A.A., *et al.* Perennial plants for biofuel production: Bridging genomics and field research. *Biotechnology Journal*, 2015, **10**(4), pp.505-507.
54. Abraha, M., *et al.* Evapotranspiration of annual and perennial biofuel crops in a variable climate. *GCB Bioenergy*, 2015, **7**(6), pp.1344-1356.
55. Zah, R., *et al.* *Future Perspectives of 2nd Generation Biofuels*. Hochschulverlag AG, 2010, pp.9.
56. Kumar, P., *et al.* Methods for Pretreatment of Lignocellulosic Biomass for Efficient Hydrolysis and Biofuel Production. *Industrial & Engineering Chemistry Research*, 2009, **48**(8), pp.3713-3729.
57. Singh, N.R. Chapter 5 Biofuels. *In: The Biofuels Handbook*. The Royal Society of Chemistry, 2011, pp.160-198.
58. Mohan, D., C.U. Pittman and P.H. Steele. Pyrolysis of Wood/Biomass for Bio-oil: A Critical Review. *Energy & Fuels*, 2006, **20**(3), pp.848-889.
59. Prins, M.J., K.J. Ptasiński and F.J.J.G. Janssen. Torrefaction of wood: Part 2. Analysis of products. *Journal of Analytical and Applied Pyrolysis*, 2006, **77**(1), pp.35-40.
60. Higman, C. and M. Van Der Burgt. Chapter 1 - Introduction. *In: C. HIGMAN and M.V.D. BURGT, eds. Gasification (Second Edition)*. Burlington: Gulf Professional Publishing, 2008, pp.1-9.
61. Lange, J.-P. Lignocellulose conversion: an introduction to chemistry, process and economics. *Biofuels, Bioproducts and Biorefining*, 2007, **1**(1), pp.39-48.
62. Saxena, R.C., D.K. Adhikari and H.B. Goyal. Biomass-based energy fuel through biochemical routes: A review. *Renewable and Sustainable Energy Reviews*, 2009, **13**(1), pp.167-178.
63. Malpani, S. and E. Joseph. 2, 5-Dimethylfuran as A Bio-Fuel. *IOSR-JESTFT*, 2015, **9**(5), pp.71-72.
64. Yokelson, R.J., *et al.* The Tropical Forest and Fire Emissions Experiment: overview and airborne fire emission factor measurements. *Atmos. Chem. Phys.*, 2007, **7**(19), pp.5175-5196.
65. Berndt, T. and O. Böge. Atmospheric Reaction of OH Radicals with 1,3-Butadiene and 4-Hydroxy-2-butenal. *The Journal of Physical Chemistry A*, 2007, **111**(48), pp.12099-12105.
66. Sprengnether, M., *et al.* Product analysis of the OH oxidation of isoprene and 1,3-butadiene in the presence of NO. *Journal of Geophysical Research: Atmospheres*, 2002, **107**(D15), pp.ACH 8-1-ACH 8-13.
67. Francisco-Márquez, M., *et al.* A Possible Mechanism for Furan Formation in the Tropospheric Oxidation of Dienes. *Environmental Science & Technology*, 2005, **39**(22), pp.8797-8802.
68. Roman-Leshkov, Y., *et al.* Production of dimethylfuran for liquid fuels from biomass-derived carbohydrates. *Nature*, 2007, **447**(7147), pp.982-U5.
69. Wang, J., *et al.* Efficient catalytic conversion of lignocellulosic biomass into renewable liquid biofuels via furan derivatives. *RSC Advances*, 2014, **4**(59), pp.31101-31107.
70. Tong, X., Y. Ma and Y. Li. Biomass into chemicals: Conversion of sugars to furan derivatives by catalytic processes. *Applied Catalysis A: General*, 2010, **385**(1-2), pp.1-13.
71. Binder, J.B. and R.T. Raines. Simple Chemical Transformation of Lignocellulosic Biomass into Furans for Fuels and Chemicals. *Journal of the American Chemical Society*, 2009, **131**(5), pp.1979-1985.
72. Qian, Y., *et al.* Recent progress in the development of biofuel 2,5-dimethylfuran. *Renewable and Sustainable Energy Reviews*, 2015, **41**, pp.633-646.

Chapter 2 Gas Phase Kinetics

The ability to understand the chemistry of complex systems such as those occurring in combustion requires knowledge and understanding of the kinetics of reactive species - the rates at which such species interact with each other.

2.1 Theory of Gas Phase Kinetics

For the general gas phase reaction



the change in extent of reaction $\delta\xi$ is given by:

$$\delta\xi = \frac{\delta n_Q}{\nu_Q} \quad \text{E2.1}$$

where δn_Q is the change in amount of species Q in the reaction, and ν_Q the stoichiometric number for species Q (defined as negative for reactants and positive for products). For the general reaction therefore:

$$\delta\xi = \frac{\delta n_A}{-a} = \frac{\delta n_B}{-b} = \frac{\delta n_C}{+c} = \frac{\delta n_D}{+d} \quad \text{E2.2}$$

and the rate \hat{r} of reaction is defined as:

$$\hat{r} = \frac{d\xi}{dt} = \frac{1}{\nu_Q} \frac{dn_Q}{dt} \quad \text{E2.3}$$

In most situations it is more convenient to consider the intensive rate of change of concentration, r , rather than the extensive rate of change of amount, \hat{r} . The rate r of reaction is thus more commonly defined as:

$$r = \frac{1}{\nu_Q} \frac{d\left(\frac{n_Q}{V}\right)}{dt} = \frac{1}{\nu_Q} \frac{d[Q]}{dt} \quad \text{E2.4}$$

Experimentally it has been shown that the rate r of reaction is often given by the product of a coefficient k (the rate coefficient or rate constant), and each reactant concentration raised to an experimentally determined exponent in the rate equation:

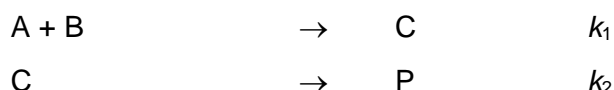
$$r = k [A]^\alpha [B]^\beta \quad \text{E2.5}$$

The exponents α and β are termed the orders of reaction with respect to reactants A and B respectively, and the overall order of the reaction is given by the sum of the exponents in the rate equation ($\alpha + \beta$). For an elementary reaction, one that takes place in a single step, the order of reaction with respect to a particular reactant is equivalent to the stoichiometric number for that reactant. The overall order of an elementary reaction, termed the molecularity of the reaction, therefore corresponds to the total number of reactant molecules participating in the reaction. An elementary reaction involving only one reactant species is therefore termed unimolecular, and is a first order reaction, an elementary reaction of two species is termed a bimolecular reaction and is second order, and an elementary reaction of three species is termed termolecular and is a third order reaction.

For an overall reaction consisting of a number of known elementary reactions it is often possible to derive the overall rate equation from the elementary rate equations using the steady state approximation. The steady state approximation (SSA) assumes that, after an initial induction period, the concentrations of reactive reaction intermediates reach a small and constant level. Thus, for the overall reaction



consisting of the elementary reactions



the rate equation for formation of product P, which may be written

$$\frac{+d[\text{P}]}{dt} = k_2 [\text{C}] \quad \text{E2.6}$$

can be simplified by application of the steady state approximation to species C:

$$\frac{+d[\text{C}]}{dt} = k_1 [\text{A}][\text{B}] - k_2 [\text{C}] \approx 0 \quad (\text{SSA}) \quad \text{E2.7}$$

giving $k_2 [\text{C}] = k_1 [\text{A}][\text{B}]$ and hence

$$\frac{+d[\text{P}]}{dt} = k_1 [\text{A}][\text{B}] \quad \text{E2.8}$$

In this case, the steady state approximation has been applied to the intermediate species C. The steady state approximation requires that for species C to have a small and invariant concentration the rate of removal of C far exceeds its rate of production, which is often the case for reactive intermediate species.

2.2 Temperature Dependence of Reaction Rates

An empirical experimental observation is that, for many reactions, the rate coefficient k varies with temperature according to the Arrhenius equation:¹

$$k = A \exp\left(-\frac{E_a}{RT}\right) \quad \text{E2.9}$$

where A is the pre-exponential factor, E_a the activation energy for reaction, R the gas constant and T the absolute temperature. The pre-exponential factor and the activation energy are described collectively as the Arrhenius parameters, and are used to parameterise the temperature dependence of k . Several theories have been advanced to explain this temperature dependence, and a brief summary of these is given below.

2.3 Bimolecular Gas Phase Reaction Rate Theory

At the most basic level, bimolecular reaction rates in the gas phase can be rationalised in terms of simple collision theory (SCT), in which atoms and molecules are treated as hard, structureless spheres undergoing elastic collisions. It is assumed that elementary bimolecular reactions are collisional processes and that, apart from in collision, no intermolecular forces are in operation. The rate, r , of reaction between two species A and B is thus equated to the collision frequency between the reactants, Z_{AB} , multiplied by the fraction, F , of colliding species with sufficient energy to overcome an energy barrier to rearrangement of electrons occurring during reaction. Thus:

$$r = Z_{AB} F \quad \text{E2.10}$$

The collision frequency, the total number of collisions between A and B in unit time, is obtained from the kinetic theory of gases and is given by:

$$Z_{AB} = V_{\text{col}} L^2 [A][B] \quad \text{E2.11}$$

where V_{col} is the 'collision volume' (the notional volume swept out by a moving molecule in unit time), L is Avogadro's constant and $[A]$ and $[B]$ are the concentrations of A and B in molar units respectively. The collision volume is determined by the product of the

collision cross-section for reaction, σ_{AB} , and the mean relative speed of molecules A and B, \bar{c}_{rel} . Thus:

$$\begin{aligned} V_{col} &= \sigma_{AB} \bar{c}_{rel} & \text{E2.12} \\ &= \sigma_{AB} \left(\frac{8k_B T}{\pi \mu} \right)^{1/2} \end{aligned}$$

where k_B is the Boltzmann constant, T the temperature and μ the reduced mass of species A and B. From (E2.11), the collision frequency therefore becomes:

$$Z_{AB} = \sigma_{AB} \left(\frac{8k_B T}{\pi \mu} \right)^{1/2} L^2 [A][B] \quad \text{E2.13}$$

The fraction, F , of molecules with sufficient energy to react on collision is given by the fraction of molecules with a kinetic energy above a certain critical value, ε , within a Boltzmann distribution of kinetic energies. The Boltzmann distribution of kinetic energies, $f(E)$, is described by:

$$f(E) = \frac{1}{k_B T} \exp\left(-E/k_B T\right) \quad \text{E2.14}$$

Integration of E2.14 between limits of ε , the critical energy for reaction, and infinity gives the fraction, F , of molecules with kinetic energy, along the line of centers, above the critical value:

$$\begin{aligned} F = f(E \geq \varepsilon) &= \int_{\varepsilon}^{\infty} \frac{1}{k_B T} \exp\left(-E/k_B T\right) dE & \text{E2.15} \\ &= \frac{1}{k_B T} \int_{\varepsilon}^{\infty} \exp\left(-E/k_B T\right) dE \\ &= \exp\left(-\varepsilon/k_B T\right) \end{aligned}$$

Simple collision theory therefore predicts the rate, r , of a bimolecular reaction between species A and B to be given by:

$$r = \sigma_{AB} \left(\frac{8k_B T}{\pi\mu} \right)^{1/2} L^2 [A][B] \exp\left(-\varepsilon/k_B T\right) \quad \text{E2.16}$$

It thus follows that, for an elementary reaction between A and B, collision theory predicts the rate coefficient, k , to be given by:

$$k = \sigma_{AB} \left(\frac{8k_B T}{\pi\mu} \right)^{1/2} L^2 \exp\left(-\varepsilon/k_B T\right) \quad \text{E2.17}$$

which resembles the experimentally determined Arrhenius equation:

$$k = A \exp\left(-E_a/RT\right) \quad \text{E2.9}$$

Although simple collision theory qualitatively predicts the broad features of many rate coefficients, notably the exponential dependence of k on temperature, and provides some insight as to the physical significance of the Arrhenius parameters, it cannot make accurate quantitative predictions of rate coefficients.¹ The limitations of the theory arise from the assumptions that molecules act as hard spheres that react instantaneously on collision, if sufficient energy is available, and that intermolecular forces and internal energy distributions are unimportant. Reactions will in fact only occur if molecules collide in such a way that, depending on the species in question, certain steric requirements are met, and reactions will not be instantaneous since a finite time is required for structural and energetic redistributions to occur. Incorporation of these ideas into SCT has proven difficult, and transition state theory, or activated complex theory, has been developed as an alternative. Transition state theory (TST) considers a reaction to take place as a trajectory across a potential energy surface (PES), as shown in Figure 2.1 for the co-

linear reaction $A + BC \rightarrow AB + C$. As A and BC come into proximity they distort and the potential energy rises to a maximum, around which the cluster of atoms is known as the activated complex, ABC^\ddagger . The exact configuration of the cluster at the peak in the potential energy surface is termed the transition state.

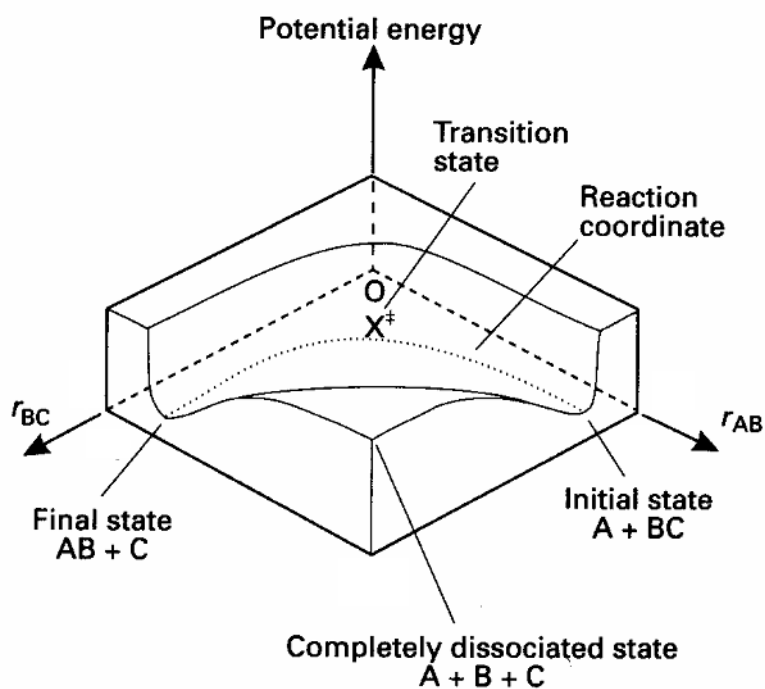
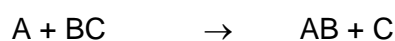


Figure 2.1 Potential energy surface for the reaction $A + BC$. Reproduced from reference 2.

Transition state theory treats the activated complex as existing in equilibrium with the reactants, and assumes that once the transition state has been reached it is inevitable that reaction products will be formed – the transition state cannot re-form the reactants. It is also assumed that the energy distribution of the reactant molecules is described by a Boltzmann distribution, and that the motion over the energy barrier is a classical process, with a single vibration of the activated complex responsible for the motion over the barrier. The single reactive vibration is considered separable from all the other vibrations and rotations of the complex.

The overall reaction



is therefore treated as



and the rate of reaction, r , is given by:

$$r = \frac{-d[A]}{dt} = \frac{-[BC]}{dt} = k_{\text{bimol}}[A][BC] \quad \text{E2.18}$$

$$= \frac{+d[AB]}{dt} = \frac{+d[C]}{dt} = k^\ddagger [ABC^\ddagger]$$

The concentration $[ABC^\ddagger]$ can be expressed from equilibrium:

$$[ABC^\ddagger] = K_{\text{eq}}[A][BC] \quad \text{E2.19}$$

since the equilibrium constant K_{eq} is given by $K_{\text{eq}} = \frac{[ABC^\ddagger]}{[A][BC]}$.

The rate is therefore described by:

$$r = k^\ddagger K_{\text{eq}}[A][BC] \quad \text{E2.20}$$

Using the general result from statistical mechanics, K_{eq} is given by:

$$K_{\text{eq}} = \frac{Q_{ABC^\ddagger}}{Q_A Q_{BC}} \exp\left(-\frac{\varepsilon}{k_B T}\right) \quad \text{E2.21}$$

where Q_i is the total partition function for species i , calculated using statistical mechanics and spectroscopic data, and ε the energy difference between the zero-point energy of the reactants ($A + BC$) and the products ($AB + C$) determined by spectroscopy.

The rate therefore becomes:

$$r = k^\ddagger \frac{Q_{ABC^\ddagger}}{Q_A Q_{BC}} \exp\left(-\varepsilon/k_B T\right) [A][BC] \quad \text{E2.22}$$

and the bimolecular rate coefficient, k_{bimol} , for the reaction is thus:

$$k_{bimol} = k^\ddagger \frac{Q_{ABC^\ddagger}}{Q_A Q_{BC}} \exp\left(-\varepsilon/k_B T\right) \quad \text{E2.23}$$

The total partition function for the activated complex Q_{ABC^\ddagger} can be separated into two components – the component, q , to the total partition function of ABC^\ddagger describing the reactive vibration, and the partition function of ABC^\ddagger excluding the reactive vibration, Q_{ABC^\ddagger}' .

$$Q_{ABC^\ddagger} = q Q_{ABC^\ddagger}' \quad \text{E2.24}$$

The partition function q can be approximated to

$$q = \frac{k_B T}{h \nu} \quad \text{E2.25}$$

where ν is the frequency of the reactive vibration, giving:

$$k_{bimol} = k^\ddagger \frac{k_B T}{h \nu} \frac{Q_{ABC^\ddagger}'}{Q_A Q_{BC}} \exp\left(-\varepsilon/k_B T\right) \quad \text{E2.26}$$

The rate coefficient k^\ddagger is determined by the frequency of the reactive vibration, ν , multiplied a transmission coefficient, κ , which accounts for the fraction of reactive vibrations that lead to product formation. The transmission coefficient is often assumed to be unity.

$$k^\ddagger = \kappa \nu \quad \text{E2.27}$$

Combining equations E.26 and E.27 therefore gives the result:

$$k_{\text{bimol}} = \kappa \frac{k_{\text{B}}T}{h} \frac{Q_{\text{ABC}^\ddagger}}{Q_{\text{A}}Q_{\text{BC}}} \exp\left(-\varepsilon/k_{\text{B}}T\right) \quad \text{E2.28}$$

which again compares well with the experimental Arrhenius equation.

While collision theory and transition state theory are based on the assumption of the presence of an energy barrier to reaction, many reactions of interest in atmospheric and combustion systems involving reactive radicals are barrierless reactions, with potential energy surfaces such as those depicted in Figure 2.2. Barrierless processes can occur when two radicals react, since there is no energy requirement for bonds to be broken before molecular rearrangement occurs to give products, or in addition reactions such as those between radicals and O₂, or radicals and species such as alkenes.³ Although collision theory and transition state theory were developed to explain reactions with energy barriers, these theories still provide good descriptions of barrierless reactions, with the result that barrierless reactions are often described by apparent negative activation energies.

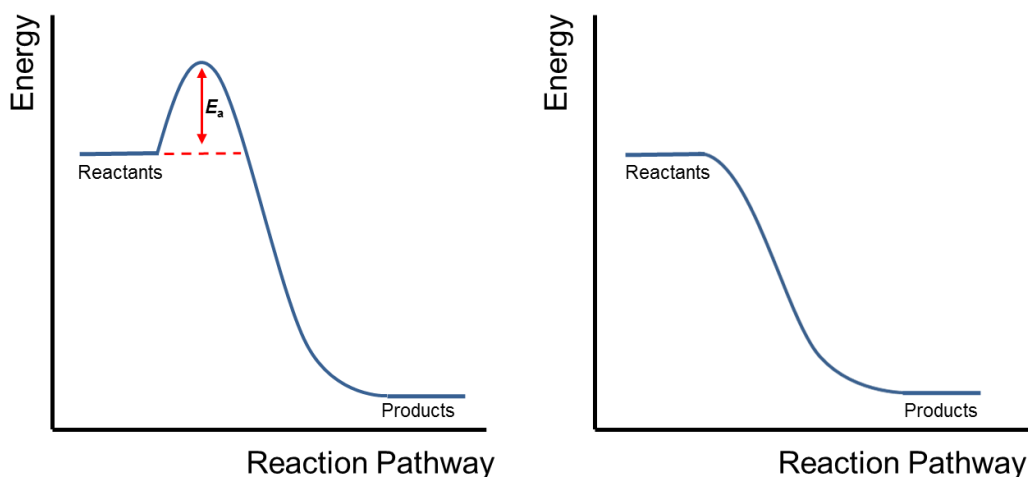
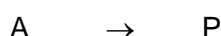


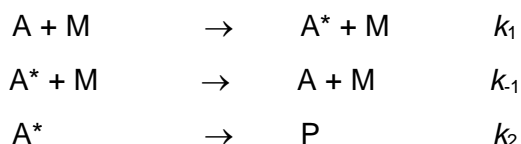
Figure 2.2 Typical potential energy surfaces with a barrier to reaction products (left) and without a barrier (right).

2.4 Unimolecular Reaction Rate Theory

At high pressures many gas phase dissociation and isomerisation reactions display first-order kinetics. The rates of such reactions also usually increase with temperature, showing that the reactant must acquire adequate energy to overcome an energy barrier to reaction. However, the observed first-order kinetics apparently preclude collisional activation, which is a bimolecular process. In the 1920s Lindemann⁴ proposed a kinetic scheme to explain the overall reaction:



consisting of the following elementary reactions:



where M is any other species that can produce or deactivate the energised molecule A*.

The rate of formation of product P from this mechanism is given by:

$$\frac{+d[P]}{dt} = k_2[A^*] \quad \text{E2.29}$$

Application of the steady state approximation to A* gives:

$$\frac{+d[P]}{dt} = \frac{k_2 k_1 [A][M]}{k_{-1}[M] + k_2} \quad \text{E2.30}$$

Although this is not first order in A, at high pressure $k_{-1}[M] \gg k_2$, which allows simplification of E2.30 to E2.31:

$$\frac{+d[P]}{dt} = \frac{k_2 k_1}{k_{-1}} [A] \quad \text{E2.31}$$

The Lindemann mechanism, therefore, predicts that the observed rate coefficient ought to decrease as the pressure is reduced, with the reaction eventually becoming second-order overall:

$$\frac{+d[P]}{dt} = k_1[A][M]$$

E2.32

since at low pressure $k_{-1}[M] \ll k_2$. The apparent first-order rate coefficient as a function of $[M]$ thus takes the form as shown in Figure 2.3.

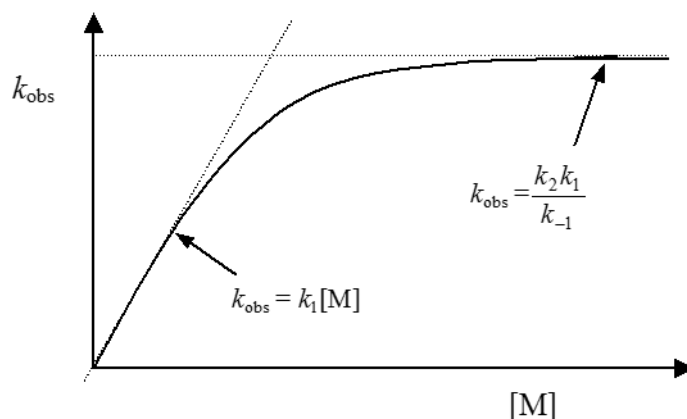


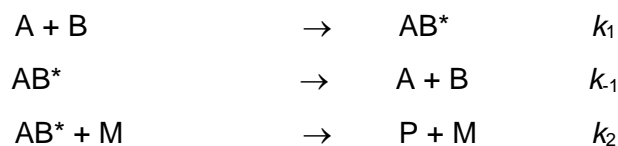
Figure 2.3 Schematic diagram of the apparent first-order rate coefficient, k , as a function of $[M]$. The observed rate is second-order at low pressures and tends to a limiting first-order value at high pressures.

2.5 Termolecular Reaction Rate Theory

A similar mechanism to that proposed by Lindemann for unimolecular kinetics can be used to explain the observed pressure dependence of many termolecular association reactions such as:



Invoking the elementary reactions:



and application of the steady state approximation to the intermediate species AB^* yields the expression

$$\frac{+d[\text{P}]}{dt} = \frac{k_2 k_1 [\text{A}][\text{B}][\text{M}]}{k_{-1} + k_2 [\text{M}]} \quad \text{E2.33}$$

The observed bimolecular rate coefficient, k_{bimol} , is therefore given by E2.33:

$$k_{\text{bimol}} = \frac{k_2 k_1 [\text{M}]}{k_{-1} + k_2 [\text{M}]} \quad \text{E2.34}$$

In a similar fashion to unimolecular reactions, at low pressure, since $k_2[\text{M}] \ll k_{-1}$, E2.33 simplifies to

$$\frac{+d[\text{P}]}{dt} = k_0 [\text{A}][\text{B}][\text{M}] \quad \text{E2.35}$$

resulting in a third-order rate equation, where $k_0 = \frac{k_2 k_1}{k_{-1}}$. At high pressure, since $k_2[\text{M}] \gg k_{-1}$,

E2.33 simplifies to

$$\frac{+d[\text{P}]}{dt} = k_{\infty} [\text{A}][\text{B}] \quad \text{E2.36}$$

resulting in a second-order rate equation, where $k_{\infty} = k_1$.

Although such mechanisms describe the qualitative behaviour of unimolecular and termolecular reactions they fail to replicate experimentally determined rate coefficients with any great quantitative accuracy. Several refinements have been made to the Lindemann mechanism, notably those by Rice and Ramsperger,⁵ Kassel,⁶ and Marcus,⁷ leading to the development of RRKM theory. RRKM theory requires accurate thermodynamic data and considers the internal energy distribution of the energised species A^* , and, similarly to transition state theory, separates the formation of A^* from that of the activated complex A^\ddagger :





RRKM theory can often accurately reproduce experimental results when reliable thermodynamic data is available. Unfortunately, reliable thermodynamic data are not available for many of the transient species and, as a result, RRKM theory cannot always be used. However, Troe⁸ has shown that introduction of a broadening factor, F , itself a function of k_0 and k_∞ , applied to E2.35 can accurately replicate the pressure dependence of many experimentally determined rate coefficients.

$$k_{\text{bimol}} = \frac{k_0 [M] k_\infty}{k_0 [M] + k_\infty} \times F \quad \text{E2.37}$$

where

$$F = F_c \left\{ 1 + \left(\log_{10} \left\{ \frac{k_0 [M]}{k_\infty} \right\} \right)^2 \right\}^{-1} \quad \text{E2.38}$$

The exact value of F_c depends on the specific reaction in question, but it has been shown that a value of 0.6 provides an adequate description for many termolecular reactions of interest in atmospheric and combustion systems.⁹ A more detailed description has also been provided by Troe⁸ to describe rate coefficients with broad falloff curves:

$$F = \frac{(1 + k_0 [M] / k_\infty)}{(1 + (k_0 [M] / k_\infty)^n)^{1/n}} \quad \text{E2.39}$$

$$n = \left(\frac{\ln(2)}{\ln(2/F_c)} \right) \left((1-b) + b \left(k_0 [M] / k_\infty \right)^q \right) \quad \text{E2.40}$$

$$q = \frac{(F_c - 1)}{\ln(F_c / 10)} \quad \text{E2.41}$$

2.6 Concluding Remarks

Theoretical descriptions of gas phase kinetics provide valuable insights into the nature of fundamental chemical and physical processes, and developments in such descriptions now enable good approximations to molecular behaviour. However, all theories require experimental verification, and the theory of reaction kinetics is no exception. Experimental principles and techniques used to study gas phase reaction kinetics are discussed in the following chapter.

2.7 References

1. Arrhenius, S. Über die Reaktionsgeschwindigkeit bei der Inversion von Rohrzucker durch Säuren. *Zeitschrift für Physikalische Chemie*, 1889, **4**(1), p.226.
2. Pilling, M.J. and P.W. Seakins. *Reaction Kinetics*. Oxford Science Publications. Oxford: Oxford University Press, 1995.
3. Daranlot, J., A. Bergeat, F. Caralp, P. Caubet, M. Costes, W. Forst, J.-C. Loison and K.M. Hickson Gas-Phase Kinetics of Hydroxyl Radical Reactions with Alkenes: Experiment and Theory. *ChemPhysChem*, 2010, **11**(18), pp.4002-4010.
4. Lindemann, F.A., S. Arrhenius, I. Langmuir, N.R. Dhar, J. Perrin and W.C. McC. Lewis. Discussion on "the radiation theory of chemical action". *Transactions of the Faraday Society*, 1922, **17**(0), pp.598-606.
5. Rice, O.K. and H.C. Ramsperger. Theories of unimolecular gas reactions at low pressures. *Journal of the American Chemical Society*, 1927, **49**(7), pp.1617-1629.
6. Kassel, L.S. Studies in Homogeneous Gas Reactions. I. *The Journal of Physical Chemistry*, 1928, **32**(2), pp.225-242.
7. Marcus, R.A. Unimolecular Dissociations and Free Radical Recombination Reactions. *The Journal of Chemical Physics*, 1952, **20**(3), pp.359-364.
8. Troe, J. Theory of thermal unimolecular reactions at low pressures. I. Solutions of the master equation. *The Journal of Chemical Physics*, 1977, **66**(11), pp.4745-4757.
9. S. P. Sander, R.R.F., D. M. Golden, M. J. Kurylo, R. E. Huie, V. L. Orkin, G. K. Moortgat, A. R. Ravishankara, C. E. Kolb, M. J. Molina,. Chemical Kinetics and Photochemical Data for Use in Atmospheric Studies. *Evaluation Number 14, JPL Publication 02-25, Jet Propulsion Laboratory, Pasadena, CA., USA*, 2002.

Chapter 3 Experimental Techniques

This chapter outlines the experimental techniques used to study the kinetics of rapid gas phase reactions. Such techniques require the measurement of the change in concentration, or some property that can be related to concentration, of one or more of the reactants or products in the reaction as a function of time. Experimental techniques used to study rapid reaction rates can be broadly classified into relative, in which kinetics are measured relative to those of well known reactions, or absolute, in which the kinetics are measured independently of any other reaction.

Examples of relative and absolute methods relevant to this work will be provided in this chapter. A detailed description of the laser flash photolysis-laser induced fluorescence (LFP-LIF) technique used in this study is also provided in this chapter.

3.1 Kinetic Techniques

3.1.1 Relative Rate Method

The relative rate method measures the loss of a reactant relative to that of a reference compound in the presence of a reactive species mixed in a reaction vessel such as a chamber. The ratio of k_1/k_2 is determined from the rate of change of concentration of the substrates and the reference compounds (R3.1-R3.2) as well as their rates of disappearance. Because it is a relative rate method, the absolute concentrations do not need to be known - measuring the decay of one compound relative to a compound with a defined rate coefficient. Monitoring techniques include gas chromatography (GC) and Fourier transform infrared spectroscopy (FT-IR).¹



In relative rate experiments the consumption of the reactant, R_1 , due to reaction with a reactive species, for example OH, is governed by the rate law:

$$\frac{-d[R_1]}{dt} = k_1[OH][R_1] \quad \text{E3.1}$$

$$\frac{-d[R_2]}{dt} = k_2[OH][R_2] \quad \text{E3.2}$$

Assuming that reactions with OH are the only loss process, integration over time gives:

$$[R_1]_t = -k_1 \int_0^t [OH] \cdot dt + [R_1]_0 \quad \text{E3.3}$$

$$[R_2]_t = -k_2 \int_0^t [OH] \cdot dt + [R_2]_0 \quad \text{E3.4}$$

which can be rearranged to

$$\ln\left(\frac{[R_1]_0}{[R_1]_t}\right) = -k_1 \int_0^t [OH] \cdot dt \quad \text{E3.5}$$

$$\ln\left(\frac{[R_2]_0}{[R_2]_t}\right) = -k_2 \int_0^t [OH] \cdot dt \quad \text{E3.6}$$

E3.5 and E3.6 can be equated to

$$\ln\left(\frac{[R_1]_0}{[R_1]_t}\right) = \frac{k_1}{k_2} \ln\left(\frac{[R_2]_0}{[R_2]_t}\right) \quad \text{E3.7}$$

A plot of $\ln([R_1]_0/[R_1]_t)$ vs $\ln([R_2]_0/[R_2]_t)$ will be linear with a gradient of k_1/k_2 and an intercept of zero.² Relative reactant concentrations are measured by detection techniques such as gas chromatography (3.2.1).

The advantage of the relative rate method is that reactive species, which often have short lifetimes and are present in very low concentrations, need not be measured, however, because of these low concentrations experiments are performed over timescales of 10-20 minutes.

In contrast to relative rate experiments, absolute methods do not require previous knowledge of the kinetics of a reference compound. Compared to the chamber experiments described above, which are typically performed on the timescale of minutes, the absolute techniques discussed here are performed on more rapid timescales, with a range of techniques available to investigate chemistry occurring on different timescales, and under different conditions of temperature and pressure. Each kinetic technique can be coupled to a range of detection techniques, and these will also be discussed.

3.1.2 Discharge Flow

The discharge flow (DF) technique is a system used to study the kinetics of gas phase reactions, usually occurring on a timescale of seconds to milliseconds and below pressures of 10^3 Pa. The technique is named due to the microwave discharge that generates a reactive species immediately prior to injection into a flow tube, such as A from a precursor A_2 , which then reacts with a co-reactant B, (R3.3-R3.4).¹



The setup, as shown in Figure 3.1, consists of a main flow tube, along which the reactive product flows, and a moveable injector, from which the co-reactant is added to the main flow tube. Typically, the added reactant, B, is in excess of the radical concentration giving pseudo-first-order conditions for the radical decay.^{1,3,4} The relative concentrations of species are monitored at the detection point.

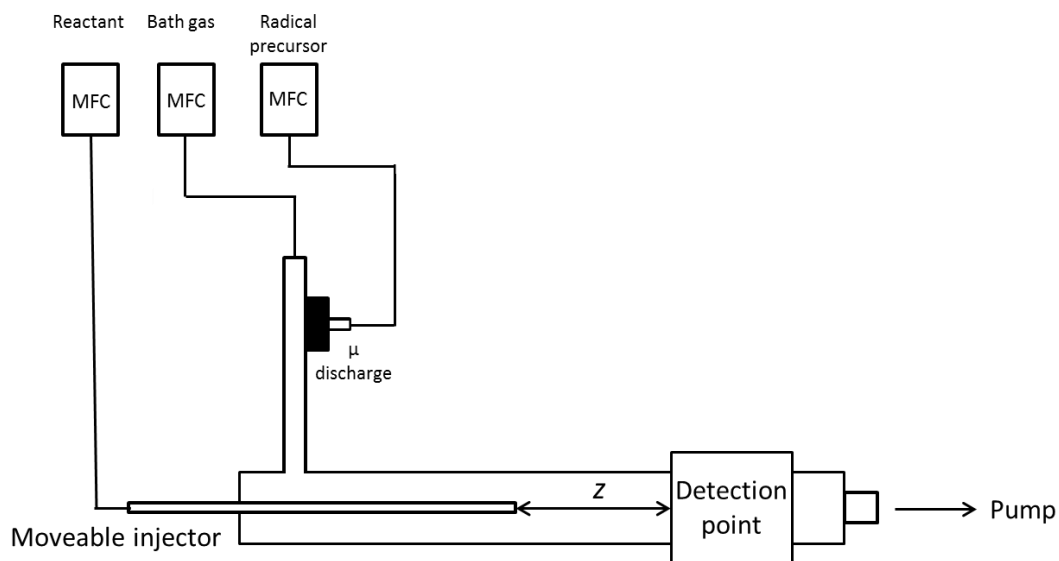


Figure 3.1 Schematic of discharge flow set up, where z is the distance between reaction initiation and detection

Mixing of the reactants at the tip of the moveable injector initiates the reaction, with the reaction time limited by the distance over which the reactants mix (i.e. the distance between the tip of the injector and the detector). The time between initiation and product detection can be calculated if the velocity of the gas mixture in the flow tube is known (E3.8).

$$t = z/v \quad \text{E3.8}$$

where t is the time between initiation and detection (i.e. the reaction time), z is the distance between initiation and detection and v is linear the flow velocity.¹ It is essential the gas flow from the injector mixes homogeneously with the gas flow of the main flow tube and that radial concentration gradients (i.e. across the flow tube) are kept to a minimum, in order for mixing timescale to be short when compared with the reaction timescale.³ A concentration vs time profile of the reaction, from which the rate coefficient can be determined, is found by adjusting the injector position along the flow tube and measuring the signal associated with radical concentration at each point whilst the flow rate is held constant.

An advantage of the discharge flow set up is several detection techniques are suited to be used in conjunction, including resonance fluorescence, laser induced fluorescence, laser magnetic resonance and mass spectrometry.

The disadvantages of using the DF technique arise from the need of very high flow velocities, meaning large quantities of reactants are required. Additionally there will be first-order loss at the walls of the flow tube from heterogeneous reactions, although this can be inhibited somewhat by a wall coating to remove radicals from the surface.^{3,4}

3.1.3 *Shock Tube*

Shock tubes are used in high temperature and pressure kinetic studies, conditions relevant to combustion. A shock tube consists of two chambers separated by a diaphragm, one chamber contains gas-phase stable reactants and precursors and the other an inert gas (sometimes referred to as the “driver” gas) at high pressure (Figure 3.2).⁵ The “shock” is a rapid increase in pressure through the chamber. When the diaphragm is punctured under pressure, a shock wave propagates through the reaction mixture and reflects off the wall resulting in a rapid heating of the gas mixture to up to thousands of Kelvin. This effect produces highly reactive species through the rapid dissociation of the precursor, without the need of a discharge lamp or laser pulse. Most dissociation reactions are endothermic and high temperatures shift the equilibrium towards the products. The temperature rise can be controlled through different compositions of the inert gas and varying the pressure in the chamber. The composition of the gas mixture after the shock initiation is monitored in real time through spectroscopic methods. Reactions can be carried out at sub-atmospheric of up to 500 atm and temperatures from 500 K up to thousands of Kelvin.

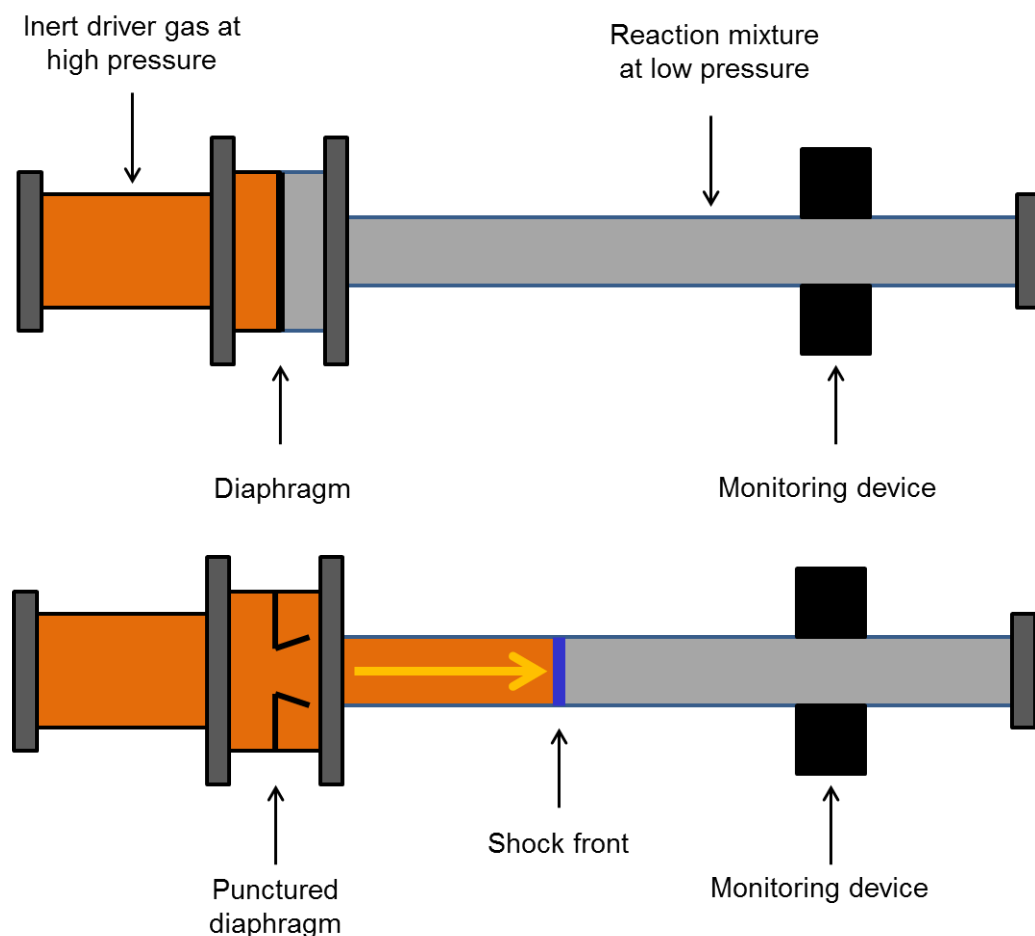


Figure 3.2 Top: shock tube setup before diaphragm is punctured. Bottom: shock tube after diaphragm is punctured showing the shock front as the high and low pressure gases meet.

There are limitations to this method. The rapid heating is not selective for the desired molecules and may lead to partial dissociation of all species in the reaction chamber, resulting in a mixture of reactive species in the chamber with many reactions occurring simultaneously in addition to the reaction being studied. No signal averaging is possible with shock tube experiments and signal to noise ratios are low. Modelling the kinetics of this kind of system can be difficult.

3.1.4 Rapid Compression Machine

A rapid compression machine (RCM) simulates a single compression stroke of an internal combustion engine. A RCM consists of a chamber with a piston where a fuel-oxidizer mixture is introduced into the reaction chamber and is rapidly compressed by the piston in a process relatively close to adiabatic compression.⁶ The rapid compression

results in an elevation of temperature and pressure within the reaction chamber, conditions which are suited to investigating the autoignition characteristics of a given reaction mixture, such as ignition delay time and heat release rate.

RCM experiments provide data on the pressure change within the reaction chamber as a function of time during and after the compression. Figure 3.3 shows typical pressure traces using nitrogen and argon gases, demonstrating the rapid rise in pressure during the compression stroke followed by a gradual decrease in pressure due to heat loss from the end of compression.

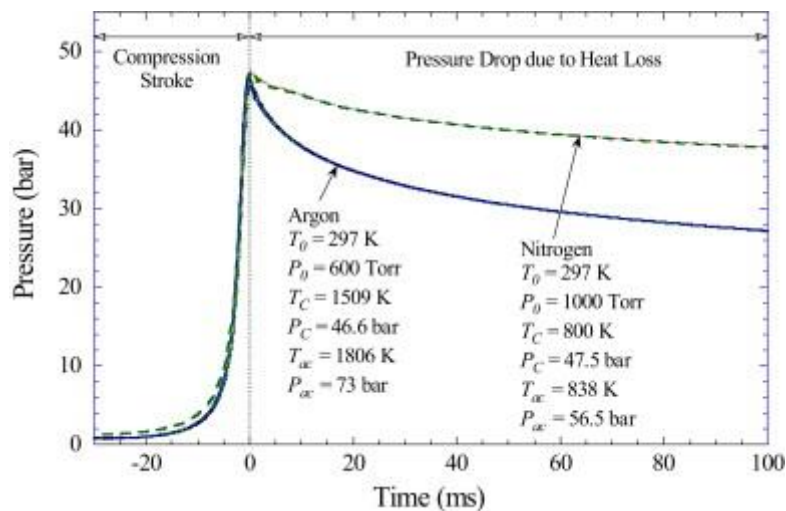


Figure 3.3 Typical pressure traces for inert gas tests in a RCM⁶

RCMs are primarily used to determine the ignition delay time of a fuel as a function of temperature, pressure and fuel-oxidizer ratio. RCMs can be equipped with diagnostics to determine the temperature of flow fields inside the reaction chamber and measure the concentrations of reactants, intermediates and products produced during combustion.

RCMs have advantages over other high pressure and temperature techniques such as shock tubes, where the experimental timescale is limited to under 10 ms due to interference from the reflected shock wave. The experimental timescale of an RCM is an order of magnitude longer as the limit to the experimental duration is by heat loss to the wall of the chamber. However, reproducibility between different RCMs under similar conditions have been found to be qualitatively different.⁷⁻¹⁰

3.1.5 Flash Photolysis

The flash photolysis technique was developed in 1949 by Norrish and Porter for which they won the Nobel Prize in Chemistry in 1967. Flash photolysis is a pump-probe technique that uses a short duration flash of high intensity light (the “pump”) to initiate a reaction by photodissociation of a suitable precursor. A second light source (the “probe”) is then used to probe the reaction mixture at various time delays to build up a picture of the reaction concentration-time behaviour (Figure 3.4).

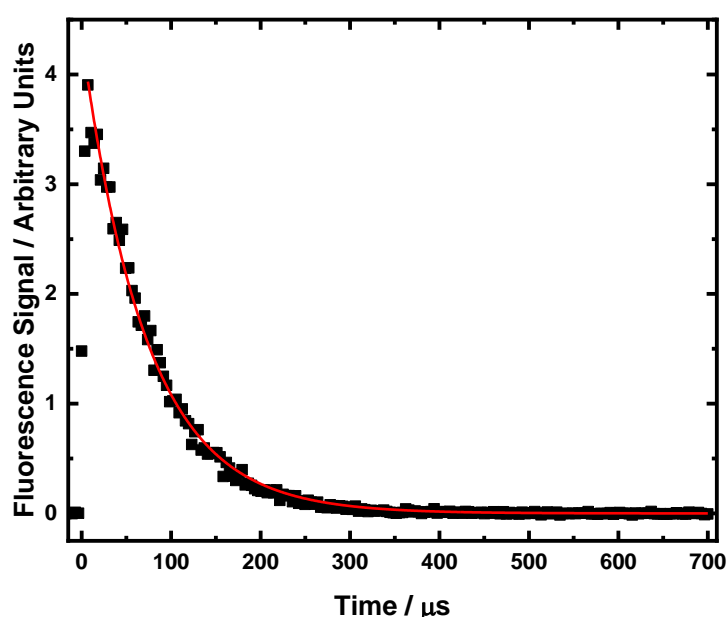


Figure 3.4 Typical flash photolysis decay measured by laser induced fluorescence (LFP-LIF), black points are experimental data. Red line is exponential fit to give k .

Flash photolysis allows the analysis of reactions on a wide range of timescales; these can be from femtoseconds to milliseconds depending on the nature of the photolysis source.^{1,4,11} Species produced after the flash are often monitored through spectroscopic methods as a function of time, described later in this chapter. The conventional method of producing the photolysis flash is through a gas flash lamp, which is rapidly discharged and where the wavelength of light is dependent on the gas mixture of the lamp. Flashlamps have been replaced with lasers in recent years, with lasers allowing

experiments to be measured on the femtosecond timescale owing to the short duration of the laser pulse.

Lasers have high specificity when compared to flashlamps because unlike flashlamps, which have a broadband output, lasers can be tuned to specific wavelengths, giving control over which species is photolysed. Lasers can be operated at high pulse repetition rates which allow data to be collected swiftly. The rate of data collection is only limited by the rate at which fresh reactant samples can be added to the cell between each laser pulse to avoid secondary chemistry.

Typically, reactants and precursors are pre-mixed and flowed into a photolysis cell at pressures of up to 10 atmospheres, overcoming the mixing time and pressure limitations of flow systems. The rapid production of reactants following the photolysis of precursors decouples the kinetics of reactant production from the kinetics of subsequent reactions and allows for fast reactions to be measured^{1,4} Probe light is directed into the centre of the cell and the reaction is monitored within the probe region thus minimising interference from wall loss. Secondary chemistry may occur if the co-reactant is photolysed at the wavelength of the flash, although this can be avoided by using a co-reactant that does not photolyse at this wavelength or by using different precursors that both photolyse to give the desired reactants. This is minimised by laser photolysis.

Reactant concentration is often in large excess of the initial radical concentration to give pseudo-first-order conditions. Under these conditions, a bimolecular rate constant may be obtained from the pseudo-first-order radical decay rates.⁴

3.2 Analytical Techniques

3.2.1 Gas Chromatography

Gas chromatography (GC) is a technique used to analyse volatile species in the gas phase. Components of a sample are dissolved in a solvent and vaporised to separate and distribute analytes between a stationary and mobile phase. In GC the mobile phase

is an inert gas, such as helium, which carries the analyte through a heated column and the stationary phase is typically a solid adsorbent. In a gas mixture, the analyte with more volatility will elute fastest, the time it takes for an analyte to elute is known as the retention time. GC timescales depend on the retention time of the analytes.

GC has several advantages, including high resolution of peaks, reproducibility of retention times, high precision and accuracy and little decomposition of the sample mixture.¹² However, only sufficiently volatile samples can be analysed by GC, of which numerous molecules do not meet the requirements. Sample gas mixtures that do meet volatility requirements must be thermally stable to avoid degradation upon injection to the heated column. Also, analysis by GC can be slow when compared to other analytic techniques such as resonance fluorescence and laser-induced fluorescence.

3.2.2 Mass Spectrometry

Mass spectrometry (MS) is an analytical technique that identifies ionic species based on the mass-to-charge ratio, m/z , and abundance of charged particles.^{1,13} Species of interest may be ionised through several suitable methods: thermally, by applying an electric field or by impacting energetic electrons, ions or photons (E3.9).¹⁴ The choice of ionisation method is dependent on the nature of the sample. Soft ionisation methods such as electrospray ionisation (ESI) and matrix-assisted laser desorption/ionisation (MALDI) result in little fragmentation. Hard ionisation methods such as field ionisation (FI), fast atom bombardment (FAB), secondary ion mass spectroscopy (SIMS), chemical impact ionisation (CI) and electron impact ionisation (EI) result in a high degree of fragmentation.

After the initial ionisation, the energetically unstable molecular ion, M^+ , may fragment into smaller ions and free radicals (E3.9).



Ions are separated according to their m/z ratio and detected proportionally to their abundance. Specific m/z may be selected by a quadrupole so that only a certain mass is detected.¹ A quadrupole achieves this by filtering ions as they move between four metal rods across which varying RF fields are applied such that only ions of a certain m/z will have the correct trajectory to reach the detector while others will collide with the rods and be lost.¹⁵

Another method to differentiate between ions in an MS experiment is to use a time-of-flight (TOF) instrument. Ions are accelerated through an electric field towards the detector and ions with the same charge will have identical kinetic energy as a result. The velocity of the ions depends on the m/z and so time taken to reach the detector will depend on the charge of the ion. This method is advantageous over the quadrupole instrument as it allows all the ions generated to be observed simultaneously. Time-resolved TOF can simultaneously monitor multiple ion species on a millisecond timescale.¹⁶

3.2.3 Absorption Spectroscopy

Absorption spectroscopy can be used to monitor fast reactions by measuring the absorbance of light at a particular wavelength. Absorbance, A , is defined by the Beer-Lambert law (E3.10):

$$A = \ln\left(\frac{I_0}{I}\right) = \sigma cl \quad \text{E3.10}$$

where σ is the cross section, c is the concentration and l is the pathlength of the light through species sample. Species concentrations are directly proportional to absorbance and can be found if the absorbance, cross sections and pathlength are known. The ratio of transmitted light intensity to incident light intensity, I/I_0 , can be measured as a function of time to give the change in concentration of the measured species throughout the reaction.¹⁷

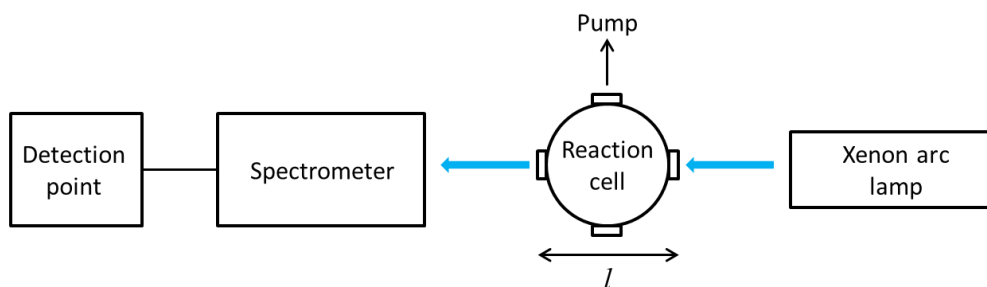


Figure 3.5 Schematic of absorption spectroscopy.

Noise issues may arise with this technique, for example, small changes in intensity can be monitored, however, a small change in I compared to I_0 can lead to poor signal-to-noise ratio. This issue can be overcome by introducing multipass optics to increase the pathlength which in turn increases absorbance according to E3.10. There can be problems when measuring in the UV region of the spectrum as many species have unstructured spectra in this region and may be difficult to identify. Moreover, spectra may be unidentifiable if more than one reactant or product absorbs at the monitoring wavelength.¹⁷ However, the development of tuneable UV, visible and IR lasers has greatly enhanced the selectivity and sensitivity of kinetic absorption spectroscopy.

3.2.4 Resonance Fluorescence

Resonance fluorescence (RF) is a technique commonly used for monitoring the concentration of atomic species as well as a limited number of molecular species.^{1,11} RF involves monitoring species generated in the gas phase by observing the intensity of light emitted by the species after excitation with radiation of the same wavelength (Figure 3.6).¹⁸

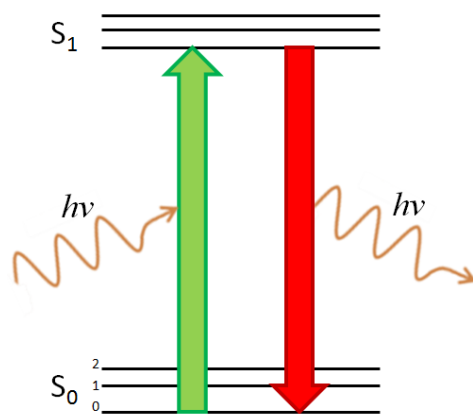


Figure 3.6 Resonance fluorescence is fluorescence from a species in which the light emitted is at the same frequency as the light absorbed.

An unreactive gas (e.g. He) containing a trace amount of precursor for the atom or molecule of interest is passed through a microwave discharge to generate excited state atoms or radicals, these excited atoms can return to the ground state by emitting a photon of light, in a process known as fluorescence.¹ The emitted radiation will be of the same wavelength as the exciting radiation of the excited atom or molecule (known as on-resonant fluorescence).¹¹ Fluorescence is proportional to atomic concentration and hence why the technique is used to monitor concentrations.

3.2.5 Laser induced fluorescence

Laser induced fluorescence (LIF) spectroscopy is a fluorescence technique similar to RF which uses lasers to provide a more tuneable light source allowing excitation of a number of species. This allows for a wider series of species to be measured. In LIF, a species is excited to an upper electronic state from which it can undergo several processes, shown in the Jablonski diagram in Figure 3.7.

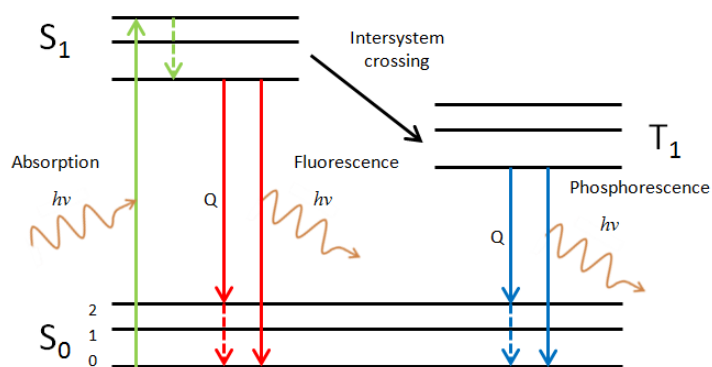


Figure 3.7 Jablonski diagram showing the possible fates of an excited energy state.

In LIF the process analysed is fluorescence, where molecules relax back to the ground electronic state and fluoresce by emitting a photon (red line). Before a species returns to the ground state there is a loss in vibrational energy, as a result the emitted photon can be of a longer wavelength than the excitation photon (off-resonant fluorescence) or of the same wavelength (on-resonant fluorescence).

From an excited state (S_1) excess vibrational energy may be lost through radiationless internal conversion (IC) to the lowest vibrational level of the first excited state (dashed green line). Radiationless deactivation through internal conversion to the ground state (S_0) can also occur (dashed red line). Additionally, the excited state of a species may undergo intersystem crossing (ISC) to the lowest vibrational level of the triplet state, (T_1), from which it can phosphoresce (blue line) or undergo IC to the ground state. However, the $T_1 \rightarrow S_0$ transition is spin forbidden and occurs on a slower timescale than other processes. Competition occurs between the processes, and often LIF is performed at low pressures to avoid quenching.

The fluorescent signal is proportional to the number of ground state molecules present in the reaction mixture; therefore fluorescence intensity provides a relative measure of the concentration of species. LIF has a high signal-to-noise ratio giving the technique high sensitivity.

LIF is a sensitive technique and is known as a zero background technique because only the desired wavelength is detected therefore avoiding interference from all other

wavelengths and the background. Low concentrations of the species of interest can be monitored even in the presence of other species.

A disadvantage of LIF is that it is only suitable for species that fluoresce, so larger molecules or radicals with more vibrational modes would be difficult to monitor as they have more vibrational modes that are more likely to undergo IC and radiationless transitions than fluorescence.

3.3 Details of the Apparatus and Kinetic Methods Used in This Work

The following section outlines the specific apparatus used during this work, including the photolysis and probe lasers utilised to initiate radicals, the spectroscopy of the radical detection, the reaction cells required to reach the desired temperatures and the overall experimental procedure. Figure 3.8 shows a schematic of the experimental set up used to carry out the work in this thesis.

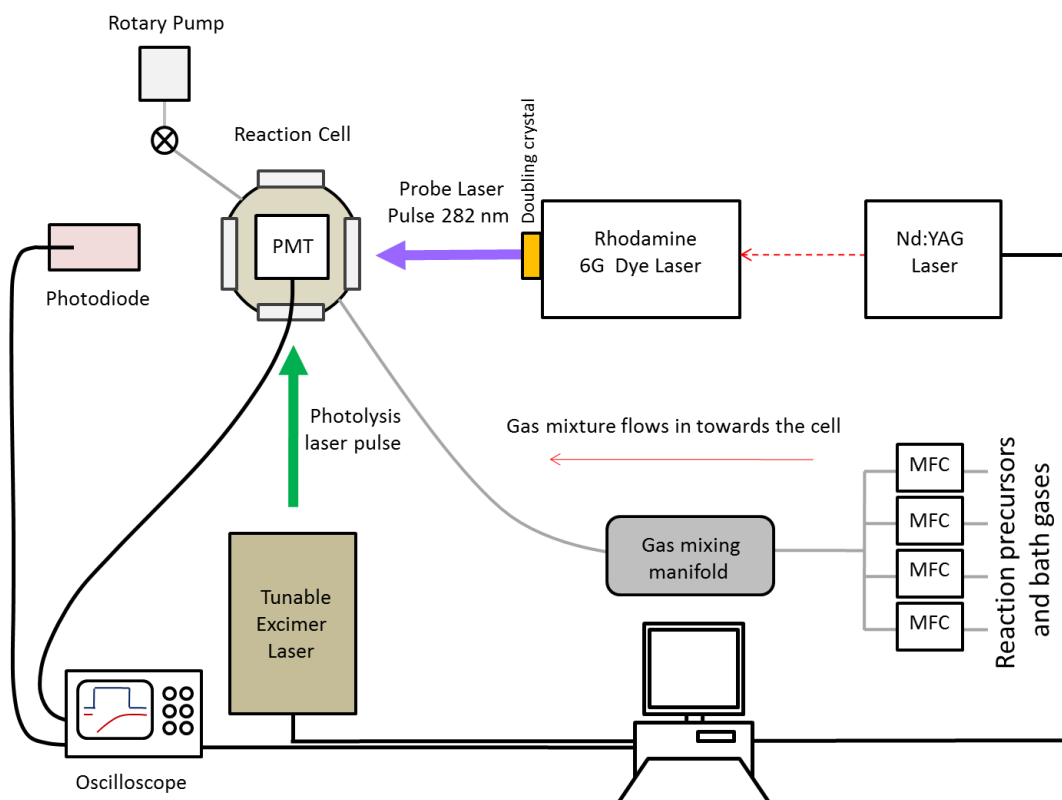


Figure 3.8 Schematic of the experimental set up used in this work

3.3.1 Radical Generation

3.3.1.1 Excimer Laser

Excimer lasers are pulsed gas lasers that operate in the near-ultraviolet region of the spectrum. Excimer lasers (from excited-dimers) are also known as exciplex lasers, named after the excited diatomic complex which is electronically excited to produce laser light. Excimer lasers produce laser light using noble halide gases, such as KrF ($\lambda = 248$ nm), by promoting the gas to an excited state which then fluoresces as it returns to the ground state. A KrF exciplex is produced when a mixture of Kr/F₂/He gases are ionized by a pulsed electrical discharge to form Kr⁺ and F⁻ ions, which combine to form the KrF exciplex. Exciplex compounds are bound to the upper electronic state but have a dissociative ground state. This is exploited in excimer lasers, the repulsive forces between ground state atoms means the ground state never becomes significantly occupied, and so a population inversion occurs between the excited and dissociative ground state.¹ The laser wavelength depends on the exciplex composition, as each

exciplex has a different energy separations. Excimer lasers can operate between 1 and 100 Hz with energy outputs between 300-500 kJ mol⁻¹.

3.3.1.2 Nd:YAG Laser

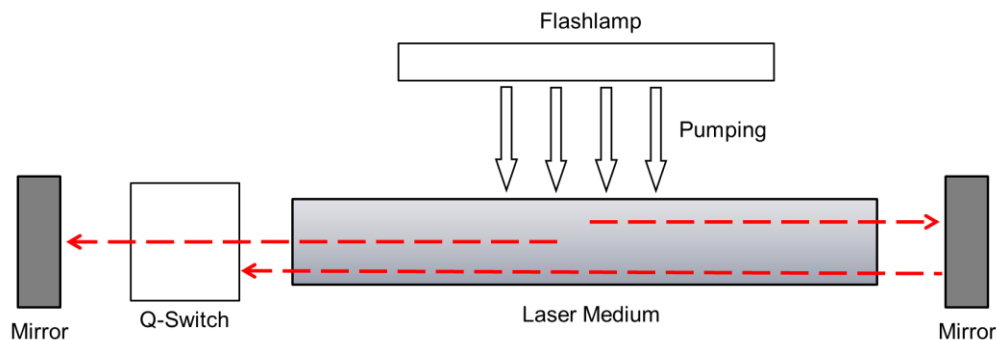


Figure 3.9 Principal concepts of a laser system

An Nd:YAG laser is one that consists of a neodymium-doped yttrium aluminium garnet ($\text{Nd:Y}_3\text{Al}_5\text{O}_{12}$) crystal as a lasing source. A simple schematic of a typical Nd:YAG laser is shown in Figure 3.9. A flashlamp is fired to produce broadband light (pump) across the near-UV, visible and near-IR range of the electromagnetic spectrum. The light enters the laser rod and a small percentage of the pumping light is absorbed by Nd ions found within the YAG crystal lattice. If the flashlamp pumping is sufficiently strong it will initiate a population inversion within the energy levels of the Nd ions. A photon passing through the laser rod at the same frequency as the lasing transition will be amplified by an induction decay of some of the ions from the upper to lower state in stimulated emission. Mirrors either side of the rod will reflect the amplified light back into the rod, resulting in significant amplification of light at the wavelength of the lasing transition. One of the two mirrors consists of a partially reflective surface to allow most light to pass through. Nd:YAG lasers have a fundamental wavelength output of 1064 nm in the near-IR with harmonics of 532, 355 and 266 nm.¹⁹

3.3.1.3 Dye Laser

Dye lasers use an organic liquid dye as the laser medium, allowing dye lasers to be tuneable across many wavelengths compared to lasers that use solid or gaseous media.

In a dye laser, the laser medium is situated between two mirrors to create a cavity, one of the two mirrors consists of a partially reflective surface to allow most light to pass through and escape the cavity. The laser dye is excited to a singlet state by a short pulse of monochromatic light from a flash lamp. The molecule undergoes rapid vibrational relaxation and fluoresces to the ground state, the speed of this process means a population inversion can be achieved between the ground vibrational levels of the upper electronic state and the vibrationally excited levels of the ground electronic state. Each time light passes through the excited dye the solution gains intensity through spontaneous emission, which will occur in all directions over a wide range of frequencies. A number of photons of the fluorescent light will reflect off the cavity mirrors back into the dye medium and, if they are of the correct frequency, stimulate emission. The stimulated emission will be of the same direction and frequency and will also be reflected back into the cavity, resulting in more stimulated emission. Stimulated emission will dominate over spontaneous fluorescence. As one of the mirrors allow some light to pass through, a monochromatic laser beam is produced. The resulting beam can undergo a phenomena known as frequency doubling, where the input beam is doubled in optical frequency (half the vacuum wavelength) by a crystal and propagated in the same direction as the input beam. The process is also known as second-harmonic generation.²⁰

3.3.2 Radical Detection

3.3.2.1 OH Spectroscopy

The experimental work discussed in this thesis focuses on the monitoring of the OH radical *via* off-resonance LIF, where OH radicals are excited at ~282 nm ($A^2\Sigma(v = 1) \leftarrow X^2\Pi(v = 0)$) and subsequent fluorescence is observed at ~308 nm. A comparison between off- and on-resonant transitions can be seen in Figure 3.10.

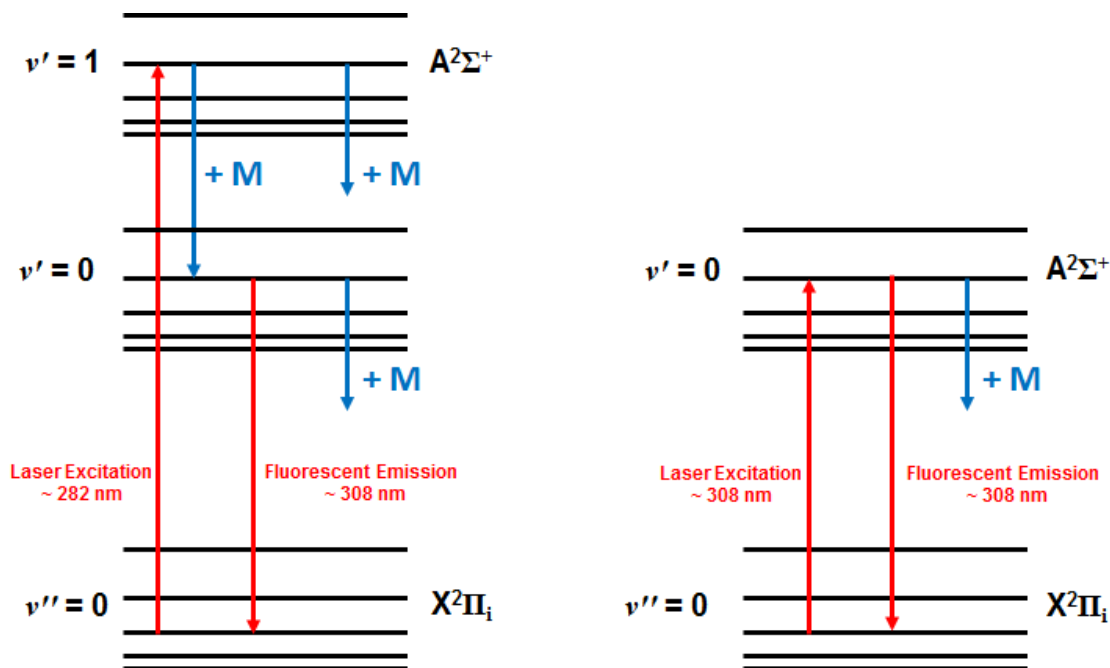


Figure 3.10 Schematic energy level diagram showing the transitions relevant to off- and on- resonant fluorescence of the OH radical following the A – X electronic transition. Collisional energy transfer processes are presented in blue.

3.3.2.2 Detection by Photomultiplier Tube

OH radicals were detected using a photomultiplier tube (PMT). A PMT is a photon detection instrument used to sensitively monitor spectroscopic measurements by converting light into measurable signal. A PMT consists of several components, a photosensitive cathode, multiple dynodes and an anode, contained inside a vacuum tube. A schematic of a typical PMT can be seen in Figure 3.11. Light enters the photocathode and is converted into an electrical signal through the production of electrons. The electrical flux is focused onto the first of several dynodes by a focusing electrode and is amplified to a useful level by the emission of secondary electrons. This multiplication is repeated at each successive dynode, each of which has a slightly higher voltage than the electrode preceding it. The amplified secondary electrons emitted from the final dynode reach an anode. The electron flux collected by the anode is large enough to provide the final output signal.

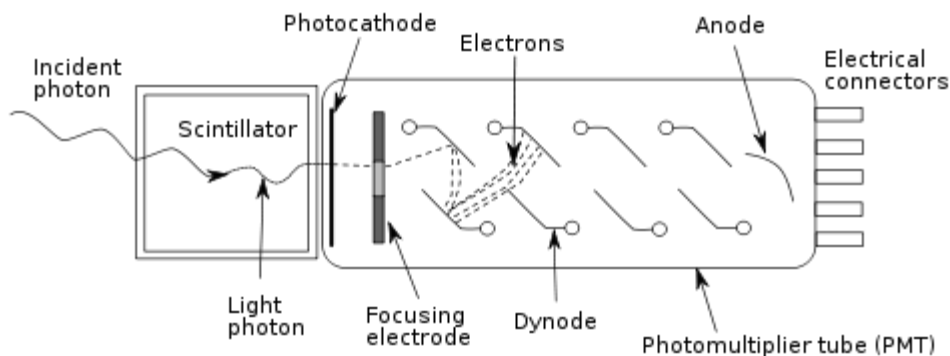


Figure 3.11 A schematic of a photomultiplier tube.²¹

3.3.3 Reaction Cells

Two different stainless steel reaction cells were required to achieve the desired temperature range, one for temperatures above room temperature and one for sub-ambient temperatures, schematics of which can be seen in Figure 3.12 and Figure 3.13. The reaction cells featured five windows fitted with optics that allowed laser and fluorescent light to pass through.

High temperature experiments were carried out using a stainless steel reaction cell mounted with resistance cartridge heaters within the cell walls that could reach up to 770 K, with an error of the temperature measurement of ± 1 K. Temperatures were controlled using a commercial temperature controller and temperatures in the reactor were measured by K-type thermocouples close to the reaction zone. The windows of the cell were cooled by a flow of water surrounding them. Experiments were conducted at temperatures between 298 K and 770 K.

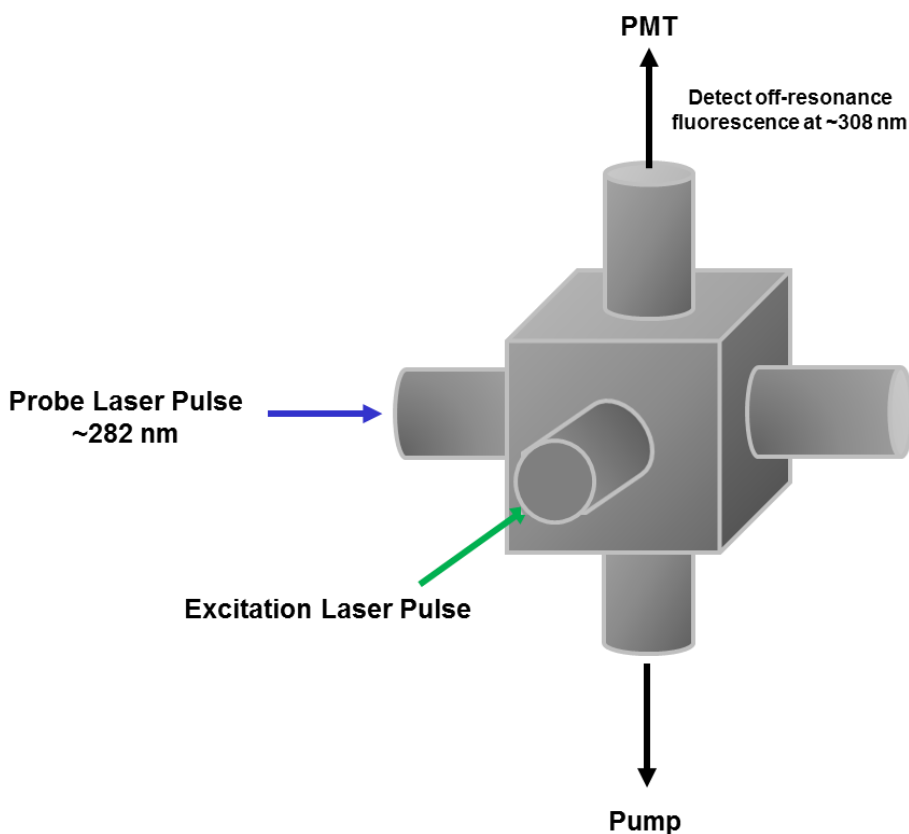


Figure 3.12 Reaction cell used for high temperature (298-770 K) experiments conducted in this thesis

To achieve sub-ambient temperatures a bath was fitted to a second reaction cell and filled with a mixture of ethylene glycol and methanol and cryogenically cooled. The bath was insulated using polystyrene and the temperature of the bath and within the cell was measured using K-type thermocouples. Experiments were conducted at temperatures between 251 K and 298 K.

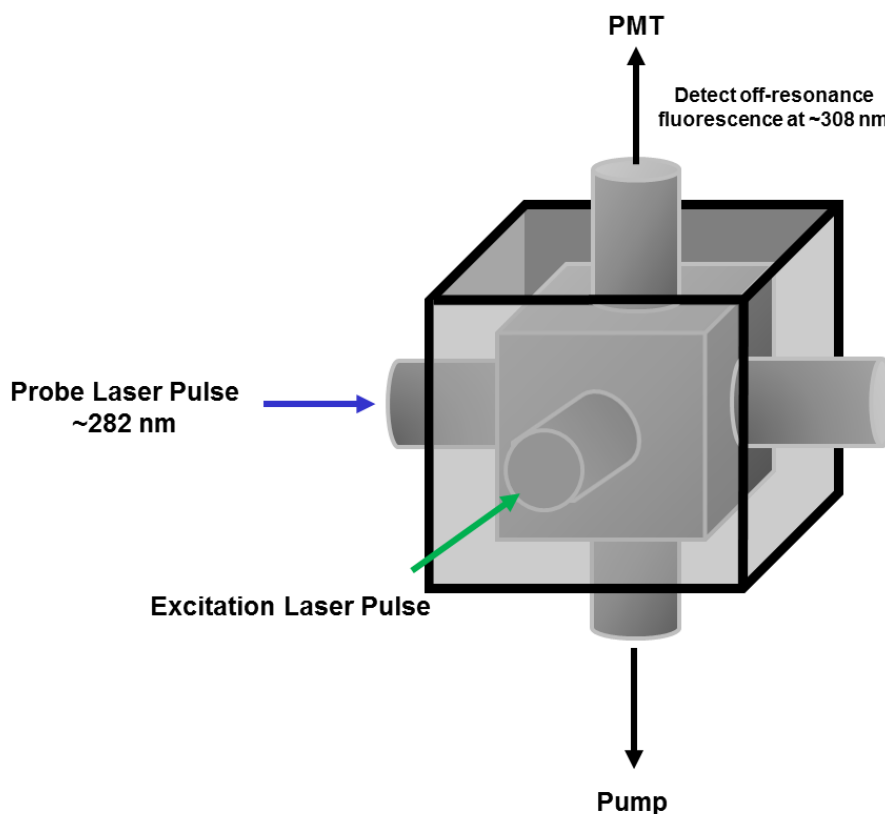


Figure 3.13 Reaction cell used for low temperature (251-298 K) experiments conducted in this thesis

3.3.4 Pressure Readings

The total pressure in the reaction cell, monitored by a capacitance manometer, was controlled by a needle valve on the exhaust of the cell. Pressures of between 4 and 350 Torr (Leybold CERAVAV and MKS Baratron) could be achieved within the reactor and pressures of up to 1300 Torr within the vacuum line where reactant/bath gas mixtures were made up in glass bulbs. The pressure gauges operate by measuring the change in capacitance with the change in pressure between a diaphragm and powered electrode within the gauge. For low pressures (sub mTorr) of the vacuum line pressures were measured using a Pirani gauge which contains a heated thermal filament. Thermal conductivity of a gas varies with pressure which allows the gauges to monitor the change in pressure by measuring the change in temperature of the filament.

3.3.5 Gas Sample Preparation

The concentration of reactants within the cell for each experiment was calculated from the total number density of gas molecules in the cell using the ideal gas law, and the concentration and relative flow rates of the gases used. Reagent samples were made up in glass bulbs on a vacuum line, where the concentrations of the bulbs were determined using a barometer. OH radical precursors were flowed into the cell with a bath gas via a gas bubbler. Reactants were flowed through a gas manifold where they were pre-mixed prior to entering the reaction cell. Reactant flow into the cell was constant to ensure a fresh gas sample was present in the cell for each photolytic pulse. Gas flows into the cell were controlled by mass flow controllers (MFCs) connected to a digital readout box. MFCs were calibrated at least once a year by varying the gas flow into the MFC and monitoring the displacement of bubbles through a flowtube. An example of an MFC calibration can be seen in Figure 3.14.

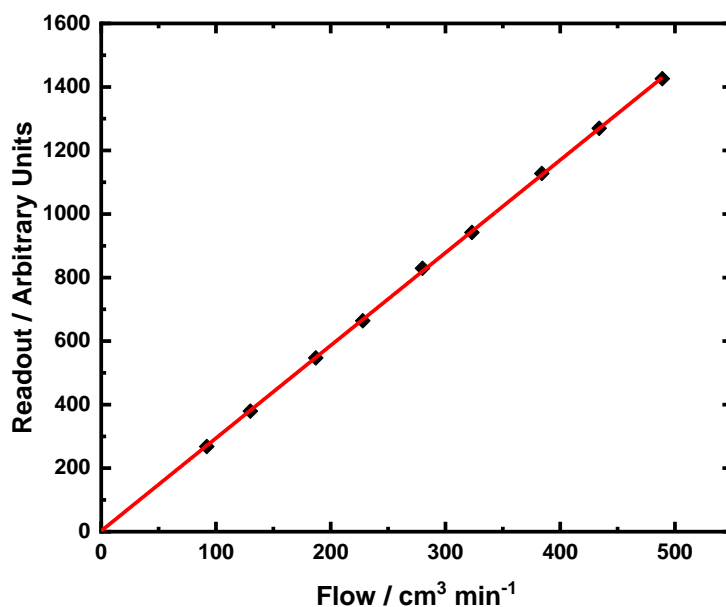


Figure 3.14 A typical calibration for an MFC (SN: 906LS002) in N₂.

3.3.6 Experimental Procedure

For reactions carried out at room temperature and above, a stainless steel reaction cell was mounted with resistance cartridge heaters within the cell walls that could reach up to 770 K. Temperatures were controlled using a commercial temperature controller and temperatures in the reactor were measured by K-type thermocouples close to the reaction zone. Experiments were conducted at temperatures between 298 K and 770 K.

For reactions carried out at sub-ambient temperatures, a stainless steel reaction cell was immersed in a bath which was filled with ethylene glycol and methanol and cryogenically cooled by a refrigerated immersion probe (LabPlant Refrigerated Immersion Probe, RP-100CD), to temperatures of 251 K.

Reactions were initiated when OH radicals were produced *via* the photolysis of a suitable precursor using the 4th harmonic of a pulsed Nd:YAG photolysis laser at $\lambda = 266$ nm. The photolysis laser beam was introduced into the reactor through one of the side arms and had a typical fluence of ~ 60 mJ cm⁻². A pulse repetition frequency of 10 Hz was used for the majority of the study except when experiments were conducted at lower pulse repetition rates to ensure there were no interferences from photolysis products.

OH radicals were excited at $\lambda = 282$ nm ($A^2\Sigma(v = 1) \leftarrow X^2\Pi(v = 0)$), by off-resonance LIF using the frequency doubled 532 nm out of an Nd:YAG (Continuum Powerlite 8010) to pump a dye laser (Spectra Physics PDL-3) operating on Rhodamine-6-G dye. The off-resonant OH fluorescence at $\lambda \sim 308$ nm, passed through an interference filter (Barr Associates, 308 ± 5 nm), was detected by a PMT (Electron tube 9813 QB) mounted perpendicular to the photolysis and probe laser beams. The PMT signal was integrated on an oscilloscope (LeCroy LT262), digitized and passed to a computer for analysis. The probe and photolysis beams cross in the cell to maximise overlap and avoid heterogeneous loss of OH radicals at the walls. Laser power was monitored by a photodiode mounted behind the reaction cell and fluorescence signals were normalised to laser power during analysis. A delay between the photolysis and probe lasers was

controlled by a digital delay generator and varied to enable the monitoring of the OH profile as a function of time following the photolysis of the gas mixture. Kinetic traces, an example of which is given in Figure 3.15, were taken over 200 time point and typically averaged 8 times.

3.4 Kinetic Analysis

For general reactions, the following process is used to analyse kinetics of a pseudo-first-order system. Other systems described in this thesis may require other kinetics equations for analysis and are provided where appropriate (Chapter 8).

Reactions were carried out under pseudo-first-order conditions such that the concentration of the reactant was always in large excess of the reactive species, OH. Under these conditions the primary loss of OH is through the reaction with the reactant (R3.5), other losses such as the reaction with the precursor, loss at the cell walls or diffusion are presented by the first-order loss, R3.6.



For the bimolecular reaction between OH and a reactant, the change in the OH concentration with time is given by:

$$\frac{-d[\text{OH}]}{dt} = k_{3.5}[\text{OH}][\text{reactant}] + k_{3.6}[\text{OH}] \quad \text{E3.11}$$

where k_5 is the rate coefficient associated to the OH loss in R3.5 and $k_{3.6}$ is the first order loss in R3.6. If [reactant] is in great excess over [OH] then this can be simplified to:

$$\begin{aligned} \frac{-d[\text{OH}]}{dt} &= k'[\text{OH}] + k_{3.6}[\text{OH}] \quad \text{E3.12} \\ &= [\text{OH}](k' + k_{3.6}) \end{aligned}$$

where $k_6' = k_6[\text{reactant}]$ and the reaction is pseudo-first-order. This can be integrated:

$$\int_{[\text{OH}]_0}^{[\text{OH}]_t} \frac{1}{[\text{OH}]} \cdot d[\text{OH}] = \int_0^t -(k' + k_{3,6}) \cdot dt \quad \text{E3.13}$$

$$\ln \left(\frac{[\text{OH}]_t}{[\text{OH}]_0} \right) = -(k' + k_{3,6})t \quad \text{E3.14}$$

$$[\text{OH}]_t = [\text{OH}]_0 \exp(-(k' + k_{3,6})t) \quad \text{E3.15}$$

where $[\text{OH}]_0$ is initial OH concentration, $[\text{OH}]_t$ is OH concentration after time t and k' is the pseudo-first-order rate coefficient. As OH fluorescence signal is directly proportional to $[\text{OH}]$, no absolute concentrations are directly measured. Instead, the expression for the decay of OH can be written as:

$$S_t = S_0 \exp(-(k' + k_{3,6})t) \quad \text{E3.16}$$

where $[S]_0$ is the initial is OH fluorescence signal, $[S]_t$ is signal after time t , k' is the pseudo-first-order rate coefficient and $k_{3,6}$ is the first-order loss of OH.

E3.16 can therefore be fitted to the observed OH decay profiles to determine the pseudo-first-order rate coefficient, k' . Figure 3.15 shows a typical fluorescence decay trace of OH over time, a single exponential is fitted to the trace according to E3.16.

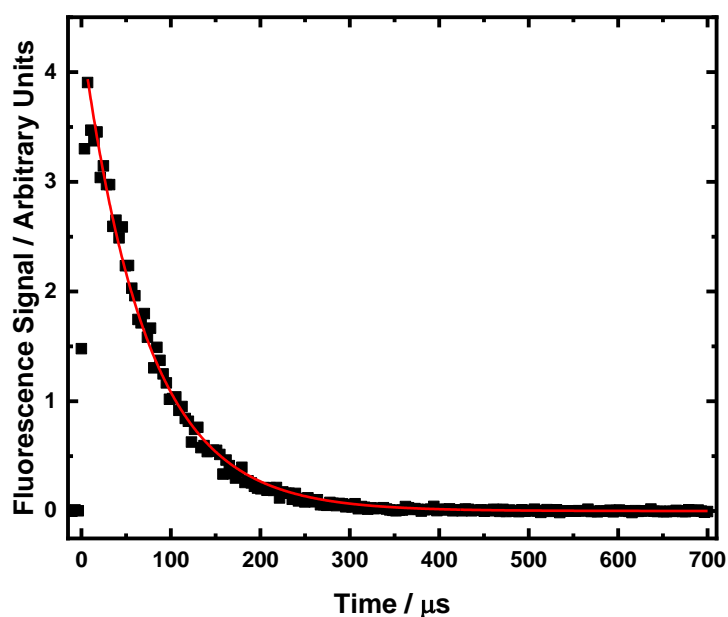


Figure 3.15 OH fluorescence decay at $[\text{furan}] = 4.06 \times 10^{14} \text{ molecule cm}^{-3}$ at 298 K and 50 Torr with a H_2O_2 precursor. $k' = (13885 \pm 122) \text{ s}^{-1}$ according to E3.16. The fit of E3.16 is applied from $t = 10 \mu\text{s}$ to avoid the points produced from photolytic laser pick up by the PMT.

If the experimental concentration of the excess reactant is varied, several pseudo-first-order decay coefficients can be measured. Subsequently, a plot of k' against $[\text{reactant}]$ at various concentrations (Figure 3.16) should be linear and the bimolecular rate coefficient, k , can then be obtained from the gradient of the plot.

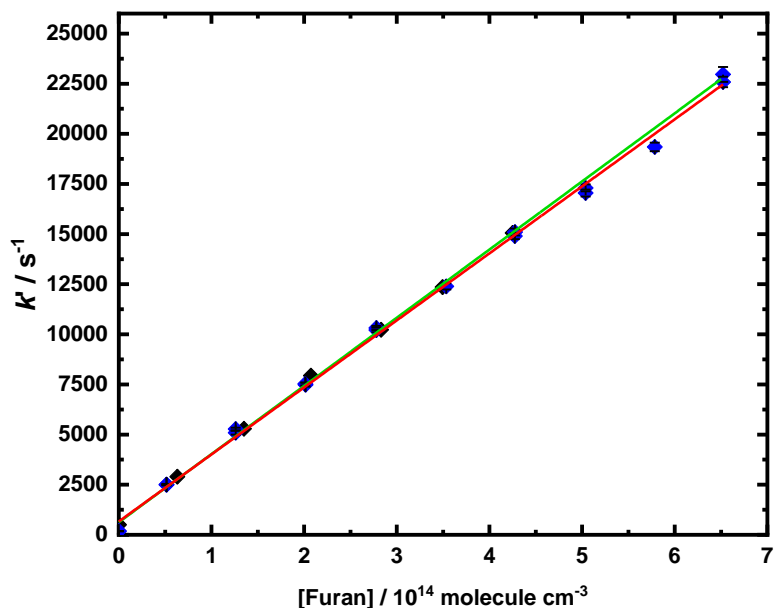


Figure 3.16 Bimolecular plots for the reaction of OH + furan at 298 K at 4 Torr (black diamonds) and 95 Torr (blue diamonds) the slopes of which give $k = (3.40 \pm 0.10) \times 10^{-11} \text{ cm}^3 \text{ molecule}^{-1} \text{ s}^{-1}$ (red line) and $k = (3.30 \pm 0.10) \times 10^{-11} \text{ cm}^3 \text{ molecule}^{-1} \text{ s}^{-1}$ (green line) respectively. Note some 1σ error bars are smaller than symbols.

3.5 References

1. Pilling, M.J. and P.W. Seakins. *Reaction Kinetics*. Oxford Science Publications. Oxford: Oxford University Press, 1995, pp.2,3.
2. Barnes, I., *et al.* Reactivity studies of organic substances towards hydroxyl radicals under atmospheric conditions. *Atmospheric Environment (1967)*, 1982, **16**(3), pp.545-550.
3. Howard, C.J. Kinetic measurements using flow tubes. *The Journal of Physical Chemistry*, 1979, **83**(1), pp.3-9.
4. Atkinson, R. Kinetics and mechanisms of the gas-phase reactions of the hydroxyl radical with organic compounds under atmospheric conditions. *Chemical Reviews*, 1986, **86**(1), pp.69-201.
5. Davis, H.J., *et al.* *Shock tube techniques and instrumentation*. Washington, D.C.: U.S. Army Material Command, Harry Diamond Laboratories, 1969,
6. Sung, C.-J. and H.J. Curran. Using rapid compression machines for chemical kinetics studies. *Progress in Energy and Combustion Science*, 2014, **44**, pp.1-18.
7. Minetti, R., *et al.* Comparison of oxidation and autoignition of the two primary reference fuels by rapid compression. *Symposium (International) on Combustion*, 1996, **26**(1), pp.747-753.
8. Griffiths, J.F., P.A. Halford-Maw and C. Mohamed. Spontaneous ignition delays as a diagnostic of the propensity of alkanes to cause engine knock. *Combustion and Flame*, 1997, **111**(4), pp.327-337.
9. Silke, E.J., H.J. Curran and J.M. Simmie. The influence of fuel structure on combustion as demonstrated by the isomers of heptane: a rapid compression machine study. *Proceedings of the Combustion Institute*, 2005, **30**(2), pp.2639-2647.

10. Würmel, J. and J.M. Simmie. CFD studies of a twin-piston rapid compression machine. *Combustion and Flame*, 2005, **141**(4), pp.417-430.
11. Wayne, R.P. *Principles and applications of photochemistry*. Oxford University Press, Incorporated, 1988,
12. Schomburg, G., *et al.* Sampling techniques in capillary gas chromatography. *Journal of Chromatography A*, 1977, **142**, pp.87-102.
13. De Hoffmann, E. and V. Stroobant. *Mass Spectrometry: Principles and Applications*. Wiley, 2013,
14. Gross, J.H. and P. Roepstorff. *Mass Spectrometry: A Textbook*. Springer Berlin Heidelberg, 2011,
15. Dawson, P.H. *Quadrupole Mass Spectrometry and Its Applications*. Elsevier Science, 2013,
16. Blitz, M.A., *et al.* Time-of-flight mass spectrometry for time-resolved measurements. *Review of Scientific Instruments*, 2007, **78**(3), p.034103.
17. Pilling, M.J. and I.W.M. Smith. *Modern Gas Kinetics*. Blackwell Scientific Publications, 1987,
18. M. Nic, J.J., B. Kosata; Updates Compiled by A. Jenkins. *Resonance Fluorescence Technique*. IUPAC. Compendium of Chemical Terminology, 2nd ed. (the "Gold Book"). Blackwell Scientific Publications, Oxford (1997), 2006,
19. Cremers, D.a.a.R.L.J. *Handbook of Laser-Induced Breakdown Spectroscopy*. Hoboken, N.J.: Wiley, 2013,
20. Franken, P.A., *et al.* Generation of Optical Harmonics. *Physical Review Letters*, 1961, **7**(4), pp.118-119.
21. Eisaman, M.D., *et al.* Invited Review Article: Single-photon sources and detectors. *Review of Scientific Instruments*, 2011, **82**(7), p.071101.

Chapter 4 Kinetic Study of the OH + Furan Reaction as a Function of Temperature and Pressure

4.1 Background and Previous Work

Furan (*oxole*, C₄H₄O, Figure 4.1) is an aromatic heterocyclic ether that can be produced from lignocellulosic waste and has been suggested as a potential second generation biofuel. The chemistry of the combustion of biofuels has been discussed in Chapter 1. The hydroxyl radical (OH) is the primary oxidant of biofuels under low temperature combustion conditions. Figure 4.1 shows the structure and possible reaction sites of furan with OH. The OH radical is able to add to the double bond of furan at either the C1 or C2 site. The OH radical is also able to abstract the hydrogen from the C1 or C2 site under certain conditions.

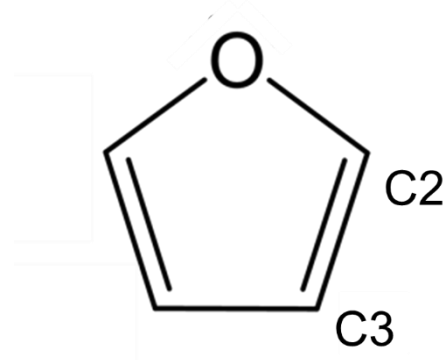


Figure 4.1 Structure of furan with numbered carbons.

Previous studies of gas phase reactions of OH radicals and furans have typically focused on the kinetics of OH radicals with the unsubstituted furan under limited conditions of temperature and pressure, with most studies performed at room temperature and atmospheric pressure. Only one investigation in the literature has studied the temperature dependence of the reaction between OH and furan under low temperature combustion conditions (<1000 K), which is a key parameter for combustion and atmospheric modelling.

4.1.1 Studies of OH + Furan at Low Temperature (<1000 K)

The first investigation into the gas phase reaction between furan and the OH radical was performed by Lee and Tang¹ in 1982, where they report a rate coefficient of $k = (10.50 \pm 0.80) \times 10^{-11} \text{ cm}^3 \text{ molecule}^{-1} \text{ s}^{-1}$. They employed a discharge flow-resonance fluorescence (DF-RF) technique to carry out direct measurements at 298 K and total pressures of 1-5 Torr in He buffer gas. The DF-RF technique is described in Chapter 3.

Lee and Tang used Pyrex coated Teflon flow tube cured at 530 K to reduce OH radical recombination at the tube wall. OH radicals were generated from the H atom titration with a large excess of NO₂ (R4.1-R4.2), where H atoms were produced *via* microwave discharge of H₂ gas in He carrier gas.



The reactions were carried out under pseudo-first-order conditions where the reactant concentration was in large excess over the OH radical concentration. Bimolecular rate coefficients were determined from a plot of k_{obs} (k') against reactant concentrations as seen in Figure 4.2.

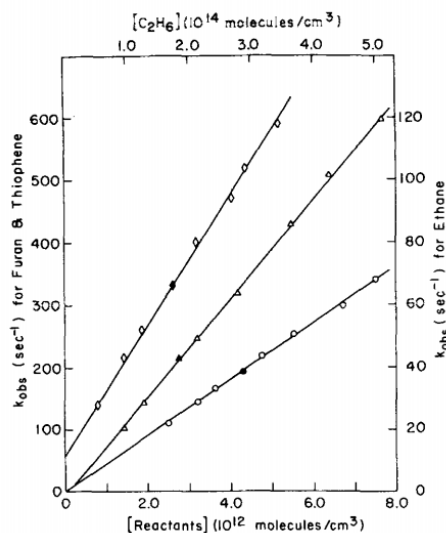
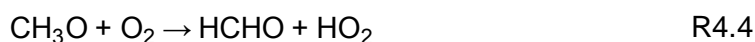


Figure 4.2 k_{obs} (k') vs. reactant concentration for furan (diamond), ethane (triangle) and thiophene (circle), reported by Lee and Tang¹

Lee and Tang reported that excess NO_2 was required in the titration of H atoms. In experiments carried out without NO_2 in large excess, plots were no longer linear and a bimolecular rate coefficient could not be deduced from the gradient.

Atkinson *et al.*² obtained rate coefficients for the reactions of OH radicals with furan using continuous photolysis-gas chromatography (CP-GC) with flame ionization at 298 K, experiments were carried out in air at 735 Torr. Irradiations were carried out in a cylindrical Teflon reaction bag surrounded by blacklights (typically $\lambda \sim 350\text{-}400$ nm). OH radicals were generated *via* the photolysis of methyl nitrite (CH_3ONO) in air at wavelengths >290 nm (R4.3-R4.5). NO was introduced to the reaction mixture to promote the formation of OH from HO_2 and titrate the O_3 generated as a result of NO_2 photolysis. Atkinson *et al.* reported that furan photolysis was negligible under experimental conditions employed.



Rates were determined using the relative rate method, which is explained in more detail in Chapter 3. The rate coefficients for the OH radical reactions were found relative to the

rate coefficient for the reaction of OH radicals with *n*-hexane. The ratio of $k_{\text{OH+furan}}/k_{\text{OH+n-hexane}}$ was obtained from the gradient of the plot of $\ln([\text{furan}]_0/[\text{furan}]_t)$ against $\ln([\text{n-hexane}]_0/[\text{n-hexane}]_t)$ (Figure 4.3), measured as 7.04 ± 0.50 . Based on a rate coefficient for the reaction of OH + *n*-hexane³ of $k = (5.70 \pm 0.09) 10^{-12} \text{ cm}^3 \text{ molecule}^{-1} \text{ s}^{-1}$, Atkinson *et al.* determined a bimolecular rate coefficient for OH + furan as $k = (4.02 \pm 0.28) \times 10^{-11} \text{ cm}^3 \text{ molecule}^{-1} \text{ s}^{-1}$ which is significantly slower than that reported by Lee and Tang ($k = (10.50 \pm 0.80) \times 10^{-11} \text{ cm}^3 \text{ molecule}^{-1} \text{ s}^{-1}$). In agreement with Lee and Tang, Atkinson *et al.* suggested the reaction of OH radicals with furan proceed *via* addition to the double bond and note that the OH radical is highly reactive towards furan when compared to simple alkenes. For example, the reaction of OH + ethene⁴ has a rate coefficient of $k = 8.43 \times 10^{-12} \text{ cm}^3 \text{ molecule}^{-1} \text{ s}^{-1}$ and that for OH + propene⁴ has a rate coefficient of $k = 2.60 \times 10^{-11} \text{ cm}^3 \text{ molecule}^{-1} \text{ s}^{-1}$.

There are no data for the reaction of OH and *n*-hexane currently available in the IUPAC database, however the Leeds MCM^{5,6} provides a rate coefficient taken from Atkinson *et al.*⁴ of $k = 1.53 \times 10^{-17} T^2 \exp(414/T) \text{ cm}^3 \text{ molecule}^{-1} \text{ s}^{-1}$ which gives a value at 298 K of $k = 5.6 \times 10^{-12} \text{ cm}^3 \text{ molecule}^{-1} \text{ s}^{-1}$, which is in agreement with the rate coefficient reported by Barnes *et al.*⁷ of $k = 5.64 \times 10^{-11} \text{ cm}^3 \text{ molecule}^{-1} \text{ s}^{-1}$. Using these rate coefficients for OH + *n*-hexane, an updated rate coefficient for the reaction of OH with furan is $k = (3.94 \pm 0.28) \times 10^{-11} \text{ cm}^3 \text{ molecule}^{-1} \text{ s}^{-1}$.

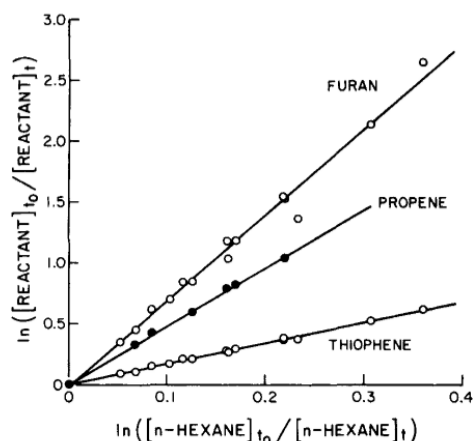


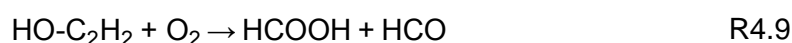
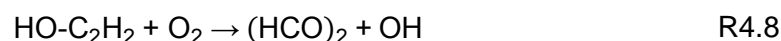
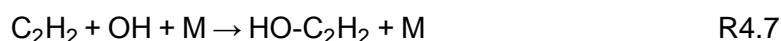
Figure 4.3 Plots for the experimental data for OH + furan from relative rate experiments using *n*-hexane as a reference compound from Atkinson *et al.*²

Wine and Thompson⁸ investigated the reactions of OH radicals with furan and thiophene using time-resolved resonance fluorescence spectroscopy to determine the rate coefficients for the reactions. OH radicals were generated *via* the flash photolysis of water at wavelengths between 165 nm and 185 nm (R4.6). A detailed description of these techniques can be seen in Chapter 3.

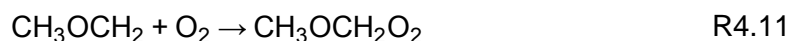
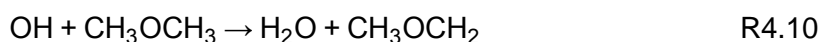


Experiments were carried out under slow flow conditions (in Ar) to avoid build-up of reaction or photolysis products. Reactions were carried out under pseudo-first-order conditions and the room temperature rate coefficient was found to be $k = (4.04 \pm 0.61) \times 10^{-11} \text{ cm}^3 \text{ molecule}^{-1} \text{ s}^{-1}$. These results are in good agreement with Atkinson *et al.* and therefore in disagreement with the results of Lee and Tang ($k = (10.50 \pm 0.80) \times 10^{-11} \text{ cm}^3 \text{ molecule}^{-1} \text{ s}^{-1}$). Several bath gases were used in the previous studies,^{2,9,10} including air, for which the possibility of OH recycling by O₂ was not discussed. However, as rates generally agree between experiments by Atkinson *et al.* ($k = (4.01 \pm 3.0) \times 10^{-11} \text{ cm}^3 \text{ molecule}^{-1} \text{ s}^{-1}$) where air was and those by Wine and Thompson ($k = (4.04 \pm 0.61) \times 10^{-11} \text{ cm}^3 \text{ molecule}^{-1} \text{ s}^{-1}$) where O₂ was not present, it can be concluded that OH recycling by O₂ has not taken place.

If the rate of reaction were dependent on oxygen concentration, it could indicate the possibility of OH radical recycling, where an OH radical is produced as a product of the reaction. OH recycling results in biexponential OH decay traces, where the initial OH fluorescence falls as the OH reacts, but unlike in single exponential decays, does not reach the baseline as the recycled OH is produced. For example in the reaction of acetylene, C₂H₂, with OH (R4.7-R4.9):¹¹



Another example of OH recycling is demonstrated in the reaction of OH and the fuel dimethylether (R4.10-R4.13)¹²:



To rule out the possibility that reactive free radicals as the result of photodissociation of reactants could contribute to the OH decay profile, Wine and Thompson carried out experiments where the flash intensity was varied by a factor of 4-5 thereby varying initial concentrations of any photolytic product. All results were found to be independent of flash intensity. Additionally, experiments were carried out over a range of pressures (30-150 Torr) and no dependence on pressure was found.

To investigate the temperature dependence of the bimolecular rate coefficient, Wine and Thompson performed experiments over a range of temperatures (254-425 K). The temperature dependence was found to be negative for all reactions studied and Arrhenius parameters for OH + furan were determined to be $A = (1.32 \pm 0.29) \times 10^{-11} \text{ cm}^3 \text{ molecule}^{-1} \text{ s}^{-1}$ and $-E_a/R = (333 \pm 67) \text{ K}$. Arrhenius plots for this experiment can be

seen in Figure 4.4. This supports theories suggested by both the previous studies that the reaction pathway occurs through the addition of an OH radical to the π system in furan. A negative temperature dependence suggests a barrierless addition reaction. An H abstraction by OH would result in a positive temperature dependence due to the energy barrier to remove an H atom from the reactant.

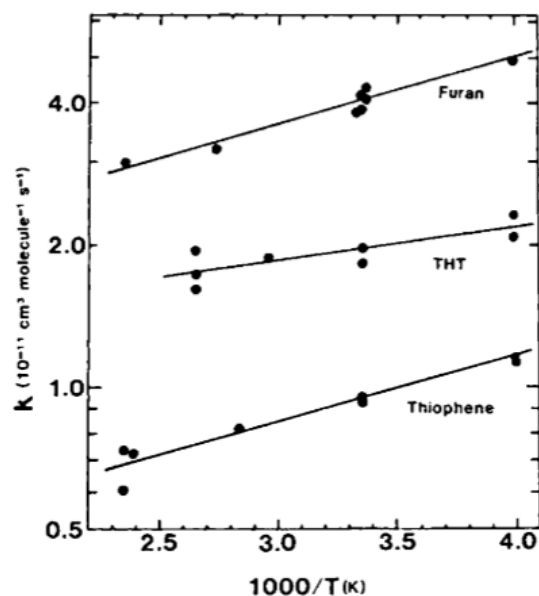


Figure 4.4 Arrhenius plots for the reaction of OH with furan, tetrahydrothiophene (THT) and thiophene reported by Wine and Thompson⁸

Room temperature rate coefficients reported by Wine and Thompson⁸ for furan are in good agreement with Atkinson *et al.* and highlight the discrepancies with Lee and Tang's results. Such inconsistencies were also observed when looking at the analogous reaction of OH + thiophene (C₄H₄S) performed in these studies. Atkinson *et al.* determined a rate coefficient of $(9.58 \pm 0.38) \times 10^{-12} \text{ cm}^3 \text{ molecule}^{-1} \text{ s}^{-1}$ for OH + thiophene, and Wine and Thompson $(9.52 \pm 1.43) \times 10^{-12} \text{ cm}^3 \text{ molecule}^{-1} \text{ s}^{-1}$. Lee and Tang determined a much faster rate of $(4.77 \pm 0.63) \times 10^{-11} \text{ cm}^3 \text{ molecule}^{-1} \text{ s}^{-1}$. The results of the discharge flow method disagree with photolysis methods results by a factor of five. This could be due to secondary chemistry at the walls of the flow tube occurring despite the efforts of Lee and Tang to reduce such homogeneous reactions.

A comparison with other previous studies of OH + thiophene show further disagreement with Lee and Tang's results. Wallington¹³ studied the reaction using flash photolysis-resonance fluorescence (FP-RF) and measured a rate coefficient of $k = 8.52 \times 10^{-12} \text{ cm}^3 \text{ molecule}^{-1} \text{ s}^{-1}$, which is 5.6 times slower than the rate coefficient reported by Lee and Tang. Martin *et al.*¹⁴ also measured the reaction of OH + thiophene using the discharge flow-electron paramagnetic resonance technique and measured a rate coefficient of $k = (1.20 \pm 0.10) \times 10^{-11} \text{ cm}^3 \text{ molecule}^{-1} \text{ s}^{-1}$ which is 3.98 times slower than the rate coefficient reported by Lee and Tang. The discrepancies between the studies of both furan and thiophene indicate a systematic error in the results of Lee and Tang.

Bierbach *et al.*⁹ investigated furan and three furan derivatives: 2-methylfuran, 2-ethylfuran and 2,5-dimethylfuran. This experimental method was similar to that carried out by Atkinson *et al.*, where room temperature rate coefficients were measured using continuous photolysis-gas chromatography (CP-GC) at 760 Torr. The relative rate method was used to determine rate coefficients, using propene as the reference compound, where the rate coefficients of $2.60 \times 10^{-11} \text{ cm}^3 \text{ molecule}^{-1} \text{ s}^{-1}$ for OH + propene was used, taken from the review by Atkinson *et al.*⁴

OH radicals were generated *via* the photolysis of methyl nitrite (R4.3-R4.5) at wavelengths between 320 nm and 480 nm. Bierbach *et al.* reported the use of control experiments which showed furan and its alkylated derivatives to be subject to photolysis and wall losses and it was reported that losses were negligible compared to loss by reaction with OH radicals. No details were given on the control experiments performed.

The bimolecular room temperature rate coefficient of OH + furan was reported as $k = (4.19 \pm 0.21) \times 10^{-11} \text{ cm}^3 \text{ molecule}^{-1} \text{ s}^{-1}$ (Figure 4.5) and found to be in good agreement with Atkinson *et al.* and Wine and Thompson. The rate coefficients for the reaction of OH with 2-methylfuran (2-MF), 2-ethylfuran (2-EF) and 2,5-dimethylfuran (2,5-DMF) were the first to be reported in the literature and were determined to be $k_{\text{OH}+2\text{-MF}} = (6.19 \pm 0.30) \times 10^{-11} \text{ cm}^3 \text{ molecule}^{-1} \text{ s}^{-1}$, $k_{\text{OH}+2\text{-EF}} = (10.77 \pm 2.11) \times 10^{-11} \text{ cm}^3 \text{ molecule}^{-1} \text{ s}^{-1}$ and

$k_{\text{OH}+2,5\text{-DMF}} = (13.21 \pm 0.92) \times 10^{-11} \text{ cm}^3 \text{ molecule}^{-1} \text{ s}^{-1}$. These results show an increasing reaction rate when compared to the unsubstituted furan. These trends will be discussed further in Chapter 5.

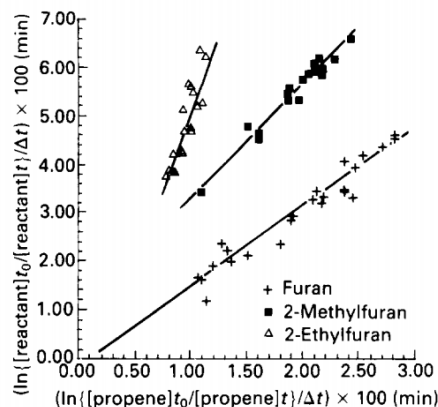


Figure 4.5 Relative rate plot for furan, 2-MF and 2-EF from relative rate experiments using propene as a reference compound reported by Bierbach *et al.*⁹

Tuazon *et al.*¹⁰ investigated the reaction between the hydroxyl radical and several organochlorine compounds using the relative rate method described previously. Furan was employed as a reference compound for the experiment to measure the rate coefficient for OH + 3-chloro-2-chloromethyl-1-propene. In addition to furan, isoprene was used as a second reference compound.

Furan and isoprene were quantitatively monitored by gas chromatography with flame ionization detection (GC-FID) and OH radicals were produced *via* the photolysis of methyl nitrite in air, at wavelengths of $\geq 290 \text{ nm}$, as previously described (R4.3-R4.5). Experiments were carried out at 295 K and 735 Torr in N_2 bath gas. The rate coefficient used for the reaction between OH and isoprene was $k_{\text{OH}+\text{isoprene}} = (9.60 \pm 0.43) \times 10^{-11} \text{ cm}^3 \text{ molecule}^{-1} \text{ s}^{-1}$ according to Atkinson *et al.*³. The measured rate coefficient, $k_{\text{OH}+\text{furan}} = (3.98 \pm 0.35) \times 10^{-11} \text{ cm}^3 \text{ molecule}^{-1} \text{ s}^{-1}$, was found to be in agreement with Atkinson *et al.*, Wine and Thompson and Bierbach *et al.*

Aschmann *et al.*¹⁵ investigated the rate of reaction of OH with several furan derivatives: 2- and 3-methyl furan (3-MF), 2,5- and 2,3-dimethylfuran (2,3-DMF) using the CP-GC

technique at 296 K and 735 Torr in a chamber study. OH radicals were produced *via* the photolysis of methyl nitrite (R15-R17) at $\lambda > 300$ nm and NO was introduced to promote the formation of OH radicals and to titrate the O₃ formed from subsequent NO₂ photolysis. The relative rate method was used employing 1,3,5-trimethylbenzene as a reference compound, using a rate coefficient of $k = 5.67 \times 10^{-11} \text{ cm}^3 \text{ molecule}^{-1} \text{ s}^{-1}$ taken from Atkinson *et al.*¹⁶

Several bath gases were used in the previous studies, including air, for which the possibility of OH recycling by O₂ was not discussed (see section 1.2.4 in Chapter 1 the OH recycling mechanism). However, as rates generally agree between experiments where air was and was not used, it can be concluded that OH recycling by O₂ has not taken place.

Wine and Thompson⁸ use the photolysis of water vapour in Ar to generate OH radicals. The formation of H radicals in this process and their possible effect on the rate of reaction is not discussed, but again as the rates agree it would seem H radicals do not have a significant, if any, effect on the rate.

Lee and Tang reported fast rate coefficients that were not replicated in subsequent studies. This discrepancy in results for OH + furan is similar to OH + thiophene. The use of the discharge flow technique where homogeneous reactions could take place is a possibility for the faster observed rate, this could be investigated if further studies using this technique were carried out.

During the investigation of the work for this thesis a student at the Karlsruhe Institute of Technology, Dr Julia Eble, also carried out a study into the oxidation of furans under low temperature combustion conditions. At the time of writing, the work by Dr Eble remains unpublished, however, it has been provided for comparison in this thesis.

Eble¹⁷ investigated the reactions of OH radicals with furan, 2-MF and 2,5-DMF using LFP-LIF to determine the rate coefficients for the reactions, a detailed description of this

technique can be seen in Chapter 3. OH radicals were generated *via* the flash photolysis of nitric acid (HNO₃) at 248 nm (R4.6).



Experiments were carried out in He under pseudo-first-order conditions where the furan reactants were in excess over the OH radicals. The room temperature rate coefficient was found to be $k = (3.45 \pm 0.34) \times 10^{-11} \text{ cm}^3 \text{ molecule}^{-1} \text{ s}^{-1}$.

These results are in good agreement with those for OH + furan reported by Atkinson *et al.*, $k = (4.02 \pm 0.28) \times 10^{-11} \text{ cm}^3 \text{ molecule}^{-1} \text{ s}^{-1}$; Wine and Thompson, $k = (4.07 \pm 0.29) \times 10^{-11} \text{ cm}^3 \text{ molecule}^{-1} \text{ s}^{-1}$ and Tuazon *et al.*, $k = (3.98 \pm 0.35) \times 10^{-11} \text{ cm}^3 \text{ molecule}^{-1} \text{ s}^{-1}$. However, the results of Eble are not within the error limits of the rate coefficients reported by Lee and Tang or Bierbach *et al.*, with 70.3 % and 32.9 % percentage difference, respectively.

It was noted by Eble that gaseous HNO₃ can catalytically decompose at room temperature on many surfaces, and one of the major products of the decomposition is NO₂, which can rapidly react with OH¹⁸ and therefore requires attention. However it was reported that the production of NO₂ was very slow when compared to the timescales of the experiment. HNO₃ mixtures were used for a maximum of 4 days to keep NO₂ concentrations as low as possible.

Eble reported results were found to be independent of flash intensity. Experiments were carried out over a range of pressures, 2 - 10 bar (1500 - 7500 Torr), and no dependence on pressure was observed.

To investigate the temperature dependence of the bimolecular rate coefficient, Eble performed experiments over a range of temperatures (295 - 570 K). The temperature dependence was found to be negative for all reactions studied and Arrhenius parameters for furan were determined to be $A = (5.91 \pm 0.64) \times 10^{-12} \text{ cm}^3 \text{ molecule}^{-1} \text{ s}^{-1}$ and $-E_a/R = (536 \pm 38) \text{ K}$. Arrhenius plots for this experiment can be seen in Figure 4.6. Although

room temperature rate coefficients agree, when compared to Wine and Thompson the Arrhenius parameters found by Eble are not in agreement. The A factor found by Eble is 44.8 % that of the A factor found by Wine and Thompson ($A = (1.32 \pm 0.29) \times 10^{-11} \text{ cm}^3 \text{ molecule}^{-1} \text{ s}^{-1}$) and the $-E_a/R$ is 161 % greater than that of Wine and Thompson ($-E_a/R = (333 \pm 67) \text{ K}$). Both studies were carried out using the LFP-LIF technique, however the studies used different methods to generate the OH radicals, R6 vs R14. Additional OH sinks from possible impurities present in the system could result in an apparent faster rate coefficient. For example, in a system where impurities are present in the furan sample, the kinetics (discussed in Chapter 3) would be affected:

$$\frac{-d[\text{OH}]}{dt} = k_f[\text{OH}][\text{furan}] + k_x[\text{OH}][\text{X}] + k_{\text{diff}}[\text{OH}] \quad \text{R4.15}$$

where the pseudo-first-order rate coefficient of OH + furan, k_f , would appear larger than it is if $[\text{X}]$ scaled linearly with the furan concentration.

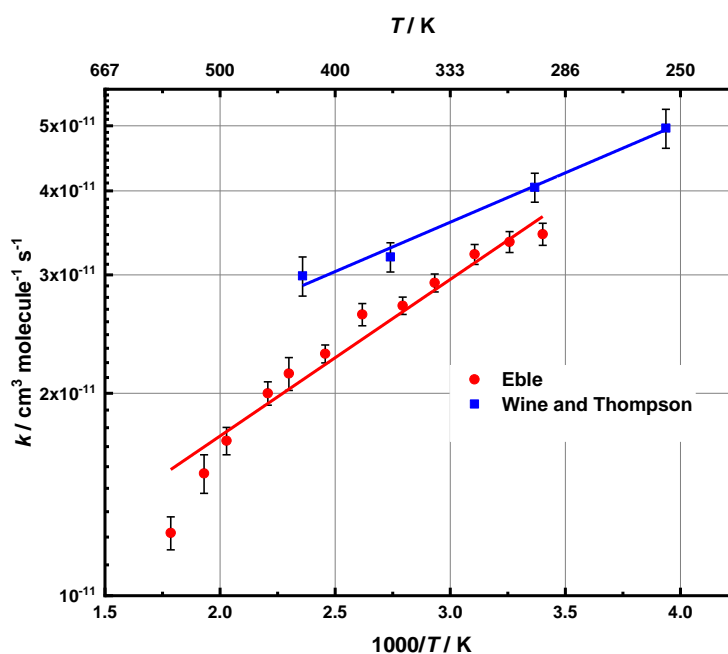


Figure 4.6 Arrhenius plot for OH + furan from Wine and Thompson⁸ from 254-425 K and 30-150 Torr and Eble¹⁷ from 296-570 K and 2 to 10 bar.

Reference	<i>T</i> / K	<i>p</i> / Torr	Technique	<i>k</i> / 10 ⁻¹¹ cm ³ molecule ⁻¹ s ⁻¹	Reference Compound	<i>k</i> _{OH+ref} / Literature <i>k</i> _{OH+ref}	<i>k</i> _{updated} / 10 ⁻¹¹ cm ³ molecule ⁻¹ s ⁻¹
Lee & Tang ¹	298	1-5 (He)	DF-RF	10.5 ± 0.85	Ethane	0.96 ¹⁹	10.1 ± 0.82
Atkinson <i>et al.</i> ²	298	735 (Air)	CP-GC	4.02 ± 0.28	<i>n</i> -hexane	1.02 ⁵	4.10 ± 0.29
Wine & Thompson ⁸	254-425	30-150 (Ar)	FP-RF	4.07 ± 0.29*	-	-	-
Bierbach <i>et al.</i> ⁹	298	760 (N ₂)	CP-GC	4.91 ± 0.21	propene	0.90 ¹⁹	5.16 ± 0.22
Tuazan <i>et al.</i> ¹⁰	295	735 (N ₂)	CP-GC	3.98 ± 0.35	isoprene	0.96 ¹⁹	3.82 ± 0.34
Eble ¹⁷	296	1500-7600 (He)	LFP-LIF	3.45 ± 0.34*	-	-	-

Table 4.1 Room temperature rate coefficients for previous studies of the OH reaction with furan. DF-RF Discharge flow resonance fluorescence. CP-GC continuous photolysis gas chromatography. FP-RF flash photolysis resonance fluorescence. LFP-LIF laser flash photolysis-laser induced fluorescence. *Results from absolute measurement technique. Results obtained using the relative rate method are provided as reported and updated for current recommendations for the rate coefficients of the reference reactions.

4.1.2 Studies of OH + Furan at High Temperature (>1000 K)

High temperature measurements of the kinetics of OH + furan have been made by Elwardany *et al.*²⁰ using a shock tube with He driver gas over the temperature range of 928 - 1388 K and a pressure range of 1.17-1.95 atm (889 - 1482 Torr). OH radicals were generated *via* the thermal decomposition of *tert*-butylhydroperoxide ((CH₃)₃COOH) and monitored by UV absorption spectroscopy at ~306 nm. Reactions were performed under pseudo-first-order conditions so that the concentration of furan was in excess over that for OH. The minimum experimental temperature was limited by the need to thermally decompose the precursor ((CH₃)₃COOH) in order to produce OH radicals. Experiments were performed using various initial compositions and pressures, with results found to be independent of mixture composition and pressure.

Elwardany *et al.* report their results as the modified Arrhenius expression $k = 1.30 \times 10^{-21} \times T^3 \exp(1866.7/T) \text{ cm}^3 \text{ molecule}^{-1} \text{ s}^{-1}$. This parameterisation leads to a predicted room temperature rate coefficient of $k = 1.81 \times 10^{-11} \text{ cm}^3 \text{ molecule}^{-1} \text{ s}^{-1}$, which is significantly lower than the measurements at 298 K reported in the literature (Table 4.1). Elwardany *et al.* note this difference and conclude that it is an indication that OH addition pathways dominate at low temperatures in contrast to abstractions at high temperatures. There is a slight non-Arrhenius curvature for the reaction of OH with furan, shown in Figure 4.7, which can be attributed to the change in mechanism from addition to abstraction as the temperature of the system rises.

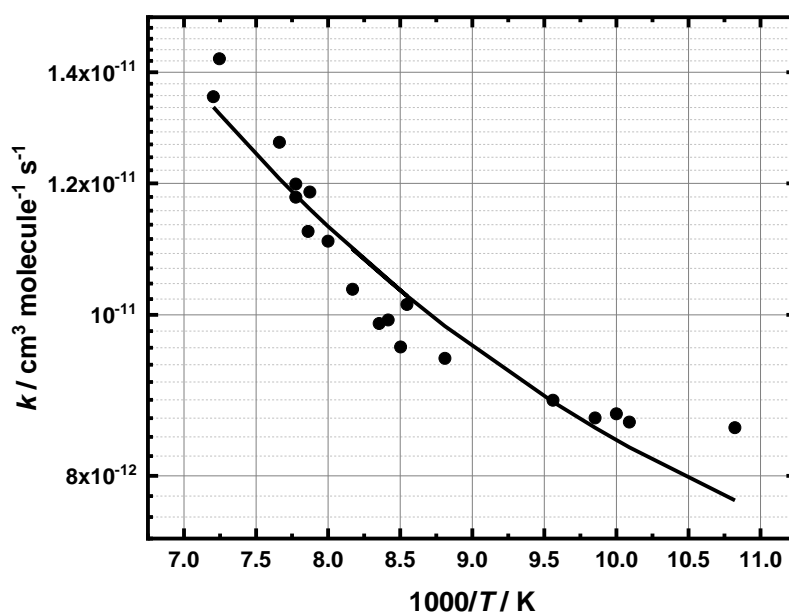
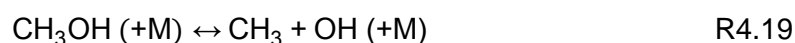
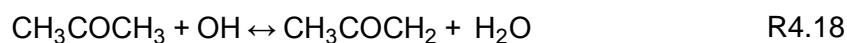
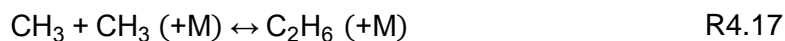


Figure 4.7 Rate coefficient of OH + furan reported by Elwardany *et al.* between 924-1388 K. Black line is the Arrhenius fit reported by Elwardany *et al.* as $k = 1.30 \times 10^{-21} \times T^3 \exp(1866.7/T) \text{ cm}^3 \text{ molecule}^{-1} \text{ s}^{-1}$. No error for the data was provided.

Elwardany *et al.* note interference by secondary chemistry as a result of $(\text{CH}_3)_3\text{COOH}$ decomposition (R4.16-R4.19) and performed experiments using two different mixtures (228 ppm furan with 11 ppm $(\text{CH}_3)_3\text{COOH}$ /30 ppm H_2O in Ar and 167 ppm furan with 13 ppm $(\text{CH}_3)_3\text{COOH}$ /36 ppm H_2O in Ar) to investigate if the mixture composition and secondary chemistry affected the measured rates, but reaction rates were found to be independent of the mixture composition.



4.1.3 Theoretical Studies of OH + Furan

Theoretical studies of reaction kinetics and mechanisms have been also attempted. Grosjean and Williams²¹ investigated structure-reactivity relationships (SRR) and linear free-energy relationships (LFER) for environmentally important chemical reactions of a range of unsaturated contaminants in air and water. They estimated a rate coefficient of $k = 6.71 \times 10^{-11} \text{ cm}^3 \text{ molecule}^{-1} \text{ s}^{-1}$ for the gas phase reaction of OH radicals with furan, these results are approximately 1.5 times greater than the rate coefficients found experimentally.

Mousavipour *et al.*²² studied the kinetics and mechanism of the reaction of OH radicals with furan using DFT (Density Functional Theory), G3MP2 (Gaussian/Møller-Plesset), and CCSD (Coupled-Cluster Singles and Doubles theory) computational methods. They reported that the most probable addition site for OH is at the C1 position (Figure 4.1), which is in agreement with the suggestion made by Bierbach *et al.*⁹ Mousavipour *et al.* report this channel leads to a ring-opening product, Figure 4.8.

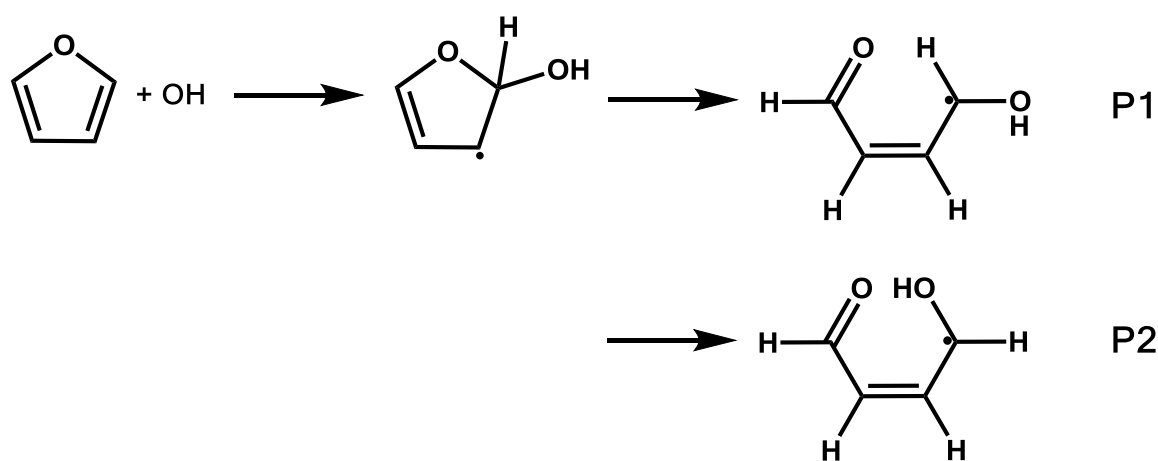


Figure 4.8 Ring-opening products reported by Mousavipour *et al.* from the addition of OH to the C1 site in furan.

Mousavipour *et al.* calculated rate coefficients for the individual reaction channels using an RRKM-TST model, as well as a calculation for the overall rate coefficient for the consumption of reactants in the addition of the OH radical to the C1 carbon using a method which combines chemical activation distribution functions and the multichannel

RRKM method. Mousavipour *et al.* reported a rate constant for OH + furan of $1.9 \times 10^{14} T^{1.57} \exp(-17/RT)$ L mol⁻¹ s⁻¹ which equates to $3.16 \times 10^{-7} T^{1.57} \exp(-17/RT)$ cm³ molecule⁻¹ s⁻¹ resulting in $k_{(298\text{ K})} = 4.09 \times 10^{-11}$ cm³ molecule⁻¹ s⁻¹ at room temperature. This result is within the experimental uncertainties of the results reported by Atkinson *et al.*, Wine and Thompson and Tuazon *et al.* (Table 4.1).

4.1.4 Combustion Models of Furan

There have been several previous modelling studies into furan chemistry at temperatures relevant to high temperature combustion, these are discussed in detail in Chapter 7 and briefly here. Tian *et al.*²³ estimated the rate coefficients of the OH addition to furan (R4.20) and the OH abstraction, from the C1 (R4.21) and C2 (R4.22) carbons, from rate coefficients of the oxidation of small, linear alkenes at high temperatures suggested by Heyberger *et al.*²⁴



Tian *et al.* estimate rate coefficients of $2.70 \times 10^{12} \exp(1040/RT)$ cm³ mol⁻¹ s⁻¹ for R4.20 and $2.26 \times 10^6 T^2 \exp(-2780/RT)$ cm³ mol⁻¹ s⁻¹ for R4.21 and R4.22 which equate to room temperature rate coefficients of 4.49×10^{-12} cm³ molecule⁻¹ s⁻¹ and 3.23×10^{-13} cm³ molecule⁻¹ s⁻¹ respectively. A comparison of the model for OH + furan by Tian *et al.* to the previously described Arrhenius fits to Wine and Thompson, Eble and Elwardany *et al.* can be seen in Figure 4.11. The model by Tian *et al.* underpredicts rate coefficients at low temperatures (<1000 K) when compared to Wine and Thompson and Eble, and similarly underpredicts rate coefficients at high temperature (>1000 K) when compared to the work by Elwardany *et al.*

Liu *et al.*²⁵ coupled computation modelling with an investigation into the study of furan flames above 1000 K by electron-ionization molecular beam mass spectrometry (EI-MBMS) and gas chromatography (GC). Mole fractions of reactants, products and stable

and reactive intermediates were measured. Liu *et al.* reported that a comparison of the presented kinetic model with experimental results and the kinetic model produced by Tian *et al.*²³ showed reasonable agreement, as shown in Figure 4.9. Liu *et al.* provide a schematic for the furan high temperature combustion mechanism shown in Figure 4.10.

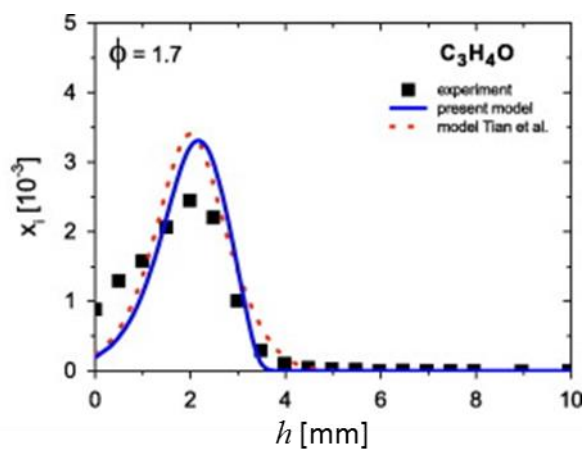


Figure 4.9 Results for the production of acrolein (C_3H_4O) from OH addition to furan reported by Liu *et al.*²⁵ from EI-MBMS experiments (black squares) compared to the model of Liu *et al.* (blue solid line) and the model by Tian *et al.*²³ (dashed red line). H refers to the distance from the burner in the EI-MBMS set up and x_i is the mole fraction.

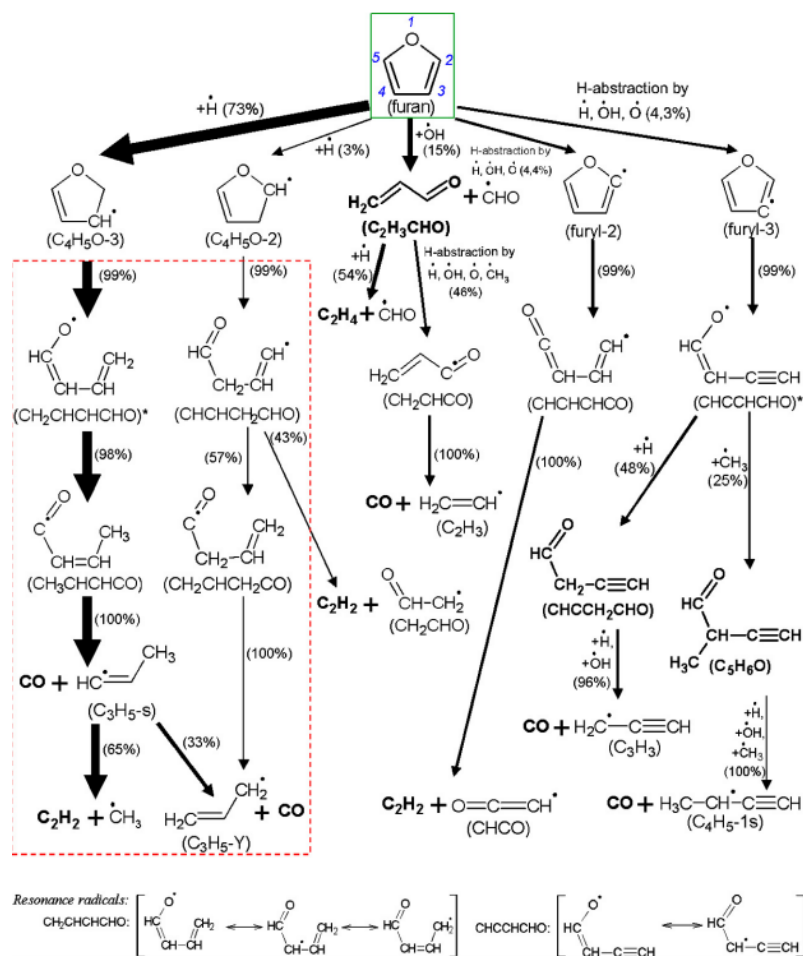


Figure 4.10 Flow-rate analysis for the consumption of furan in a fuel-rich furan flame ($\phi = 1.7$) corresponding to a simulated temperature of 1135 K taken from the study by Liu *et al.*²⁵

Figure 4.11 shows the Arrhenius fits to experimental data compared to the theoretical study by Mousavipour *et al.* and the combustion models by Tian *et al.* and Liu *et al.* At temperatures below 1000 K, both models under predict the rate coefficients compared to those seen experimentally. At high temperature, the Tian *et al.* model also under predicts the rate coefficients reported by Elwardany *et al.*, whereas Liu *et al.*, who report the same rate coefficients as Tian *et al.* for the addition reactions at lower temperatures, slightly over-predict at the higher temperatures.

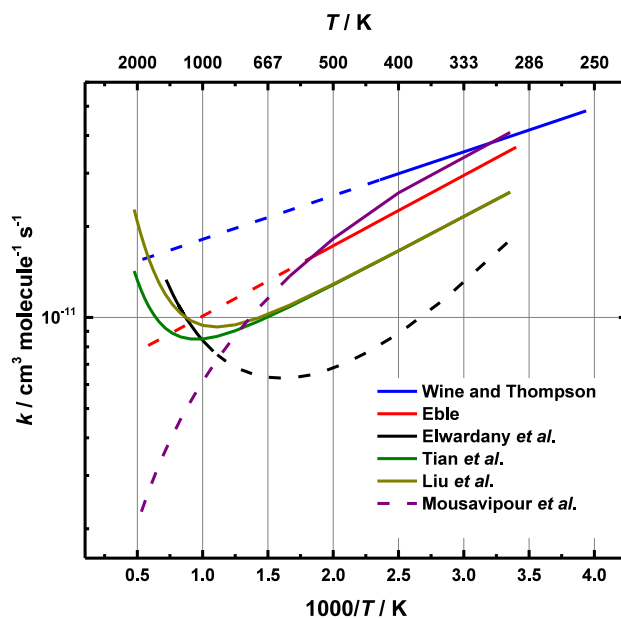


Figure 4.11 Arrhenius fits (solid lines) and extrapolations (dashed lines) to Wine and Thompson (blue), Eble (red), Elwardany *et al.* (black), Tian *et al.* (green) and Liu *et al.* (brown) for the reaction of OH + furan.

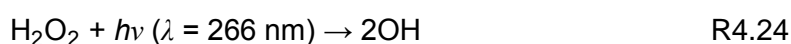
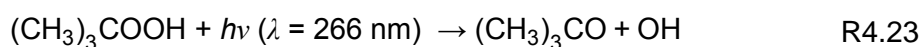
The importance of OH radical initiated oxidation of furan in both atmospheric and combustion environments warrants a better understanding of this chemistry. The current combustion models by Tian *et al.* and Liu *et al.* estimate lower rate coefficients than those seen experimentally in both the low and high temperature combustion regions. To accurately deduce the implications of the reaction of OH + furan using combustion models, the rate coefficients need to be well defined at temperatures relevant to low temperature combustion. This work has extended the temperature range of the rate coefficients for the OH + furan system previously described in the literature by Wine and Thompson from 254 - 425 K to 298 - 595 K using LFP-LIF. Results will be compared with data present in the literature as well as the currently unpublished work produced by Eble.

4.2 Experimental Procedure

Experiments were carried out as described in Chapter 3 and so only a brief outline will be given here.

This work investigates the rate of reaction between OH radicals and furan using laser flash photolysis to initiate the reaction and laser induced fluorescence (LIF) to monitor the OH radical. Furan (Sigma Aldrich, 99 %) was degassed and purified by a series of freeze-pump-thaw cycles and prepared at a known concentration (typically between 1×10^{13} and 1×10^{15} molecule cm^{-3}) in N_2 and stored in a glass bulb. N_2 (BOC, oxygen free, 99 %) and O_2 (BOC, 99 %) were used as supplied. A known flow of N_2 was passed through a bubbler containing *tert*-butylperoxide ($(\text{CH}_3)_3\text{COOH}$) (Sigma Aldrich, 70 % v/v aqueous) or hydrogen peroxide (H_2O_2) (Sigma Aldrich, 50 % v/v aqueous) to entrain the peroxide precursor into the gas flow. Reactions were carried out at pressures between 4 and 100 Torr and temperatures between 298 and 595 K.

Reactions were initiated when OH radicals were produced *via* the photolysis of either $(\text{CH}_3)_3\text{COOH}$ ($298 \text{ K} < T < 500 \text{ K}$ or H_2O_2 ($298 \text{ K} < T < 635 \text{ K}$) (R4.23-R4.25) using the 4th harmonic of a pulsed Nd:YAG photolysis laser at $\lambda = 266 \text{ nm}$.



The reaction was carried out under pseudo-first-order conditions such that the concentration of furan was always in a large excess of OH. Under these conditions the loss of OH is through the reaction with furan (R4.25) and other losses such as reaction with precursor, or diffusion, can be represented as a first-order-loss (R4.26).



An example of the pseudo-first-order loss can be seen in Figure 4.12. Analysis of the pseudo-first-order loss and derivation of the fit, E4.1, has been described in Chapter 3.

$$S_t = S_0 \exp(-(k_{\text{obs}} + k_{\text{loss}})t) \quad \text{E4.1}$$

where S_0 is the initial OH fluorescence signal, S_t is signal after time t , k_{obs} is the pseudo-first-order rate coefficient and k_{loss} is the first-order-loss of OH.

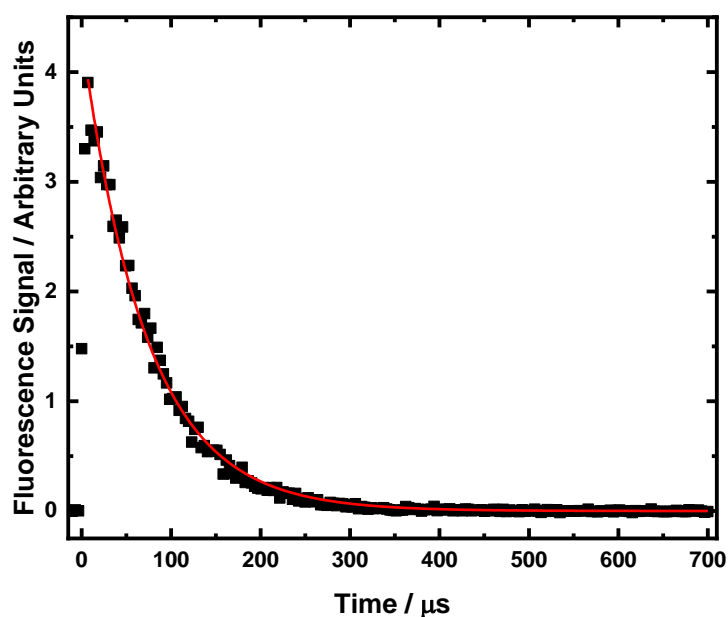


Figure 4.12 OH fluorescence decay at $[\text{furan}] = 4.06 \times 10^{14} \text{ molecule cm}^{-3}$ at 298 K and 50 Torr. $k_{\text{obs}} = (13885 \pm 122) \text{ s}^{-1}$ according to E4.1. With H_2O_2 precursor.

4.3 Results and Discussion

4.3.1 Kinetics at 298 K

Experiments were performed at room temperature between 4 and 95 Torr. Figure 4.12 shows a typical OH fluorescence decay, fit with the pseudo-first-order rate decay expression in E4.1. Figure 4.13 shows two examples of bimolecular plots for the reaction of OH + furan at 298 K. At the lowest pressure investigated, 4 Torr ($1.31 \times 10^{17} \text{ molecule cm}^{-3}$), the rate coefficient was measured to be $k = (3.40 \pm 0.04) \times 10^{-11} \text{ cm}^3 \text{ molecule}^{-1} \text{ s}^{-1}$. For the highest pressure of 95 Torr ($3.08 \times 10^{18} \text{ molecule cm}^{-3}$) the rate coefficient was measured to be $k = (3.30 \pm 0.05) \times 10^{-11} \text{ cm}^3 \text{ molecule}^{-1} \text{ s}^{-1}$. Errors in the bimolecular rate coefficients arise from statistical error when fitting E4.1 to the data to find k' and from the line of best fit when finding k from $[\text{furan}]$ vs k' .

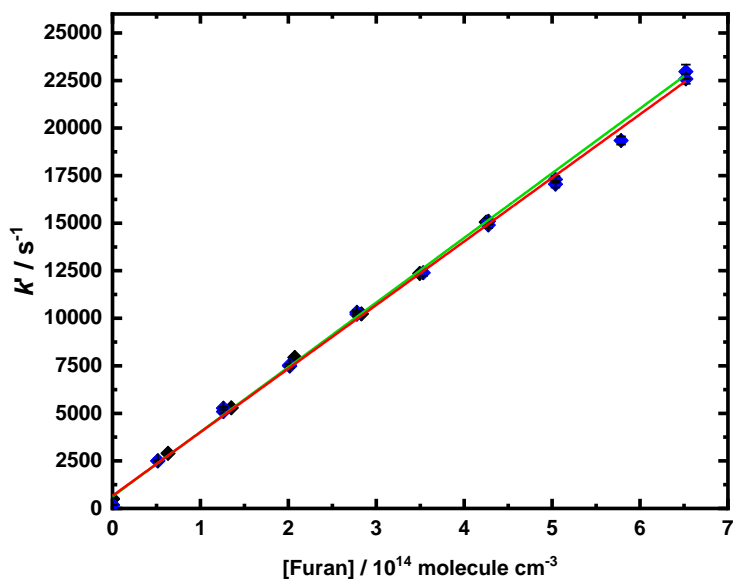


Figure 4.13 Bimolecular plots for the reaction of OH + furan at 298 K at 4 Torr with H₂O₂ precursor (black diamonds) and 95 Torr with (CH₃)₃COOH precursor (blue diamonds) the slopes of which give $k = (3.40 \pm 0.10) \times 10^{-11} \text{ cm}^3 \text{ molecule}^{-1} \text{ s}^{-1}$ (red line) and $k = (3.30 \pm 0.10) \times 10^{-11} \text{ cm}^3 \text{ molecule}^{-1} \text{ s}^{-1}$ (green line) respectively. Note some 1 σ error bars are smaller than symbols.

The overall average rate coefficients for reaction of OH with furan at room temperature and it was determined as $k = (3.34 \pm 0.48) \times 10^{-11} \text{ cm}^3 \text{ molecule}^{-1} \text{ s}^{-1}$ and at 298 K appears to be at, or close to, the high-pressure limit (Figure 4.14). The error associated with the overall rate coefficient is the standard deviation of the average (2 σ).

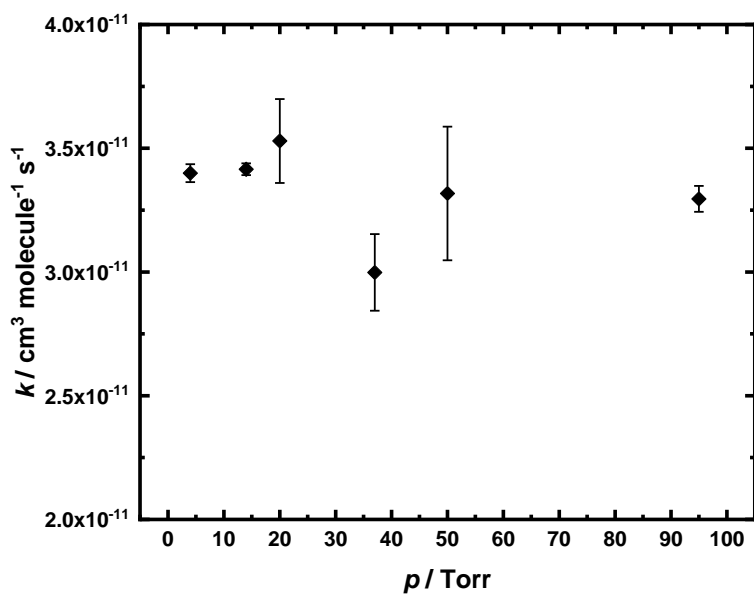


Figure 4.14 Pressure dependence of OH + furan at 298 K. Symbols represent averages at each pressure where a mixture of H₂O₂ and (CH₃)₃COOH precursors were employed.

Furan oxidation has received some attention previously in the literature. A comparison of this work with former studies (Figure 4.15, Table 4.2) show the average rate coefficient measured for the reaction of OH + furan at 298 K during this investigation, $k = (3.34 \pm 0.48) \times 10^{-11} \text{ cm}^3 \text{ molecule}^{-1} \text{ s}^{-1}$ is within error (2σ) of the previous studies with the range of $k = 3.91 - 4.07 \times 10^{-11} \text{ cm}^3 \text{ molecule}^{-1} \text{ s}^{-1}$ (discounting Lee and Tang results owing to the reasons discussed earlier).

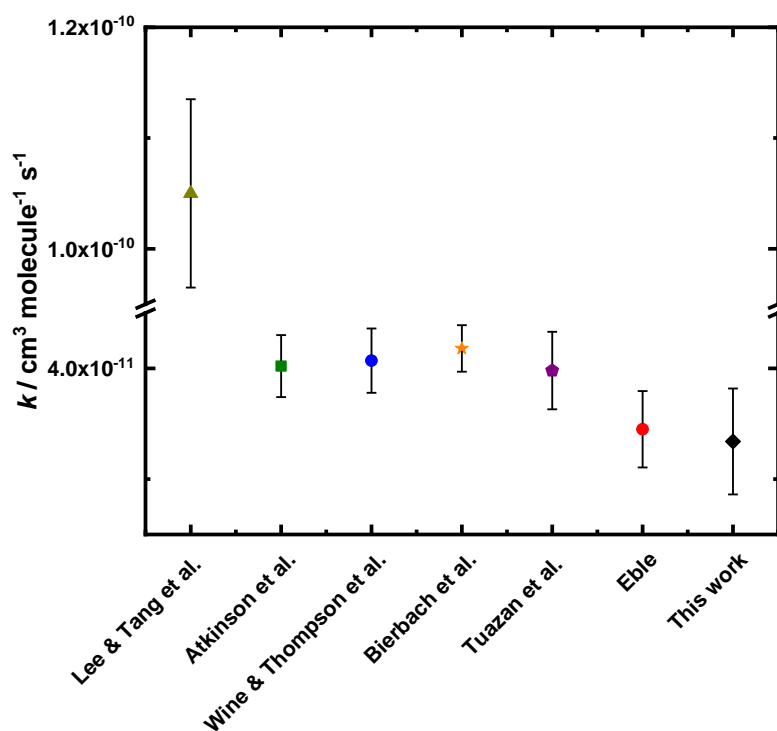


Figure 4.15 Literature room temperature rate coefficients for OH + furan with results from this work

Reference	$k_{298\text{ K}} / 10^{-11} \text{ cm}^3$ molecule ⁻¹ s ⁻¹	% Uncertainty	% Difference between this work and literature
Lee & Tang ¹	10.5 ± 0.85	8.10	68.2
Atkinson <i>et al.</i> ²	4.02 ± 0.28	6.97	16.9
Wine & Thompson ⁸	4.07 ± 0.29	7.13	17.9
Bierbach <i>et al.</i> ⁹	4.18 ± 0.21	5.02	20.1
Tuazan <i>et al.</i> ¹⁰	3.98 ± 0.36	9.05	16.3
Eble ¹⁷	3.45 ± 0.34	10	3.2
This work	3.34 ± 0.48	14.37	-

Table 4.2 Room temperature rate coefficients for the reaction of OH + furan from this work and previous studies. Results for this work are given as an average of all experiments over 298 K and errors are given as 2σ .

Mesh filters were introduced to the path of the photolysis laser to reduce the laser power to examine the effect that laser power, and therefore for potential photolysis of furan, had on the observed kinetics. The filters reduced the amount of light in the photolysis beam to 10, 25 and 50 %. As demonstrated in Figure 4.16, there was no significant change in the rate of decay of OH radicals under pseudo-first-order conditions by any of the filters applied. Pseudo-first-order rate coefficients of the fluorescence decays can be seen in Table 4.3.

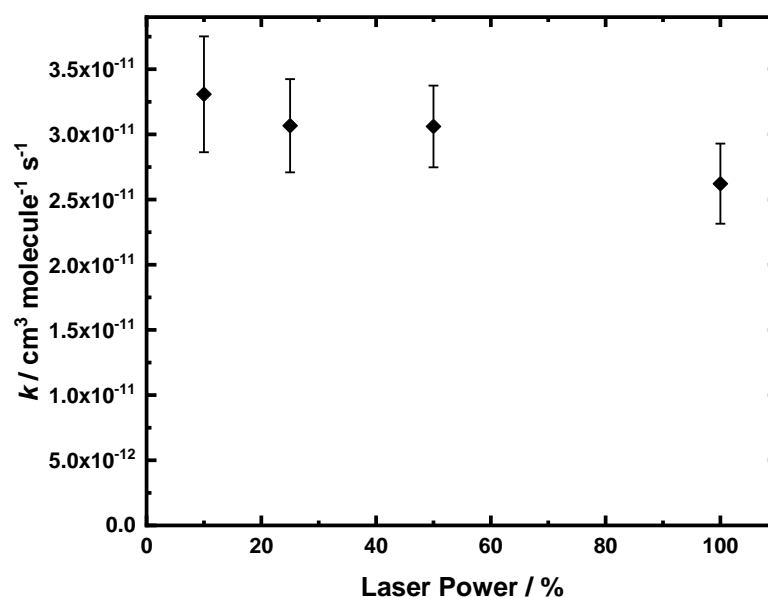


Figure 4.16 Effect of laser power on k for the reaction of OH + furan at $[\text{furan}] = 4.39 \times 10^{14} \text{ molecule cm}^{-3}$. 100 % laser power $\sim 60 \text{ mJ cm}^{-2}$ fluence.

Laser Power / %	$k / 10^{11} \text{ cm}^3 \text{ molecule}^{-1} \text{ s}^{-1}$
100	2.62 ± 0.31
50	3.07 ± 0.36
25	3.06 ± 0.31
10	3.31 ± 0.44

Table 4.3 Bimolecular rate coefficients from the decays of OH + furan at 298 K and 50 Torr with mesh filters applied to the photolysis laser beam. 100 % laser power $\sim 60 \text{ mJ cm}^{-2}$ fluence.

To rule out any dependence on the concentration of oxygen present in the system, experiments were carried out at several temperatures (298, 460, 548 and 595 K), pressures (20, 50 and 90 Torr) and oxygen concentrations from 0 to $4.50 \times 10^{16} \text{ molecule cm}^{-3}$. No significant dependence on oxygen was found at the temperatures or pressures studied, one example is shown in Figure 4.17 and demonstrates that the rate coefficient shows no significant change with oxygen concentration at 298 K and 50 Torr. Similar

results were obtained at other temperatures and pressures and can be found in the Appendix.

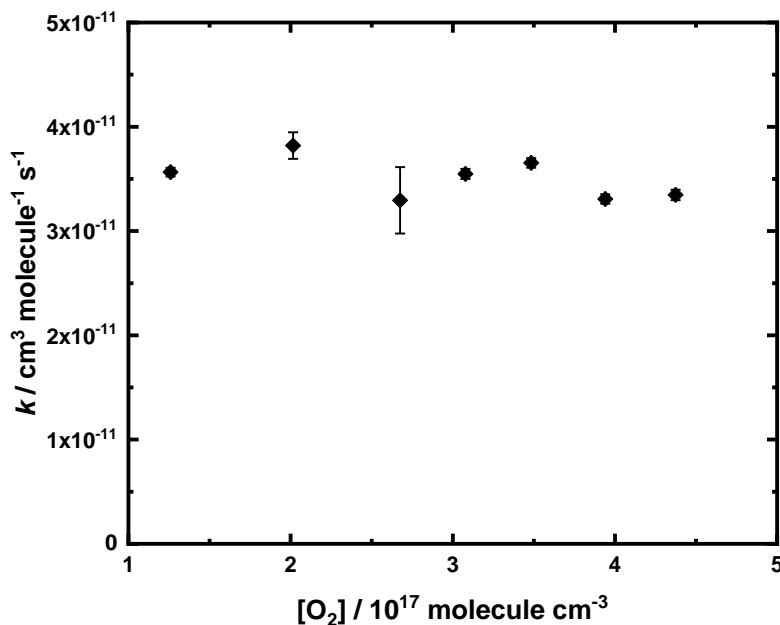


Figure 4.17 Oxygen dependence of the reaction of OH + furan at 298 K and 50 Torr. Note some errors bar may be smaller than symbols.

4.3.2 OH Radical Precursors

Experiments were carried out over a range of temperatures. At temperatures below 500 K the photolysis of *tert*-butylhydroperoxide ((CH₃)₃COOH) was used as an OH radical source. However, above 500 K fluorescence signals from OH radicals were observed in the system before photolysis, indicating OH radicals were being produced from a source other than photolysis, most likely the thermal decomposition of the (CH₃)₃COOH precursor. In order to determine if the fluorescence signal observed was real, the probe laser wavelength was changed from the $\lambda = 282$ nm ($A^2\Sigma(v = 1) \leftarrow X^2\Pi(v = 0)$), Q₁(2) transition to a wavelength that would not induce fluorescence in OH radicals if present. This change in wavelength resulted in a loss of signal, indicating the fluorescence signal was real and not a result of light scatter.

Consequently, on photolysis, the change in OH signal was reduced compared to experiments at lower temperatures when the (CH₃)₃COOH precursor thermally was

stable. Figure 4.18 shows two traces, the right-hand side trace is experimental data performed at 500 K and 50 Torr and demonstrates the OH signal present before photolysis ($t < 0$), and the smaller change in signal on photolysis and poorer signal to noise compared to experiments at lower temperatures. The left side trace shows experimental data performed at 298 K and 50 Torr. Before the photolysis laser is fired ($t < 0$) the fluorescence signal is at, or close to, 0. When the photolysis laser is fired at $t = 0$ the fluorescence signal increases immediately and is clearly distinguishable from the background signal, demonstrating the precursor is thermally stable and OH radicals are produced as a result of precursor photolysis only.

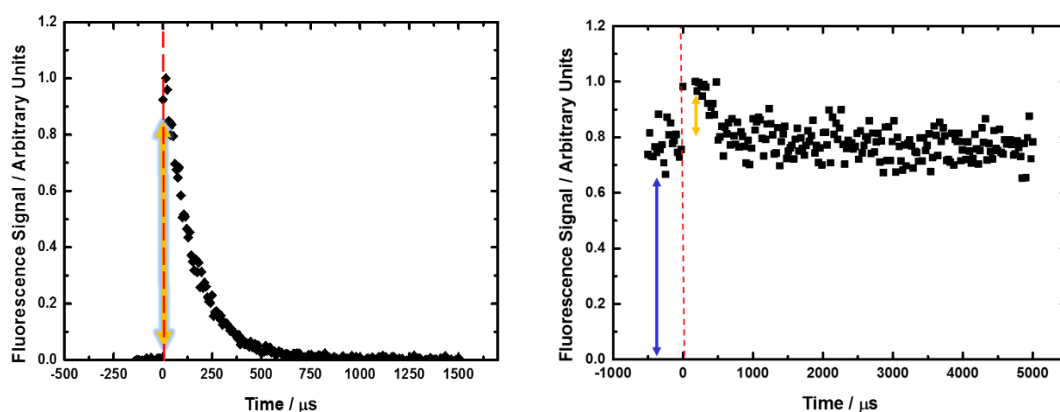


Figure 4.18 Left: fluorescence decay of OH at 298 K where $(\text{CH}_3)_3\text{COOH}$ is thermally stable. Red dashed line shows time of photolysis. Blue arrow indicates signal produced before photolysis. Yellow arrow indicates signal produced on photolysis. Right: fluorescence decay of OH at 500 K with thermal decomposition of $(\text{CH}_3)_3\text{COOH}$.

4.3.3 Effects of Pressure and Temperature

To investigate pressure dependence at temperatures above 298 K, reactions were carried out over a range of temperatures and pressures (Table 4.4). No pressure dependence was observed over the conditions investigated, indicating the reaction is at, or close to, the high pressure limit.

Temperature / K	Pressure / Torr	$k / 10^{11} \text{ cm}^3 \text{ molecule}^{-1} \text{ s}^{-1}$
298	4	3.34 ± 0.04
	14	3.42 ± 0.02
	20	3.53 ± 0.17
	37	3.00 ± 0.16
	50	3.32 ± 0.27
	95	3.30 ± 0.50
	Average	3.34 ± 0.48
380	25	2.31 ± 0.06
	50	2.70 ± 0.15
	95	2.62 ± 0.05
	Average	2.54 ± 0.20
460	5	1.89 ± 0.06
	50	1.59 ± 0.41
	70	1.38 ± 0.05
	100	1.59 ± 0.27
	Average	1.62 ± 0.21
548	20	1.54 ± 0.06
	45	1.60 ± 0.05
	90	1.38 ± 0.06
	95	1.36 ± 0.06
	Average	1.47 ± 0.12
595	10	1.23 ± 0.06
	20	1.43 ± 0.07
	40	1.18 ± 0.07
	90	1.23 ± 0.05
	Average	1.27 ± 0.11

Table 4.4 Average rate coefficients for OH + furan with standard deviation at several temperatures. A mixture of H₂O₂ and (CH₃)₃COOH precursors were employed.

This work has extended the low temperature (<1000 K) range previously described in the literature of the investigation into OH + furan from 425 K to 595 K, average rate coefficients for each temperature can be seen in Table 4.5, and individual rate coefficients can be seen in the Appendix.

T / K	$k / 10^{11} \text{ cm}^3 \text{ molecule}^{-1} \text{ s}^{-1}$
298	3.34 ± 0.48
340	2.97 ± 0.23
380	2.54 ± 0.20
420	2.40 ± 0.06
460	1.62 ± 0.21
500	2.03 ± 0.05
548	1.47 ± 0.12
595	1.27 ± 0.11

Table 4.5 Average rate coefficients for OH + furan at temperatures between 298 and 595 K. A mixture of H_2O_2 and $(\text{CH}_3)_3\text{COOH}$ precursors were employed. Individual rate coefficients can be seen in the Appendix.

The Arrhenius equation, E4.2, was fit to the data from this work and results show a clear negative temperature dependence (Figure 4.19), as seen with the previous measurements by Wine and Thompson and Eble. Parameters of the fit can be seen in Table 4.6.

$$k = A \exp\left(-\frac{E_a}{RT}\right) \quad \text{E4.2}$$

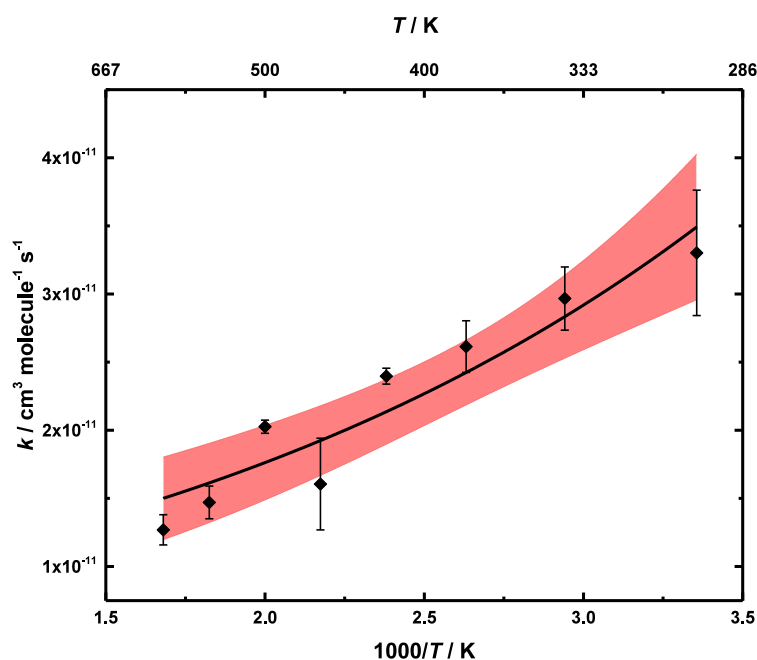


Figure 4.19 Arrhenius plot of this work with 95 % confidence limits. Arrhenius parameters from E4.2 are $A = (6.43 \pm 1.27) \times 10^{-12} \text{ cm}^3 \text{ molecule}^{-1} \text{ s}^{-1}$ and $-E_a/R = (510 \pm 71) \text{ K}$.

A comparison of the fit of E4.2 to the data from this work and that of Wine and Thompson and Eble can be seen in Figure 4.20.

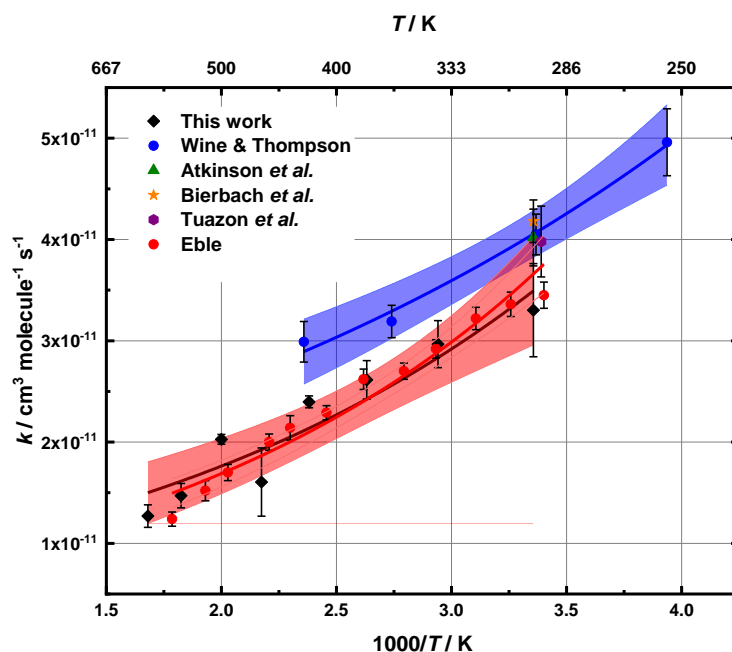


Figure 4.20 Arrhenius plots of OH + furan from this work (black diamonds), Eble (red circles) and Wine and Thompson (blue circles) where lines represent Arrhenius fits to respective data, results of which can be seen in Table 4.6.

Study	Temperature Range / K	$A / 10^{-11} \text{ cm}^3$ $\text{molecule}^{-1} \text{ s}^{-1}$	$-E_a/R / \text{K}$
Wine & Thompson	254-424	1.30 ± 0.30	333 ± 67
Eble	294-560	0.54 ± 0.06	570 ± 41
This work	298-595	0.64 ± 0.13	510 ± 71

Table 4.6 Comparison of Arrhenius parameters for the reaction of OH + furan between this work, Eble, and Wine and Thompson

The temperature dependence of the reaction of OH + furan at low temperatures has previously been investigated by Wine and Thompson over the temperature range of 254

- 424 K. The pre-exponential factor, A , reported by Wine and Thompson is twice as large as that measured in this work, and the $-E_a/R$ reported by Wine and Thompson is 1.5 times smaller than that found in this study. As previously described when comparing the results of Wine and Thompson to that of Eble, Wine and Thompson reported rate coefficients that were typically higher than those determined in this work and that of Eble, resulting in differences in the Arrhenius parameters. These differences could be a result of secondary chemistry from impurities present during the experiments by Wine and Thompson, as discussed previously.

When compared to the Arrhenius parameters reported by Eble, who investigated the temperature dependence from 294 - 560 K, there is good agreement between both the A factors and the activation energies. A fit to the combined data of the two studies (Figure 4.21) gives an A factor of $(6.13 \pm 0.60) \times 10^{-12} \text{ cm}^3 \text{ molecule}^{-1} \text{ s}^{-1}$ and an $-E_a/R$ of $(523 \pm 34) \text{ K}$.

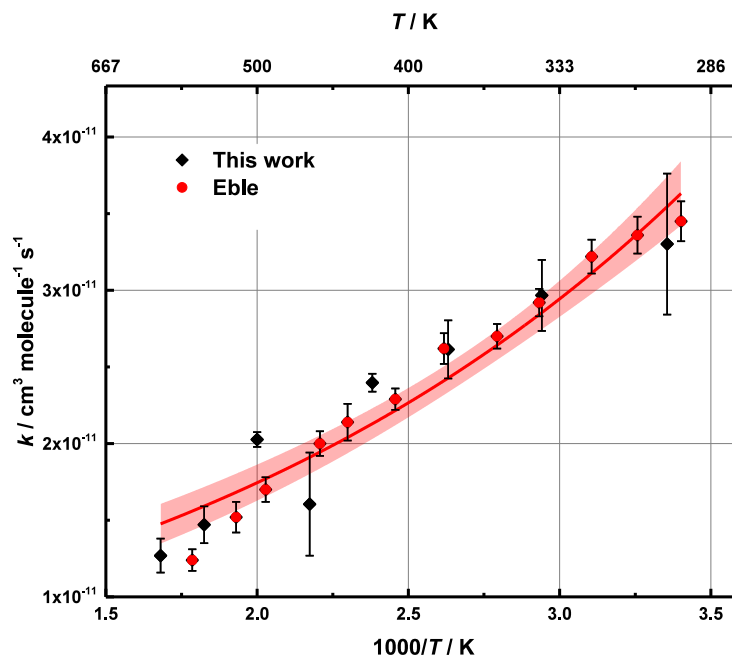


Figure 4.21 Arrhenius plot of the fit of E2 to the combined data sets of this work and Eble for OH + furan.

The temperature dependence observed in this work indicates that the rate coefficient decreases with increasing temperature. The dependence of k on temperature is similar to OH-addition to alkenes observed previously,²⁶⁻³⁰ such as C₂H₄, C₃H₆ and C₄H₈, which indicates OH-addition to a double bond, and thus a negative temperature dependence, corresponds to a barrierless reaction, as shown in Figure 4.22.

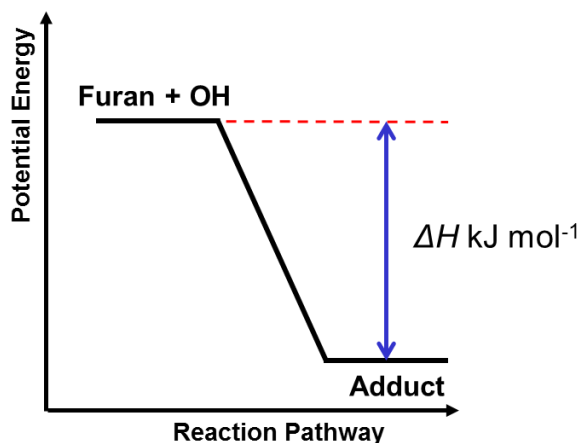


Figure 4.22 Example potential energy surface showing a barrierless addition reaction between OH + furan.

The bond formation in the addition reaction between the OH radical and the double bond of the furan ring has enough energy to proceed to the adduct, unlike abstraction reactions which require a greater energy to break a bond and have a barrier above the entrance channel. As more energy is added to the system as the temperature rises, there is increased competition between the addition and abstraction channels of the reaction between OH and furan.

Figure 4.23 shows the results of the work previously described and those of the shock tube experiments performed by Elwardany *et al.* for temperatures between 924-1388 K and shows there are two distinct temperature regimes governing the kinetics of the reaction of OH + furan. The Elwardany *et al.* study exhibits a positive temperature dependence from 924-1388 K, whereas results from this work display a negative dependence from 298-595 K.

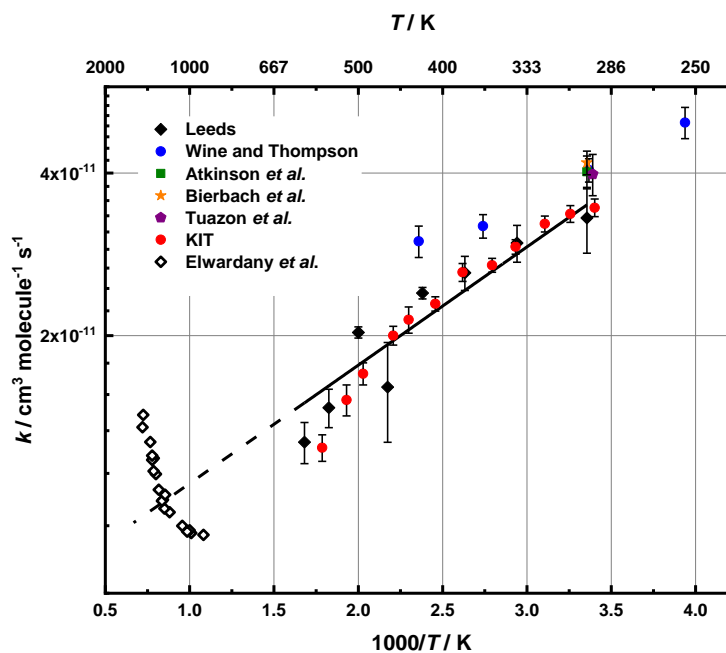


Figure 4.23 The temperature dependent kinetics of OH + furan. Black open diamonds represent Elwardany *et al.* data for high-temperature (924-1388 K) shock tube experiments. Symbols for experiments carried out at 298 K can be found in the graph key. This work is represented by black diamonds, the black line of fit to the data according to E4.2 and the dashed blackline is the extrapolation of E4.2 to the high temperature range.

The chemistry of the reaction between OH radicals and furan, as described previously, can occur *via* the addition of the radical to the furan ring, or by the abstraction of an H atom from the C1 or C2 carbon (Figure 4.1). The decreasing rate coefficient with increasing temperature in the low-temperature region corresponds to a barrierless addition process. The increasing rate coefficient with increasing temperature in the high-temperature region corresponds to abstraction processes, where there is sufficient energy in the system to break bonds. This behaviour can be described by an expression combining two sets of Arrhenius parameters:

$$k = A_1 T^{n_1} \exp\left(\frac{-E_{a1}}{RT}\right) + A_2 T^{n_2} \exp\left(\frac{-E_{a2}}{RT}\right) \quad \text{E4.3}$$

where, for the addition of OH to furan, A_1 represents the pre-exponential factor, n_1 is the exponent of T and E_{a1} is the activation energy. For the H abstraction of furan by OH, A_2 represents the pre-exponential factor, n_2 is the exponent of T and E_{a2} is the activation energy.

Fits of E4.3 to the combined data sets for this work and the work of Elwardany *et al.* and for this work, Eble and Elwardany *et al.* can be seen in Table 4.7. The fit of E4.3 to the data sets can be seen in Figure 4.24 where it can be seen there is general agreement of the six fitted parameters between the two data sets as the fit to work by this study, Eble and Elwardany *et al.* lies within the 95 % confidence limits of the fit to the work by this study and Elwardany *et al.*. The total uncertainty in k is found from the percentage difference between the fit of E4.3 and the upper and lower confidence limits, and was determined as 5.83 ± 3.12 %.

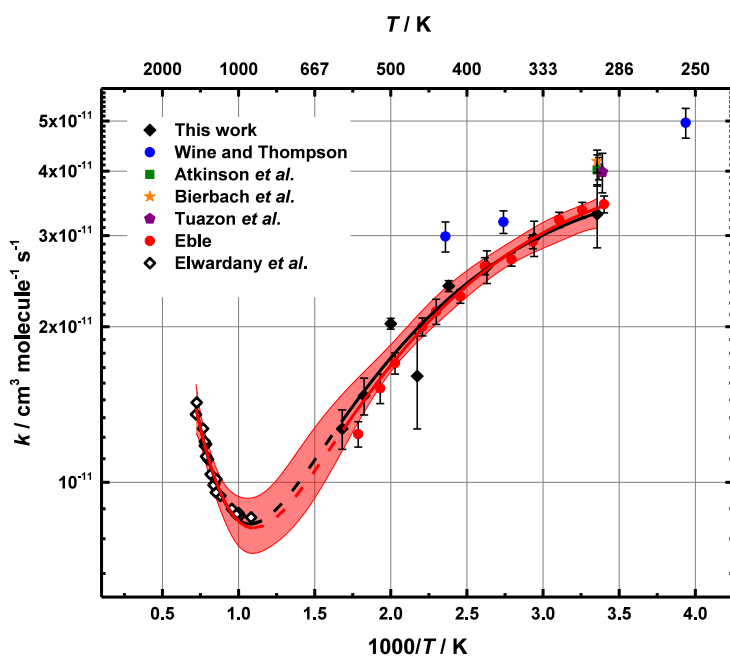


Figure 4.24 The effect of temperature OH + furan. Results from this work (black solid diamonds), Wine and Thompson (blue solid circles), Eble (red circles) and Elwardany *et al.* (open black diamonds). Fit to E4.3 to the combined data from this work and Elwardany *et al.* (black line) and from this work, Eble and Elwardany *et al.* (red line) with 95 % confidence limits.

Parameter	Fit to this work & Elwardany <i>et al.</i>	Fit to this work, Eble & Elwardany <i>et al.</i>
$A_1 / \text{cm}^3 \text{s}^{-1}$	0.16	1.30
n_1	-3.44	-3.77
$E_{a1}/R / \text{K}$	806	882
$A_2 / \text{cm}^3 \text{s}^{-1}$	1.20×10^{-24}	6.44×10^{-24}
n_2	4.00	3.76
$E_{a2}/R / \text{K}$	-1500	-1537

Table 4.7 Arrhenius parameters from the fit of E4.3 to the combined data from this work and Elwardany *et al.* and from this work, Eble and Elwardany *et al.*

The change in kinetic behaviour with an increase in temperature is similar to those recently reported by Khaled *et al.*³¹ of the oxidation of alkenes over two temperature regimes. Khaled *et al.* investigated the temperature dependence of the OH radical with *cis*-1,3-pentadiene, *trans*-1,3-pentadiene, 1,4-pentadiene and 1,3-butadiene in a low (294-468 K) and high (881-1348 K) temperature regime. Low temperature data were obtained experimentally using laser flash photolysis with laser induced fluorescence. High temperature data were obtained using the shock tube technique coupled with UV absorption. Results can be seen in Figure 4.25.

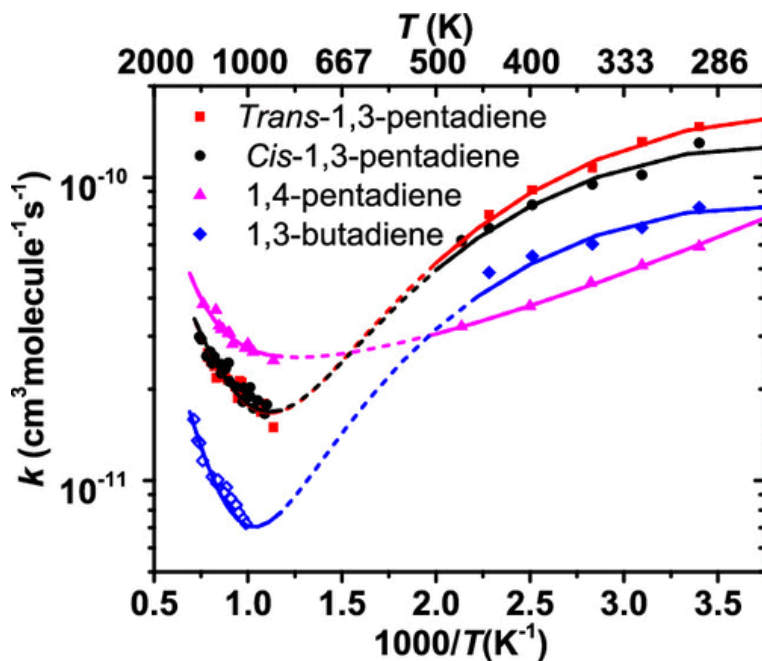


Figure 4.25 Khaled *et al.*³¹ reported Arrhenius plot for the total rate coefficients of OH radical reactions with 1,3-butadiene, *cis/trans*-1,3-pentadiene and 1,4-pentadiene. Lines represent the best fit to the experimental rate coefficients.

When the E4.3 fit is compared to rate parameters used by Tian *et al.*²³ and Liu *et al.*²⁵ in combustion models, it can be seen there is an under prediction of the rate coefficients by both models, except in the region between 887 and 1000 K where the models over predict the rate coefficient (Figure 4.26). There is a clear need for combustion models to incorporate low temperature kinetics in order to accurately predict the chemistry of furan biofuels in the low temperature region of combustion.

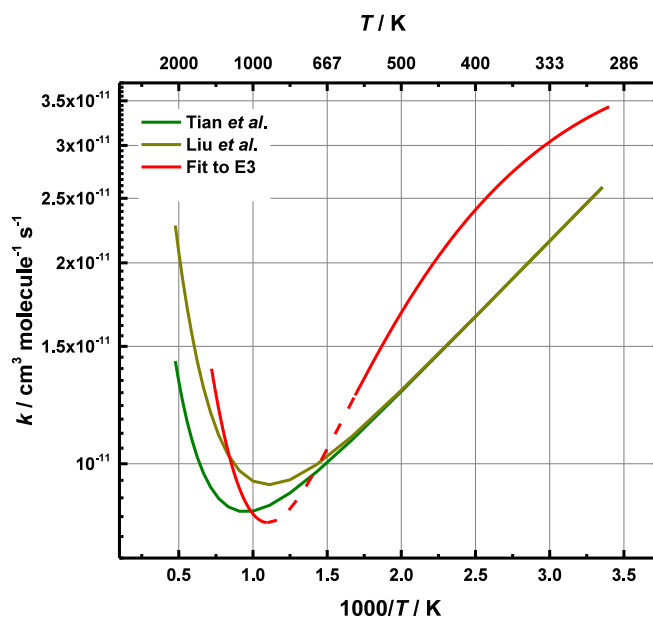


Figure 4.26 Comparison of the fit of E4.3 to data from this work compared to the model produced by Liu *et al.*²⁵ and Tian *et al.*²³ for OH + furan.

4.4 Conclusion

The kinetics of the reaction of OH + furan has been investigated in the pressure range of 4-100 Torr and at temperatures between 298 and 595 K relevant to low-temperature combustion. The study was carried out using laser flash photolysis-laser induced fluorescence (LFP-LIF). This investigation has extended the temperature range of low temperature combustion of furans (<1000 K) available in the literature.

The average room temperature rate coefficient, $k = (3.34 \pm 0.48) \times 10^{-11} \text{ cm}^3 \text{ molecule}^{-1} \text{ s}^{-1}$, is within uncertainties of the rate coefficients report by Atkinson *et al.*, Wine and Thompson, Tuazon *et al.* and Eble. Over all temperatures investigated the reaction appears to be at, or close to, the high-pressure limit.

Results demonstrate a negative temperature dependence for the reaction of OH + furan over temperatures between 298 K and 595 K, with $-E_a/R = (510 \pm 71) \text{ K}$. This temperature dependence is consistent with the behaviour observed in previous studies.

This work has been analysed in combination with the low temperature kinetic data provided by Eble and the shock tube data obtained by Elwardany *et al.* in order to assess

the kinetics of the reaction over a wide temperature range. The data was fit to a double modified Arrhenius to obtain Arrhenius parameters that describe the low and high temperature kinetics of the OH + furan system. The kinetics from this work can be employed in combustion models in order to accurately predict rate coefficients of the reaction at temperature relevant to low temperature combustion, as the current models by Tian *et al.* and Liu *et al.* estimate rate coefficients slower than those seen experimentally at temperature below 1000 K.

4.5 References

1. Lee, J.H. and I.N. Tang. Absolute rate constants for the hydroxyl radical reactions with ethane, furan, and thiophene at room temperature. *The Journal of Chemical Physics*, 1982, **77**(9), pp.4459-4463.
2. Atkinson, R., S.M. Aschmann and W.P.L. Carter. Kinetics of the reactions of O₃ and OH radicals with furan and thiophene at 298 ± 2 K. *International Journal of Chemical Kinetics*, 1983, **15**(1), pp.51-61.
3. Atkinson, R., *et al.* Rate constants for the reaction of OH radicals with a series of alkanes and alkenes at 299 ± 2 K. *International Journal of Chemical Kinetics*, 1982, **14**(5), pp.507-516.
4. Atkinson, R. Kinetics and mechanisms of the gas-phase reactions of the hydroxyl radical with organic compounds under atmospheric conditions. *Chemical Reviews*, 1986, **86**(1), pp.69-201.
5. Saunders, S.M., *et al.* Protocol for the development of the Master Chemical Mechanism, MCM v3 (Part A): tropospheric degradation of non-aromatic volatile organic compounds. *Atmos. Chem. Phys.*, 2003, **3**(1), pp.161-180.
6. Jenkin, M.E., *et al.* Protocol for the development of the Master Chemical Mechanism, MCM v3 (Part B): tropospheric degradation of aromatic volatile organic compounds. *Atmos. Chem. Phys.*, 2003, **3**(1), pp.181-193.
7. Barnes, I., *et al.* Oxidation of sulphur compounds in the atmosphere: I. Rate constants of OH radical reactions with sulphur dioxide, hydrogen sulphide, aliphatic thiols and thiophenol. *Journal of Physical Chemistry*, 1986, **4**(4), pp.445-466.
8. Wine, P.H. and R.J. Thompson. Kinetics of OH reactions with furan, thiophene, and tetrahydrothiophene. *International Journal of Chemical Kinetics*, 1984, **16**(7), pp.867-878.
9. Bierbach, A., I. Barnes and K.H. Becker. Rate coefficients for the gas-phase reactions of hydroxyl radicals with furan, 2-methylfuran, 2-ethylfuran and 2,5-dimethylfuran at 300 K. *Atmospheric Environment Part a-General Topics*, 1992, **26**(5), pp.813-817.
10. Tuazon, E., *et al.* A study of the atmospheric reactions of 1,3-dichloropropene and other selected organochlorine compounds. *Archives of Environmental Contamination and Toxicology*, 1984, **13**(6), pp.691-700.
11. Lockhart, J., *et al.* Mechanism of the Reaction of OH with Alkynes in the Presence of Oxygen. *The Journal of Physical Chemistry A*, 2013, **117**(26), pp.5407-5418.
12. Eskola, A.J., *et al.* Analysis of the Kinetics and Yields of OH Radical Production from the CH₃OCH₂ + O₂ Reaction in the Temperature Range 195–650 K: An Experimental and Computational study. *The Journal of Physical Chemistry A*, 2014, **118**(34), pp.6773-6788.

13. Wallington, T.J. Kinetics of the gas phase reaction of OH radicals with pyrrole and thiophene. *International Journal of Chemical Kinetics*, 1986, **18**(4), pp.487-496.
14. Martin, D., J.L. Jourdain and G. Lebras. Kinetic study for the reactions of OH radicals with dimethylsulfide, diethylsulfide, tetrahydrothiophene, and thiophene. *International Journal of Chemical Kinetics*, 1985, **17**(12), pp.1247-1261.
15. Aschmann, S.M., *et al.* Kinetics of the Reactions of OH Radicals with 2- and 3-Methylfuran, 2,3- and 2,5-Dimethylfuran, and E- and Z-3-Hexene-2,5-dione, and Products of OH + 2,5-Dimethylfuran. *Environmental Science & Technology*, 2011, **45**(5), pp.1859-1865.
16. Atkinson, R. and J. Arey. Atmospheric Degradation of Volatile Organic Compounds. *Chemical Reviews*, 2003, **103**(12), pp.4605-4638.
17. Eble, J.S.R. *Ignition of oxygenated hydrocarbons: Mechanism and elementary steps*. thesis, Karlsruhe Institute of Technology (KIT), 2017.
18. Burkholder, J.B.S., S. P.; Abbatt, J. P. D.; Barker, J. R.; Huie, R. E.; Kolb, C. E.; Kurylo, M. J.; Orkin, V. L.; Wilmouth, D. M.; Wine, P. H. Chemical Kinetics and Photochemical Data for Use in Atmospheric Studies, Evaluation No. 18. *In*: Pasadena, CA : Jet Propulsion Laboratory, National Aeronautics and Space Administration, 2015.
19. *IUPAC Task Group on Atmospheric Chemical Kinetic Data Evaluation – Data Sheet HO_x_VOC64*. 2009.
20. Elwardany, A., *et al.* A chemical kinetic study of the reaction of hydroxyl with furans. *Fuel*, 2016, **166**, pp.245-252.
21. Grosjean, D. and E.L. Williams li. Environmental persistence of organic compounds estimated from structure-reactivity and linear free-energy relationships. Unsaturated aliphatics. *Atmospheric Environment. Part A. General Topics*, 1992, **26**(8), pp.1395-1405.
22. Mousavipour, S.H., S. Ramazani and Z. Shahkolahi. Multichannel RRKM-TST and Direct-Dynamics VTST Study of the Reaction of Hydroxyl Radical with Furan. *The Journal of Physical Chemistry A*, 2009, **113**(12), pp.2838-2846.
23. Tian, Z., *et al.* An experimental and kinetic investigation of premixed furan/oxygen/argon flames. *Combustion and Flame*, 2011, **158**(4), pp.756-773.
24. Heyberger, B., *et al.* Oxidation of small alkenes at high temperature. *International Journal of Chemical Kinetics*, 2002, **34**(12), pp.666-677.
25. Liu, D., *et al.* Combustion chemistry and flame structure of furan group biofuels using molecular-beam mass spectrometry and gas chromatography – Part I: Furan. *Combustion and Flame*, 2014, **161**(3), pp.748-765.
26. Atkinson, R.a.P., And J. N. Pitts. Rate constants for the reaction of OH radicals with ethylene over the temperature range 299–425 °K. *The Journal of Chemical Physics*, 1977, **66**(3), pp.1197-1201.
27. Cleary, P.A., *et al.* Determination of the temperature and pressure dependence of the reaction OH + C₂H₄ from 200–400 K using experimental and master equation analyses. *Physical Chemistry Chemical Physics*, 2006, **8**(48), pp.5633-5642.
28. Daranlot, J., *et al.* Gas-Phase Kinetics of Hydroxyl Radical Reactions with Alkenes: Experiment and Theory. *ChemPhysChem*, 2010, **11**(18), pp.4002-4010.
29. Tully, F.P. and J.E.M. Goldsmith. Kinetic study of the hydroxyl radical-propene reaction. *Chemical Physics Letters*, 1985, **116**(4), pp.345-352.
30. Smith, R.H. Rate constant for the gaseous reaction between hydroxyl and propene. *The Journal of Physical Chemistry*, 1983, **87**(9), pp.1596-1600.
31. Khaled, F., *et al.* Insights into the Reactions of Hydroxyl Radical with Diolefins from Atmospheric to Combustion Environments. *The Journal of Physical Chemistry A*, 2019, **123**(11), pp.2261-2271.

Chapter 5 Kinetic Study of the OH + 2-Methylfuran Reaction as a Function of Temperature and Pressure

5.1 Background and Previous Work

2-Methylfuran (2-MF, C₅H₆O, Figure 5.1) is an aromatic heterocyclic ether that can be generated for use as a biofuel¹ or emitted into the atmosphere from anthropogenic sources such as combustion of fossil fuels, biomass burning and waste processing, or emitted biogenically from plants. The chemistry of the combustion of biofuels has been discussed previously in Chapter 1. The aromaticity of 2-MF makes it reactive towards oxidising species such as the OH radical, which is the primary oxidant of the atmosphere and of biofuels under low temperature combustion conditions. The OH radical can either add to the furan ring of 2-MF at the C2 or C3 site or abstract a hydrogen from the C1 or C3 sites (Figure 5.1).

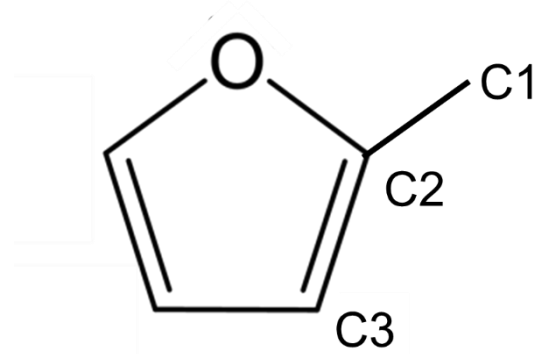


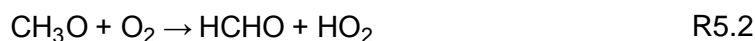
Figure 5.1 Structure of 2-Methylfuran (2-MF) with numbered carbons

5.1.1 Studies of OH + furan at low temperature (<1000 K)

The following investigations into the oxidation of 2-MF by OH radicals have been previously described in Chapter 4 for the unsubstituted furan, therefore only a brief outline of experimental descriptions will be given here.

Bierbach *et al.*² performed the first investigation into OH + MF, experiments were carried out at room temperature and 760 Torr and rate coefficients were measured by continuous photolysis-gas chromatography (CP-GC) and using the relative rate method,

described in detail in Chapter 3. Propene was the chosen reference compound with a rate coefficient of $2.60 \times 10^{-11} \text{ cm}^3 \text{ molecule}^{-1} \text{ s}^{-1}$ for OH + propene taken from the review by Atkinson *et al.*³ OH radicals were generated *via* the photolysis of methyl nitrite (R5.1-R5.3) at wavelengths between 320 nm and 480 nm.



The bimolecular room temperature rate coefficient of OH + 2-MF was reported as $k = (6.19 \pm 0.30) \times 10^{-11} \text{ cm}^3 \text{ molecule}^{-1} \text{ s}^{-1}$.

Aschmann *et al.*⁴ also employed the CP-GC technique and relative rate method to investigate 2-MF oxidation. Experiments were performed at 296 K and 735 Torr. OH radicals were produced *via* the photolysis of methyl nitrite (R15-R17) at $\lambda > 300 \text{ nm}$ and Aschmann *et al.* note the introduction of NO into the system in order to titrate O_3 produced from NO_2 photolysis. 1,3,5-trimethylbenzene was chosen as a reference compound with a rate coefficient of $k = 5.67 \times 10^{-11} \text{ cm}^3 \text{ molecule}^{-1} \text{ s}^{-1}$ taken from Atkinson *et al.*⁵ The rate coefficient of 2-MF + OH was reported by Aschmann *et al.* as $k = (7.31 \pm 0.35) \times 10^{-11} \text{ cm}^3 \text{ molecule}^{-1} \text{ s}^{-1}$, this result is not within error of the rate coefficient reported by Bierbach *et al.* Both studies account for possible secondary chemistry as a result of NO_2 formation by including additional NO in the system to titrate O_3 generated following NO_2 photolysis.

Although the reported rate coefficient reported by Aschmann *et al.* is not within error of that reported by Bierbach *et al.*, when comparing the relative rate coefficients using updated sources for the reference compounds, the rate coefficient for Bierbach *et al.* falls within the range of potential rate coefficients for the work by Aschmann *et al.* depending on the literature source used for OH + 1,3,5-trimethylbenzene, as shown in Table 5.1.

A study by Eble⁶ was unpublished at the time of writing, however, was provided for comparison in this thesis. Eble investigated the reaction of OH + 2-MF using the LFP-LIF technique. Experiments were carried out in He and at temperatures between 296 and 566 K and pressures of 2, 5 and 10 bar (1520, 3800 and 7600 Torr). OH radicals were generated *via* the flash photolysis of nitric acid (HNO₃) at 248 nm (R5.4). To avoid potential secondary chemistry as a result of NO₂ formation from HNO₃ decomposition, the OH precursor mixture was replaced regularly.



Experiments were performed under pseudo-first-order conditions and the room temperature bimolecular rate coefficient of OH + 2-MF was reported by Eble as $k = (6.80 \pm 0.30) \times 10^{-11} \text{ cm}^3 \text{ molecule}^{-1} \text{ s}^{-1}$, which is in good agreement with those reported by both Bierbach *et al.* $k = (6.19 \pm 0.30) \times 10^{-11} \text{ cm}^3 \text{ molecule}^{-1} \text{ s}^{-1}$ and Aschmann *et al.* $k = (7.31 \pm 0.35) \times 10^{-11} \text{ cm}^3 \text{ molecule}^{-1} \text{ s}^{-1}$.

Over the temperature range studied (296 – 566 K) Eble found a negative temperature dependence with Arrhenius parameters of $k = (6.54 \pm 0.94) \times 10^{-12} \exp((715 \pm 49)/T) \text{ cm}^3 \text{ molecule}^{-1} \text{ s}^{-1}$. The Arrhenius plot for this experiment can be seen in Figure 5.2.

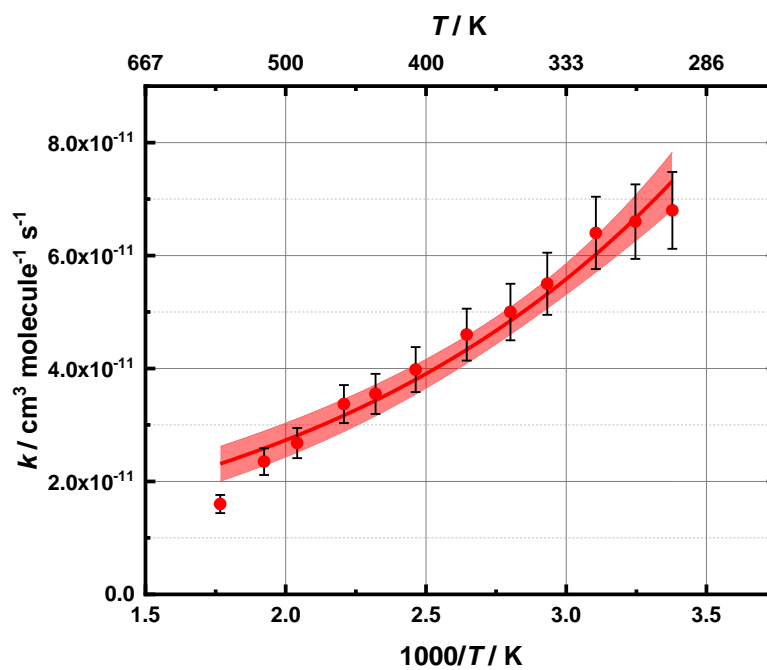


Figure 5.2 Arrhenius plot for OH + 2-MF from Eble.⁶ From 296-566 K and averaged over 2, 5 and 10 bar.

Study	T Range / K	p Range / Torr	Technique	$k_{\text{OH}+2\text{-MF}} / 10^{-11} \text{ cm}^3$ molecule ⁻¹ s ⁻¹	Reference Compound	$k_{\text{OH}+ \text{ref}} / 10^{-11} \text{ cm}^3$ molecule ⁻¹ s ⁻¹	Literature $k_{\text{OH}+ \text{ref}}$ / 10^{-11} cm^3 molecule ⁻¹ s ⁻¹	Updated $k_{\text{OH}+2\text{-MF}}$ / 10^{-11} cm^3 molecule ⁻¹ s ⁻¹
Bierbach <i>et al.</i> ²	298	760	CP-GC	6.19 ± 0.30	<i>trans</i> -2-butene	2.60 ⁷	6.40 ⁸	6.88 ± 0.35
Aschmann <i>et al.</i> ⁴	296	735	CP-GC	7.31 ± 0.35	1,3,5- trimethylbenzene	5.67 ⁵	6.84 ± 0.10 ⁹ 4.09 ± 0.56 ¹⁰	8.82 ± 0.41 5.28 ± 0.32
Eble ⁶	296	1500- 7600	LPF-LIF	6.80 ± 0.30	-	-	-	-

Table 5.1 Literature rate coefficients for the oxidation of 2-MF by the OH radical and for the reaction of OH with reference compounds used in the relative rate experiments. Updated rate coefficients using recent literature for those reference compounds are shown. Values for *trans*-2-butene are taken from current IUPAC recommendations. Values for 1,3,5-trimethylbenzene are the highest and lowest rate coefficients available in the current literature.

5.1.2 Studies of OH + 2-MF at High Temperature (>1000 K)

Elwardany *et al.*¹¹ performed the first high temperature investigation into the oxidation of 2-MF by OH using a shock tube with a He driver gas, as previously described in Chapter 4. Experiments were carried out between 890 and 1333 K and from 1.17 to 1.95 atm (889 - 1482 Torr). The thermal decomposition of $(\text{CH}_3)_3\text{COOH}$ was used as an OH precursor and OH radicals were monitored by UV absorption spectroscopy at ~ 306 nm.

Elwardany *et al.* report their results as Arrhenius expression of $k = 1.47 \times 10^{-10} \exp(-2285/T) \text{ cm}^3 \text{ molecule}^{-1} \text{ s}^{-1}$. These parameterisations lead to a predicted room temperature rate coefficient of $k = 6.87 \times 10^{-14} \text{ cm}^3 \text{ molecule}^{-1} \text{ s}^{-1}$, which is significantly lower than the values reported in the literature (Table 5.1), however, as described in Chapter 4, the chemistry surrounding the temperature dependence of the OH + furans systems are complex and so it is not appropriate to extrapolate to room temperature here. Results can be seen in Figure 5.3.

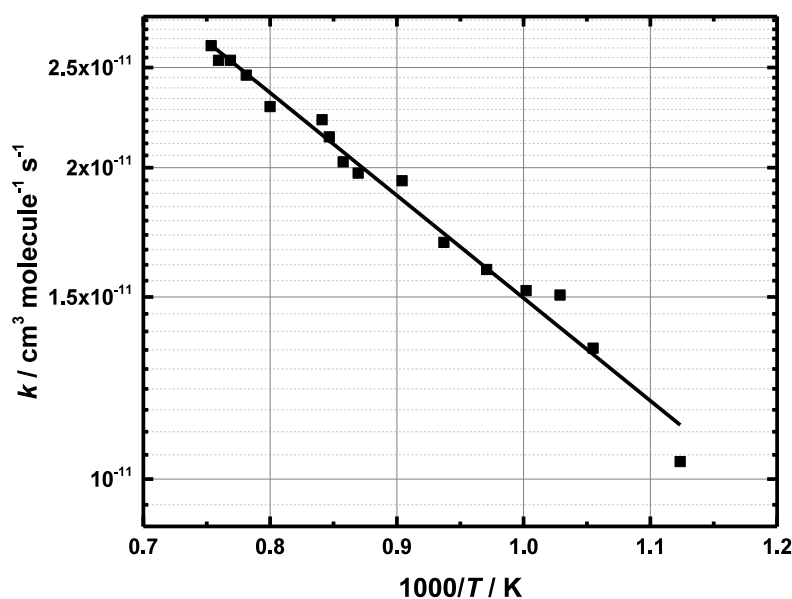


Figure 5.3 Rate coefficient of OH + 2-MF reported by Elwardany *et al.* between 890-1333 K. Black line is the Arrhenius fit reported by Elwardany *et al.* as $k = 1.47 \times 10^{-10} \times T^3 \exp(-2285.7/T) \text{ cm}^3 \text{ molecule}^{-1} \text{ s}^{-1}$.

5.1.3 Theoretical Studies of OH + 2-MF

Theoretical investigations have also been carried out on the OH + 2-MF system. Structure-reactivity relationships (SRR) and linear free-energy relationships (LFER) were investigated by Grosjean and Williams.¹² They estimated a rate coefficient of $k = 11.1 \times 10^{-11} \text{ cm}^3 \text{ molecule}^{-1} \text{ s}^{-1}$ for the gas phase reaction of OH radicals with 2-MF. These results are approximately 1.8 times greater than the rate coefficients found experimentally.

Davis and Sarathy investigated the OH + 2-MF system using the G4¹³ and CBS-QB3¹⁴ methods, more details of which can be found in Chapter 7. The study determined the bond dissociation energies and reaction enthalpies, barrier heights and the high pressure rate expressions for possible reaction pathways following the addition of the OH radical to the 2-MF ring. Davis and Sarathy found OH addition at the C2 and C5 position to be the most favoured addition pathways, as well as the H abstraction by OH at the methyl site, as the pathways lead to the formation of resonance stabilised intermediates.

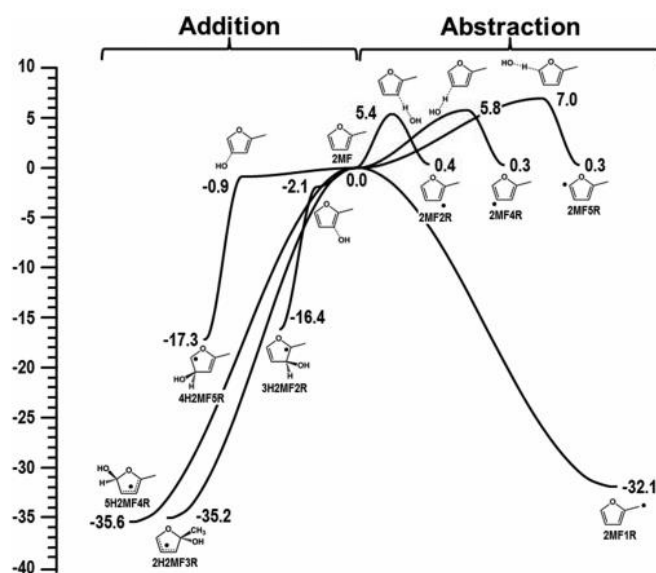


Figure 5.4 PES of OH + 2-MF showing the addition and abstraction channels from Davis and Sarathy.¹⁵ Energies are in kcal mol⁻¹ and are an average of calculations at the CBS-QB3 and G4 levels of theory.

5.1.4 Combustion Models of 2-MF

There have been some previous modelling studies into the chemistry of 2-MF at temperatures relevant to high temperature combustion that contain the oxidation of 2-MF by OH of interest in this thesis. These studies are discussed in detail in Chapter 7 and so only a brief description will be given here.

Tran *et al.*¹⁶ developed a model to outline the kinetics of 2-MF pyrolysis. The OH abstraction reactions included in the model (R5.5-R5.6) represent the abstraction of an H atom by OH at the methyl site in 2-MF (Figure 5.5) and from the C5 carbon (Figure 5.6).

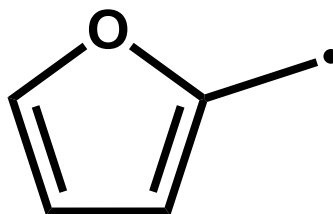


Figure 5.5 Schematic of furylCH₂ as a result of the reaction between OH and 2-MF

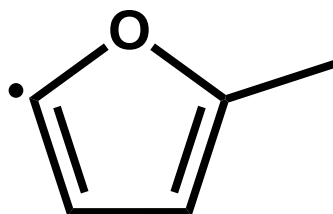
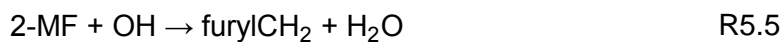


Figure 5.6 Schematic of MF-yl-2 as a result of the reaction between OH and 2-MF



Tran *et al.* estimate rate coefficients of $5.10 \times 10^3 T^{3.133} \exp(-2155/RT) \text{ cm}^3 \text{ mol}^{-1} \text{ s}^{-1}$ for R5.5 and $2.26 \times 10^6 T^2 \exp(-2780/RT) \text{ cm}^3 \text{ mol}^{-1} \text{ s}^{-1}$ for R5.6 which equate to $8.47 \times 10^{-21} T^{3.133} \exp(-9016/RT) \text{ cm}^3 \text{ molecule}^{-1} \text{ s}^{-1}$ and $3.75 \times 10^{-18} T^2 \exp(-1160/RT) \text{ cm}^3 \text{ molecule}^{-1}$

s⁻¹. Resulting in room temperature rate coefficients of $4.76 \times 10^{-13} \text{ cm}^3 \text{ molecule}^{-1} \text{ s}^{-1}$ and $3.32 \times 10^{-13} \text{ cm}^3 \text{ molecule}^{-1} \text{ s}^{-1}$ for R5.5 and R5.6 respectively. These extrapolations are from high temperature calculations to room temperature and therefore are not appropriate for a comparison to other room temperature experimental results.

Somers *et al.*¹⁷ produced a detailed kinetic mechanism consisting of 2059 reactions and 391 species to describe the oxidation of 2-MF. For the reactions between OH radicals and 2-MF, Somers *et al.* incorporated data from the mechanism for the oxidation of 2,5-DMF previously reported by Somers *et al.*¹⁸ and from the oxidation of the unsubstituted furan by Mousavipour *et al.*¹⁹ More details of these studies can be found in Chapter 6 and Chapter 7.

These models have been used to investigate the combustion properties of 2-MF, and have calculated pyrolytic behaviour, ignition delay times and laminar burning velocities to complement experimental results. There is a clear need for low-temperature oxidation kinetic data to help construct accurate oxidation models of furans if they are to be employed as biofuels in low temperature combustion environments.

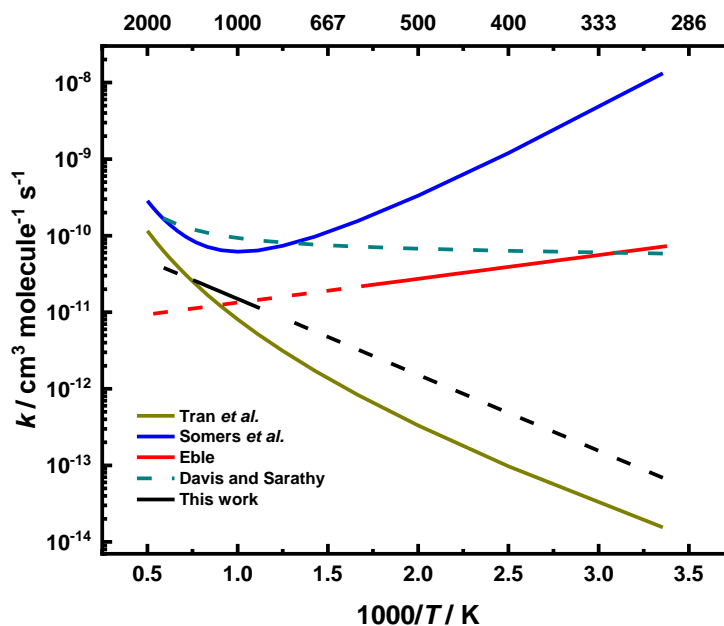


Figure 5.7 Comparison of combustion models (key inset) with Arrhenius fits to experimental data of Eble and Elwardany *et al.* for OH + 2-MF.

The current available literature on the low temperature oxidation of 2-MF, with the exception of the unpublished work by Eble, is limited to room temperature studies and the study by Elwardany *et al.* which focuses on the reaction in the high temperature regime (>1000 K). The aim of this work is to investigate the oxidation of 2-MF at temperatures relevant to low temperature combustion in order to bridge the gap between the room and high temperature literature data in order to better improve combustion models which currently poorly describe the kinetics of 2-MF oxidation at low temperatures. This chapter describes the kinetic study of the OH + 2-MF reaction, extending across a temperature range of 298-770 K.

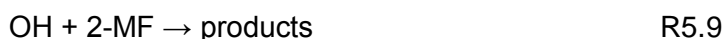
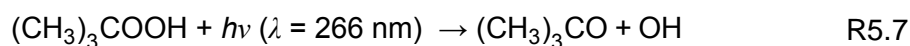
5.2 Experimental Procedure

Experiments were carried out as described in Chapter 3 and so only a brief outline will be given here.

This work investigates the rate of reaction between OH radicals and 2-MF using flash photolysis to initiate the reaction and laser induced fluorescence (LIF) to monitor the OH radical. 2-MF (Sigma Aldrich, 99 %) was degassed and purified by a series of freeze-

pump-thaw cycles and prepared at a known concentration (typically between 1×10^{13} and 1×10^{15} molecule cm^{-3}) in N_2 and stored in a glass bulb. N_2 (BOC, oxygen free, 99 %) and O_2 (BOC, 99 %) were used as supplied. A known flow of N_2 was passed through a bubbler containing *tert*-butylperoxide ($(\text{CH}_3)_3\text{COOH}$) (Sigma Aldrich, 70 % v/v aqueous) or hydrogen peroxide (H_2O_2) (Sigma Aldrich, 50 % v/v aqueous) to entrain the peroxide into precursor gas flow. Reactions were carried out at pressures between 20 and 150 Torr and temperatures between 298 and 770 K.

Reactions were initiated when OH radicals were produced *via* the photolysis of a suitable precursor ($(\text{CH}_3)_3\text{COOH}$ 298 K < T < 500 K or H_2O_2 298 K < T < 770 K) (R5.7-R5.9) using the 4th harmonic of a pulsed Nd:YAG photolysis laser at $\lambda = 266$ nm.



The reaction was carried out under pseudo-first-order conditions such that the concentration of 2-MF was always in a large excess of OH. Under these conditions the loss of OH is through the reaction with 2-MF (R5.9) and other losses such as reaction with precursor, or diffusion, can be represented as a first-order-loss (R5.10).



An example of the pseudo-first-order loss can be seen in Figure 5.8. Analysis of the pseudo-first-order loss and derivation of the fit, E5.1, has been described in Chapter 3.

$$S_t = S_0 \exp(-(k_{\text{obs}} + k_{\text{loss}})t) \quad \text{E5.1}$$

where S_0 is the initial OH fluorescence signal, S_t is signal after time t , k_{obs} is the pseudo-first-order rate coefficient and k_{loss} is the first-order-loss of OH.

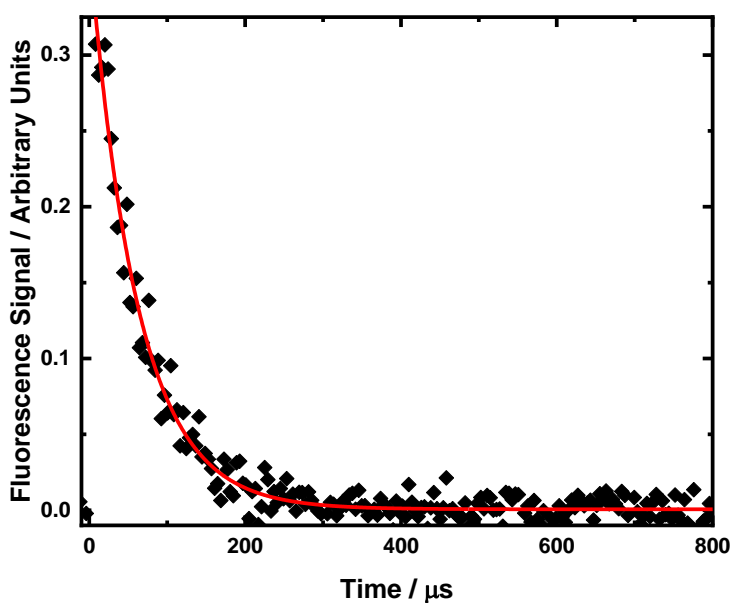


Figure 5.8 OH fluorescence decay at $[2\text{-MF}] = 4.04 \times 10^{14} \text{ molecule cm}^{-3}$ at 298 K and 20 Torr.
 $k_{\text{obs}} = (29320 \pm 708) \text{ s}^{-1}$. H_2O_2 precursor used.

5.3 Results and Discussion

5.3.1 Kinetics at 298 K

Experiments were performed at room temperature between 20 and 150 Torr. Figure 5.9 shows two examples of bimolecular plots for the reaction of OH + 2-MF at 298 K. At the lowest pressure investigated, 20 Torr ($1.31 \times 10^{17} \text{ molecule cm}^{-3}$), the rate coefficient was measured to be $k = (7.64 \pm 0.26) \times 10^{-11} \text{ cm}^3 \text{ molecule}^{-1} \text{ s}^{-1}$. For the highest pressure of 95 Torr ($3.08 \times 10^{18} \text{ molecule cm}^{-3}$) the rate coefficient was determined to be $k = (7.38 \pm 0.37) \times 10^{-11} \text{ cm}^3 \text{ molecule}^{-1} \text{ s}^{-1}$.

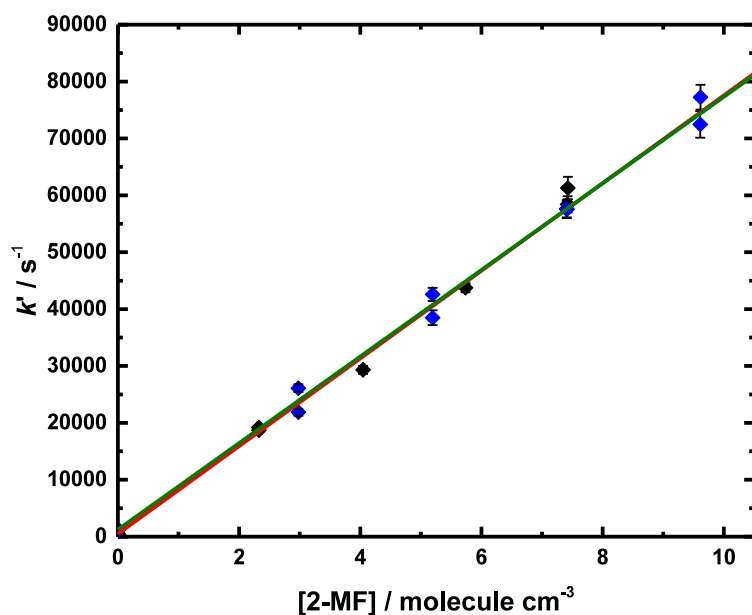


Figure 5.9 Bimolecular plots for the reaction of OH + 2-MF at 298 K at 20 Torr using H₂O₂ precursor (black diamonds) and 95 Torr using (CH₃)₃COOH precursor (blue diamonds) the slopes of which give $k = (7.82 \pm 0.27) \times 10^{-11} \text{ cm}^3 \text{ molecule}^{-1} \text{ s}^{-1}$ (red line) and $k = (7.64 \pm 0.15) \times 10^{-11} \text{ cm}^3 \text{ molecule}^{-1} \text{ s}^{-1}$ (green line) respectively. Note some 1σ error bars are smaller than symbols.

The overall average rate coefficients for reaction of OH with 2-MF at room temperature was determined as $k = (7.34 \pm 0.30) \times 10^{-11} \text{ cm}^3 \text{ molecule}^{-1} \text{ s}^{-1}$, where the error is 1σ , and at 298 K appears to be at, or close to, the high-pressure limit (Figure 5.10). Errors in the bimolecular rate coefficients arise from statistical error when fitting E5.1 to the data to find k' and from the line of best fit when finding k from [2-MF] vs k' .

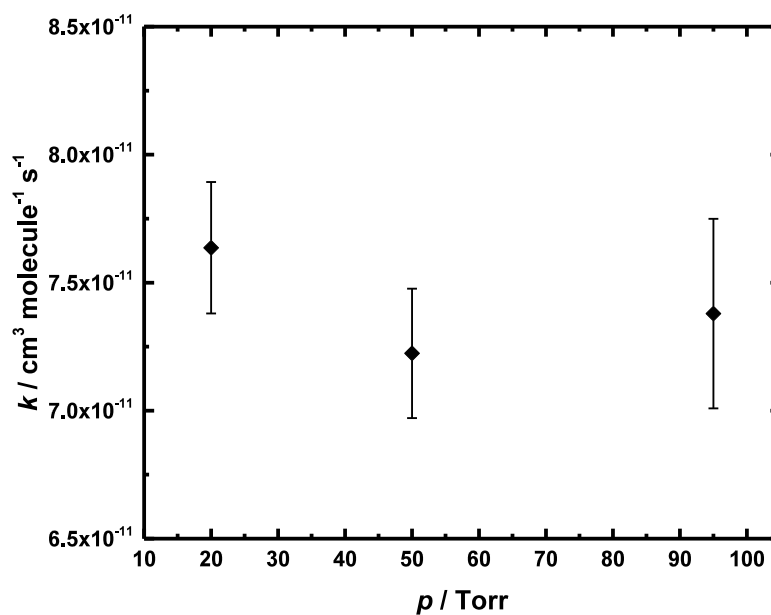


Figure 5.10 Pressure dependence of OH + 2-MF at 298 K. Symbols represent averages at each pressure where a mixture of H₂O₂ and (CH₃)₃COOH precursors were employed.

2-MF oxidation has received some attention previously in the literature. A comparison of this work with former studies shows the average rate coefficient measured for the reaction of OH + 2-MF during this investigation, $k = (7.34 \pm 0.30) \times 10^{-11} \text{ cm}^3 \text{ molecule}^{-1} \text{ s}^{-1}$ (Figure 5.11). These results are in good agreement with the rate coefficient reported by Aschmann *et al.* $k = (7.31 \pm 0.35) \times 10^{-11} \text{ cm}^3 \text{ molecule}^{-1} \text{ s}^{-1}$ and Eble, $k = (6.80 \pm 0.30) \times 10^{-11} \text{ cm}^3 \text{ molecule}^{-1} \text{ s}^{-1}$. Results are not within error of the work by Bierbach *et al.* $k = (6.19 \pm 0.30) \times 10^{-11} \text{ cm}^3 \text{ molecule}^{-1} \text{ s}^{-1}$, whose reported rate coefficient also lies outside the error limits of the work by Aschmann *et al.* and Eble.

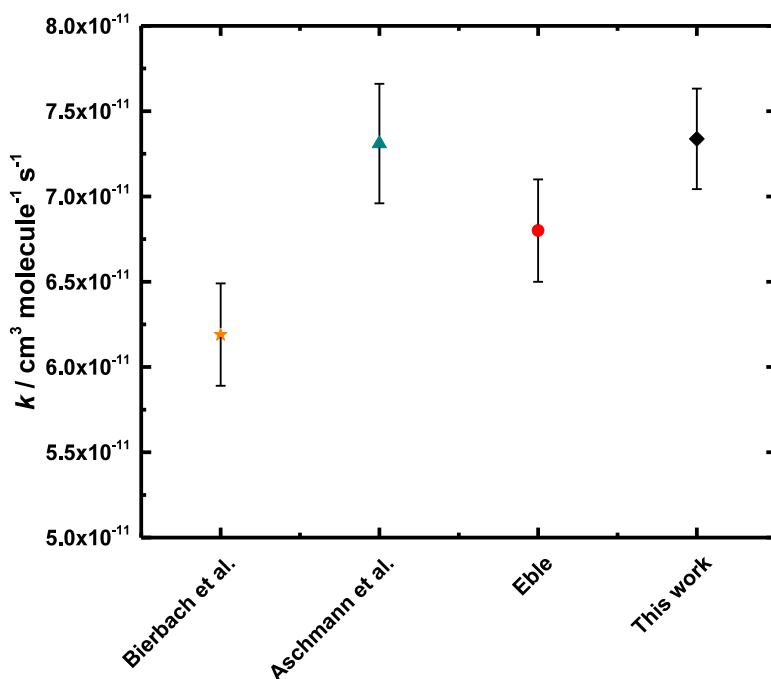


Figure 5.11 Literature room temperature rate coefficients for OH + 2-MF with results from this work

Reference	$k_{298\text{ K}} / 10^{-11} \text{ cm}^3 \text{ molecule}^{-1} \text{ s}^{-1}$	% Uncertainty	% Difference between this work and literature
Bierbach <i>et al.</i>	6.19 ± 0.30	20.6	15.7
Aschmann <i>et al.</i>	7.31 ± 0.35	20.1	0.4
Eble	6.80 ± 0.30	22.7	7.4
This work	7.34 ± 0.30	22.5	-

Table 5.2 Room temperature rate coefficients for the reaction of OH + 2-MF from this work and previous studies. Results for this work are given as an average of all experiments over 298 K.

To determine if the reaction was subject to the effects of photolysis, the path of the photolysis beam was filtered by 10, 25 and 50 % by wire meshes to reduce the amount of light entering the cell. As demonstrated in Figure 5.12, there was no significant change in the bimolecular rate coefficient as a result of the filters applied. Rate coefficients of the fluorescence decays can be seen in Table 5.3.

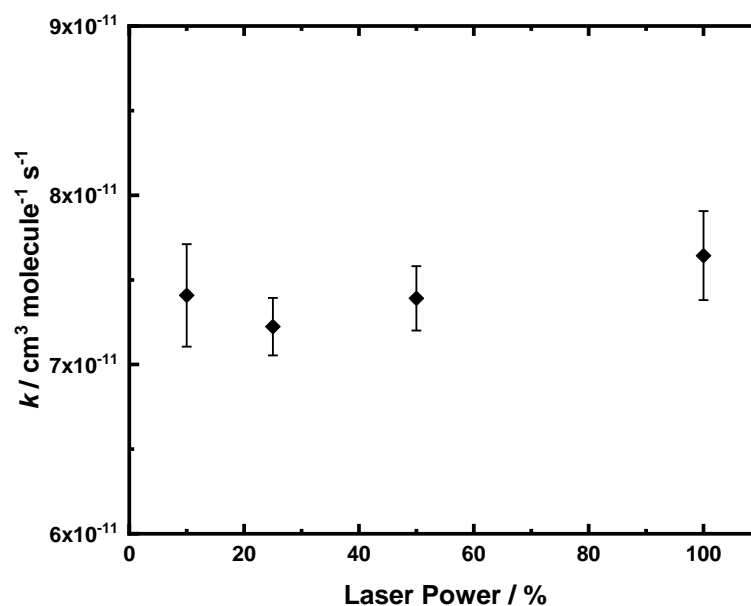


Figure 5.12 Effect of laser power on k for the reaction of OH + 2-MF at 298 K and 50 Torr. Rate coefficient found to be independent of laser power. 100 % laser power $\sim 60 \text{ mJ cm}^{-2}$ fluence.

Laser Power / %	$k / \text{cm}^3 \text{ molecule}^{-1} \text{ s}^{-1}$
10	7.41 ± 0.30
25	7.22 ± 0.17
50	7.39 ± 0.19
100	7.64 ± 0.26

Table 5.3 Bimolecular rate coefficients from the decays of OH + 2-MF at 298 K and 50 Torr with mesh filters applied to the photolysis laser beam. 100 % laser power $\sim 60 \text{ mJ cm}^{-2}$ fluence.

5.3.2 Effects of Pressure and Temperature

To investigate pressure dependence at temperatures above 298 K, reactions were carried out over a range of temperatures and pressures. No pressure dependence was observed over the conditions investigated, indicating the reaction is at, or close to, the high pressure limit.

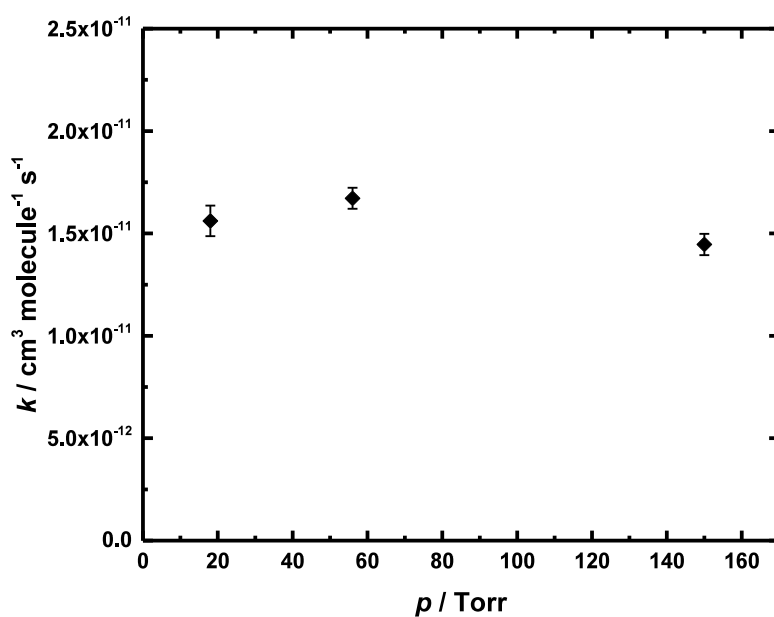


Figure 5.13 Pressure dependence on 2-MF + OH at 660 K

This work has investigated the reaction of 2-MF and OH in the low temperature region (< 1000 K) extending the results available in the literature from 298 K to 770 K, averages of results can be seen in Table 5.4.

T / K	$k / 10^{11} \text{ cm}^3 \text{ molecule}^{-1} \text{ s}^{-1}$
298	7.34 ± 0.29
340	6.12 ± 0.25
380	5.17 ± 0.30
420	4.60 ± 0.20
460	3.95 ± 0.12
500	3.75 ± 0.36
580	1.99 ± 0.05
668	1.56 ± 0.11
770	1.06 ± 0.04

Table 5.4 Average rate coefficients for OH + MF at temperatures between 298 and 770 K, errors are 1σ . A mixture of H_2O_2 and $(\text{CH}_3)_3\text{COOH}$ precursors were employed. Individual rate coefficients can be seen in the Appendix.

The Arrhenius equation, E5.2, was fit to the results from this work, parameters of which can be seen in Table 5.5. The results of the fit of E5.2 to this work can be seen in Figure 5.14.

$$k = A \exp\left(-\frac{E_a}{RT}\right) \quad \text{E5.2}$$

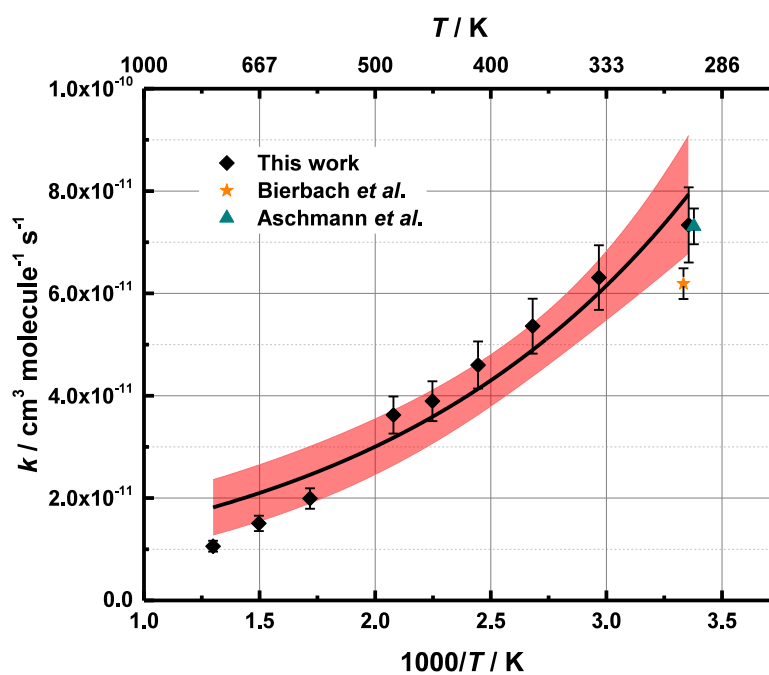


Figure 5.14 Arrhenius plot of OH + 2-MF from this work (black diamonds) with Arrhenius fit to data (black line) with 95 % confidence limits. Arrhenius parameters for this work are $A = (7.17 \pm 0.16) \times 10^{-12} \text{ cm}^3 \text{ molecule}^{-1} \text{ s}^{-1}$ and $-E_a/R = (716 \pm 79) \text{ K}$.

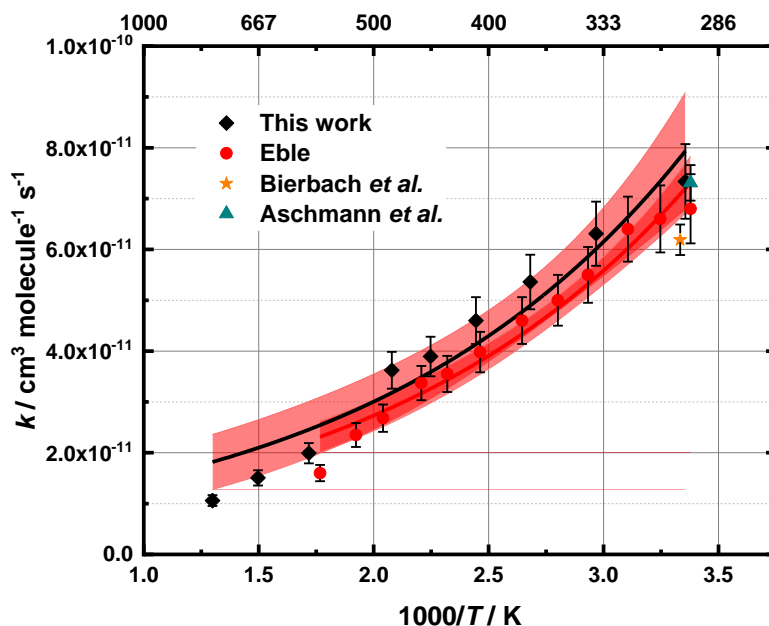


Figure 5.15 Arrhenius plot of OH + 2-MF from this work (black diamonds) and Eble (red circles) with Arrhenius fit to data, this work (black line, light with 95 % confidence limits) and Eble (red line, dark red with 95 % confidence limits). Arrhenius parameters for this work are $A = (7.17 \pm 0.16) \times 10^{-12} \text{ cm}^3 \text{ molecule}^{-1} \text{ s}^{-1}$ and $-E_a/R = (716 \pm 79) \text{ K}$.

Study	Temperature Range / K	$A / 10^{-12} \text{ cm}^3$ $\text{molecule}^{-1} \text{ s}^{-1}$	$-E_a/R / \text{K}$
Eble	296-566	6.54 ± 0.94	714 ± 49
This work	298-770	7.17 ± 0.16	716 ± 79

Table 5.5 Comparison of Arrhenius parameters for the reaction of OH + 2-MF between this work and Eble. The reaction was found to have a negative temperature dependence, suggesting the reactions proceed through a barrierless addition pathway. The Arrhenius parameters from E5.2 were found to be $A = (7.17 \pm 0.16) \times 10^{-12} \text{ cm}^3 \text{ molecule}^{-1} \text{ s}^{-1}$ and $-E_a/R = (716 \pm 79) \text{ K}$. There is good agreement between the Arrhenius parameters from this work and those of Eble, as seen in Table 5.5.

Figure 5.16 shows the results of this work and those of the shock tube experiments performed by Elwardany *et al.* for temperatures between 890-1333 K and shows there are two distinct temperature regimes governing the kinetics of the reaction of OH + 2-

MF. The Elwardany *et al.* study exhibits a positive temperature dependence from 890-1333 K, whereas results from this work display a negative dependence from 298-770 K.

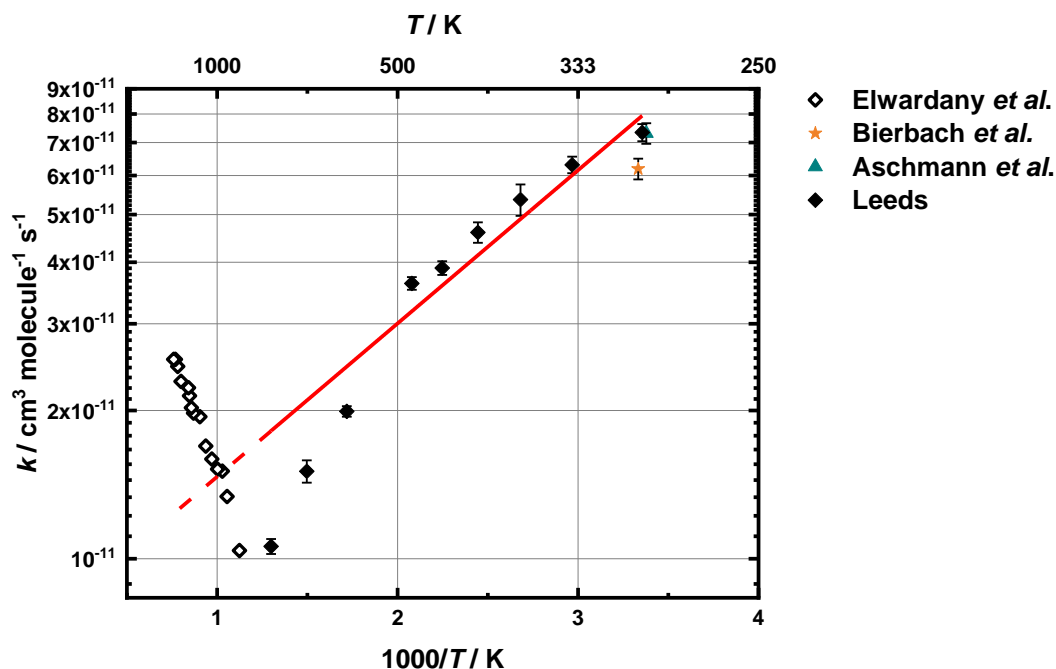


Figure 5.16 The temperature dependent kinetics of OH + 2-MF. Black open diamonds represent Elwardany *et al.* data for high-temperature (890-1333 K) shock tube experiments. Symbols for experiments carried out at 298 K can be found in the graph key. This work is represented by black diamonds, the red line of fit to the data according to E5.2 and the dashed red line is the extrapolation of E5.2 to the high temperature range.

The chemistry of the reaction between OH radicals and 2-MF, as described previously, can occur *via* the addition of the radical to the furan ring, or by the abstraction of an H atom from the C2 or C3 carbon (Figure 5.1). This behaviour can be described by a double modified Arrhenius expression:

$$k = A_1 T^{n_1} \exp\left(\frac{-E_{a1}}{RT}\right) + A_2 T^{n_2} \exp\left(\frac{-E_{a2}}{RT}\right) \quad \text{E5.3}$$

where, for the addition of OH to 2-MF, A_1 represents the pre-exponential factor, n_1 is the exponential of T and E_{a1} is the activation energy. For the H abstraction of 2-MF by OH, A_2 represents the pre-exponential factor, n_2 is the exponential of T and E_{a2} is the activation energy.

Fits of E5.3 to the combined data sets for this work and the work of Elwardany *et al.* and for this work, Eble and Elwardany *et al.* can be seen in Table 5.6. The fit of E5.3 to the data sets can be seen in Figure 5.17.

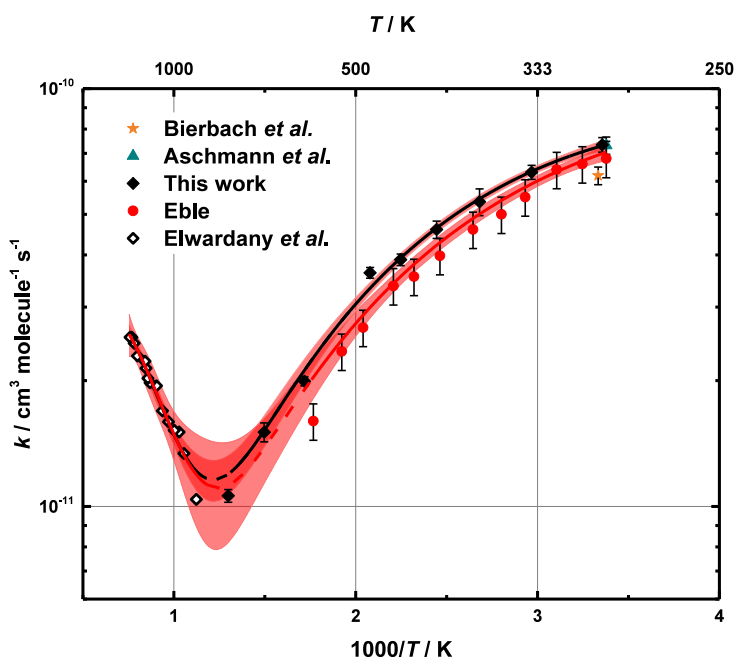


Figure 5.17 The effect of temperature OH + 2-MF. Results from this work (black solid diamonds), Eble (red circles) and Elwardany *et al.* (open black diamonds). The black line represents the modified Arrhenius fit E5.3 to the combined data from this work and Elwardany *et al.* (light red 95 % confidence limits) and to this work, Eble and Elwardany *et al.* (dark red 95 % confidence limits).

Parameter	Fit to this work &	Fit to this work, Eble
	Elwardany <i>et al.</i>	& Elwardany <i>et al.</i>
$A_1 / \text{cm}^3 \text{ s}^{-1}$	94.78	10.94
n_1	-4.31	-4.02
$E_{a1}/R / \text{K}$	1000	845
$A_2 / \text{cm}^3 \text{ s}^{-1}$	1.08×10^{12}	1.97×10^{12}
n_2	-6.16	-6.25
$E_{a2}/R / \text{K}$	10417	10394

Table 5.6 Arrhenius parameters from the fit of E5.3 to the combined data from this work and Elwardany *et al.* and from this work, Eble and Elwardany *et al.*

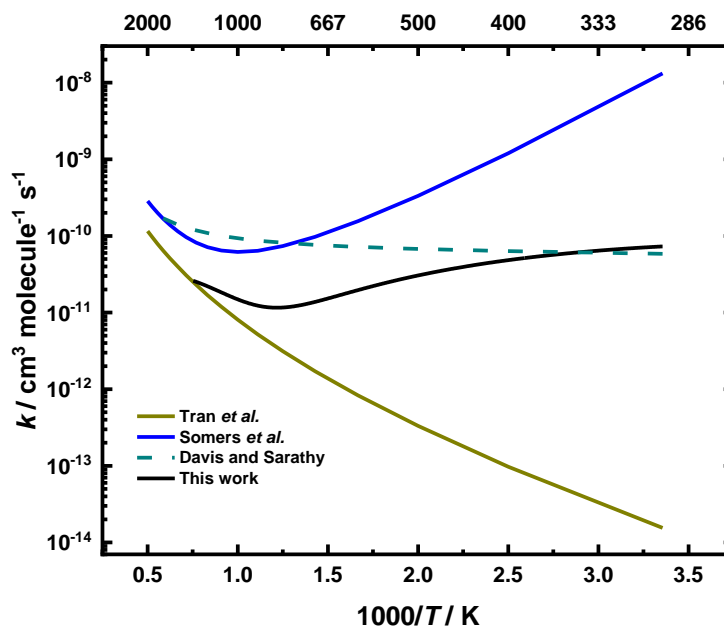


Figure 5.18 Comparison of the fit of E5.3 to Davis and Sarathy¹⁵, Tran *et al.*¹⁶ and Somers *et al.*¹⁸ for OH + 2-MF.

When the E5.3 fit is compared to models available in the literature, shown in Figure 5.18, it is clear that the lack of low-temperature data is contributing significantly to the over prediction, or in the case of Tran *et al.*, over prediction, of the rate coefficients at these lower temperatures. These discrepancies between modelled and observed rate coefficients are discussed in detail in Chapter 7.

5.4 Conclusion

The kinetics of the reaction of OH + 2-MF have been investigated in the pressure range of 20-150 Torr and at temperatures between 298 and 770 K relevant to low-temperature combustion. The study was carried out using laser flash photolysis-laser induced fluorescence (LFP-LIF). This investigation has extended the temperature range of low-temperature combustion of furans (<1000 K).

The average room temperature rate coefficient, as $k = (7.38 \pm 0.37) \times 10^{-11} \text{ cm}^3 \text{ molecule}^{-1} \text{ s}^{-1}$, is within uncertainties of the rate coefficient report by Aschmann *et al.*, $(7.31 \pm 0.35) \times 10^{-11} \text{ cm}^3 \text{ molecule}^{-1} \text{ s}^{-1}$ and Eble, $k = (6.80 \pm 0.30) \times 10^{-11} \text{ cm}^3 \text{ molecule}^{-1} \text{ s}^{-1}$, however it is not within the uncertainties of the rate coefficient reported by Bierbach

et al. $k = (6.19 \pm 0.30) \times 10^{-11} \text{ cm}^3 \text{ molecule}^{-1} \text{ s}^{-1}$. There is a 16 % difference between the rate coefficient reported by Bierbach *et al.* and the observed average rate coefficient in this work at 298 K.

Over the temperature range investigated the reaction appears to be at, or close to, the high-pressure limit. Results demonstrate a negative temperature dependence for the reaction of OH + 2-MF over temperatures between 298 K and 770 K, with $-E_a/R = (716 \pm 79) \text{ K}$ which is in agreement with the results of Eble, $-E_a/R = (714 \pm 49) \text{ K}$ (296 -566 K).

The result were analysed in combination with the work of Eble (296-566 K) and Elwardany *et al.* (890-1333 K) by fitting the data to a double modified Arrhenius expression to obtain parameters that describe the low and high temperature kinetics of the OH + furan system.

The work reported in this chapter can be inserted into current combustion models of 2-MF to better predict the complex chemistry of the oxidation of 2-MF at temperatures below 1000 K where the low temperature combustion of biofuels occurs.

5.5 References

1. Thewes, M., M. Muether, S. Pischinger, M. Budde, A. Brunn, A. Sehr, P. Adomeit and J. Klankermayer. Analysis of the Impact of 2-Methylfuran on Mixture Formation and Combustion in a Direct-Injection Spark-Ignition Engine. *Energy & Fuels*, 2011, **25**(12), pp.5549-5561.
2. Bierbach, A., I. Barnes and K.H. Becker. Rate coefficients for the gas-phase reactions of hydroxyl radicals with furan, 2-methylfuran, 2-ethylfuran and 2,5-dimethylfuran at 300 K. *Atmospheric Environment Part a-General Topics*, 1992, **26**(5), pp.813-817.
3. Atkinson, R. Kinetics and mechanisms of the gas-phase reactions of the hydroxyl radical with organic compounds under atmospheric conditions. *Chemical Reviews*, 1986, **86**(1), pp.69-201.
4. Aschmann, S.M., N. Nishino, J. Arey and R. Atkinson. Kinetics of the Reactions of OH Radicals with 2- and 3-Methylfuran, 2,3- and 2,5-Dimethylfuran, and E- and Z-3-Hexene-2,5-dione, and Products of OH + 2,5-Dimethylfuran. *Environmental Science & Technology*, 2011, **45**(5), pp.1859-1865.
5. Atkinson, R. and J. Arey. Atmospheric Degradation of Volatile Organic Compounds. *Chemical Reviews*, 2003, **103**(12), pp.4605-4638.
6. Eble, J.S.R. *Ignition of oxygenated hydrocarbons: Mechanism and elementary steps*. thesis, Karlsruhe Institute of Technology (KIT), 2017.
7. Atkinson, R. Gas-phase tropospheric chemistry of organic compounds: A review. *Atmospheric Environment. Part A. General Topics*, 1990, **24**(1), pp.1-41.

8. IUPAC Task Group on Atmospheric Chemical Kinetic Data Evaluation – Data Sheet HO_x_VOC64. 2009.
9. Alarcón, P., B. Bohn and C. Zetzsch. Kinetic and mechanistic study of the reaction of OH radicals with methylated benzenes: 1,4-dimethyl-, 1,3,5-trimethyl-, 1,2,4,5-, 1,2,3,5- and 1,2,3,4-tetramethyl-, pentamethyl-, and hexamethylbenzene. *Physical Chemistry Chemical Physics*, 2015, **17**(19), pp.13053-13065.
10. Ohta, T. and T. Ohyama. A set of rate constants for the reactions of OH radicals with aromatic hydrocarbons. *Bulletin of the Chemical Society of Japan*, 1985, **58**(10), pp.3029-3030.
11. Elwardany, A., E. Es-Sebbar, F. Khaled and A. Farooq. A chemical kinetic study of the reaction of hydroxyl with furans. *Fuel*, 2016, **166**, pp.245-252.
12. Grosjean, D. and E.L. Williams II. Environmental persistence of organic compounds estimated from structure-reactivity and linear free-energy relationships. Unsaturated aliphatics. *Atmospheric Environment. Part A. General Topics*, 1992, **26**(8), pp.1395-1405.
13. Curtiss, L.A., P.C. Redfern and K. Raghavachari. Gaussian-4 theory. 2007, **126**(8), p.084108.
14. J. A. Montgomery Jr, M.J.F., J. W. Ochterski, G. A. Petersson. A complete basis set model chemistry. VII. Use of the minimum population localization method. *The Journal of Chemical Physics*, 2000, **112**(15), pp.6532-6542.
15. Davis, A.C. and S.M. Sarathy. Computational Study of the Combustion and Atmospheric Decomposition of 2-Methylfuran. *The Journal of Physical Chemistry A*, 2013, **117**(33), pp.7670-7685.
16. Tran, L.-S., C. Togbé, D. Liu, D. Felsmann, P. Oßwald, P.-A. Glaude, R. Fournet, B. Sirjean, F. Battin-Leclerc and K. Kohse-Höinghaus. Combustion chemistry and flame structure of furan group biofuels using molecular-beam mass spectrometry and gas chromatography – Part II: 2-Methylfuran. *Combustion and Flame*, 2014, **161**(3), pp.766-779.
17. Somers, K.P., J.M. Simmie, W.K. Metcalfe and H.J. Curran. The pyrolysis of 2-methylfuran: a quantum chemical, statistical rate theory and kinetic modelling study. *Physical Chemistry Chemical Physics*, 2014, **16**(11), pp.5349-5367.
18. Somers, K.P., J.M. Simmie, F. Gillespie, C. Conroy, G. Black, W.K. Metcalfe, F. Battin-Leclerc, P. Dirrenberger, O. Herbinet, P.-A. Glaude, P. Dagaut, C. Togbé, K. Yasunaga, R.X. Fernandes, C. Lee, R. Tripathi and H.J. Curran. A comprehensive experimental and detailed chemical kinetic modelling study of 2,5-dimethylfuran pyrolysis and oxidation. *Combustion and Flame*, 2013, **160**(11), pp.2291-2318.
19. Mousavipour, S.H., S. Ramazani and Z. Shahkolahi. Multichannel RRKM-TST and Direct-Dynamics VTST Study of the Reaction of Hydroxyl Radical with Furan. *The Journal of Physical Chemistry A*, 2009, **113**(12), pp.2838-2846.

Chapter 6 Kinetic Study of the OH + 2,5-Dimethylfuran Reaction as a Function of Temperature and Pressure

6.1 Background and Previous Work

Both furan and 2-methylfuran have been proposed as biofuels, however it is the 2,5-dimethylfuran (2,5-DMF) that shows the most promise. With a similar energy density to gasoline, a high boiling point and insolubility in water, 2,5-DMF is the favourable choice of biofuel over low carbon biofuels, such as ethanol, currently in commercial use (Table 6.1).

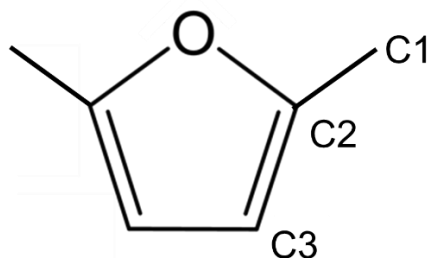


Figure 6.1 Structure of 2,5-DMF with labelled carbon sites

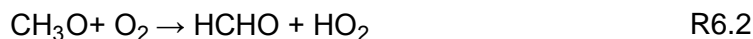
Property	Gasoline	2,5-DMF	Ethanol
Energy Density / MJ dm ⁻³	32.2	31.5	25
Boiling point / °C	85	92	78
Solubility in water	Insoluble	Insoluble	Miscible
Research octane number	95-98	119	108.6
Auto-ignition <i>T</i> / °C	420	285.85	434

Table 6.1 Comparison of the physical properties of the fuels gasoline, 2,5-DMF and ethanol.¹

6.1.1 Studies of OH + 2,5-DMF at Low Temperature (<1000 K)

The following investigations into the oxidation of 2,5-DMF by OH radicals have previously been described in Chapters 4 and 5, details of the experimental techniques reported here can be found in Chapter 3.

Bierbach *et al.*² investigated the oxidation of 2,5-DMF by OH radicals using CP-GC at 298 K and 760 Torr. Unlike for the reactions of OH with furan and 2-MF, where propene was used as the reference compound, Bierbach *et al.* used *trans*-2-butene as the reference compound for the reactions involving 2,5-DMF, with OH + *trans*-2-butene as $k = 6.32 \times 10^{-11} \text{ cm}^3 \text{ molecule}^{-1} \text{ s}^{-1}$ taken from Atkinson *et al.*³ The photolysis of methyl nitrite at wavelengths between 320 nm and 480 nm generated OH radicals (R6.1-R6.3).



The rate coefficient for the reaction of OH with 2,5-DMF was determined to be $k = (1.32 \pm 0.10) \times 10^{-10} \text{ cm}^3 \text{ molecule}^{-1} \text{ s}^{-1}$. Current IUPAC recommendations for the reaction rate coefficients of the reference species used is $k = 6.4 \times 10^{-11} \text{ cm}^3 \text{ molecule}^{-1} \text{ s}^{-1}$ for OH + *trans*-2-butene.⁴ Once the observed relative rates are adjusted for the current IUPAC recommendations for the reference compound, the rate coefficient becomes $k = (1.34 \pm 0.10) \times 10^{-10} \text{ cm}^3 \text{ molecule}^{-1} \text{ s}^{-1}$, which are within error with the value reported by Bierbach *et al.*

Aschmann *et al.*⁵ investigated the rate of reaction of OH with 2,5-DMF using the CP-GC technique at 296 K and 735 Torr in a chamber study. OH radicals were also produced *via* the photolysis of methyl nitrite (R1-R3) at $\lambda > 300 \text{ nm}$ in the presence of NO to avoid additional chemistry by the titration of O₃ formed as a result of NO₂ photolysis. The relative rate method was used employing 1,3,5-trimethylbenzene as a reference compound ($k = 5.67 \times 10^{-11} \text{ cm}^3 \text{ molecule}^{-1} \text{ s}^{-1}$) taken from Atkinson *et al.*⁶ The rate

coefficient was reported as $k = (1.25 \pm 0.04) \times 10^{-10} \text{ cm}^3 \text{ molecule}^{-1} \text{ s}^{-1}$. When compared to Bierbach *et al.* the results of Aschmann *et al.* are within error for the reaction involving 2,5-DMF, as shown in Table 6.2.

Currently, there is no IUPAC recommendation for the reaction of OH with 1,3,5-trimethylbenzene, and no review of the reaction available in the literature. According to the present literature, rate coefficients for the reaction of OH with 1,3,5-trimethylbenzene extend from $k = (4.09 \pm 0.56) \times 10^{-11} \text{ cm}^3 \text{ molecule}^{-1} \text{ s}^{-1}$ reported by Ohta *et al.*⁷ to $k = (6.84 \pm 0.10) \times 10^{-11} \text{ cm}^3 \text{ molecule}^{-1} \text{ s}^{-1}$ reported by Alarcón *et al.*⁸ Once the observed relative rates are adjusted for these the rate coefficient for OH + 2,5-DMF becomes $k = (0.90 \pm 0.04) \times 10^{-10} \text{ cm}^3 \text{ molecule}^{-1} \text{ s}^{-1}$ and $k = (3.22 \pm 0.04) \times 10^{-10} \text{ cm}^3 \text{ molecule}^{-1} \text{ s}^{-1}$ for Ohta *et al.* and Alarcón *et al.* respectively. Neither of these values are within error of the value reported by Aschmann *et al.* indicating 1,3,5-trimethylbenzene may not be a reliable reference compound. Values of the rate coefficients of OH with 2,5-DMF and reference compounds can be seen in Table 6.2.

An investigation by Eble⁹ into the reaction of the OH radical with 2,5-DMF used LFP-LIF to determine the rate coefficients for the reactions in He. The photolysis of nitric acid (HNO₃) at 248 nm was the source of OH radicals (R6.4). Secondary chemistry that could potentially occur from the catalytic decomposition of gaseous HNO₃ to NO₂ was minimized by replacing HNO₃ mixtures regularly. Eble reported results were found to be independent of flash intensity.



2,5-DMF was in excess over the OH radicals to obtain pseudo-first-order conditions. The room temperature rate coefficient was measured as $k = (9.2 \pm 0.4) \times 10^{-11} \text{ cm}^3 \text{ molecule}^{-1} \text{ s}^{-1}$, which is not within the error limits of the room temperature rate coefficients of OH + 2,5-DMF reported by Bierbach *et al.* or Aschmann *et al.* with a 30.3 % and 26.4 % percentage difference, respectively. However, when compared to the possible updated relative rate coefficients, the work is in agreement with the lowest updated values for the

work by Aschmann *et al.*, $k = (0.90 \pm 0.04) \times 10^{-10} \text{ cm}^3 \text{ molecule}^{-1} \text{ s}^{-1}$ based on the reference rate by Ohta *et al.*⁷

The temperature dependence of the reaction was investigated from 295 – 557 K, a negative temperature dependence was found with Arrhenius parameters for OH + 2,5-DMF determined to be $k = (7.42 \pm 0.85) \times 10^{-12} \exp((747 \pm 44)/T) \text{ cm}^3 \text{ molecule}^{-1} \text{ s}^{-1}$. The Arrhenius plot for this experiment can be seen in Figure 6.2. Experiments were carried out over a range of pressures, 2 - 10 bar (1500 - 7500 Torr), and no dependence on pressure was observed.

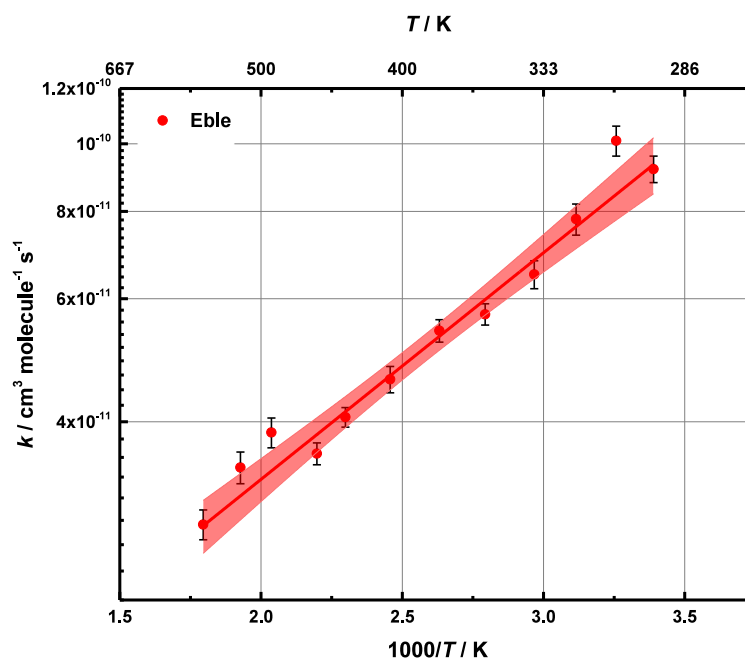


Figure 6.2 Arrhenius plot for OH + 2,5-DMF from Eble.⁹ From 296-557 K and 2 to 10 bar (1520-7600 Torr). Arrhenius parameters are $A = (7.42 \pm 0.85) \times 10^{-12} \text{ cm}^3 \text{ molecule}^{-1} \text{ s}^{-1}$ and $-E_a/R = (747 \pm 44) \text{ K}$.

Study	Reference Compound	T Range / K	p Range / Torr	Technique	$k_{\text{OH}+2,5\text{-DMF}} / 10^{-10} \text{ cm}^3 \text{ molecule}^{-1} \text{ s}^{-1}$	$k_{\text{OH}+\text{ref}} / 10^{-11} \text{ cm}^3 \text{ molecule}^{-1} \text{ s}^{-1}$	Literature $k_{\text{OH}+\text{ref}}$	Updated $k_{\text{OH}+2,5\text{-DMF}}$
							$/ 10^{-11} \text{ cm}^3 \text{ molecule}^{-1} \text{ s}^{-1}$	$/ 10^{-10} \text{ cm}^3 \text{ molecule}^{-1} \text{ s}^{-1}$
Bierbach <i>et al.</i> ²	<i>trans</i> -2-butene	298	760	CP-GC	1.32 ± 0.10	6.32^3	6.40^4	1.34 ± 0.10
Aschmann <i>et al.</i> ⁵	1,3,5-trimethylbenzene	296	735	CP-GC	1.25 ± 0.04	5.67^6	6.84 ± 0.10^8	3.22 ± 0.04
							4.09 ± 0.56^7	0.90 ± 0.04
Eble ⁹	-	295-557	1500-7600	LFP-LIF	$0.92 \pm 0.04^*$	-	-	-

Table 6.2 Literature rate coefficients for the oxidation of 2,5-DMF by the OH radical and for the reaction of OH with reference compounds used in the relative rate experiments. Updated rate coefficients using recent literature for those reference compounds are shown. Values for *trans*-2-butene are taken from current IUPAC recommendations. Values for 1,3,5-trimethylbenzene are the highest and lowest rate coefficients available in the current literature. *Results from absolute measurement technique.

6.1.2 Studies of OH + 2,5-DMF at High Temperatures (>1000 K)

There is evidence in the literature that the abstraction channels are favoured at higher temperatures, Elwardany *et al.*¹⁰ reported the first rate coefficients measured in a high-temperature regime (>1000 K) for the reaction of OH radicals with 2,5-DMF and reported a positive temperature dependence for experiments performed over 915 K.

The reaction of OH + 2,5-DMF was studied by Elwardany *et al.* using a shock tube over a temperature range of 915-1278 K and pressures of 1.2-1.7 atm (900-1400 Torr). The thermal decomposition of *tert*-butyl hydroperoxide ((CH₃)₃COOH) was used as a source of OH radicals, which were monitored by UV absorption spectroscopy at ~ 306 nm. Reactions were performed under pseudo-first-order conditions, so that the concentrations of 2,5-DMF were in great excess over those of OH radicals in each experiment. Results found to be independent of the mixture composition and pressure, over the pressure range of 1.2 - 1.7 atm (912 – 1292 Torr).

Elwardany *et al.* report their results as an Arrhenius expression of $k = 1.71 \times 10^{-10} \exp(-2128/T) \text{ cm}^3 \text{ molecule}^{-1} \text{ s}^{-1}$. This parameterisation leads to a predicted room temperature rate coefficient of $k = 1.35 \times 10^{-13} \text{ cm}^3 \text{ molecule}^{-1} \text{ s}^{-1}$, which is significantly lower than the values (1.32 ± 0.10) , (1.25 ± 0.04) and $(0.92 \pm 0.04) \times 10^{-10} \text{ cm}^3 \text{ molecule}^{-1} \text{ s}^{-1}$ reported by Bierbach *et al.*, Aschmann *et al.* and Eble respectively. Elwardany *et al.* note this difference in room temperature rates and conclude that it is an indication that OH addition pathways dominate at low temperatures in contrast to abstraction at high-temperatures.

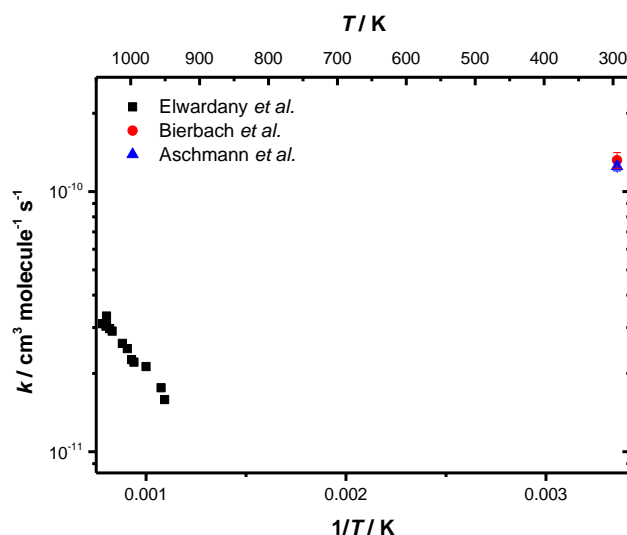


Figure 6.3 Literature rate coefficients for the reaction of OH + 2,5-DMF. Elwardany *et al.* study was carried out at 1.2-1.7 atm. Bierbach *et al.* and Aschmann *et al.* studies were carried out at 760 and 735 Torr respectively.

Figure 6.3 shows the current literature rate coefficients for the reaction of OH + 2,5-DMF and demonstrates that there are no data in the literature describing the reaction at temperatures between 298 K and 900 K which are relevant to low temperature combustion. Additionally, no investigations into the effect of pressure on the reaction have been carried out at either room temperature or in the higher temperature study.

Aschmann *et al.*¹¹ carried out a product study of the reaction of OH radicals with 2,5-DMF in the presence of NO using direct air sampling atmospheric pressure ionization tandem mass spectrometry (API-MS) and gas chromatography with flame ionization and mass spectrometric detectors (GC-FID and GC-MS). Experiments were carried out at (296 ± 2) K and ~ 735 Torr. Observed products include unsaturated 1,4-dicarbonyls, unsaturated carbonyl-acids and hydroxyl-furanones and from 2,5-DMF unsaturated carbonyl-esters. Aschmann *et al.* suggested possible subsequent reactions that follow the addition of OH to 2,5-DMF, as shown in Figure 6.4.

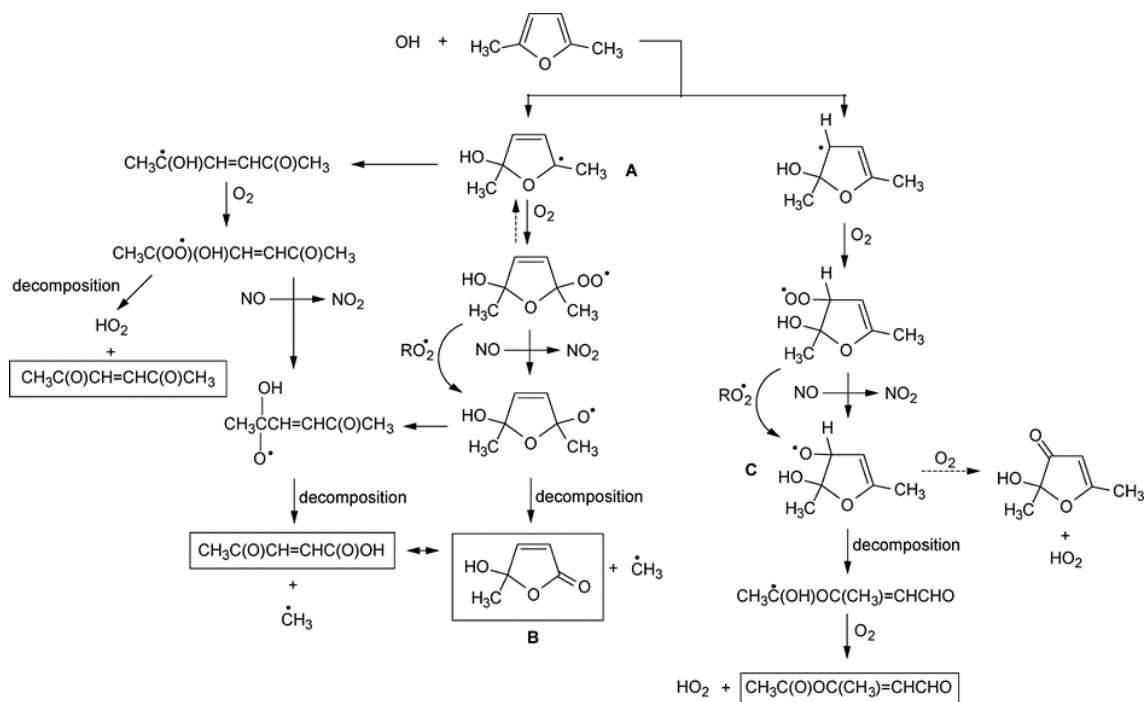


Figure 6.4 Possible reactions after initial OH radical addition to 2,5-DMF suggested by Aschmann *et al.*¹¹ The product of OH + 2,5-DMF can react with O₂ leading to a peroxy radical (RO₂). This peroxy radical can react with the NO in the system leading to the production of an alkoxy radical (RO) and NO₂. However, the RO₂ radicals will undergo a different fate under NO-free conditions, such as isomerisation to a QOOH radical, which can further react with oxygen to form O₂QOOH, which are involved in chain branching.¹²

6.1.3 Theoretical Studies of OH + 2,5-DMF

There have been several previous theoretical studies into 2,5-DMF chemistry at temperatures relevant to high-temperature combustion. The first investigation focused on the thermal decomposition of 2,5-DMF in the temperature range of 500-2000 K. Simmie and Metcalfe¹³ studied H-abstraction reactions by OH using compound methods CBS-QB3¹⁴ and CBS-APNO¹⁵, G3¹⁶ and G3MP2B3¹⁷ to compute the geometries, frequencies and single point energies of the reactants, transition states and products. Intrinsic reaction coordinate (IRC) calculations were employed to connect transition states with reactants and products.

To calculate rate coefficients Simmie and Metcalfe used the MultiWell-2010 program,¹⁸ which can solve internal energy master equations for reactions. The program calculates time-dependent concentrations, yields, vibrational distributions and rate coefficients as a function of temperature and pressure.

Rate coefficient calculations were reported as $k = 1.69 \times 10^{-20} T^{3.13} \exp(-1085/T) \text{ cm}^3 \text{ molecule}^{-1} \text{ s}^{-1}$ for the abstraction of an H atom from the methyl group by an OH radical, and $k = 6.53 \times 10^{-20} T^{2.67} \exp(-3871/T) \text{ cm}^3 \text{ molecule}^{-1} \text{ s}^{-1}$ for the H-abstraction by OH from the C3 position of the furan ring.

6.1.4 Combustion Models of 2,5-DMF

A more detailed description of combustion models for 2,5-DMF in the literature can be found in Chapter 7, a brief outline of the models will be given here.

Somers *et al.*¹⁹ developed a detailed chemical kinetic mechanism to describe the combustion of 2,5-DMF. The CBS-QB3²⁰, CBS-APNO²¹ and G3²² levels of theory were used to calculate optimised geometries, frequencies and single point energies for reactants and transition states with Gaussian 03²³ and 09²⁴ programs. IRC calculations were used to connect transition states with products and reactants. From the IRC analysis a pre-reaction complex was found, but it is noted that such complexes are not likely to be important in the temperature range of the study and therefore its influences are not accounted for in the rate coefficient calculations.

Both addition and abstraction pathways for the reaction of the OH radical with 2,5-DMF were included in the Somers *et al.* mechanism. Only the C2 addition pathway (R6.5) is included as it is assumed by Somers *et al.* that addition to the C3 site led to less stable radical intermediates.



They report that at the temperatures studied an H atom transfer reaction is found to be the dominant removal pathway of 2,5-DMF. The rate coefficients for H atom abstraction by OH in this mechanism are based on those reported by the Simmie and Metcalfe¹³, however Somers *et al.* report greater activation energies in both expressions. For the abstraction of a H atom from the methyl group by an OH radical (R6.6) Somers *et al.* report $k = 1.69 \times 10^{-20} T^{3.13} \exp(-2160/T) \text{ cm}^3 \text{ molecule}^{-1} \text{ s}^{-1}$, and for the H-abstraction by OH from the C3 position of the furan ring (R6.7) $k = 6.53 \times 10^{-20} T^{2.67} \exp(-7890/T) \text{ cm}^3 \text{ molecule}^{-1} \text{ s}^{-1}$, calculated using the MultiWell-2010¹⁸ program. When compared to experiments carried out at higher temperatures by Elwardany *et al.*, the model by Somers *et al.* overestimates the rate coefficient by up to a factor of 2 at 600 K to a factor of 7 at 1200 K. A comparison of the studies can be seen in Figure 6.5.

For association reactions of the system, Somers *et al.* note that OH radical addition to the furan ring in 2,5-DMF leads to the formation of methyl vinyl ketone ($\text{CH}_3\text{C}(\text{O})\text{CH}=\text{CH}_2$) and an acetyl radical (CH_3CO). A rate coefficient for this addition was calculated using the MultiWell-2010 program and was determined to be $k = 3.67 \times 10^{-20} T^{2.45} \exp(7251/T) \text{ cm}^3 \text{ molecule}^{-1} \text{ s}^{-1}$ at the high-pressure limit over the temperature range of 600-2000 K. An uncertainty of a factor of 3 in the high-pressure limiting rate coefficient is estimated for the addition process. This predicts a room temperature rate coefficient of $k = 1.56 \times 10^{-3} \text{ cm}^3 \text{ molecule}^{-1} \text{ s}^{-1}$ which is seven orders of magnitude faster than the experimental values of $k = (1.32 \pm 0.10) \times 10^{-10} \text{ cm}^3 \text{ molecule}^{-1} \text{ s}^{-1}$ and $k = (1.25 \pm 0.04) \times 10^{-10} \text{ cm}^3 \text{ molecule}^{-1} \text{ s}^{-1}$ reported by Bierbach *et al.*² and Aschmann *et al.*⁵

Togbé *et al.*²⁵ developed a kinetic model for the thermal decomposition of 2,5-DMF using the CHEMKIN²⁶ program. For the abstraction of an H atom from the C3 of the carbon ring by OH (R6.7) and the abstraction of an H atom from one of the methyl groups (R6.6), rate coefficients were based on the work by Simmie and Metcalfe¹³.

The OH radical addition to 2,5-DMF (R6.5) is given as $k = 1.32 \times 10^{-11} \exp(670/T) \text{ cm}^3 \text{ molecule}^{-1} \text{ s}^{-1}$, this rate coefficient is an estimate by Togbé *et al.* based on the

reaction of OH radicals with furan according to Atkinson *et al.*²⁷ For reactions at 298 K this rate coefficient predicts a value of $k = 1.23 \times 10^{-10} \text{ cm}^3 \text{ molecule}^{-1} \text{ s}^{-1}$ which is in agreement with both experimental values of $k = (1.32 \pm 0.10) \times 10^{-10} \text{ cm}^3 \text{ molecule}^{-1} \text{ s}^{-1}$ and $k = (1.25 \pm 0.04) \times 10^{-10} \text{ cm}^3 \text{ molecule}^{-1} \text{ s}^{-1}$ reported by Bierbach *et al.*² and Aschmann *et al.*⁵ These rate coefficients for both H atom abstraction and OH addition were replicated by Cheng *et al.*²⁸ for their own model of 2,5-DMF pyrolysis.

A comparison of the models discussed here as well as the theoretical study by Simmie and Metcalfe is shown in comparison with the work by Eble and Elwardany *et al.* in Figure 6.5. All the models estimate the high temperature rate coefficients based on the work by Simmie and Metcalfe and overestimate the rates when compared to the work by Elwardany *et al.* For the low temperature data observed by Bierbach *et al.*, Aschmann *et al.* and Eble, the models underpredict the rate coefficients by orders of magnitude

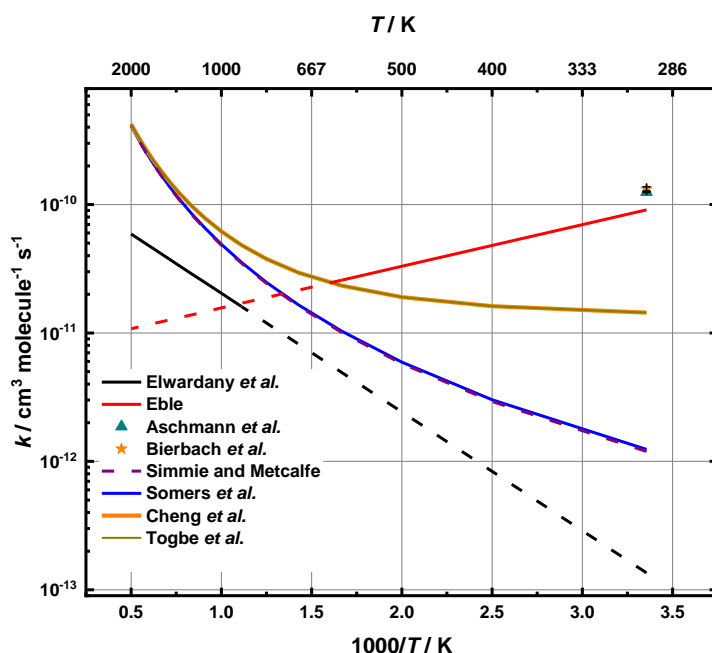


Figure 6.5 Comparison of combustion models (key inset) with Arrhenius fits to experimental data of Eble and Elwardany *et al.* for of OH + 2,5-DMF. Note the Togbe *et al.* and Cheng *et al.* studies report the same rate coefficients.

Currently, the number of experimental 2,5-DMF oxidation studies in the literature is limited to room temperature studies or those carried out in the high temperature regime

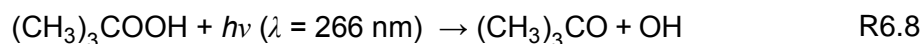
(>1000 K). There are no available data in the literature that focuses on the reaction in the low-temperature regime (<1000 K) relevant to low temperature combustion. Theoretical studies into the low temperature regime of the oxidation of 2,5-DMF are also lacking.

This chapter reports an extensive kinetic study of the OH + 2,5-DMF reaction and demonstrates that this investigation has extended previous measurements of the rate coefficients of OH radicals with 2,5-DMF. Experiments were performed at various pressures (20-150 Torr) and temperatures (298-635 K) relevant to low temperature auto-ignition in combustion in order to parameterise kinetics of combustion conditions.

6.2 Experimental Procedure

Experiments were carried out as described in Chapter 3 and so only a brief outline will be given here.

This work investigates the rate of reaction between OH radicals and 2,5-DMF using flash photolysis to initiate the reaction and laser induced fluorescence (LIF) to monitor the OH radical. 2,5-DMF (Sigma Aldrich, 99 %) was degassed and purified by a series of freeze-pump-thaw cycles and prepared at a known concentration (typically between 1×10^{13} molecule cm^{-3} and 1×10^{15} molecule cm^{-3}) in N_2 and stored in a glass bulb. N_2 (BOC, oxygen free, 99.99 %) and O_2 (BOC, 99.99 %) were used as supplied. A known flow of N_2 was passed through a bubbler containing *tert*-butyl hydroperoxide ($(\text{CH}_3)_3\text{COOH}$, $T < 500$ K, Sigma Aldrich, 70 % v/v aqueous) or hydrogen peroxide (H_2O_2 , $298 \text{ K} < T < 700$ K, Sigma Aldrich, 50 % v/v aqueous) to entrain the peroxide into the precursor gas flow. Reactions were initiated when OH radicals were produced *via* the photolysis of a suitable precursor ($(\text{CH}_3)_3\text{COOH}$ $298 \text{ K} < T < 500 \text{ K}$ and H_2O_2 $298 \text{ K} < T < 635 \text{ K}$) (R6.8-R6.10) using the 4th harmonic of a pulsed Nd:YAG photolysis laser at $\lambda = 266 \text{ nm}$.





The photolysis laser beam was introduced into the reactor through one of the side arms and had a typical fluence of $\sim 60 \text{ mJ cm}^{-2}$. A pulse repetition frequency of 10 Hz was used for the majority of the study except when experiments were conducted at lower repetition rates to ensure there were no interferences from photolysis products.

The reaction was carried out under pseudo-first-order conditions such that the concentration of 2,5-DMF was always in large excess of OH. Under these conditions, the loss of OH is through the reaction with 2,5-DMF (R6.7) and other losses such as reaction with the precursor, or diffusion, can be represented as a first-order loss (R6.11).



An example of the pseudo-first-order loss can be seen in Figure 6.6. Analysis of the pseudo-first-order loss and derivation of the fit, E6.1, has been described in Chapter 3.

$$S_t = S_0 \exp(-k't) \quad \text{E6.1}$$

where S_0 is the initial OH fluorescence signal, S_t is signal after time t , k_{obs} is the pseudo-first-order rate coefficient and k_{loss} is the first-order-loss of OH.

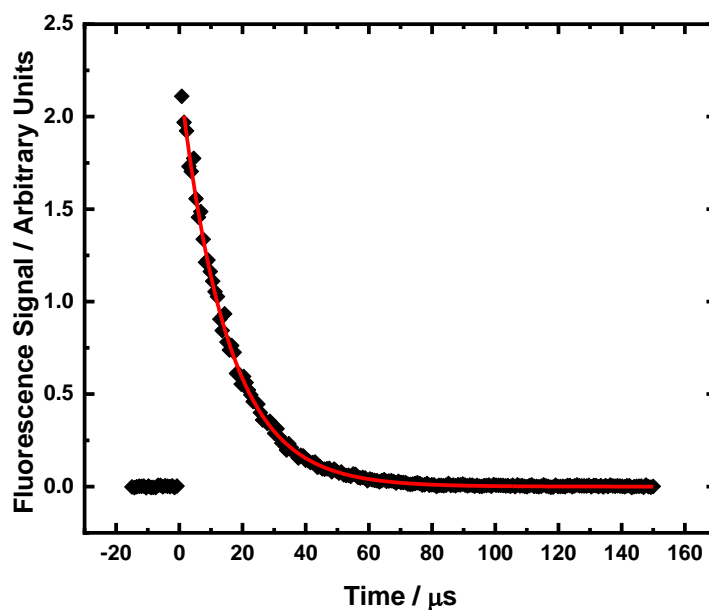


Figure 6.6 Observed OH fluorescence signal in the presence of excess 2,5-DMF at 298 K and 50 Torr, $[2,5\text{-DMF}] = 1.4 \times 10^{14} \text{ cm}^3 \text{ molecule}^{-1}$. Black squares are experimental data, red line is the exponential fit E6.1. From E6.1, $k' = (14700 \pm 130) \text{ s}^{-1}$. $(\text{CH}_3)_3\text{COOH}$ used as OH precursor.

6.3 Results and Discussion

6.3.1 Kinetics at 298 K

Experiments were performed at room temperature between 20 and 150 Torr. At least two experiments were carried out at each pressure and rate coefficients reported here are averages, with the exception of 125 Torr where only one experiment was performed.

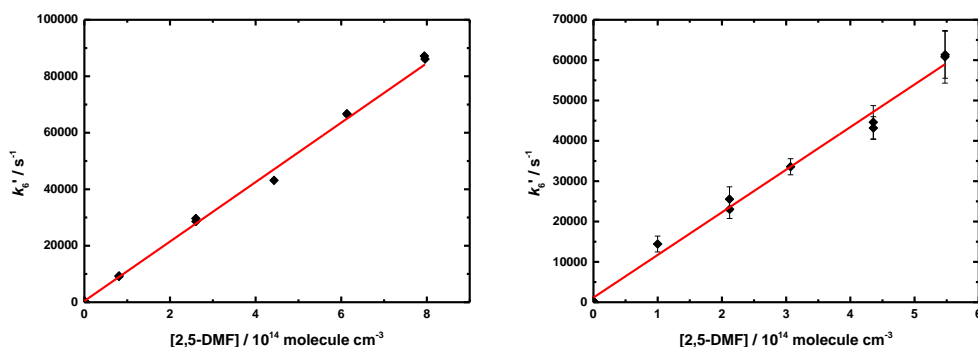


Figure 6.7 Bimolecular plots for the reaction of OH + 2,5-DMF at 298 K. Left plot is at 20 Torr, the slope of which gives $k = (1.08 \pm 0.10) \times 10^{-10} \text{ cm}^3 \text{ molecule}^{-1} \text{ s}^{-1}$ and the intercept is $(352 \pm 63) \text{ s}^{-1}$. Right plot is at 150 Torr, the slope of which gives $k = (1.07 \pm 0.10) \times 10^{-10} \text{ cm}^3 \text{ molecule}^{-1} \text{ s}^{-1}$ and the intercept is $(257 \pm 11) \text{ s}^{-1}$. Note some 1σ error bars are smaller than symbols. $(\text{CH}_3)_3\text{COOH}$ (left) and H_2O_2 (right) precursors used.

Figure 6.7 shows two examples of bimolecular plots for the reaction of OH + 2,5-DMF at 298 K. At the lowest pressure investigated, 20 Torr (6.48×10^{17} molecule cm^{-3}), the rate coefficient was determined to be $k = (1.20 \pm 0.10) \times 10^{-10}$ cm^3 molecule $^{-1}$ s $^{-1}$. For the highest pressure of 150 Torr (4.86×10^{18} molecule cm^{-3}) the rate coefficient was determined to be $k = (1.11 \pm 0.10) \times 10^{-10}$ cm^3 molecule $^{-1}$ s $^{-1}$. These are within error of both the studies in the literature which were performed close to atmospheric pressure. At 298 K the reaction thus appears to be at, or close to, the high-pressure limit at the pressures investigated. The average rate coefficient for OH + 2,5-DMF over all pressures studied at 298 K is $k = (1.14 \pm 0.11) \times 10^{-10}$ cm^3 molecule $^{-1}$ s $^{-1}$. Errors in the bimolecular rate coefficients arise from statistical error when fitting E6.1 to the data to find k' and from the line of best fit when finding k from $[2,5\text{-DMF}]$ vs k' . The results are shown in Figure 6.8. At 75 Torr the average rate coefficient is $(1.15 \pm 0.15) \times 10^{-10}$ cm^3 molecule $^{-1}$ s $^{-1}$ with an error of standard deviation arising from scatter in the data.

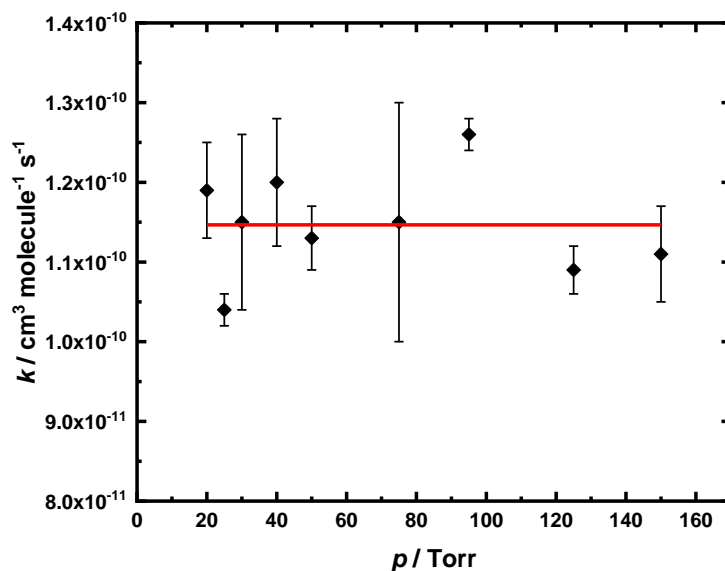


Figure 6.8 Effect of pressure on the rate coefficient for OH + 2,5-DMF at 298 K. Black diamonds are averages rate coefficients at each pressure. Red line shows the average of the data points. Error bars are 1σ . A mixture of H_2O_2 and $(\text{CH}_3)_3\text{COOH}$ precursors were employed.

In order to investigate the potential photolysis had on the reaction, the amount of light in the photolysis beam was reduced by the introduction of mesh filters. The filters reduced

the amount of light in the photolysis beam to 10, 25 and 50 %. As demonstrated in Figure 6.9, there was no significant change in the rate coefficient of the OH + 2,5-DMF reaction by any of the filters applied. Rate coefficients can be seen in Table 6.3.

Laser Power Percentage / %	$k / 10^{11} \text{ cm}^3 \text{ molecule}^{-1} \text{ s}^{-1}$
100	1.35 ± 0.03
50	1.34 ± 0.04
25	1.45 ± 0.03
10	1.28 ± 0.03

Table 6.3 Rate coefficients for OH + 2,5-DMF at 410 K and 50 Torr with mesh filters applied to the photolysis laser beam. 100 % laser power $\sim 60 \text{ mJ cm}^{-2}$ fluence.

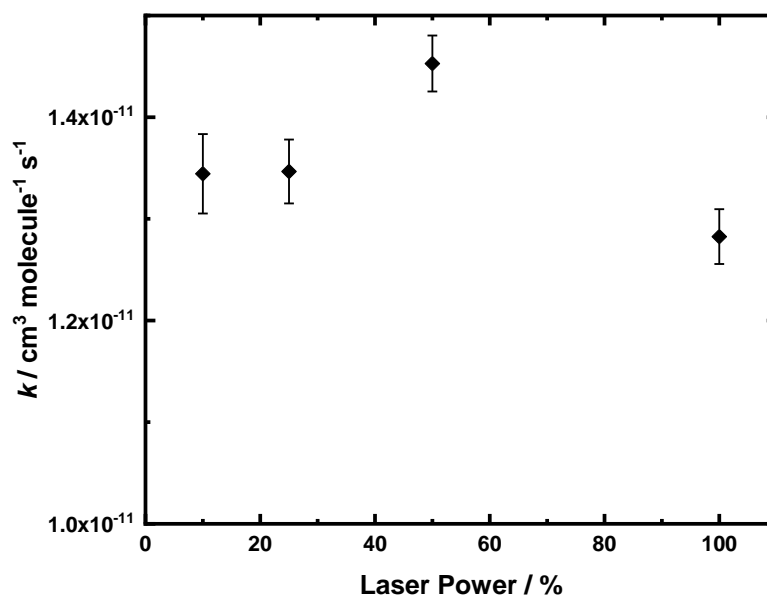


Figure 6.9 Bimolecular rate coefficients for the reaction of OH + 2,5-DMF at 410 K and 50 Torr with mesh filters applied. 100 % laser power $\sim 60 \text{ mJ cm}^{-2}$ fluence.

To rule out a dependence on the concentration of oxygen present in the system, experiments were carried out at several temperatures (298, 500 and 635 K), pressures (20, 50 and 90 Torr) and oxygen concentrations from 0 to $4.50 \times 10^{16} \text{ molecule cm}^{-3}$. No significant dependence on oxygen was found at the temperatures or pressures studied, one example is shown in Figure 6.10 and demonstrates that the rate coefficient changes

insignificantly with an increase of oxygen concentration. The lack of O₂ effects shown in this work demonstrates that no recycling of OH radicals takes place during this reaction under the experimental conditions investigated.

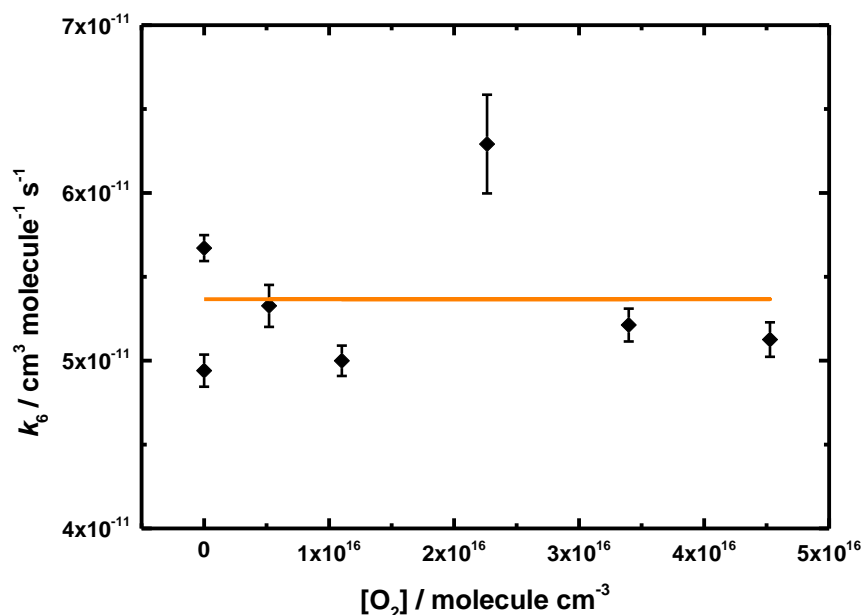


Figure 6.10 OH + 2,5-DMF in the presence of N₂ and O₂ at 635 K, 50 Torr. Orange line indicates an average value of $k = (5.37 \pm 0.47) \times 10^{-11} \text{ cm}^3 \text{ molecule}^{-1} \text{ s}^{-1}$.

2,5-DMF oxidation has received some attention previously in the literature. A comparison of this work with former studies show the average rate coefficient measured for the reaction of OH + 2,5-DMF during this investigation, $k = (1.11 \pm 0.11) \times 10^{-10} \text{ cm}^3 \text{ molecule}^{-1} \text{ s}^{-1}$ (Figure 6.11). These results are in good agreement with the rate coefficient reported by Bierbach *et al.* $k = (1.25 \pm 0.05) \times 10^{-10} \text{ cm}^3 \text{ molecule}^{-1} \text{ s}^{-1}$ and Aschmann *et al.* $k = (1.32 \pm 0.10) \times 10^{-10} \text{ cm}^3 \text{ molecule}^{-1} \text{ s}^{-1}$. Results are not within error of the work by Eble, $k = (9.20 \pm 0.40) \times 10^{-11} \text{ cm}^3 \text{ molecule}^{-1} \text{ s}^{-1}$ with an 18.7 % percentage difference.

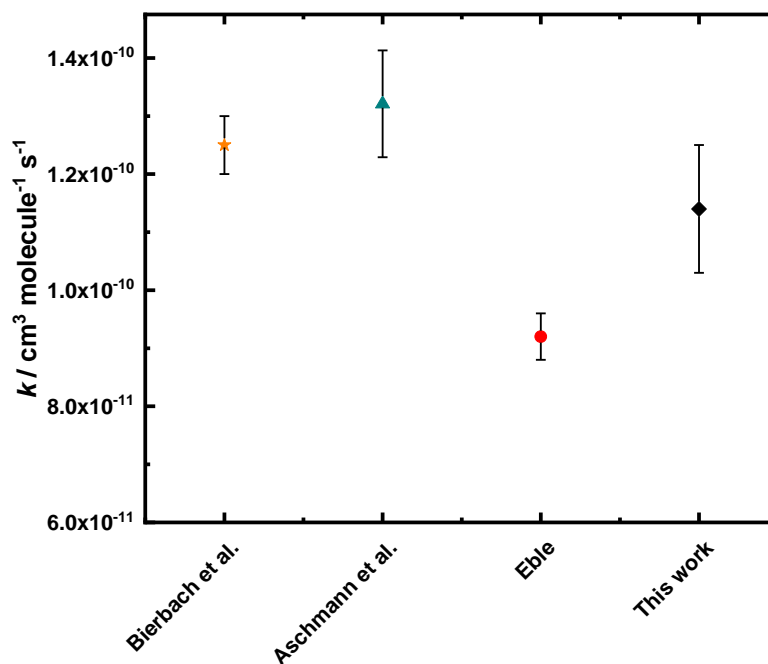


Figure 6.11 Literature room temperature rate coefficients for OH + 2,5-DMF with results from this work.

6.3.2 Effects of Pressure and Temperature

A detailed investigation into the pressure dependence of OH + 2,5-DMF has been carried out at several temperatures (298-635 K). Rate coefficients were measured over pressures between 20 and 150 Torr in N_2 . At 298 K the reaction did not display any significant pressure dependence over the experimental pressure range investigated and appears to be at, or close to, the high pressure limit. At temperatures of 410 K and above, the rate coefficient for OH + 2,5-DMF does display significant dependence on pressure. Figure 6.12 shows the rate coefficients at 410 K which increase from a value of $k = (5.15 \pm 0.20) \times 10^{-11} \text{ cm}^3 \text{ molecule}^{-1} \text{ s}^{-1}$ at 20 Torr ($4.71 \times 10^{17} \text{ molecules cm}^{-3}$) to $k = (6.83 \pm 0.14) \times 10^{-11} \text{ cm}^3 \text{ molecule}^{-1} \text{ s}^{-1}$ at 150 Torr ($3.53 \times 10^{18} \text{ molecules cm}^{-3}$).

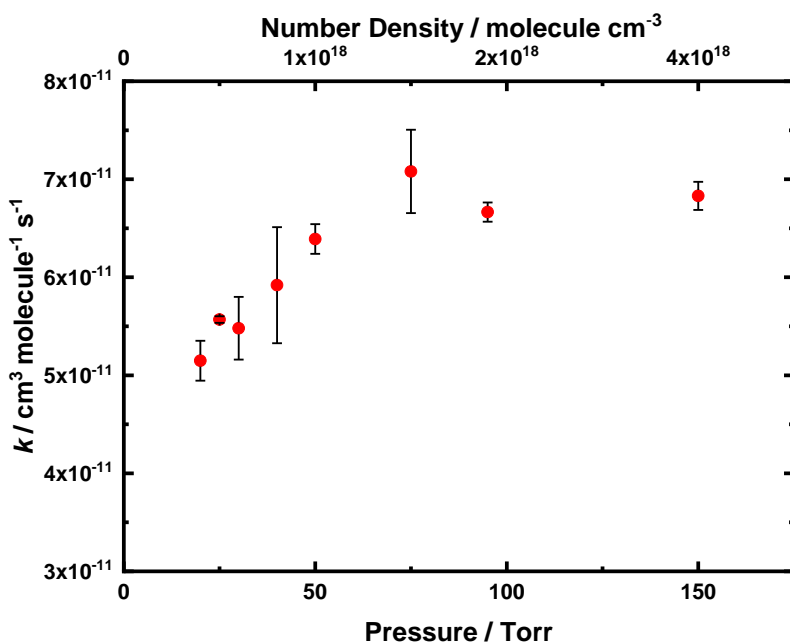


Figure 6.12 Effect of pressure on the rate coefficient for OH + 2,5-DMF at 410 K. Error bars are 1σ . Note some error bars are smaller than symbols.

The chemistry of pressure-dependent kinetics has been described in Chapter 2. A description of the ‘fall-off’ region in pressure dependent kinetics was formulated by Troe²⁹ based on the Lindemann unimolecular fall-off. The Troe formula is a simplified parameterisation of pressure and temperature dependence:

$$k = \left(\frac{k_0(T)[M]}{1 + \frac{k_0(T)[M]}{k_\infty(T)}} \right) F_c \left\{ 1 + \left[\log_{10} \left(\frac{k_0(T)[M]}{k_\infty(T)} \right) \right] \right\}^{-1} \quad \text{E6.2}$$

where k is the bimolecular rate coefficient and F_c is the broadening factor. In this instance, F_c is fixed at a typical value of 0.6.³⁰ k_0 is the low-pressure limit rate coefficient and k_∞ is the high-pressure limit rate coefficient, which can be described by the Arrhenius expressions:

$$k_0 = A_0 \exp(-E_{a0}/RT) \quad \text{E6.3}$$

$$k_\infty = A_\infty \exp(-E_{a\infty}/RT) \quad \text{E6.4}$$

Figure 6.13 shows the fitting of the Lindemann and Troe forms to the data from this work at 550 K over pressures from 20 Torr (3.51×10^{17} molecules cm^{-3}) to 150 Torr (2.63

$\times 10^{18} \times 10^{18}$ molecules cm^{-3}). The fits are very similar, indicating the chosen F_c value is appropriate and that the Troe fit of E6.2 is not sensitive to the broadening factor. Both IUPAC⁴ and JPL³¹ use the Troe expression to report pressure dependent kinetics therefore it will be used to describe pressure-dependent kinetics throughout this chapter.

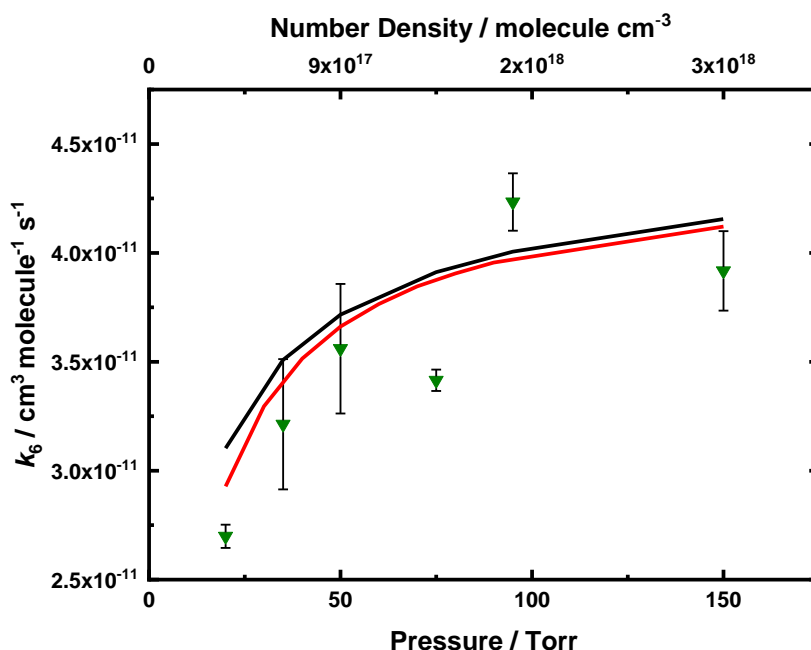


Figure 6.13 Troe (E6.2, black line) and Lindemann (E2.33-E2.36, red line) equations fitted to data at 550 K over pressures from 20 Torr (3.51×10^{17} molecule cm^{-3}) to 150 Torr (2.63×10^{18} molecule cm^{-3}) in N_2 .

A large data set has been measured and a plot of the rate coefficients for the reaction at several temperatures (298-635 K) is shown as a function of pressure (20-150 Torr) in Figure 6.14. Results are tabulated in the appendix of this chapter. E6.2 was fit to the data and Arrhenius parameters were determined as follows: $A_0 = (2.80 \pm 1.60) \times 10^{-29} \text{ cm}^6 \text{ molecule}^{-1} \text{ s}^{-1}$, $E_{a0}/R = (-1930 \pm 220) \text{ K}$, $A_\infty = (1.50 \pm 0.10) \times 10^{-11} \text{ cm}^3 \text{ molecule}^{-1} \text{ s}^{-1}$ and $E_{a\infty}/R = (-640 \pm 24) \text{ K}$. Figure 6.15 shows the observed rate coefficients at individual temperatures.

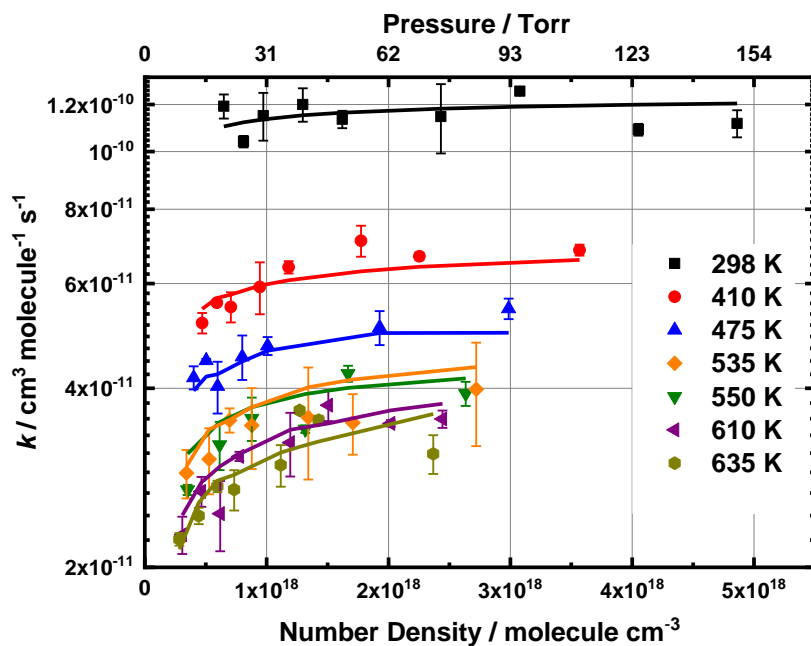
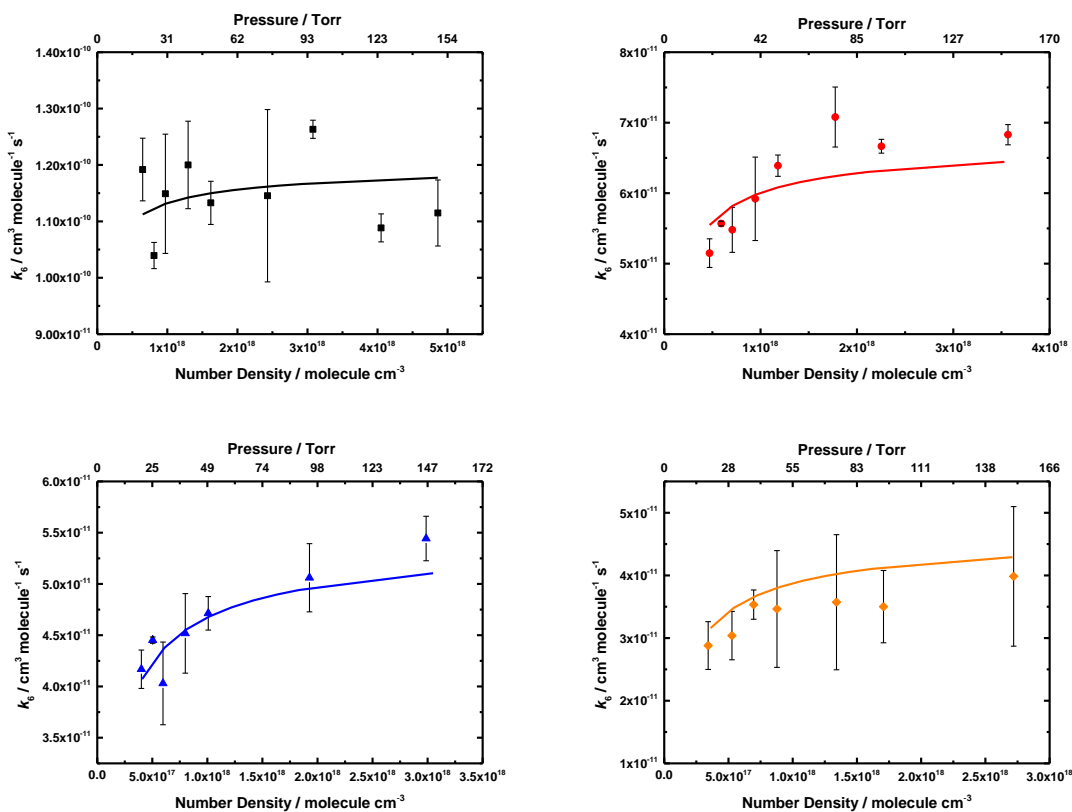


Figure 6.14 Bimolecular rate coefficients for OH + 2,5-DMF at 298 K (■), 410 K (●), 475 K (▲), 535 K (◆), 550 K (▼), 610 K (◄) and 635 K (◐) in N_2 at pressures between 20 and 150 Torr. Solid lines show the fit to E6.2. Error bars are 1σ . Note some error bars are smaller than symbols.



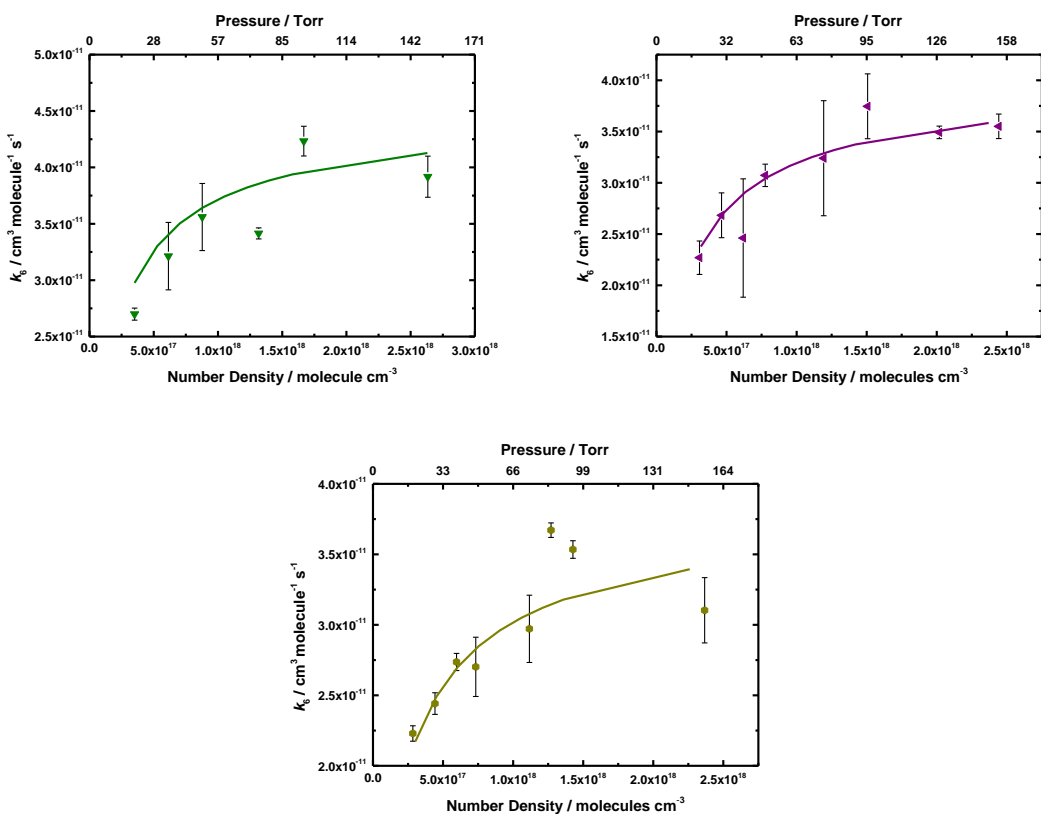


Figure 6.15 Plots showing the bimolecular rate coefficients for OH + 2,5-DMF at 298 K (■), 410 K (●), 475 K (▲), 535 K (◆), 550 K (▼), 610 K (◆) and 635 K (●) in N₂ at pressures between 20 and 150 Torr. Solid lines show the fit to E6.2. Error bars are 1σ. Note some error bars are smaller than symbols.

A comparison of the Troe parameterised rate coefficients to the observed experimental results is shown in Figure 6.16. The slope was determined as 0.90 ± 0.02 and the intercept as $(3.60 \pm 0.97) \times 10^{-12} \text{ cm}^3 \text{ molecule}^{-1} \text{ s}^{-1}$.

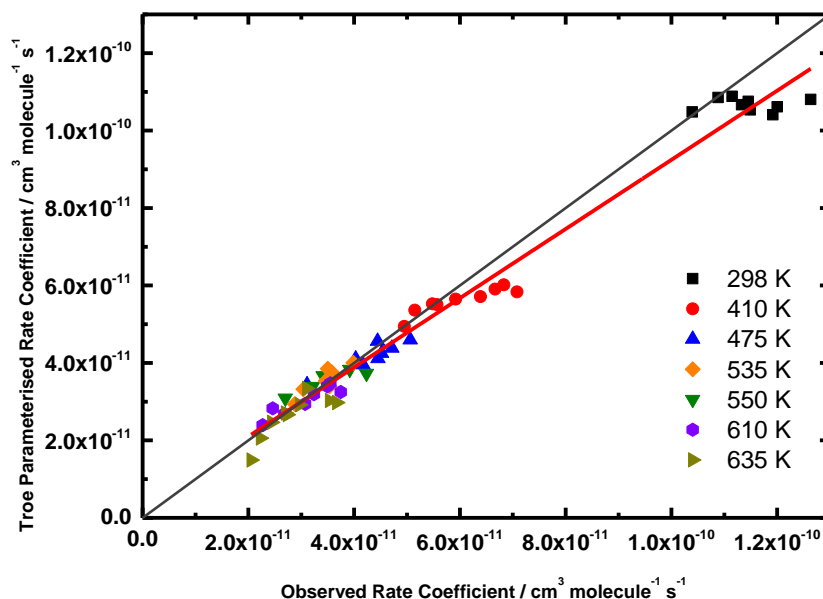


Figure 6.16 Comparison of rate coefficients determined from Troe parameterisation of data with the observed rate coefficients from experimental data. The slope was determined as 0.90 ± 0.02 and the intercept as $(3.60 \pm 0.97) \times 10^{-12} \text{ cm}^3 \text{ molecule}^{-1} \text{ s}^{-1}$.

Temperature dependent kinetics arise from the change in energy in a reaction system due to a variation in temperature, resulting in a changing rate coefficient. As previously seen in the results of OH + furan in Chapter 4 and OH + 2-MF in Chapter 5, the results from this study found the reaction of OH + 2,5-DMF to have a negative temperature dependence. For a specific pressure, the rate coefficient was found to slow with an increase in temperature.

From the Arrhenius equation, E6.5, the high pressure limit rate coefficient, k_∞ , was calculated using the pre-exponential factor, A_∞ , and activation energy, $E_{a\infty}$, from the Troe expression, E11. A fit to the results from this work were compared to the temperature dependent work by Eble which was shown to have no pressure dependence over 2-10 bar (1500-7500 Torr) and thus assumed to be at the high pressure limit. Results can be seen in Table 6.4.

$$k = A \exp\left(-\frac{E_a}{RT}\right)$$

E6.5

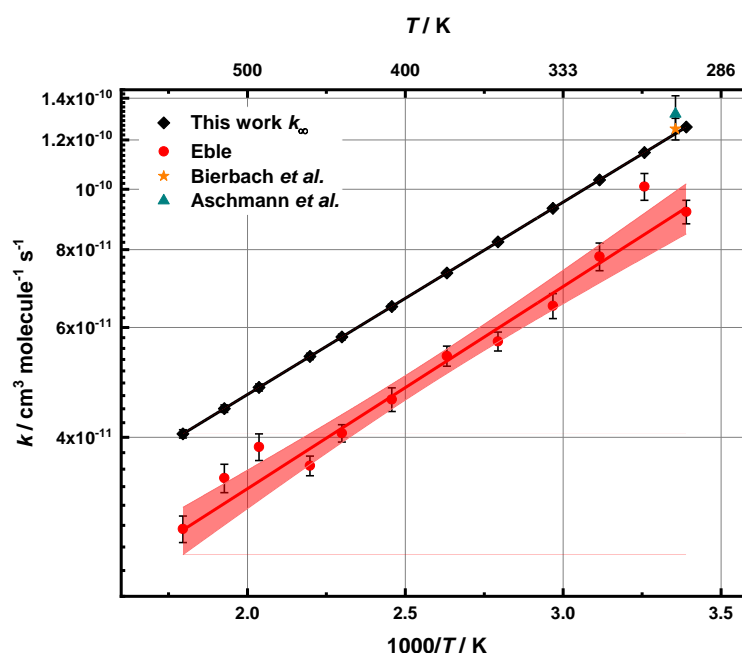


Figure 6.17 Arrhenius plot of this work (k_{∞} , black diamonds) and Eble (red circles) with Arrhenius fit to data, this work (black line) and Eble (red line) with 95 % confidence limits. Arrhenius parameters are shown in Table 6.4.

Study	Temperature Range / K	$A / 10^{-12} \text{ cm}^3$ $\text{molecule}^{-1} \text{ s}^{-1}$	$-E_a/R / \text{K}$
Eble	295-557	7.42 ± 0.85	747 ± 44
This work	298-770	11.3	711

Table 6.4 Comparison of Arrhenius parameters for the reaction of OH + 2,5-DMF between this work and Eble. Fit to the k_{∞} of this work means errors are significantly smaller than parameters and so are omitted here.

When compared to the work by Eble, results from Arrhenius parameters for this work give a faster rate coefficient as there is disagreement of the pre-exponential factor, A , between the two studies, with a 34.3 % difference. This is unsurprising, as the room temperature rate coefficients were also not in agreement. However, there is good agreement between the activation energies of the two studies.

Figure 6.18 shows the results of this work and those of Elwardany *et al.* and shows there are two clear temperature regimes governing the kinetics of the reaction. The Elwardany *et al.* study exhibits a positive temperature dependence from 915-1278 K, whereas results from this work display a negative dependence from 298-635 K.

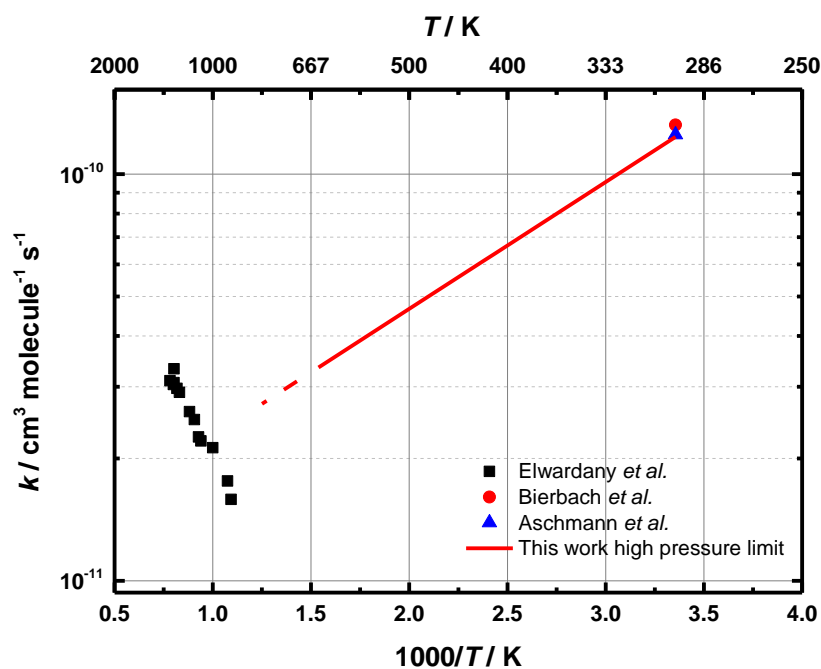


Figure 6.18 Dependence of k upon temperature for the reaction of OH + 2,5-DMF. Black squares represent Elwardany *et al.* data for high-temperature (915-1278 K) shock tube experiments, red circle represents Bierbach *et al.* at 298 K, blue triangle represents Aschmann *et al.* at 298 K, red line represents high-pressure limit rate coefficient from this work, determined from the parameterisation of E18.

The chemistry of the reaction between OH radicals and 2,5-DMF, as described previously, can occur *via* the addition of the radical to the furan ring, or by the abstraction of an H atom from the C1 methyl or C3 carbon. The decreasing rate coefficient in the low-temperature region corresponds to a barrierless addition process. The increasing rate coefficient in the high-temperature region corresponds to abstraction processes, where there is sufficient energy in the system to break bonds.

In order to fit both temperature data sets, the double modified Arrhenius expression is used:

$$k = A_1 \exp\left(\frac{-E_{a1}}{RT}\right) + A_2 \exp\left(\frac{-E_{a2}}{RT}\right) \quad \text{E6.6}$$

The fit of E6.6 to the data from this work and Elwardany *et al.* can be seen in

Figure 6.19 Rate coefficients for OH + 2,5-DMF from this work at $T = 298\text{-}635$ K at the high-pressure limit parameterised from E6.4, Elwardany *et al.* at $T = 915\text{-}1278$ K and $p = 1.2\text{-}1.7$ atm and Aschmann *et al.* and Bierbach *et al.* at 298 K and atmospheric pressure. Black line shows fit to E6.6 with 95 % confidence limits in red. The fit does not include the two slowest data points for the Elwardany *et al.* data due to the steep rate coefficient increase from 915 to 1278 K.

. Figure 6.20 shows the fit of E6.6 to the work of Eble and Elwardany *et al.* and the fit of all three data sets. Parameters from the fits can be seen in Table 6.5.

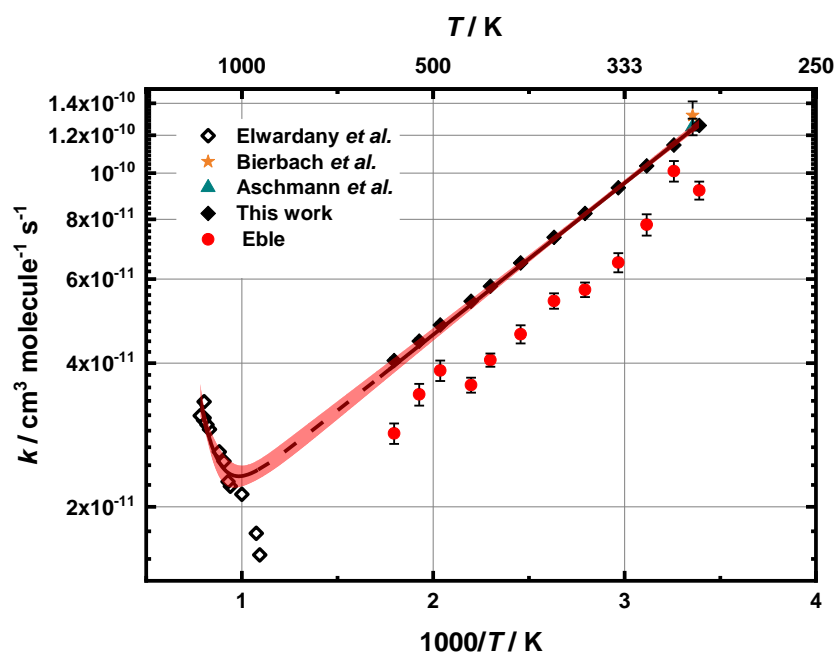


Figure 6.19 Rate coefficients for OH + 2,5-DMF from this work at $T = 298\text{-}635$ K at the high-pressure limit parameterised from E6.4, Elwardany *et al.* at $T = 915\text{-}1278$ K and $p = 1.2\text{-}1.7$ atm and Aschmann *et al.* and Bierbach *et al.* at 298 K and atmospheric pressure. Black line shows fit to E6.6 with 95 % confidence limits in red. The fit does not include the two slowest data points for the Elwardany *et al.* data due to the steep rate coefficient increase from 915 to 1278 K.

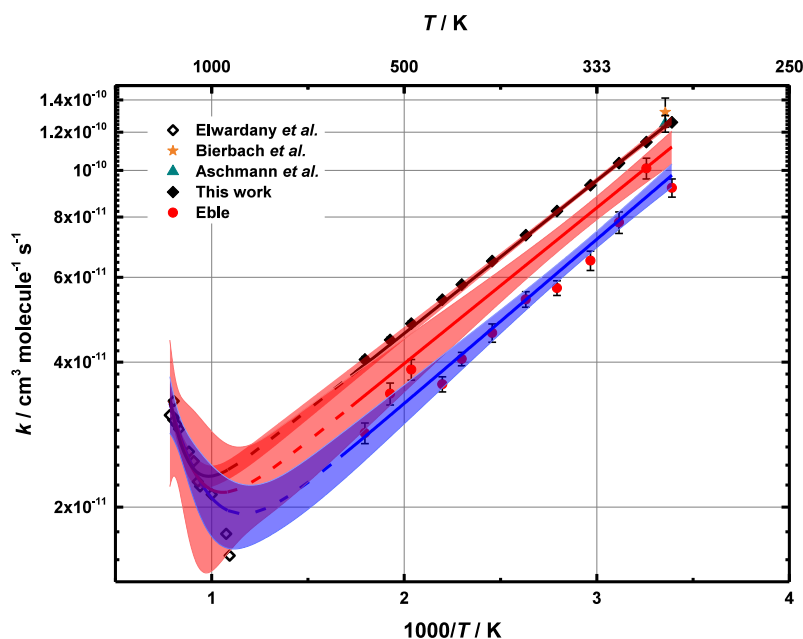


Figure 6.20 The effect of temperature on k for OH + 2,5-DMF. Results from this work (black solid diamonds), Eble (red circles) and Elwardany *et al.* (open black diamonds). Fit to E6.6 to the combined data from this work and Elwardany *et al.* (black line) and from this work, Eble and Elwardany *et al.* (red line) and Eble and Elwardany *et al.* (blue line).

Parameter	This work & Elwardany <i>et al.</i>	This work, Eble & Elwardany <i>et al.</i>	Eble & Elwardany <i>et al.</i>
$A_1 / \text{cm}^3 \text{s}^{-1}$	1.06×10^{-11}	8.96×10^{-12}	6.82×10^{-12}
n_1	0	0	0
$E_{a1}/R / \text{K}$	-731	-744	-785
$A_2 / \text{cm}^3 \text{s}^{-1}$	1.58×10^{-7}	1.09×10^{-8}	1.68×10^{-9}
n_2	0	0	0
$E_{a2}/R / \text{K}$	11870	8246	5644

Table 6.5 Arrhenius parameters from the fit of E6.6 to the combined data from this work and Elwardany *et al.* and from this work, Eble and Elwardany *et al.*

The n factor, which typically describes the curvature of data on an Arrhenius plot, for both parts of the E6.6 equation has been fixed at 0 in order to adequately fit to the data sets which are linear in Figure 6.19. As there is disagreement between the pre-exponential factor, A , between the results from this work and that of Eble (Table 6.4)

there were some issues fitting E6.6 to the complete data set, therefore only the fit to this work and Elwardany *et al.* will be discussed further in this thesis.

When the E6.6 fit to this work and Elwardany *et al.* are compared to models available in the literature, shown in Figure 6.21, it is clear that the lack of low temperature data is contributing significantly to the under prediction, or in the case of Somers *et al.*, over prediction, of the rate coefficients at these lower temperatures. These discrepancies between modelled and observed rate coefficients can be accounted for somewhat, Elwardany *et al.* and Simmie *et al.* do not consider low-temperature rate coefficients found in the literature in their fittings, and Somers *et al.* calculation for the OH-addition only accounts for theoretical rate coefficients for temperatures above 600 K.

However, although several published studies^{2,32-34} report a rate coefficient for OH + furan that is slower than those reported and described previously for OH + 2,5-DMF, the model by Togbé *et al.* agrees well with the E6.6 fit. The model is based on the addition reaction of OH radicals with furan at 298 K according to the review by Atkinson *et al.*²⁷

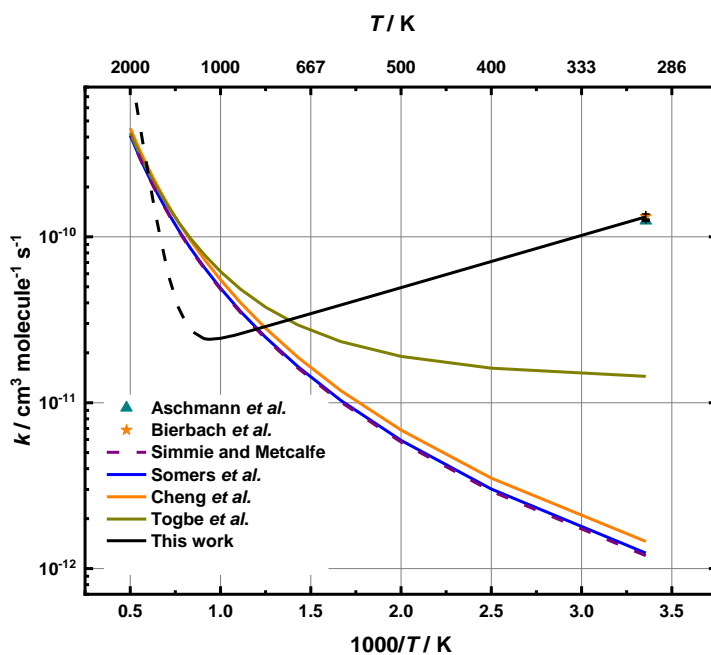


Figure 6.21 Comparison of the E6.6 fit to this work and Elwardany *et al.* (black line) and the models from the literature (key inset).

6.3.3 Reactivity of Furans with OH

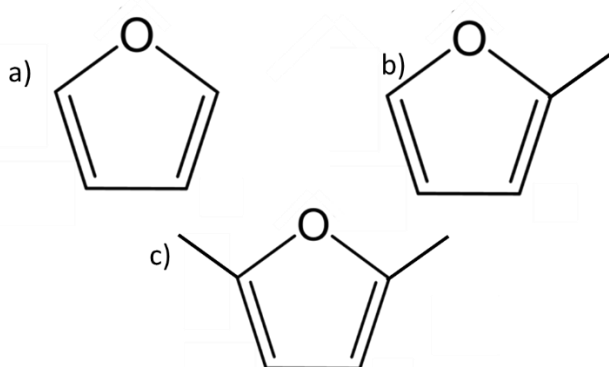


Figure 6.22 Structures of furan (a), 2-MF (b) and 2,5-DMF (c).

The effect of resonance stabilisation governs which carbon of the furan ring (Figure 6.22) the OH radical will primarily react with, as previously described in Chapter 4. Evidence of the effect of resonance stabilisation can be observed in the rate coefficients reported by Bierbach *et al.*² for the OH addition of furan, 2-MF, 2-EF and 2,5-DMF and Aschmann *et al.*⁵ for the OH addition of 2-MF, 3-MF, 2,3-DMF and 2,5-DMF. In the reaction of OH

radicals with 2-MF, the preferred reaction site is occupied, and a reduced rate could be expected. However, the rate coefficient increases in the alkylated furan, due to the inductive effect of the methyl group which enhances the reactivity of the furan ring towards the OH radical. This inductive effect increases with alkylation and 2,5-DMF results in the fastest rate of reaction with OH radicals due to two methyl groups pushing electron density into the ring. In the reactions where the favoured reaction site, C2, is blocked by a substituent group (2-MF and 2,5-DMF), the observed rate coefficient is slower than in the reactions where the C3 position is blocked.

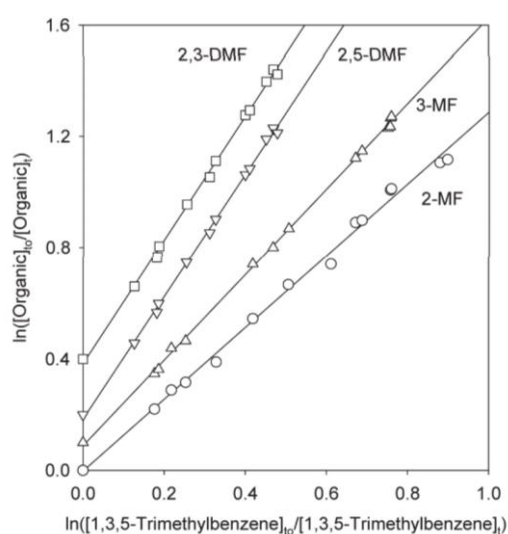


Figure 6.23 Plots for the reaction of OH radicals with 2-methylfuran (2-MF), 3-methylfuran (3-MF), 2,3-dimethylfuran (2,3-DMF), and 2,5-dimethylfuran (2,5-DMF), with 1,3,5-trimethylbenzene as the reference compound from Aschmann *et al.*⁵

This trend has been observed in the work carried out for this thesis and described in Chapters 4 and 5, where the room temperature rate coefficients for the reaction of OH with furan ($k_{\text{OH}+\text{furan}} = (3.58 \pm 0.74) \times 10^{-11} \text{ cm}^3 \text{ molecule}^{-1} \text{ s}^{-1}$), 2-MF ($k_{\text{OH}+2\text{-MF}} = (7.61 \pm 0.14) \times 10^{-11} \text{ cm}^3 \text{ molecule}^{-1} \text{ s}^{-1}$) and 2,5-DMF ($k_{\text{OH}+2,5\text{-DMF}} = (1.10 \pm 0.15) \times 10^{-10} \text{ cm}^3 \text{ molecule}^{-1} \text{ s}^{-1}$) increase with the increase in alkyl substituted groups on the furan ring. Similar trends are observed across the full temperature range investigated (Figure 6.24).

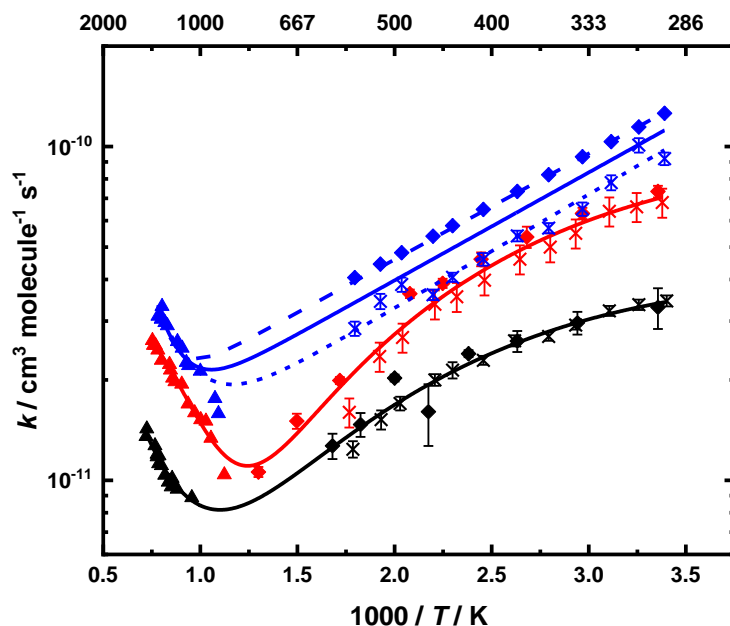


Figure 6.24 Temperature dependence across full temperature range of OH radical reaction rate coefficients with furan (black), 2-MF (red) and 2,5-DMF (blue) from this work (diamonds), Eble (crosses) and Elwardany *et al.* (triangles). Solid lines are the double modified Arrhenius fit E6.6 to all data sets, dashed line this work and Elwardany *et al.* and dotted like Eble and Elwarday *et al.*

6.4 Conclusion

The kinetics of the reaction OH + 2,5-DMF have been investigated in the pressure range 20-150 Torr and at temperatures between 298 K and 635 K relevant to low-temperature combustion. The study was carried out using laser flash photolysis-laser induced fluorescence (LFP-LIF). Measurements above 298 K are the first to be conducted in low-temperature conditions (<1000 K), additionally, this is the first investigation into the pressure dependence of this reaction at these temperatures.

The average room temperature rate coefficient, $k = (1.14 \pm 0.11) \times 10^{-10} \text{ cm}^3 \text{ molecule}^{-1} \text{ s}^{-1}$, is within the uncertainties of the rate coefficients reported by Bierbach *et al.*², $k = (1.32 \pm 0.10) \times 10^{-10} \text{ cm}^3 \text{ molecule}^{-1} \text{ s}^{-1}$ and Aschmann *et al.*⁵, $k = (1.25 \pm 0.10) \times 10^{-10} \text{ cm}^3 \text{ molecule}^{-1} \text{ s}^{-1}$. However, the results are not in agreement with Eble, $k = (9.20 \pm 0.40) \times 10^{-11} \text{ cm}^3 \text{ molecule}^{-1} \text{ s}^{-1}$.

At room temperature, the average rate coefficient for this work is at, or close to, the high-pressure limit. Results show a clear pressure dependence for reactions carried out at 410 K and above, that can be well described by the Troe formulation.

Additionally, results show there is a negative temperature dependence for the reaction of OH + 2,5-DMF over temperatures between 298 K to 635 K, with $E_{a0}/R = (-2379 \pm 262)$ K and $E_{a\infty}/R = (-489 \pm 29)$ K. This temperature dependence is consistent with previous studies into the oxidation of alkenes by the OH radical.

Results from this work provide the most detailed kinetics of 2,5-DMF oxidation at $T < 1000$ K to date, that can be applied to combustion models to aid fuel and engine development, which currently underestimate the experimental rate coefficients of low temperature combustion of 2,5-DMF by several orders of magnitude.

6.5 References

1. Qian, Y., *et al.* Recent progress in the development of biofuel 2,5-dimethylfuran. *Renewable and Sustainable Energy Reviews*, 2015, **41**, pp.633-646.
2. Bierbach, A., I. Barnes and K.H. Becker. Rate coefficients for the gas-phase reactions of hydroxyl radicals with furan, 2-methylfuran, 2-ethylfuran and 2,5-dimethylfuran at 300 K. *Atmospheric Environment Part a-General Topics*, 1992, **26**(5), pp.813-817.
3. Atkinson, R. Gas-phase tropospheric chemistry of organic compounds: A review. *Atmospheric Environment. Part A. General Topics*, 1990, **24**(1), pp.1-41.
4. IUPAC Task Group on Atmospheric Chemical Kinetic Data Evaluation – Data Sheet HOx_VOC64. 2009.
5. Aschmann, S.M., *et al.* Kinetics of the Reactions of OH Radicals with 2- and 3-Methylfuran, 2,3- and 2,5-Dimethylfuran, and E- and Z-3-Hexene-2,5-dione, and Products of OH + 2,5-Dimethylfuran. *Environmental Science & Technology*, 2011, **45**(5), pp.1859-1865.
6. Atkinson, R. and J. Arey. Atmospheric Degradation of Volatile Organic Compounds. *Chemical Reviews*, 2003, **103**(12), pp.4605-4638.
7. Ohta, T. and T. Ohyama. A set of rate constants for the reactions of OH radicals with aromatic hydrocarbons. *Bulletin of the Chemical Society of Japan*, 1985, **58**(10), pp.3029-3030.
8. Alarcón, P., B. Bohn and C. Zetzsch. Kinetic and mechanistic study of the reaction of OH radicals with the methylated benzenes: 1,4-dimethyl-, 1,3,5-trimethyl-, 1,2,4,5-, 1,2,3,5- and 1,2,3,4-tetramethyl-, pentamethyl-, and hexamethylbenzene. *Physical Chemistry Chemical Physics*, 2015, **17**(19), pp.13053-13065.
9. Eble, J.S.R. *Ignition of oxygenated hydrocarbons: Mechanism and elementary steps*. thesis, Karlsruhe Institute of Technology (KIT), 2017.
10. Elwardany, A., *et al.* A chemical kinetic study of the reaction of hydroxyl with furans. *Fuel*, 2016, **166**, pp.245-252.

11. Aschmann, S.M., *et al.* Products of the OH Radical-Initiated Reactions of Furan, 2-and 3-Methylfuran, and 2,3-and 2,5-Dimethylfuran in the Presence of NO. *Journal of Physical Chemistry A*, 2014, **118**(2), pp.457-466.
12. Scheer, A.M., *et al.* Low-temperature combustion chemistry of novel biofuels: resonance-stabilized QOOH in the oxidation of diethyl ketone. *Physical Chemistry Chemical Physics*, 2014, **16**(26), pp.13027-13040.
13. Simmie, J.M. and W.K. Metcalfe. Ab Initio Study of the Decomposition of 2,5-Dimethylfuran. *The Journal of Physical Chemistry A*, 2011, **115**(32), pp.8877-8888.
14. A complete basis set model chemistry. VII. Use of the minimum population localization method. *The Journal of Chemical Physics*, 2000, **112**(15), pp.6532-6542.
15. A complete basis set model chemistry. V. Extensions to six or more heavy atoms. *The Journal of Chemical Physics*, 1996, **104**(7), pp.2598-2619.
16. Gaussian-3 (G3) theory for molecules containing first and second-row atoms. *The Journal of Chemical Physics*, 1998, **109**(18), pp.7764-7776.
17. Gaussian-3 theory using density functional geometries and zero-point energies. *The Journal of Chemical Physics*, 1999, **110**(16), pp.7650-7657.
18. Barker, J.R. Multiple-Well, multiple-path unimolecular reaction systems. I. MultiWell computer program suite. *International Journal of Chemical Kinetics*, 2001, **33**(4), pp.232-245.
19. Somers, K.P., *et al.* A comprehensive experimental and detailed chemical kinetic modelling study of 2,5-dimethylfuran pyrolysis and oxidation. *Combustion and Flame*, 2013, **160**(11), pp.2291-2318.
20. J. A. Montgomery Jr, M.J.F., J. W. Ochterski, G. A. Petersson. A complete basis set model chemistry. VII. Use of the minimum population localization method. *The Journal of Chemical Physics*, 2000, **112**(15), pp.6532-6542.
21. Ochterski, J.W., G.A. Petersson and J.a.M. Jr. A complete basis set model chemistry. V. Extensions to six or more heavy atoms. 1996, **104**(7), pp.2598-2619.
22. Curtiss, L.A., *et al.* Gaussian-3 (G3) theory for molecules containing first and second-row atoms. 1998, **109**(18), pp.7764-7776.
23. Frisch, M., *et al.* Revision B. Gaussian. 2003.
24. M. J. Frisch, *et al.* Gaussian 09. 2009.
25. Togbé, C., *et al.* Combustion chemistry and flame structure of furan group biofuels using molecular-beam mass spectrometry and gas chromatography – Part III: 2,5-Dimethylfuran. *Combustion and Flame*, 2014, **161**(3), pp.780-797.
26. Kee, R.J., F.M. Rupley and J.A. Miller. *Chemkin-II: A Fortran chemical kinetics package for the analysis of gas-phase chemical kinetics*; Sandia National Labs., Livermore, CA (USA), 1989.
27. Atkinson, R. Kinetics and mechanisms of the gas-phase reactions of the hydroxyl radical with organic compounds under atmospheric conditions. *Chemical Reviews*, 1986, **86**(1), pp.69-201.
28. Cheng, Z., *et al.* Experimental and kinetic modeling study of 2,5-dimethylfuran pyrolysis at various pressures. *Combustion and Flame*, 2014, **161**(10), pp.2496-2511.
29. Troe, J. Theory of thermal unimolecular reactions at low pressures. I. Solutions of the master equation. *The Journal of Chemical Physics*, 1977, **66**(11), pp.4745-4757.
30. Troe, J. and V.G. Ushakov. Revisiting falloff curves of thermal unimolecular reactions. *The Journal of Chemical Physics*, 2011, **135**(5), p.054304.
31. Sander, S.P., *et al.* *Chemical Kinetics and Photochemical Data for Use in Stratospheric Modeling Supplement to Evaluation 12: Update of Key Reactions*. Evaluation Number 13. California Institute of Technology, Pasadena, California: NASA, 2000.

32. Wine, P.H. and R.J. Thompson. Kinetics of OH reactions with furan, thiophene, and tetrahydrothiophene. *International Journal of Chemical Kinetics*, 1984, **16**(7), pp.867-878.
33. Tuazon, E., *et al.* A study of the atmospheric reactions of 1,3-dichloropropene and other selected organochlorine compounds. *Archives of Environmental Contamination and Toxicology*, 1984, **13**(6), pp.691-700.
34. Atkinson, R., S.M. Aschmann and W.P.L. Carter. Kinetics of the reactions of O₃ and OH radicals with furan and thiophene at 298 ± 2 K. *International Journal of Chemical Kinetics*, 1983, **15**(1), pp.51-61.

Chapter 7 Interpretation of Experimental Results for OH + Furan and its Derivatives

Kinetic information obtained experimentally is often complemented by theoretical calculations which allow detailed interpretation of experimental results and the prediction of rate coefficients under conditions that are difficult to obtain experimentally.

This chapter describes the use of energy grained master equation calculations, using the Master Equation Solver for Multi-Energy well Reactions (MESMER), to complement the experimental results described in Chapters 4-6. Since master equation calculations require knowledge of the potential energy surface for the reactions in question, and of the energies, vibrational frequencies and rotational constants for reactants, intermediates, products and transition states, brief details will be given regarding the determination of such details, followed by a description of MESMER, the results obtained for OH + furan, OH + 2-MF and OH + 2,5-DMF, and a comparison to the experimental results described previously.

7.1.1 Electronic Structure Calculations

Electronic structure calculations can be performed to provide the information regarding the energies, vibrational frequencies and rotational constants for the species involved in the potential energy surface for a reaction that is required for subsequent master equation calculations. Such calculations involve finding the solution to the Schrödinger equation (E7.1) for the system with the minimum total energy.

$$\mathbf{H}\Psi = E\Psi \quad \text{E7.1}$$

where H is the Hamiltonian operator, Ψ is the total wave function and E is the total energy.

In order to solve the Schrödinger equation, it is necessary to provide an initial guess for the wavefunction, which is often considered as a linear combination of the atomic orbitals (i.e. the atomic wavefunctions) centred on the nuclei within the species under

consideration. Such trial wavefunctions form the basis sets for electronic structure calculations, which can be approximated further by a linear combination of Gaussian functions which describe the atomic orbitals and reduce the computational expense of any subsequent calculations. Once an appropriate trial wavefunction has been found, it can be altered systematically to search for the minimum energy configuration for the species in question, thereby defining the energy and optimum geometry for that species and enabling determination of the relevant vibrational frequencies and rotational constants.

7.1.2 *Master Equation Calculations*

Master equation calculations involve the determination of microcanonical rate coefficients through the application of statistical rate theories, such as RRKM theory as described in Chapter 2. Analysis presented in this work uses the energy grained Master Equation Solver for Multi-Energy well Reactions (MESMER), in which the rovibrational energy states for each species, including reactants, products, intermediates and transition states, are partitioned into a number of “grains” which contain a defined number of states.

The energy grains are assigned populations, usually by invoking a Boltzmann distribution over the energy grains representing the reactants and zero populations for other species, with changes in the population distribution among grains possible through collisional energy transfer *via* interactions with a thermal bath gas or through reactions controlled by the microcanonical rate coefficients in the system which involve the transformation of one species to another. These processes are summarised in Chapter 2.

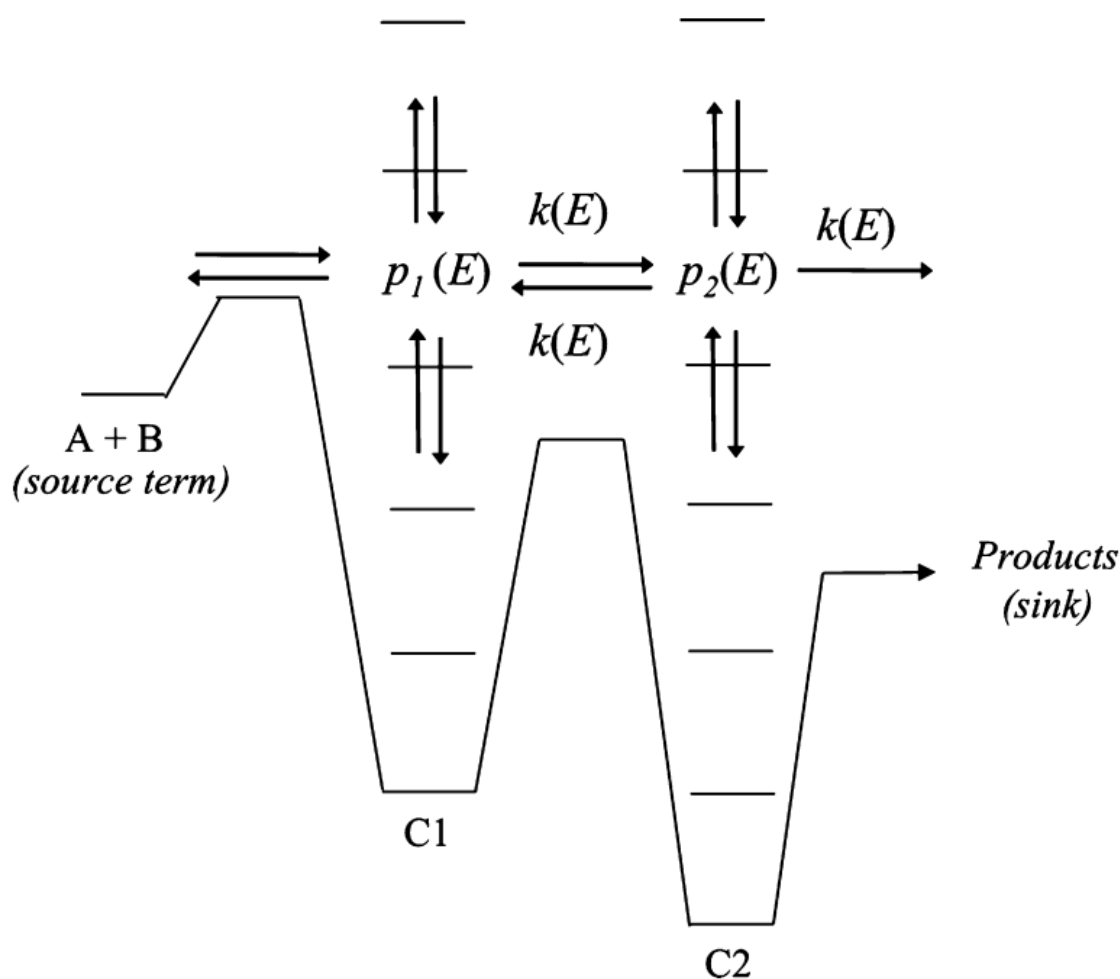


Figure 7.1 Model of the Energy Grained Master Equation for a typical reaction taken from Glowacki *et al.*¹

The reactive processes within the system are described by RRKM theory, while the collisional energy transfer is described by an exponential down model in which the average energy transferred between grains on collision is described by the parameter $\langle E \rangle_{\text{down}}$. The overall temperature and pressure dependent kinetics of the system can thus, in general, be described by the energy barriers to reaction, well depths, and the collisional energy transfer parameter $\langle E \rangle_{\text{down}}$. MESMER enables calculations of rate coefficients using defined potential energy surfaces and parameters such as $\langle E \rangle_{\text{down}}$, but also offers the ability to fine tune a given potential energy surface by fitting the barrier heights and $\langle E \rangle_{\text{down}}$ to experimental data.

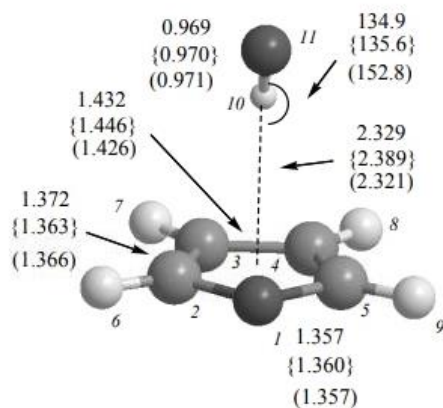
Potential energy surfaces for OH + furan and OH + 2-MF have been reported previously in the literature, and are used as the basis for MESMER calculations in this work. However, for OH + 2,5-DMF the full potential energy surface has yet to be reported. Therefore, electronic structure calculations were performed to determine the potential energy surface for OH + 2,5-DMF using the Gaussian 09 suite of programs at the M06-2x/cc-pVTZ level of theory. To validate this potential energy surface, calculations were also performed for OH + furan and OH + 2-MF at the same level of theory to compare with those reported in the literature, although these were not used in the MESMER analysis presented.

7.2 Previous work

7.2.1 ab initio Calculations and Calculation of Kinetics for OH + Furan

There have been several theoretical investigations into the reaction between OH and furan and its alkylated derivatives. Anglada² investigated the potential energy surface for OH + furan and optimized geometries and vibrational frequencies were determined for all stationary points of the PES using Gaussian 09³ at the MP2⁴ (Møller-Plesset) level with a 6-311G(d,p) basis set. Transition states were identified by the presence of an imaginary frequency and intrinsic reaction coordinate (IRC) calculations were performed on all the transition states in order to verify the connection between the reactants and products. The hydrogen-bonded pre-reactive complex (Figure 7.2) between furan and the hydroxyl radical was optimised using the MP2/6-311+G(2d,2f) level of theory.

Anglada reports that the reaction between furan and the OH radical is a complex process that begins with the formation of a pre-reactive complex (CR1), consisting of a hydrogen bond formed by an interaction between the hydrogen of the OH radical and the π system of the furan (Figure 7.2). The CR1 pre-reactive complex was calculated with the energy of $-2.6 \text{ kcal mol}^{-1}$ ($-10.9 \text{ kJ mol}^{-1}$).



CR1, C_s ($^2A''$)

Figure 7.2 Pre-reactive complex along the PES of OH + furan, geometrical parameters are bond lengths in Angstroms and bond angles in degrees. Optimized at MP2/6-311G(d,p); QCISD/6-311G(d,p), (in brackets) and MP2/6-311+G(2df,2p), (in parentheses), levels of theory.

From the pre-reactive complex the PES proceeds along two pathways, addition to the C1 carbon, or addition to the C2 carbon (Figure 7.3), leading to the formation of the C1 adduct (M1a) or the C2 adduct (M2a). Anglada notes these adducts are more stable than the reactants, with energies calculated as $-30.5 \text{ kcal mol}^{-1}$ ($-127.6 \text{ kJ mol}^{-1}$) and $-12.5 \text{ kcal mol}^{-1}$ ($-52.3 \text{ kJ mol}^{-1}$) respectively. The pathway from the pre-reactive complex to the stable adducts proceeds through transition states. The transition state (TS-CR1M1a) leads to the formation of the C1 adduct (M1a) and lies at $-0.5 \text{ kcal mol}^{-1}$ (-2.1 kJ mol^{-1}) below the reactants. The transition state (TS-CR1M2a) preceding the C2 adduct (M2a) was calculated as $3.4 \text{ kcal mol}^{-1}$ (14.2 kJ mol^{-1}) above the reactants.

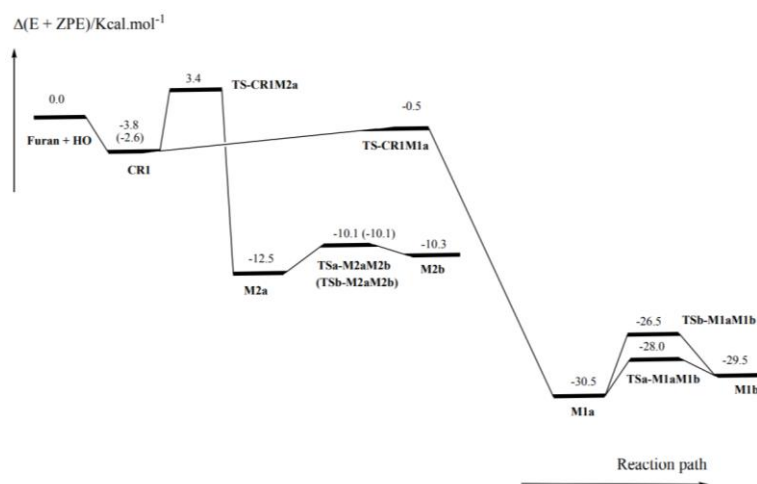


Figure 7.3 Schematic energy diagram the potential energy surface for the formation of the C1 and C2 adducts by the reaction of furan with hydroxyl radical from Anglada *et al.*

The computed energies of the addition adducts show that the C1 adduct (M1a, Figure 7.3) is about 18 kcal mol⁻¹ (75.3 kJ mol⁻¹) more stable than the C2 adduct (M2a), due to the π features of the C1 adduct M1a, which produce a stabilization effect. Moreover, the energy barrier for the formation of the C2 adduct is about 4 kcal mol⁻¹ (16.7 kJ mol⁻¹) higher than that computed for the formation of the C1 adduct, and Anglada concludes that the C2 adduct will not be formed and the C1 adduct is favoured which is in agreement with the suggestion made by Bierbach *et al.*⁵ (see Chapter 4).

Following the formation of the C1 adduct (M1a), the reaction proceeds through a ring-opening channel to form different conformers of a 4-hydroxybutenaldehyde radical (M3) (Figure 7.4). Anglada investigated several conformers of the 4-hydroxybutenaldehyde radical and found the most stable conformer to be a symmetric seven member ring structure (M3a) with a π bond delocalization across all carbons with the energy -43 kcal mol⁻¹ (-179.9 kJ mol⁻¹). The remaining conformers of lie between -22 and -33 kcal mol⁻¹ (-92 and -138 kJ mol⁻¹), below the energy of the reactants. Anglada concluded that the dominant pathway at atmospheric temperature is to the C1 position resulting in the C1 adduct.

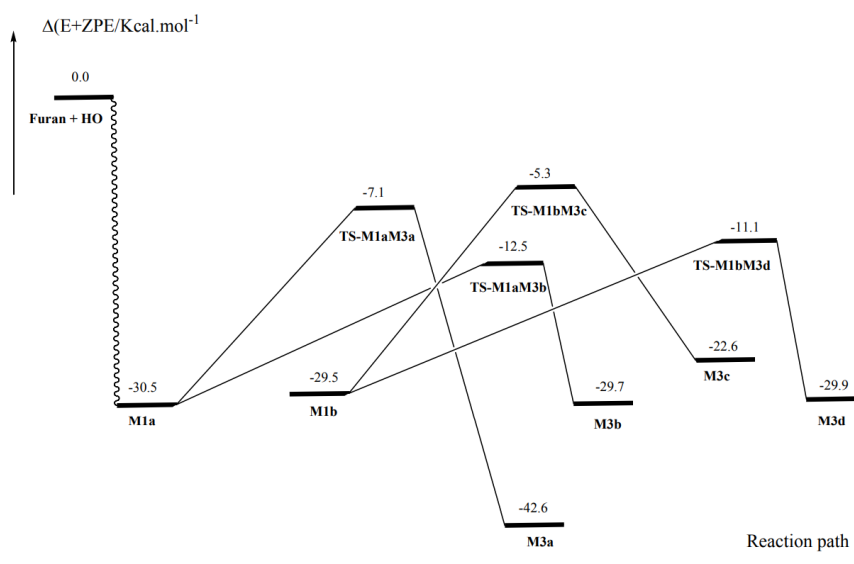


Figure 7.4 Schematic energy diagram of the potential energy surface for the ring-opening process of formation of the C1 adduct from Anglada *et al.*²

Mousavipour *et al.*⁶ studied the kinetics and mechanism of the reaction of OH radicals with furan. The Gaussian 03⁷ program was used to carry out *ab initio* calculations, stationary point geometries were optimised at the UMP2, MPWB1K and G3MP2⁸ (Gaussian 3 with MP2) levels. The overall energies were calculated using were calculated using the CCSD⁹ (Coupled Cluster Single Double) method with a 6-31+G(d,p) basis set. Harmonic vibrational frequencies were obtained at the MPWB1K/6-31+G(d,p) level and transition states were determined by the presence of an imaginary frequency. IRC calculations were used to connect transition states with reactants and products.

For the PES of OH + furan calculated at the highest level of theory using the CCSD/6-311+G(3df,2p) method (Figure 7.5) the formation of a pre-reactive complex (vw) at -16.5 kJ mol⁻¹ below the reactants is slightly more stable than the pre-reactive complex reported by Anglada at -10.9 kJ mol⁻¹, who employed the MP2/6-311G(d,p) method, which is less accurate level of theory when compared to the CCSD/6-311+G(3df,2p).

As with the Anglada PES, from the pre-reactive complex the reaction can proceed along two pathways: the addition to the C1 carbon (Int₁, -131.4 kJ mol⁻¹) through a transition state (TS₁, 1.4 kJ mol⁻¹), or the addition to the C2 carbon (Int₂, -60.8 kJ mol⁻¹) through a

transition state (TS₁, 34.4 kJ mol⁻¹). The C1 adducts are within 4 kJ mol⁻¹ of the energies reported by Anglada, and the C2 adduct is within 8.5 kJ mol⁻¹. The barriers leading to the C1 adduct within 3.5 kJ mol⁻¹, whereas the barrier leading to the C2 adduct was found to have the largest difference with Anglada at 20.2 kJ mol⁻¹ higher.

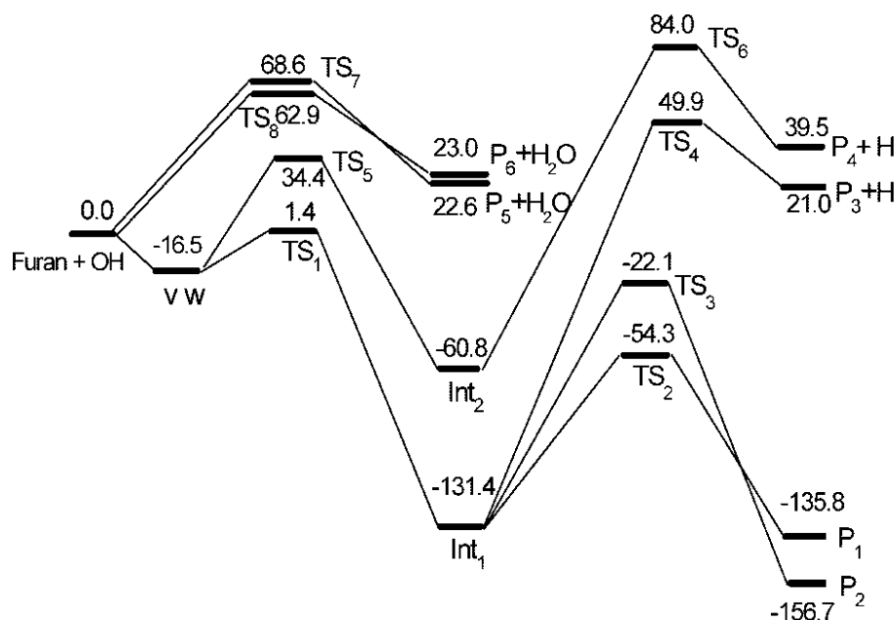


Figure 7.5 Schematic energy diagram of the potential energy surface of OH + furan in kJ mol⁻¹ at the CCSD/6-311+G(3df,2p) level of theory.

Mousavipour *et al.* suggest that the most favoured addition site for OH is at the C1 position, where the C1 adduct (Int₁) has the lowest energy at -131.4 kJ mol⁻¹, which is in agreement with the suggestion made by Bierbach *et al.*⁵ and Anglada *et al.*²

Mousavipour *et al.* calculated rate coefficients for the six individual reaction channels using an RRKM-TST model (described in Chapter 2), as well as a calculation for the overall rate coefficient for the consumption of reactants in the addition of the OH radical to the C1 carbon using a method which combines chemical activation distribution functions and the multichannel RRKM method.

Mousavipour *et al.* reported a rate for OH + furan of $1.9 \times 10^{14} T^{-1.57} \exp(-1700/RT)$ L mol⁻¹ s⁻¹ which equates to $3.60 \times 10^{-7} T^{-1.57} \exp(-1700/RT)$ cm³ molecule⁻¹ s⁻¹ resulting in

a room temperature rate coefficient of $k = 4.11 \times 10^{-11} \text{ cm}^3 \text{ molecule}^{-1} \text{ s}^{-1}$. These results agree reasonably well with experimental results described in Chapter 4.^{5,10-12}

Mousavipour *et al.* comment that rate coefficients of channels other than the addition to the C1 carbon are not significant at temperatures below 2000 K. The overall rate coefficient shows a negative temperature dependence at temperatures lower than 600 K. These results predicted that at temperatures above 2000 K the hydrogen abstraction channels become dominant.

A comparison between the effective bimolecular rate coefficients predicted by Mousavipour *et al.* and the experimental rate coefficients in the literature (more details of which can be found in Chapter 4), can be found in Figure 7.6. There is good agreement between the low temperature data and the predicted rate coefficient by Mousavipour *et al.* up to a temperature of 600 K.

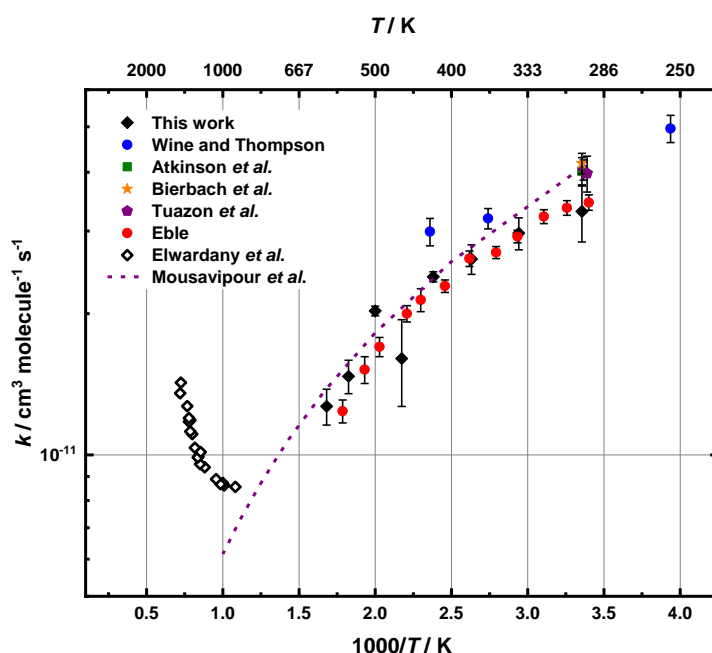


Figure 7.6 Comparison of the predicted rate coefficient reported by Mousavipour *et al.*⁶ and experimental rate coefficient reported in the literature for OH + furan.

The Arrhenius parameters reported by Mousavipour *et al.* have been employed in combustion models to describe the behaviour of 2-MF¹³ and 2,5-DMF¹⁴ by Somers *et al.* which are discussed in section 7.3.

Yuan *et al.*¹⁵ carried out a systematic study on the mechanism of OH initiated oxidation of furan and its alkylated substituents, 2-MF and 2,5-DMF, using quantum chemistry and kinetic calculations. Molecular structures were optimized at the M06-2x¹⁶ method with a 6-311++G(2df,2p) basis set using the Gaussian 09 program. Transition states were confirmed by the presence of one imaginary frequency associated with the reaction coordinate. Optimized structures were then subjected to single point energy calculations at using three different methods, the first being the ROCBS-QB3¹⁷ (Complete Basis Set), and then the RHF-UCCSD(T)/F-12a level with cc-pVDZ-F12 and cc-pVTZ-F12 basis sets.

The PES with the relative energies of all three theoretical methods can be seen in Figure 7.7. Results indicate that in the unsubstituted furan system addition to the C1 and C2 carbons occurs, forming activated adducts, of which the addition to the C1 position is favoured as a consequence of more stable energy (-139.3 kJ mol⁻¹ for C1 compared to -66.5 kJ mol⁻¹ for C2 at the cc-pVTZ-F12 level of theory). The suggestion for this favoured site is in agreement with those reported by Anglada,² Mousavipour *et al.*⁶ and Bierbach *et al.*⁵. When compared to the work by Anglada and Mousavipour *et al.*, Yuan *et al.* do not include abstraction channels. A comparison of the relative energies with the other studies described above can be seen in Table 7.1.

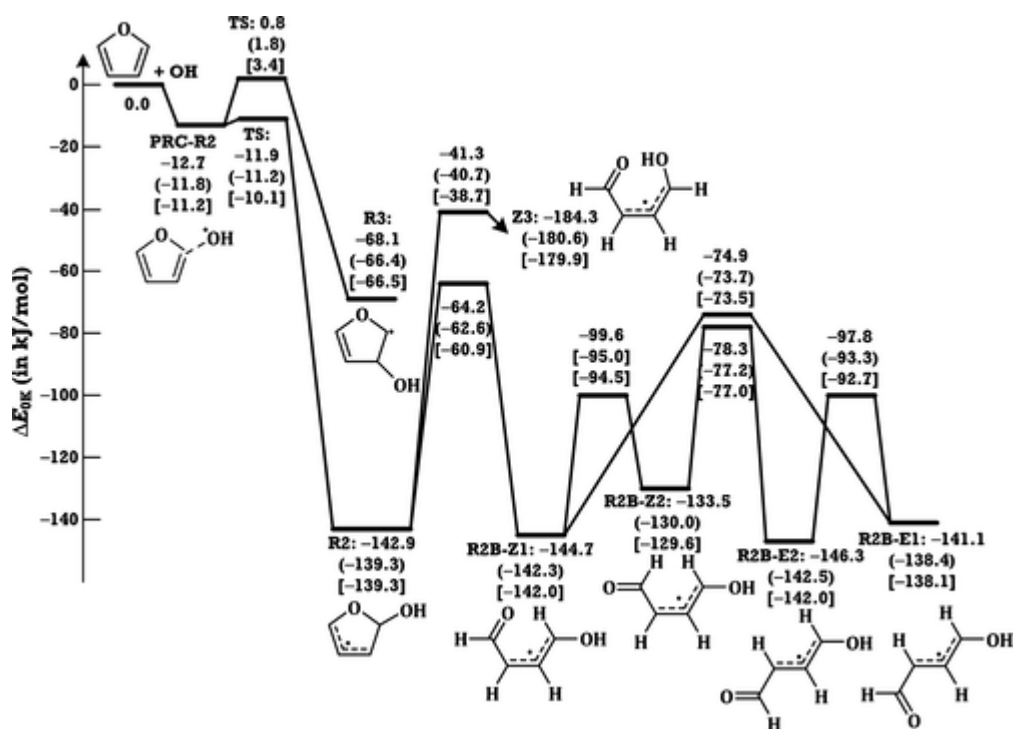


Figure 7.7 Potential energy diagram for reaction between OH and furan at levels of ROCBS-QB3, (RHF-UCCSD(T)-F12a/cc-pVDZ-F12), and [RHF-UCCSD(T)-F12a/cc-pVTZ-F12].

Species	Anglada ²	Mousavipour <i>et al.</i> ⁶	Yuan <i>et al.</i> ¹⁵
	MP2/6-311G(d,p)	CCSD(full)/ 6-311+G(3df,2p)	Average of: ROCBS-QB3, RHF-UCCSD(T)-F12a/cc-pVDZ-F12, and RHF-UCCSD(T)-F12a/cc-pVTZ-F12
Pre-reactive			
Complex	-10.9	-16.5	-11.9
Addition to C1	-127.6	-131.4	-134.5
TS1	-2.1	1.4	-10.9
Addition to C2	-52.3	-60.8	-67
TS2	14.2	34.4	2

Table 7.1 Relative energies in kJ mol⁻¹ for the formation of the C1 and C2 adducts with their associated transition states and pre-reactive complexes for OH + furan from studies by Anglada², Mousavipour *et al.*⁶ and Yuan *et al.*¹⁵

Traditional transition state theory was used to predict the rate coefficient of OH + furan at 298 K and 760 Torr. When using the energies obtained from the CBS method a rate coefficient of $k = 9.63 \times 10^{-11} \text{ cm}^3 \text{ molecule}^{-1} \text{ s}^{-1}$ was obtained, for the F12/VDZ basis set $k = 7.30 \times 10^{-11} \text{ cm}^3 \text{ molecule}^{-1} \text{ s}^{-1}$ and for F12/VTZ, $k = 4.64 \times 10^{-11} \text{ cm}^3 \text{ molecule}^{-1} \text{ s}^{-1}$. Yuan *et al.* report that only the rate coefficient found from the F12/VTZ transition state energies are in reasonable agreement with the results observed from experimental reactions.^{5,10,12,18,19}

Oxidation pathways of furan were reported and can be seen in Figure 7.8. They demonstrate that at 298 K and 750 Torr the main pathway for furan oxidation by OH is to the *E*-isomer ring-opening product (R2B-E) with a yield of 0.43 vs the *Z*-isomer (R2B-Z) at 0.33 and the C1 adduct (R2) at 0.24. These species can then further react with O₂ to form butenedials or NO to form furanones.

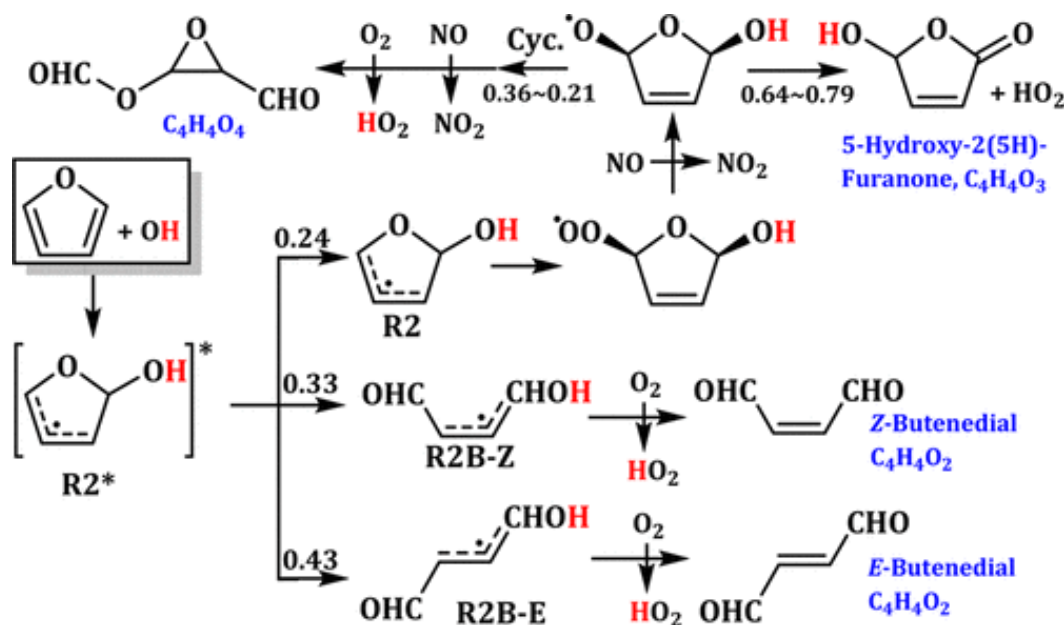


Figure 7.8 Oxidation pathways of furan proposed by Yuan *et al.* based at 298 K and 760 Torr.

7.2.2 *ab initio* Calculations and Calculation of Kinetics for OH + 2-Methylfuran

Zhang *et al.*²⁰ reported a mechanism for the OH + 2-methylfuran (2-MF) reaction with optimised geometries and vibrational frequencies calculated at the B3LYP/6-31G(d)

level of theory and energies calculated at the G4MP2B3 level. The PES can be seen in Figure 7.9. Transition states were confirmed by the presence of an imaginary frequency and reactant and product connections were confirmed by IRC calculations, all *ab initio* calculations were performed using Gaussian 03 program.

The reaction pathways included in the surface are the addition of OH to 2-MF at four possible carbon sites to form an adduct, and the abstraction of a hydrogen atom, also from four possible sites. The abstraction reactions must proceed through transition states with energies ranging from -125.29 to 120.21 kJ mol⁻¹ as seen in Figure 7.9. The association processes have no barrier and initially form the intermediates IM1 (C5 adduct, -135.60 kJ mol⁻¹) and IM2 (C2 adduct, -134.88 kJ mol⁻¹) which possess enough energy to undergo unimolecular rearrangement to the molecules CH₃C(O)CHCHC(OH)H (P6, -142.76 kJ mol⁻¹) and CH₃C(OH)CHCHC(O)H (P8, -121.60, kJ mol⁻¹) respectively *via* ring opening reactions. The ring-opening channels have transition state energies of -61.77 kJ mol⁻¹ to P6 and -58.96 kJ mol⁻¹ for P8. Unlike in the reaction of OH + furan where there is one favoured reaction channel (the addition to the C1 site), in the 2-MF system the relative energies of the adducts from addition to the C2 and C5 sites are of similar energy, meaning both channels will be favoured.

The abstraction channel with the lowest energy is a result of the H abstraction from the methyl group of 2-MF, which proceeds through a transition state with the energy of 13.11 kJ mol⁻¹ to the products P4 + H₂O, with the combined energy of -125.29 kJ mol⁻¹. Zhang *et al.* did not carry out kinetic calculations on the PES.

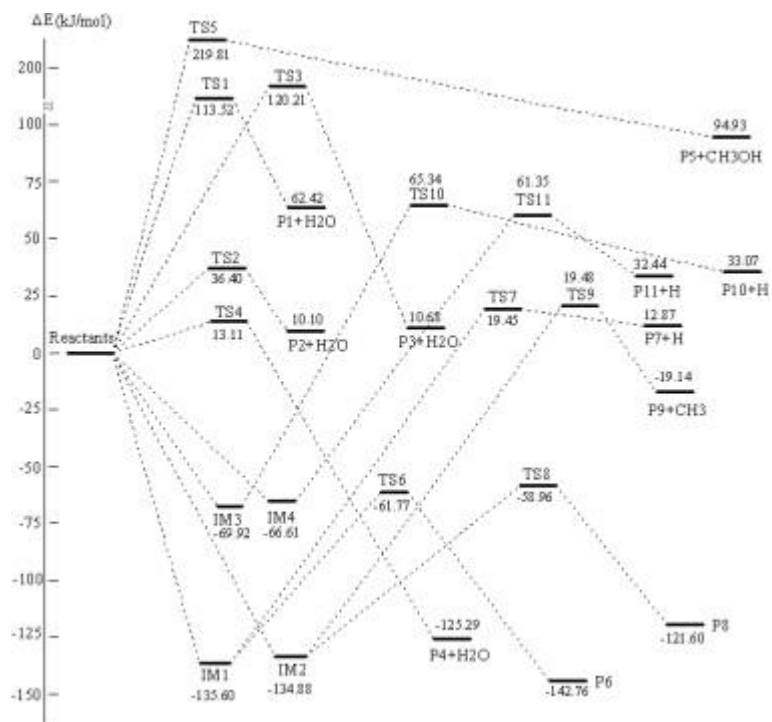


Figure 7.9 PES for the OH + 2-MF by Zhang *et al.*²⁰. Energies in kJ mol⁻¹ at 298.15 K obtained at the G3MP2B3 level of theory.

Davis and Sarathy²¹ carried out a theoretical and kinetic modelling study into the oxidation mechanism of 2-MF using the Gaussian 09 program. Molecular structures of reactants, products and transition states were initially optimized at the B3LYP-6-31G(d,p) level of theory. The lowest energy configurations were then used for CBS-QB3 and G4 methods and relative energies were provided as an average of the two methods. Transition states were confirmed by the presence of an imaginary frequency. The PES for the reaction is shown in Figure 7.10.

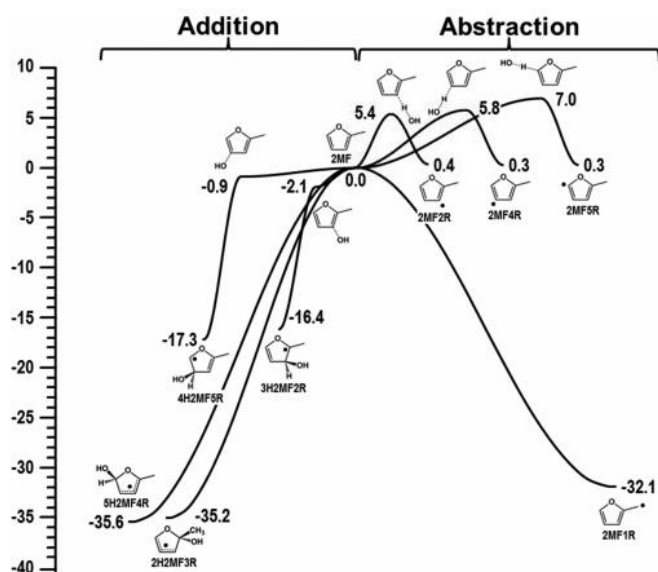


Figure 7.10 PES of OH + 2-MF showing the addition and abstraction channels from Davis and Sarathy.²¹ Energies are in kcal mol⁻¹ and an average of calculations at the CBS-QB3 and G4 methods.

Davis and Sarathy note that the addition of OH to sites C2 and C5 of 2-MF will be most favoured as they lead to the formation of more resonance stabilised intermediates. The addition to the C5 carbon (5H2MF4R) with an energy of -35.6 kcal mol⁻¹ (-148.9 kJ mol⁻¹) has a similar energy to that of the C2 addition site at -35.2 kcal mol⁻¹ (-147.3 kJ mol⁻¹). Davis and Sarathy do not report energies for subsequent ring-opening reactions. The lowest energy product of the abstraction channels is again from the methyl group (2MF1R), with an energy of -179.49 kJ mol⁻¹. In contrast to the PES by Zhang *et al.*, Davis and Sarathy report no transition state is reported for the process. The addition of OH to the C2 and C5 sites was found to be barrierless, whereas the addition the C3 and C4 sites were found to proceed through transition states with energies of -8.79 kJ mol⁻¹ and -3.76 kJ mol⁻¹, respectively. A comparison of the species energies reported by Zhang *et al.*²⁰ at the G3MP2B3 level with those reported by Davis and Sarathy can be seen in Table 7.2. The energies calculated by Davis and Sarathy are within 3 kJ mol⁻¹ those reported by Zhang *et al.* for the C3 and C4 adducts, but diverge to a difference of 9, 12.4 and 13.3 kJ mol⁻¹ for the C1 abstraction + H₂O, C2 adducts and C5 adduct, respectively.

Species	Zhang <i>et al.</i> ²⁰ G3MP2B3	Davis and Sarathy ²¹ Average of CBS-QB3 and G4
C2 adduct	-134.88	-147.28
C3 adduct	-66.61	-68.62
C4 adduct	-69.92	-72.38
C5 adduct	-135.60	-148.95
C1 abstraction + H ₂ O	-125.29	-134.30

Table 7.2 Relative energies in kJ mol⁻¹ for the formation of the addition products and the methyl abstraction product with associated transition states and pre-reactive complexes for OH + 2-MF from studies by Zhang *et al.*²⁰ and Davis and Sarathy.²¹

Reaction rate coefficients were calculated using the master equation modelling software, CHEMRATE²², at the high pressure limit and was fit to a modified Arrhenius rate expression over a 300-2500 K temperature range. Rate coefficients were reported for all abstraction channels, and the OH addition at the C3 and C4 sites, which are shown in Table 7.3. No rate coefficients were reported for the OH addition to the C2 or C5 positions, however, these are the only species on the PES described by Davis and Sarathy that do not proceed *via* a transition state. No comments were made as to why these rate coefficients have been excluded from the reported kinetics and so it is assumed that rate coefficients were calculated using a transition state theory model only. As a result, the Arrhenius parameters reported will provide an incomplete description of the chemistry of 2-MF + OH at temperatures relevant to low temperature combustion.

Reaction	$A / \text{cm}^3 \text{ molecule}^{-1} \text{ s}^{-1}$	n	$E_a / \text{kJ mol}^{-1}$
2-MF + OH \rightarrow C3+OH	4.93×10^{-19}	2.09	-13.4
2-MF + OH \rightarrow C4+OH	3.75×10^{-19}	2.14	-7.9
2-MF + OH \rightarrow C3-H	2.96×10^{-21}	3.03	19.7
2-MF + OH \rightarrow C4-H	3.20×10^{-21}	3.03	21.3
2-MF + OH \rightarrow C5-H	5.08×10^{-21}	3.4	26.4

Table 7.3 Arrhenius parameters reported by Davis and Sarathy for the OH + 2-MF reaction calculated using CHEMRATE.

Figure 7.11 shows a comparison of the reported rate coefficients with the experimental data and it can be seen that, despite no Arrhenius parameters reported for the OH addition to the C2 or C5 sites, the rate coefficients proposed by Davis and Sarathy agree reasonably well with the data at room temperature, where $k_{(298 \text{ K})} = 5.80 \times 10^{-11} \text{ cm}^3 \text{ molecule}^{-1} \text{ s}^{-1}$. However, there is a significant over estimate of the rates at temperatures above $\sim 300 \text{ K}$. Davis and Sarathy comment on the good agreement at room temperature, but do not discuss the rates at the higher temperatures.

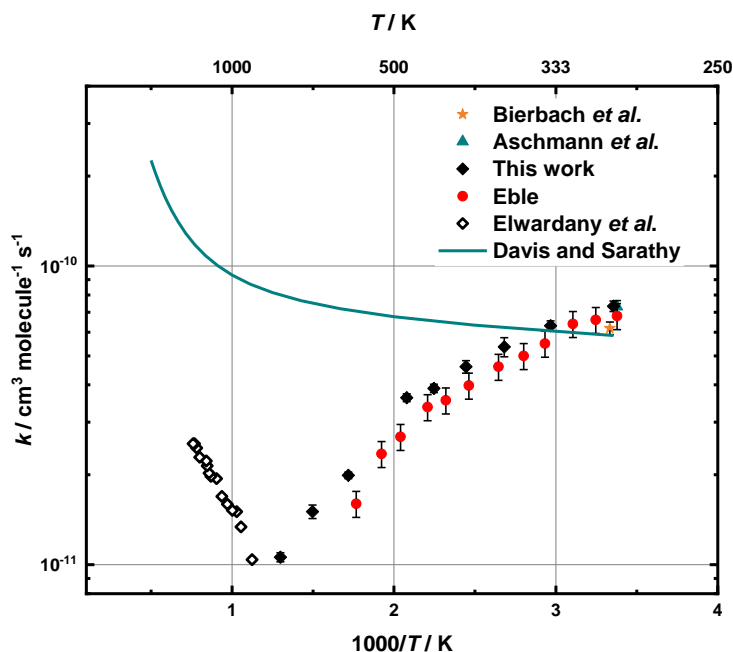


Figure 7.11 Comparison of the predicted rate coefficient reported by Davis and Sarathy²¹ and experimental rate coefficient reported in the literature for OH + 2-MF.

As previously described, Yuan *et al.* investigated the PES of the furans at three levels of theory (ROCBS-QB3, F12/VDZ, and F12/VTZ). For 2-MF, Yuan *et al.* do not provide a PES or report the calculated energies, however they do report the calculated rate coefficients at 298 K and 750 Torr. At the F12/VTZ level, which resulted in the closest rate coefficient to experimental results for the OH + furan system, Yuan *et al.* calculated overall rate coefficients at 298 K of $k = 11.6 \times 10^{-11} \text{ cm}^3 \text{ molecule}^{-1} \text{ s}^{-1}$ for 2-MF, which is not in agreement with the experimental results reported by Bierbach *et al.*⁵, Aschmann *et al.*,²³ Eble¹⁹, or the results found in experiments carried out for this thesis (Chapter 5).

The oxidation pathways suggested by Yuan *et al.* for 2-MF can be seen in Figure 7.12. The C2 adduct (R2) has the biggest individual branching ratio of 0.31, compared to the C5 adduct at 0.26. The yield sum of the ring-opening products of 2-MF amount to 0.44.

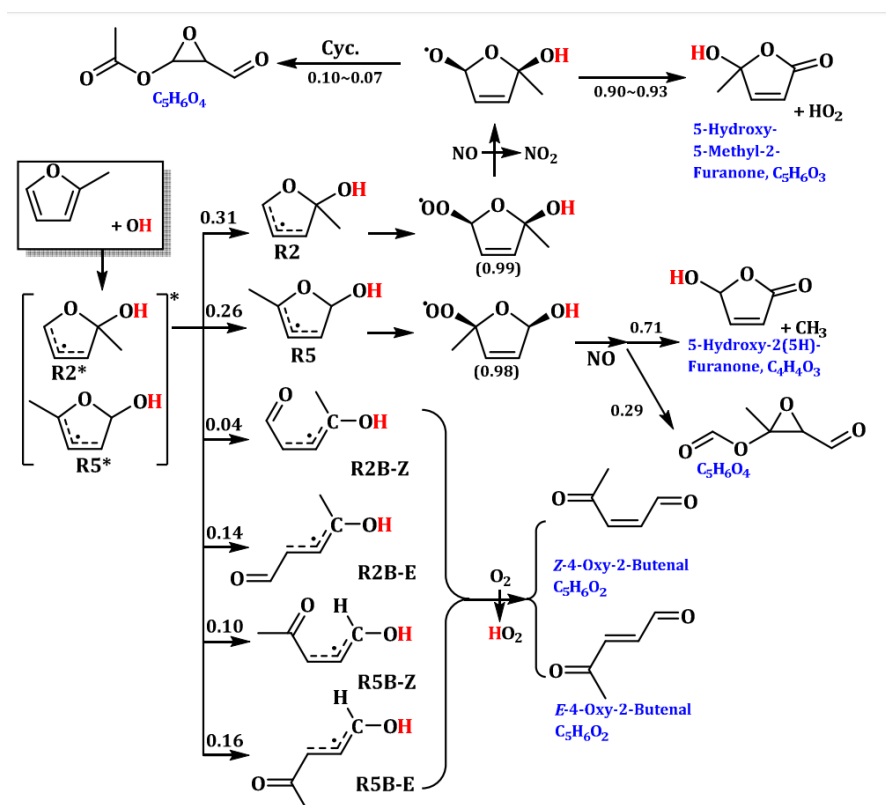


Figure 7.12 Oxidation pathways of 2-methylfuran proposed by Yuan *et al.* based on calculations at 298 K and 760 Torr.

7.2.3 *ab initio* Calculations and Calculation of Kinetics for OH + 2,5-Dimethylfuran

Simmie and Metcalfe²⁴ carried out an *ab initio* study into the pyrolysis of 2,5-DMF, of which some reaction involving OH are present. Methods utilised include CBS-QB3, CBS-APNO, G3 and G3MP2B3 to compute geometries and energies of reactants, products and transition states using the Gaussian 09 program. The H abstraction by OH at the methyl group was found to have a transition state of 15.5 kJ mol⁻¹ to a product of -133.1 kJ mol⁻¹, calculated at the G3 level. For the abstraction of an H atom from the C3 site of 2,5-DMF, Simmie and Metcalfe used three levels of theory, CBS-QB3, CBS-APNO and G3 to give an average transition state energy of 26.6 kJ mol⁻¹ to a product of 6.4 kJ mol⁻¹.

Rate coefficients were determined based on canonical transition state theory in the MultiWell-2010²⁵ master equation software. For the H atom abstraction from the methyl group the reported rate coefficients were reported as $k = 1.69 \times 10^{-20} T^{3.13} \exp(-1085/T)$ cm³ molecule⁻¹ s⁻¹. For the H abstraction from the C3 position rate coefficients were reported as $k = 6.53 \times 10^{-20} T^{2.67} \exp(-3871/T)$ cm³ molecule⁻¹ s⁻¹. When compared to experimental data in the literature (Figure 7.13) it can be seen that the rate parameters deduced by Simmie and Metcalfe over predict the rate coefficient for the reaction at temperatures above ~650 K, and under predict at temperatures below ~650 K, however this under prediction is not surprising as abstraction channels tend to dominate at higher temperatures. The rates reported by Simmie and Metcalfe have been used in several combustion models to investigate both 2,5-DMF^{14,26,27} and 2-MF^{28,29} to be discussed in the next section.

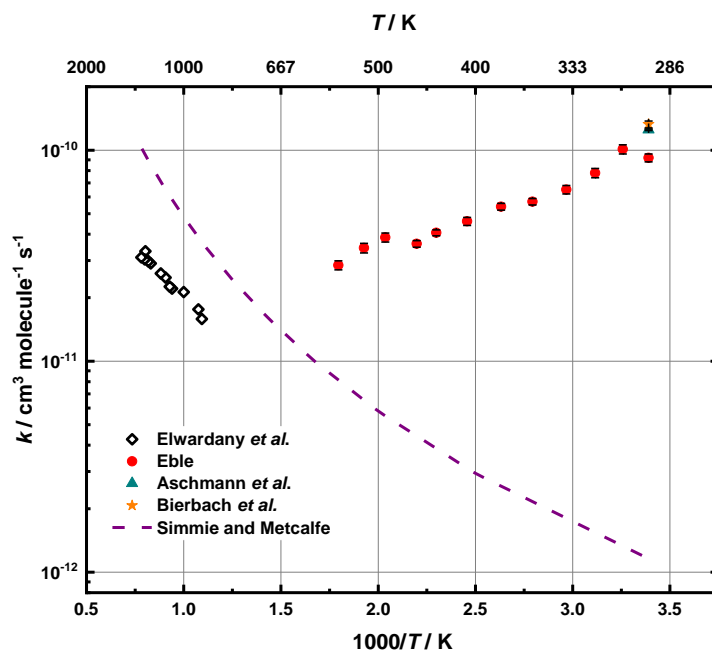


Figure 7.13 Comparison of the predicted rate coefficient reported by Simmie and Metcalfe²⁴ and experimental rate coefficient reported in the literature for OH + 2,5-DMF.

Yuan *et al.*¹⁵ also investigated the OH + 2,5-DMF reaction, however, as with the 2-MF study, they do not provide details on the energies associated with the PES they calculated. However, rate coefficients were provided, calculated from energies at the F12/VTZ level of theory, and at 298 K the rate coefficient was reported as $k = 6.33 \times 10^{-10} \text{ cm}^3 \text{ molecule}^{-1} \text{ s}^{-1}$, which is not in agreement with the experimental results reported by Bierbach *et al.*⁵, Aschmann *et al.*,²³ Eble¹⁹, or the results found in experiments carried out for this thesis (Chapter 6).

Yuan *et al.* provided a schematic of the possible branching ratios of the OH + 2,5-DMF reaction. The dominant pathway in the 2,5-DMF reaction is to the C2 adduct (R2) with a high yield of 0.72 compared to 0.19 for the *E*-isomer (R2B-*E*) and 0.09 for the *Z* (B2B-*Z*). This is in contrast to the major branching ratios seen in furan (the *E*-isomer) and 2-MF (R2 and R5).

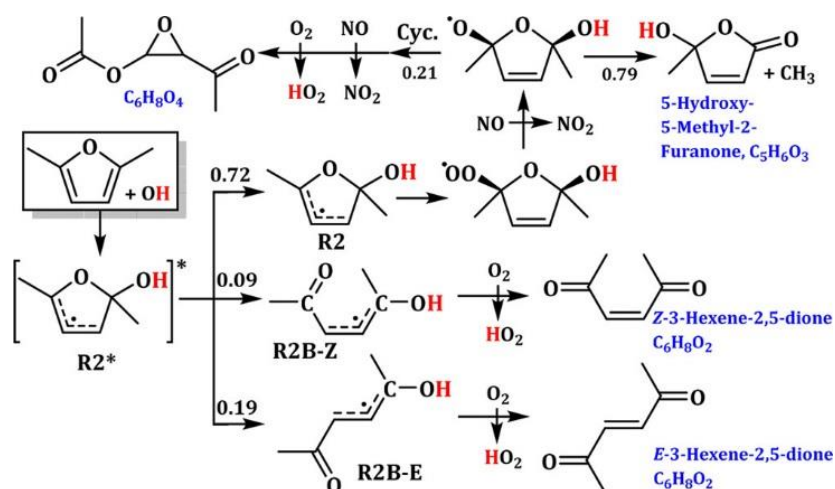
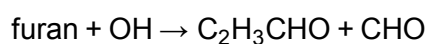


Figure 7.14 Oxidation pathways of 2,5-DMF proposed by Yuan *et al.* based on calculations at 298 K and 750 Torr.

7.2.4 Combustion Models

Combustion models are developed in order to describe the complex chemistry of the combustion process. Models consist of reaction mechanisms that can be determined from both experimental and theoretical investigations. The following section outlines the combustion models present in the literature that contain the OH radical oxidation of furans of interest in this thesis.

The first reported combustion model to include the reaction between the OH radical and furan was developed by Tian *et al.*³⁰ consisting of 206 species and 1368 reactions. The rate coefficients for the reaction of OH + furan (R7.1-R7.3) were deduced from a previous model by the same research group on the oxidation of alkenes³¹, where propene and 1-butene reactions were deduced using the EXGAS³² software, which automatically generates kinetic models for the gas-phase oxidation and combustion of alkanes, alkenes and ethers.



R7.1



Tian *et al.* estimate rate coefficients of $2.70 \times 10^{12} \exp(1040 \text{ cal}/RT) \text{ cm}^3 \text{ mol}^{-1} \text{ s}^{-1}$ for R7.1 and $2.26 \times 10^6 T^2 \exp(-2780 \text{ cal}/RT) \text{ cm}^3 \text{ mol}^{-1} \text{ s}^{-1}$ for R7.2 and R7.3 which equate to $k = 4.48 \times 10^{-12} \exp(4.3/RT) \text{ cm}^3 \text{ molecule}^{-1} \text{ s}^{-1}$ and $k = 3.75 \times 10^{-18} T^2 \exp(-11.6/RT) \text{ cm}^3 \text{ molecule}^{-1} \text{ s}^{-1}$ and room temperature rate coefficients of $2.60 \times 10^{-11} \text{ cm}^3 \text{ molecule}^{-1} \text{ s}^{-1}$ and $3.05 \times 10^{-15} \text{ cm}^3 \text{ molecule}^{-1} \text{ s}^{-1}$, respectively. The Arrhenius parameters reported by Tian *et al.* were used by other research groups for their own combustion models^{13,14,33} that included the reaction of OH + furan.

A mechanism to describe the combustion of 2,5-DMF was reported by Somers *et al.*¹⁴ consisting of 545 species and 2768 reactions. The kinetic model contained reactions for the OH addition and abstraction reactions of furan, 2-MF and 2,5-DMF. The reactions involving OH + furan were taken from the model by Tian *et al.* as previously described.

For the reaction of OH with 2,5-DMF, where the OH radical abstracts an H from the methyl group or C3 site, Somers *et al.* used the rate parameters calculated by Simmie and Metcalfe²⁴ as previously described. For the addition of OH to the furan ring at the C2 position, Somers *et al.* carried out *ab initio* calculations at the CBS-QB3, CBS-APNO and G3 levels of theory to optimise geometries, frequencies and single-point energies with the Gaussian 03 and Gaussian 09 packages. Rate parameters were determined using transition state theory with the MultiWell program. For the addition of OH to the C2 site of 2,5-DMF, Somers *et al.* calculated $k = 3.67 \times 10^{-20} T^{2.45} \exp(30000/RT) \text{ cm}^3 \text{ molecule}^{-1} \text{ s}^{-1}$.

A comprehensive study of the decomposition of 2-MF was also performed by Somers *et al.*¹³ who developed a detailed kinetic mechanism comprising of 391 species and 2059 reactions. The OH + furan reaction was included and used the Arrhenius parameters reported by Tian *et al.* For the reaction of OH + 2-MF, Somers *et al.* adapted the theoretical work by Mousavipour *et al.* who determined rate parameters from an RRKM-

TST model as previously described. Arrhenius parameters from the 2,5-DMF combustion model were also utilised.

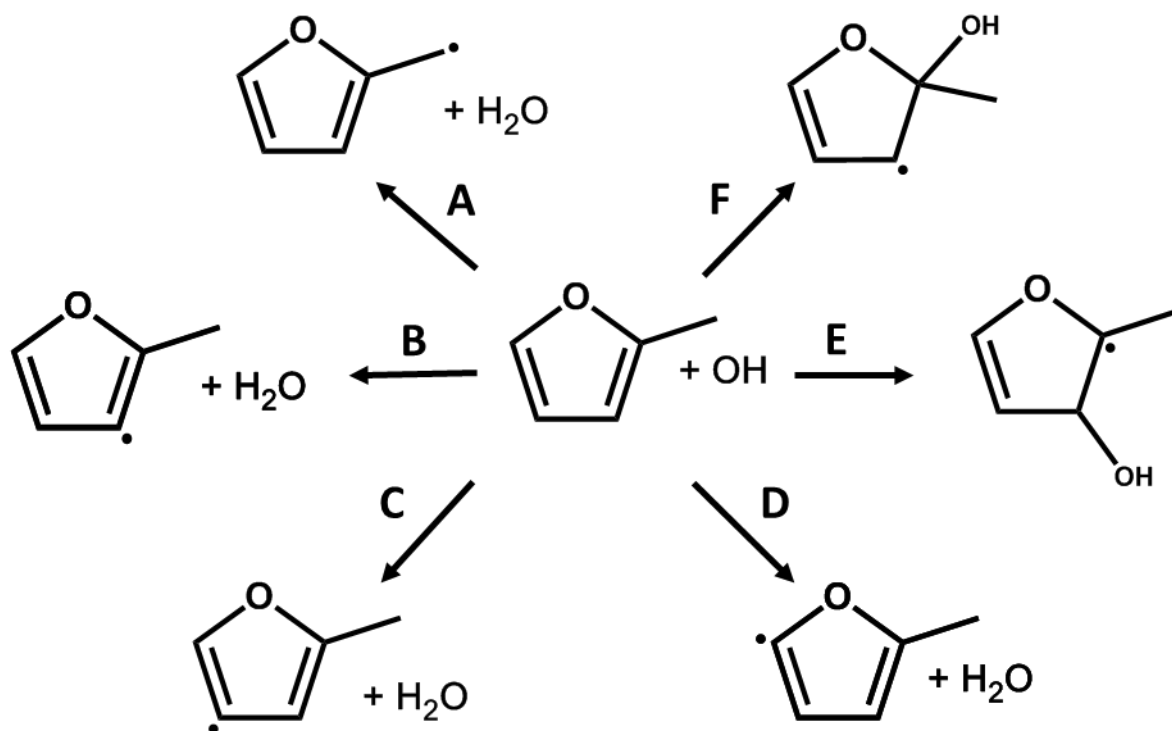


Figure 7.15 Reactions for OH + 2-MF in the 2-MF oxidation kinetic model by Somers *et al.*¹³. Corresponding Arrhenius parameters can be found in Table 7.4.

Reaction	A / cm^3 $\text{molecule}^{-1} \text{s}^{-1}$	n	$-E_a / \text{kJ}$ mol^{-1}	$k_{(298 \text{ K})} / \text{cm}^3$ $\text{molecule}^{-1} \text{s}^{-1}$	Reference Mechanism
A	8.47×10^{-21}	3.13	-9.02	9.37×10^{-13}	Simmie and Metcalfe ²⁴
B	9.13×10^{-22}	3.33	-36.80	1.56×10^{-13}	Mousavipour <i>et al.</i> ⁶
C	9.13×10^{-22}	3.33	-36.80	1.56×10^{-13}	Mousavipour <i>et al.</i>
D	6.89×10^{-22}	3.42	-40.10	1.96×10^{-13}	Mousavipour <i>et al.</i>
E	1.83×10^{-20}	2.45	30.34	2.14×10^{-14}	Simmie and Metcalfe
F	1.83×10^{-20}	2.45	30.34	1.03×10^{-17}	Simmie and Metcalfe

Table 7.4 Arrhenius parameters for the reaction of OH + 2-MF in the 2-MF oxidation kinetic model by Somers *et al.*¹³. Reaction schemes can be seen in Figure 7.15.

For reactions A, E and F (Figure 7.15, Table 7.4) Somers *et al.*¹³ used the Arrhenius parameters of OH + 2,5-DMF from the of 2,5-DMF pyrolysis by Simmie and Metcalfe²⁴.

For scheme A, which represents the H abstraction from the alkyl site by the OH radical, the pre-exponential factor, A , was halved from $A = 1.69 \times 10^{-20} \text{ cm}^3 \text{ molecule}^{-1} \text{ s}^{-1}$ in the 2,5-DMF mechanism to $A = 8.47 \times 10^{-21} \text{ cm}^3 \text{ molecule}^{-1} \text{ s}^{-1}$ in the 2-MF mechanism. The n factor (3.13) and activation energy, E_a , (9.02 kJ mol⁻¹) remained unchanged between mechanisms.

Somers *et al.* used the same method for the calculation of the rate of OH addition to the C2 and C3 position of 2-MF, represented by scheme E and F. The pre-exponential factor, A , was halved from $A = 3.67 \times 10^{-20} \text{ cm}^3 \text{ molecule}^{-1} \text{ s}^{-1}$ in the 2,5-DMF mechanism to $A = 1.83 \times 10^{-20} \text{ cm}^3 \text{ molecule}^{-1} \text{ s}^{-1}$ in the 2-MF mechanism. The n factor (2.45) and activation energy, E_a , (-30.34 kJ mol⁻¹) remained unchanged between mechanisms. As the mechanism is adapted from that of the 2,5-DMF mechanism, where 2,5-DMF is a symmetrical molecule, the 2-MF mechanism neglects Arrhenius parameters for OH addition to the C4 and C5 sites.

For reactions B, C and D Somers *et al.* used the rate coefficient for the oxidation of the unsubstituted furan by Mousavipour *et al.* where the pre-exponential factor, A , for each reaction was halved and n and $-E_a$ remained the same between mechanisms.

The adaptation of theoretical results were outlined in comments present in the reported model available in supplementary material of the literature. No comment is made within the main body of text to explain the reasons behind utilising the Mousavipour *et al.* furan data and Somers *et al.* 2,5-DMF data in this way.

Cheng *et al.*²⁶ adapted the Arrhenius parameters reported by Tian *et al.*³⁰ for the reaction of OH + furan in their 2,5-DMF combustion model. For the reaction of OH + 2-MF, the rate parameters reported by Somers *et al.*²⁸ were used. For OH + 2,5-DMF Cheng *et al.* adapted the work by Simmie and Metcalfe²⁴ for the H abstraction channels. For the addition reaction of OH + 2,5-DMF, Cheng *et al.* estimated the rate coefficient based on OH + furan from Atkinson *et al.*³⁴ as $k = 1.32 \times 10^{-11} \exp(2780/RT) \text{ cm}^3 \text{ molecule}^{-1} \text{ s}^{-1}$.

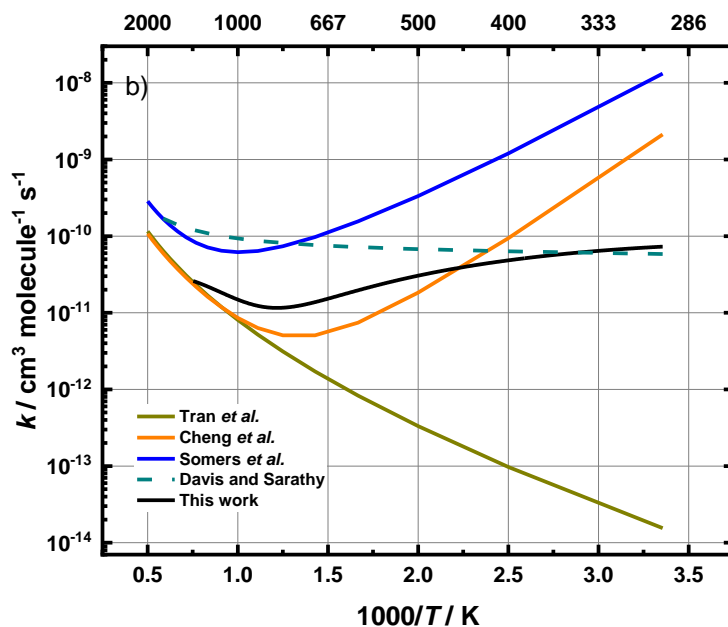
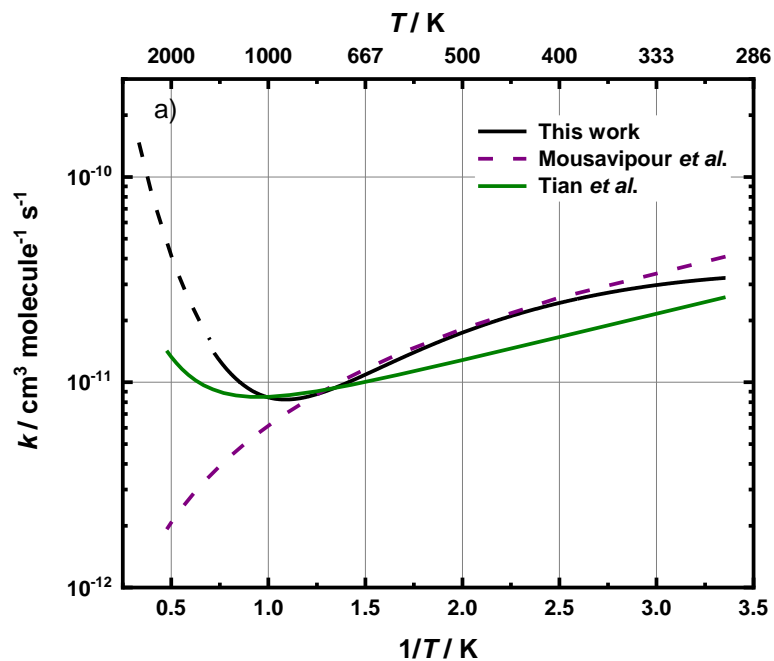
Liu *et al.*³³, Tran *et al.*²⁹ and Togbé *et al.*²⁷ jointly focused on the combustion chemistry of furan and its alkylated derivatives to produce a combustion model. For the reaction of OH + furan, the rate coefficients were based on the work by Tian *et al.*³⁰ Reporting the same rate coefficient for R7.2 and R7.3 ($k = 3.75 \times 10^{-18} T^2 \exp(-11.6/RT) \text{ cm}^3 \text{ molecule}^{-1} \text{ s}^{-1}$) and a slightly faster rate coefficient for R7.1 ($k = 4.55 \times 10^{-12} \exp(4.3/RT) \text{ cm}^3 \text{ molecule}^{-1} \text{ s}^{-1}$).

For the reaction of OH + 2-MF, Tran *et al.*²⁹ utilised the work by Simmie and Metcalfe on 2,5-DMF previously described for the abstraction of an H atom from the methyl group. The reported rate coefficient of $k_{\text{OH}+2,5\text{-DMF}} = 1.69 \times 10^{-20} T^{3.13} \exp(-9020/RT) \text{ cm}^3 \text{ molecule}^{-1} \text{ s}^{-1}$ was halved to $k_{\text{OH}+2\text{-MF}} = 8.47 \times 10^{-21} T^{3.13} \exp(-9020/RT) \text{ cm}^3 \text{ molecule}^{-1} \text{ s}^{-1}$ in attempt to describe the rate coefficient for the smaller furan. For the abstraction of an H atom from the C3 site of the furan ring, Tran *et al.* estimated the rate coefficient from furan as part of the EXGAS program, giving $k = 3.68 \times 10^{-18} T^2 \exp(-11600/RT) \text{ cm}^3 \text{ molecule}^{-1} \text{ s}^{-1}$.

For 2,5-DMF, Togbé *et al.* employed the work by Simmie and Metcalfe for the OH abstractions of H from the methyl group and C3 site of the furan ring. For the OH addition to the C2 site Togbe *et al.* estimated the rate coefficient based on the reaction of furan + OH from Atkinson *et al.*¹¹ as $k = 1.32 \times 10^{-11} \exp(-2.78/RT) \text{ cm}^3 \text{ molecule}^{-1} \text{ s}^{-1}$.

The comparison of the models available in the literature in with the experimental work described in this thesis shows clear discrepancies at temperatures relevant to low temperature combustion (Figure 7.16). Many of the models rely on reported rate coefficients of smaller molecules, in the case of Tian *et al.*³⁰ using small alkenes for the prediction of rates of OH + furan, and Cheng *et al.*²⁶ and Togbé *et al.*²⁷ using rates of OH + furan in place of the larger 2,5-DMF. Other models have relied heavily on the theoretical calculations of reaction rates, such as those by Simmie and Metcalfe, which do not accurately describe the experimental data available in the literature. Some calculated PESs are lacking in a full description of all the reaction channels available

when furans react with OH. Clearly, there is a need to incorporate rate parameters from theoretical and experiments results, that can describe the complex behaviour of furans in the low temperature combustion region.



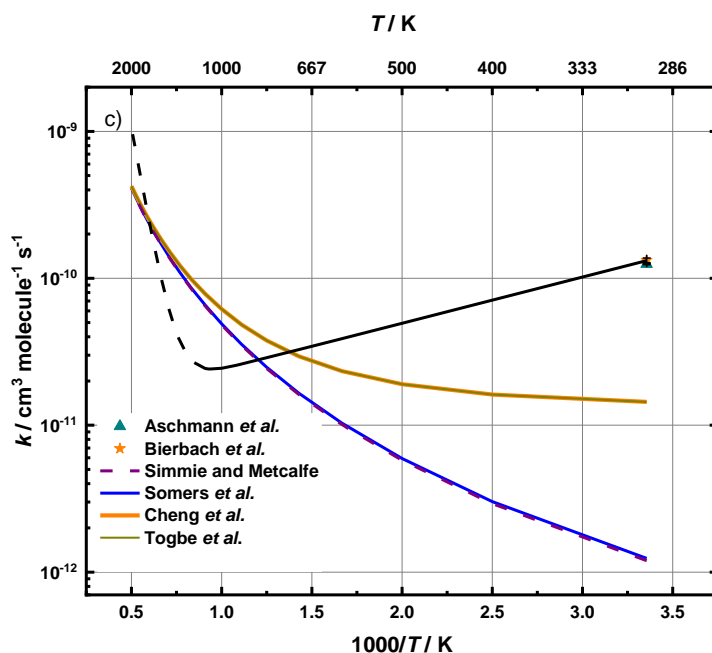


Figure 7.16 Arrhenius plots of the reactions of OH + furan (a) OH + 2-MF (b) and OH + 2,5-DMF (c) with the total predicted rate coefficient from combustion models. Theoretical rate coefficients employed in the models are also shown. The rate coefficients determined by the double modified Arrhenius fit to experiment work carried out in this thesis is also shown for each furan.

7.3 Computational Methods Used in This Work

Both electronic structure theory and master equation calculations have been performed on the systems of the oxidation of furan, 2-MF and 2,5-DMF. Geometries, force-constant matrices, vibrational frequencies, rotational constants, and electronic energies for all stationary points across the PES were derived from *ab initio* calculations at the M06-2x/cc-pVTZ level of theory using the Gaussian 09 program. Given the number of atoms involved in the reaction, this level of theory was accurate enough without limiting the calculations due to excess computational expense, determined by a comparison of species in the PES of OH + 2-MF at the desired level to that of the literature PES by Zhang *et al.*²⁰ and Davis and Sarathy²¹. Energies of species at the M06-2x/cc-pVTZ level were compared against energies at the G3MP2, CBS-QB3 and G4 levels (Figure 7.17), and gave a slope of (0.95 ± 0.04) and intercept of (7.95 ± 3.91) kJ mol⁻¹ for 18 species. Vibrational frequencies were compared, giving a slope of (0.99 ± 0.001) and intercept of

$(-2.22 \pm 2.10) \text{ cm}^{-1}$ for the 5 species compared. Comparative energies, vibrational frequencies and rotational constants can be found in Appendix.

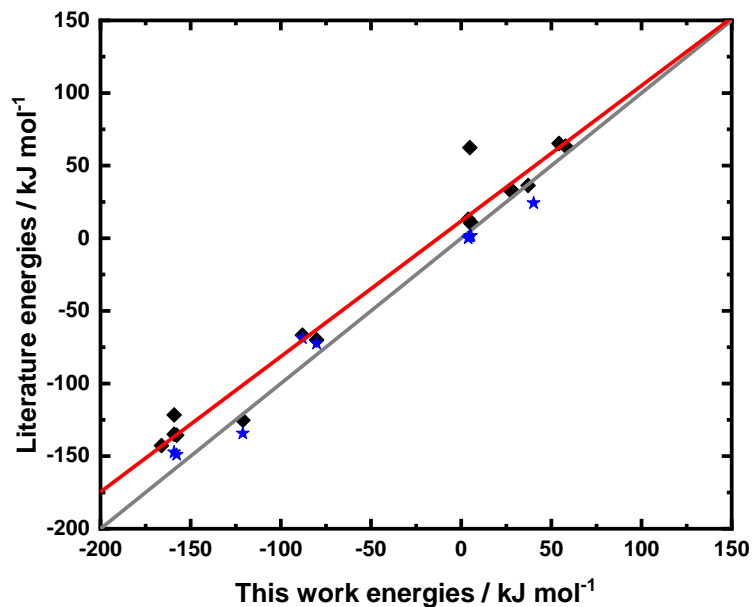


Figure 7.17 Comparison of the species energies calculated at the M06-2x/cc-pVTZ level of theory for OH + 2-MF compared to equivalent species energy calculated at the G3MP2 level of theory by Zhang *et al.*²⁰ (black diamonds) and the average of CBS-QB3 and G4 methods by Davis and Sarathy²¹ (blue stars). Species compared are: MF, C2 adduct, C3 adduct, C4 adduct, C5 adduct, C1 abstraction, C3 abstraction, C4 abstraction and C5 abstraction. The red line is the line of best fit with a slope of (0.95 ± 0.04) and an intercept of (7.95 ± 3.91) . Grey line is a 1:1.

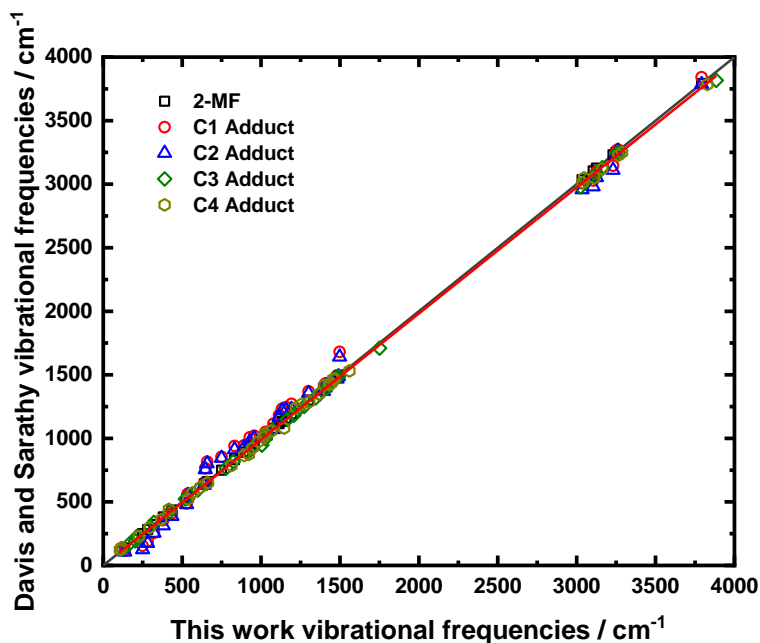


Figure 7.18 Comparison of the vibrational frequencies calculated at the M06-2x/cc-pVTZ level of theory for OH + 2-MF compared to equivalent species frequencies calculated at the CBS-QB3 and G4 level of theory by Davis and Sarathy.²¹ The red line is the line of best fit with a slope of (0.99 ± 0.001) and an intercept of (-2.22 ± 2.10) . Grey line is a 1:1.

Kinetic calculations were performed using the MESMER program previously described. RRKM theory was used to model the transfer of energy between the grains and collisional energy transfer was modelled by an exponential down model. The association of the OH radical and the reagent was modelled using the inverse Laplace transform (ILT) of the high pressure limiting rate coefficient based on a bimolecular source term input to MESMER.

As previously described, the literature provided a full PES for the OH + furan system, therefore a full surface was not calculated for this reaction. The PES by Mousavipour *et al.* was chosen as the kinetic calculations performed by Mousavipour *et al.* predicted rate coefficients in agreement with experimental results.

The PES available in the literature for the OH + 2,5-DMF reaction by Yuan *et al.* did not include abstraction reactions and was found to give a poor description of previous experimental results in the literature when used as the basis for statistical rate theory

calculations. Therefore a full PES for the reaction of OH + 2,5-DMF was calculated for this thesis at the M06-2x/cc-pVTZ level.

7.4 Results and Discussion

7.4.1 ab initio Calculations of the OH + 2,5-DMF PES

The calculated 2,5-DMF PES is summarised in Figure 7.19. The general behaviour is similar to that reported in previous work for OH + furan and OH + 2-MF. Stable reactants and products were optimised and single point energies calculated at the M06-2x/cc-pVTZ level of theory. A potential energy scan was performed to locate the transition states TS1, TS2, TS3 and TS4 at the B3LYP/3-21G level of theory. When the transition state was located, calculations at the higher theory level of M06-2x/cc-pVTZ were performed and transition states were confirmed by the presence of a single imaginary frequency. TS1 corresponds to the transition state that lies between at addition of OH to the C2 site and the subsequent ring-opening product, TS2 to the transition state between the reactants and the product of H abstraction by OH, TS3 to the transition state between the OH addition to the C3 adduct and the product from a H removal by thermal decomposition and TS4 to the product resulting from the abstraction of a H atom from the methyl group by OH.

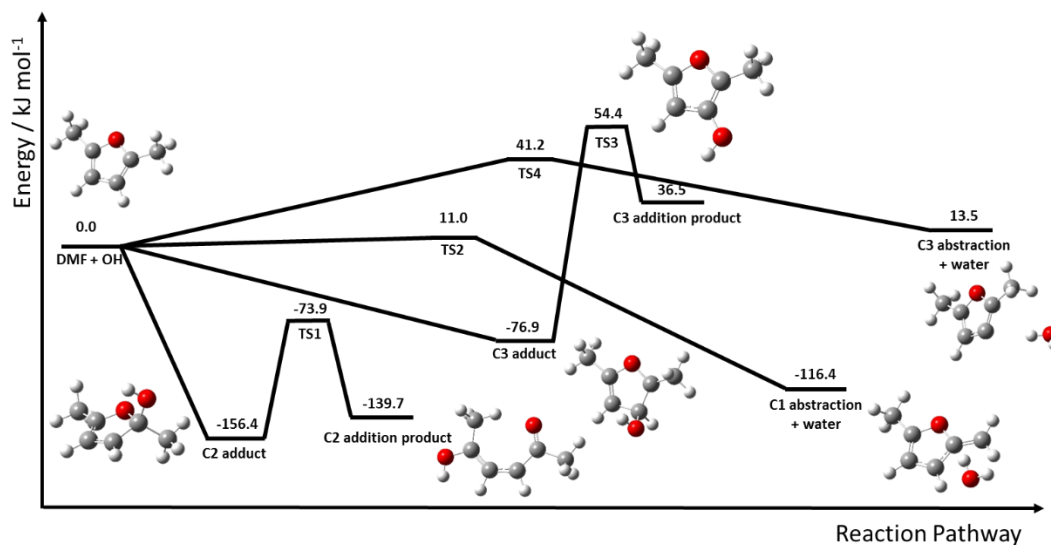


Figure 7.19 Potential energy surface of OH + 2,5-DMF calculated using Gaussian at the M06-2x/cc-pVTZ level of theory.

As described previously, and demonstrated in Chapter 6, the OH radical can undergo barrierless addition to the aromatic furan ring at sites C2 or C3 to produce radical resonance stabilised products. The PES shows the favoured reaction pathway at low temperatures is the addition at the C2 site, resulting in an energy of $-156.4 \text{ kJ mol}^{-1}$ relative to the reactants. The resulting adduct can undergo a β -scission ring opening to the product with the energy of $-139.7 \text{ kJ mol}^{-1}$, through a transition state with the energy of $-73.9 \text{ kJ mol}^{-1}$ relative to the reactants. Addition to the C3 site produces an adduct species with the energy of $-76.9 \text{ kJ mol}^{-1}$. A scan of the pathway of C3 reveals a loss of an H atom through transition state TS3 (54.4 kJ mol^{-1}) leading to a radical ring product with the energy of 36.5 kJ mol^{-1} .

OH can also interact with 2,5-DMF by abstracting an H atom from either the C1 methyl group or the C3 ring site; both attacks result in the formation of a water molecule and resonance stabilised radical products. For the methyl group abstraction, the PES shows an energy barrier of 11 kJ mol^{-1} (TS2) to the products and water which lie at an energy of $-116.4 \text{ kJ mol}^{-1}$. In comparison to the energies reported by Simmie and Metcalfe, the barriers are in reasonable agreement (11 vs 15.5 kJ mol^{-1}), however, the energy

calculated for the products is higher than that reported by Simmie and Metcalfe (-116.6 vs -133.1 kJ mol⁻¹). For the C3 site abstraction, this work found a barrier of 41.2 kJ mol⁻¹ through transition state TS4 to products at 13.5 kJ mol⁻¹, compared to a barrier of 26.6 kJ mol⁻¹ to products at 6.4 kJ mol⁻¹.

Results from this work support the suggestion made by Bierbach *et al.*⁵ that resonance stabilisation controls which addition site is favoured. The substituted C2 addition site is preferred as it leads to an additional resonance stabilised structure. This reaction channel dominates at the temperatures studied (298-635 K); however, as the temperature rises, there is enough energy within the system to activate the abstraction channels. These channels come into competition resulting in the negative temperature dependence observed throughout the experiment.

7.4.2 Master Equation Calculations of OH + Furan

The following master equation analysis uses experimental results for the OH + furan reaction carried out in this work, the result of which are described in Chapter 4. Due to the availability of potential energy surfaces in the literature, a new surface for the OH + furan reaction was not calculated. The PES by Mousavipour *et al.*⁶ at the CCSD/6-311+G(3df,2p) level of theory was employed. Rate coefficients were calculated using MESMER.

As Mousavipour *et al.* deduced from their own master equation calculations, rate coefficients of channels other than the addition to the C1 carbon are not significant at temperatures below 2000 K, and so only the C1 addition channels will be considered here. These relevant channels are shown in Figure 7.20 and the structures of the C1 and ring-opening products P1 and P2 are shown in Figure 7.21.

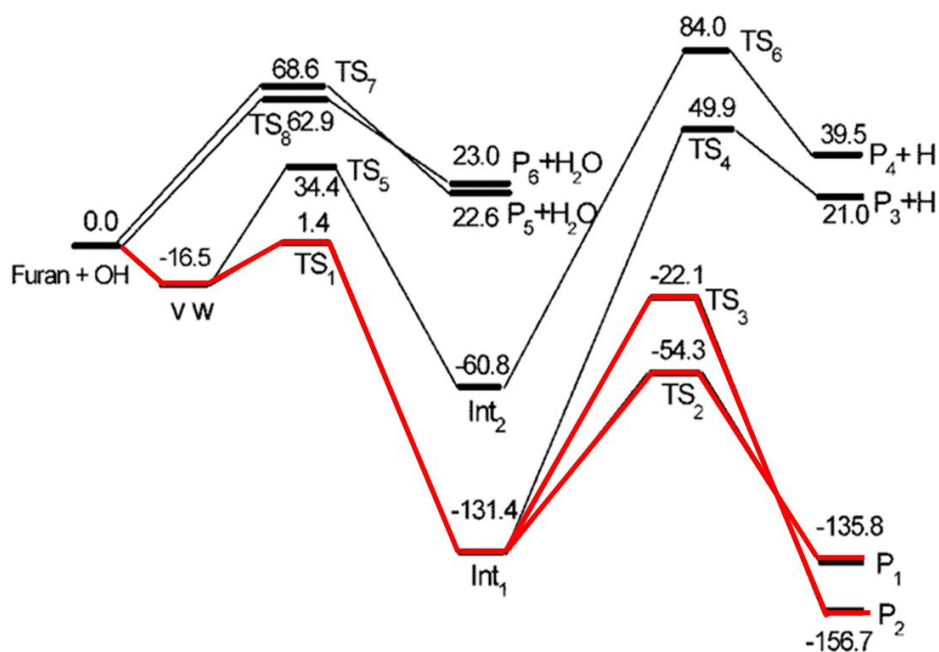


Figure 7.20 Schematic energy diagram of the potential energy surface of OH + furan in kJ mol^{-1} at the CCSD/6-311+G(3df,2p) level of theory by Mousavipour *et al.*⁶ Highlighted addition channels are those relevant temperatures below 2000 K.

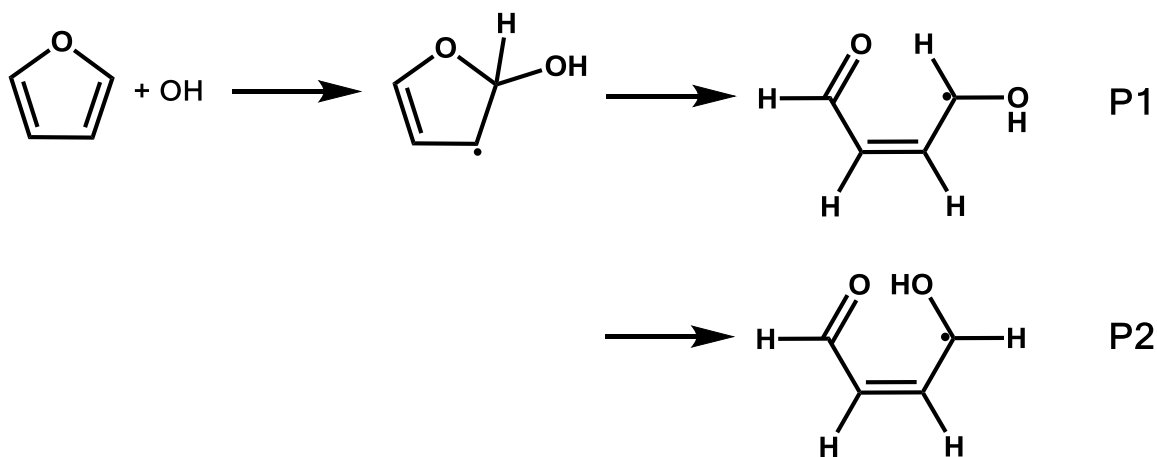


Figure 7.21 Ring-opening products reported by Mousavipour *et al.*⁶ from the addition of OH to the C1 site in furan.

The experimental data was fit to these channels using the Levenberg–Marquardt fitting routine found in MESMER:

$$\chi^2 = \sum_i \frac{(k_{\text{exp}}(\rho_i, T_i) - k_{\text{mod}}(\rho_i, T_i))^2}{\sigma_i^2} \quad \text{E7.2}$$

where $k_{\text{exp}}(p_i, T_i)$ and $k_{\text{mod}}(p_i, T_i)$ are the experimental and modelled rate coefficients at pressure p_i and temperature T_i , respectively, with σ_i^2 representing the appropriate experimental uncertainty.

An exponential down model was utilised to describe the collisional energy transfer within the system, with the average energy transferred in a downward direction on collision with the bath gas represented by $\langle \Delta E \rangle_{\text{down}}$. As experimental rate coefficients were found to be independent of pressure, the system is not sensitive to $\langle \Delta E \rangle_{\text{down}}$. A value of 400 cm^{-1} was used in the results presented below. The barrierless association reaction was treated as an inverse Laplace transform (ILT) and was fitted to the experimental data, resulting in a pre-exponential factor of $A = (3.20 \pm 0.25) \times 10^{-11} \text{ cm}^3 \text{ molecule}^{-1} \text{ s}^{-1}$ and a temperature exponent of $n = (-1.00 \pm 0.25)$.

Figure 7.22 shows the rate coefficients calculated by MESMER against the observed rate coefficients from the experiment in Chapter 4. Results are summarised in the Appendix. The slope of the line of best fit was determined as (0.92 ± 0.06) and the intercept was determined as $(1.55 \pm 1.34) \times 10^{-12} \text{ cm}^3 \text{ molecule}^{-1} \text{ s}^{-1}$.

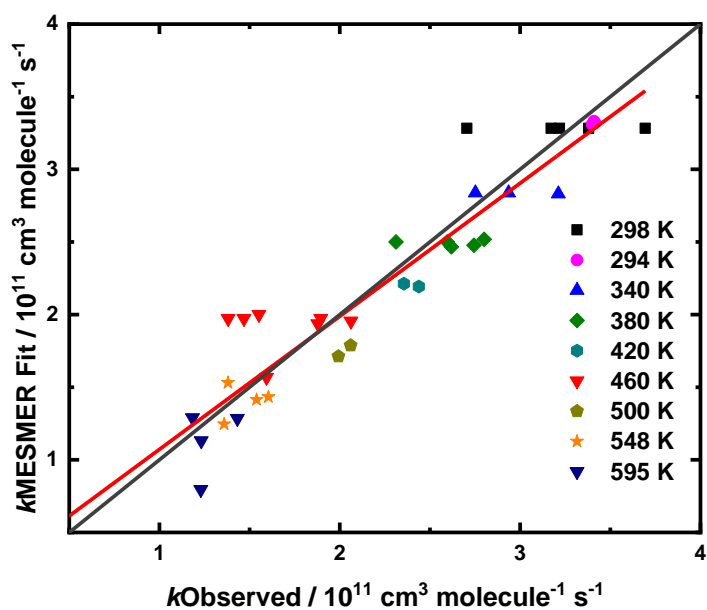


Figure 7.22 Rate coefficients for OH + furan calculated by MESMER against the observed rate coefficients from the experiment of Chapter 4. The grey line shows a 1:1 fit. The slope of the line of best fit was determined as (0.92 ± 0.06) and the intercept was determined as $(1.55 \pm 1.34) \times 10^{-12} \text{ cm}^3 \text{ molecule}^{-1} \text{ s}^{-1}$.

The optimised values for A and n were used in MESMER simulations to determine the rate coefficients at temperatures between 298 and 700 K. Simulated rate coefficients are shown in Figure 7.23. The MESMER simulated rate coefficients are within the statistical error of the experimental results at temperatures between 298 K and 420 K, however, there is a slight deviation from the experimental results at the higher temperatures.

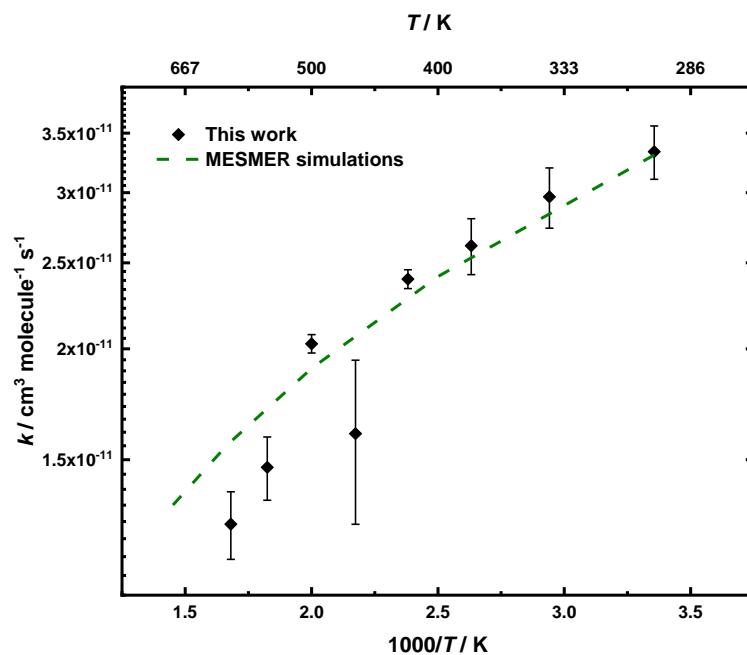


Figure 7.23 Rate coefficients for OH + furan simulated in MESMER (dashed green line) and the comparison with the experimental results discussed in Chapter 4 (black diamonds).

The calculated rate coefficients were parameterised by the expression $k = 2.17 \times 10^{-8} T^{-1.13} \exp(171.3/RT) \text{ cm}^3 \text{ molecule}^{-1} \text{ s}^{-1}$. The rate coefficients from this parameterisation fall within the 95 % confidence limits of the Arrhenius expression to the experimental results (Figure 7.24).

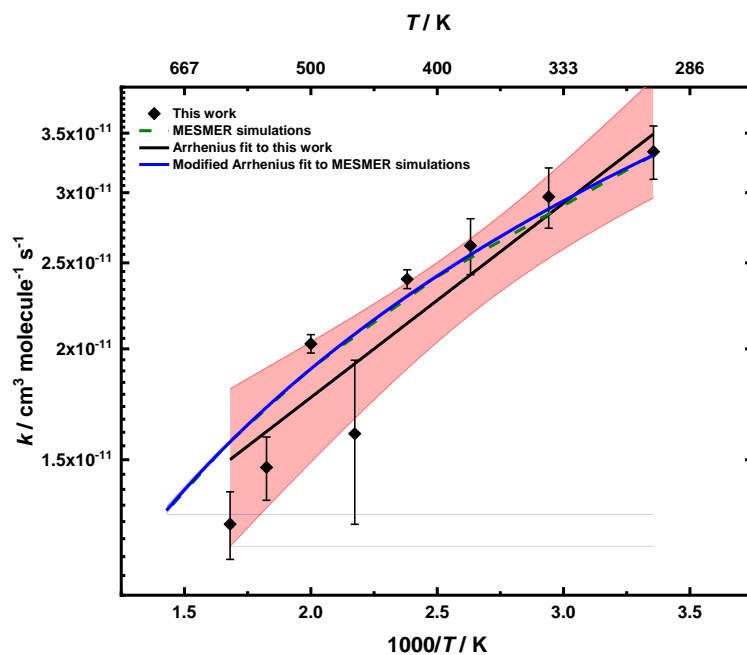


Figure 7.24 Modified Arrhenius fit to MESMER simulations for OH + furan (blue line, green dashed line) and unmodified Arrhenius fit to experimental results (black line, black diamonds) with associated 95 % confidence limits.

The yields of specific reaction channels calculated by MESMER suggest that addition channels dominate over the experimental conditions (Figure 7.25). Abstraction channels do not become significant until 2100 K, which is in agreement with the results reported by Mousavipour *et al.*⁶

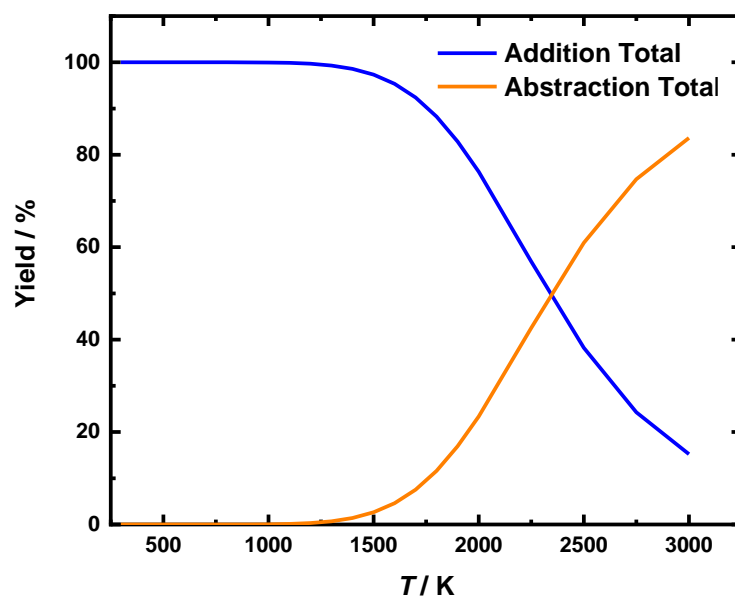


Figure 7.25 Yields for addition and abstraction channels for OH + furan predicted by MESMER at temperatures from 298 to 3000 K. The blue line represents addition and the orange line represents abstraction.

7.4.3 Master Equation Calculations of OH + 2-MF

The PES for the reaction of OH + 2-MF was discussed previously. In the surfaces calculated by Zhang *et al.*²⁰ and Davis and Sarathy²¹ the OH addition to the C2 and C5 positions were most energetically favoured. This was also found in the *ab initio* calculation carried out in this work where the C2 and C5 adducts were found to have energies of $-159.2 \text{ kJ mol}^{-1}$ and $-157.7 \text{ kJ mol}^{-1}$, respectively (Figure 7.26).

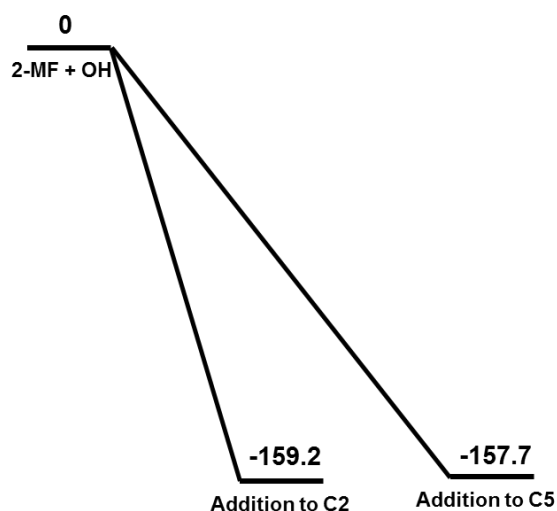


Figure 7.26 Schematic the C2 and C5 OH addition channels from a PES at the M06-2x/cc-pVTZ level.

In contrast to OH + furan, where there is a dominant addition site (Figure 7.20), the two possible addition sites in 2-MF have similar energies, resulting in difficulty when applying master equation analysis to the PES. It was not possible to fit experimental results using both channels described by ILT parameters, therefore, only the C2 addition channel was activated and it is assumed that there would be a near equal split of results between the C2 and C5 channels.

Similarly to OH + furan, a typical value $\langle \Delta E \rangle_{\text{down}}$ value of 400 cm^{-1} was chosen as the system is independent of pressure and thus not sensitive to the collisional energy transfer. The C2 channel was fit to the experimental data, resulting in a pre-exponential factor of $A = (6.68 \pm 1.52) \times 10^{-11} \text{ molecule}^{-1} \text{ cm}^3 \text{ s}^{-1}$ and a temperature exponent of $n = (-0.87 \pm 0.67)$. Figure 7.27 shows the rate coefficients calculated by MESMER against the observed rate coefficients from the experiment in Chapter 5. The slope of the line of best fit was determined as 0.98 ± 0.05 and the intercept was determined as $(3.60 \pm 21.6) \times 10^{-13} \text{ cm}^3 \text{ molecule}^{-1} \text{ s}^{-1}$.

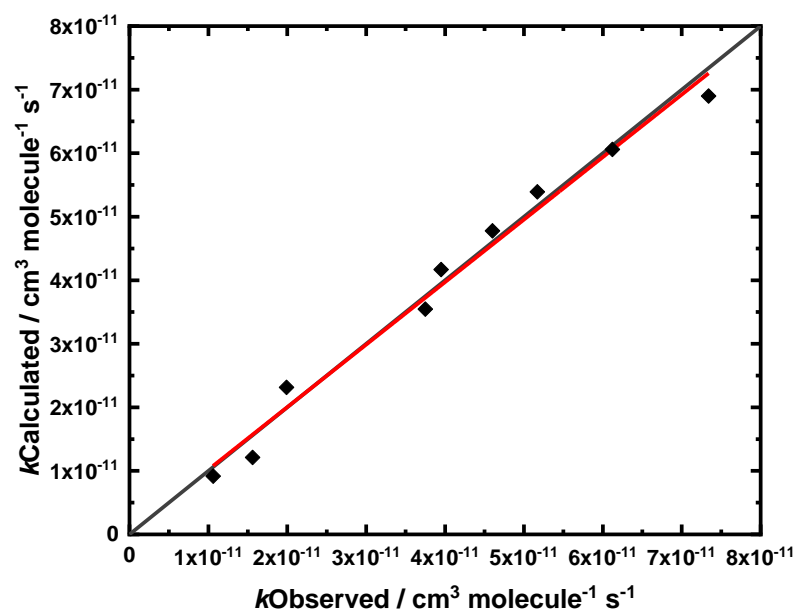


Figure 7.27 Rate coefficients for OH + 2-MF calculated by MESMER against the observed rate coefficients from the experiment discussed in Chapter 5. The grey line shows a 1:1 fit. The slope of the line of best fit was determined as 0.98 ± 0.05 and the intercept was determined as $(3.60 \pm 21.6) \times 10^{-13} \text{ cm}^3 \text{ molecule}^{-1} \text{ s}^{-1}$.

The optimised values for A and n were used in MESMER simulations to determine the rate coefficients at temperatures between 298 and 700 K. Simulated rate coefficients are shown in Figure 7.28. The MESMER simulated rate coefficients are within the statistical error of the experimental results at temperatures between 298 K and 580 K. The simulated rate coefficients are slower than the experimental rate coefficients at 680 and 770 K.

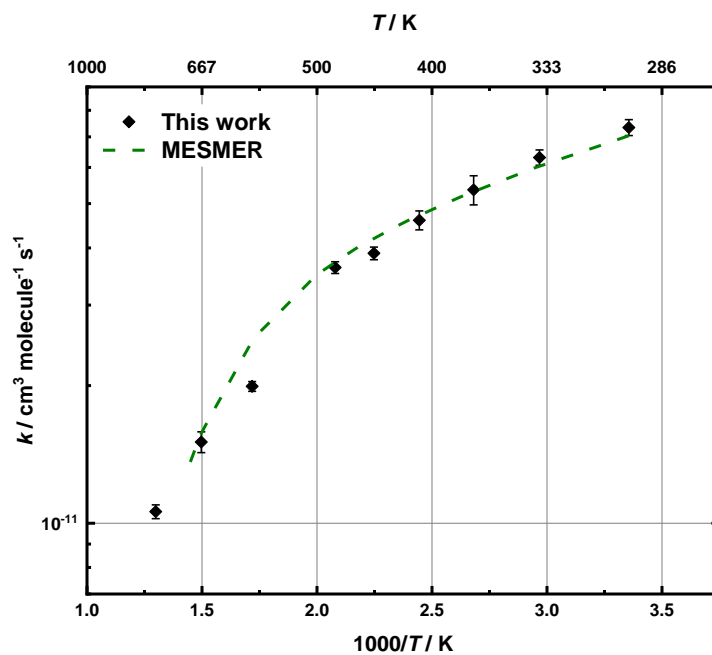


Figure 7.28 Rate coefficients for OH + 2-MF simulated in MESMER (dashed green line) and the comparison with the experimental results of Chapter 5 (black diamonds).

The calculated rate coefficients were parameterised using the modified Arrhenius expression resulting in a rate coefficient of $k = 8.57 \times 10^6 T^{-5.90} \exp(-14300/RT) \text{ cm}^3 \text{ molecule}^{-1} \text{ s}^{-1}$. From Figure 7.29 it can be seen that the experimental results lie within the statistical error of the parameterisation.

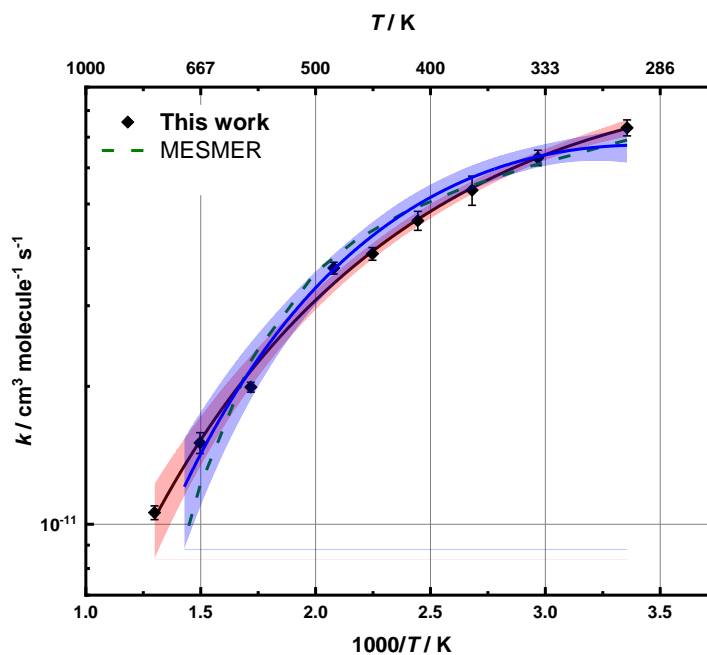


Figure 7.29 Modified Arrhenius fit to MESMER simulations of OH + 2-MF (blue line, green dashed line) and experimental results (black line, black diamonds) with associated 95 % confidence limits.

When looking at the yields of individual reaction channels in the OH + 2-MF system predicted by MESMER, the abstraction channels appear to dominate at temperatures above ~ 465 K. This results from the lower barrier to the abstraction from the methyl group (4 kJ mol^{-1}) compared to OH + furan, where the lowest barrier to abstraction is 62.9 kJ mol^{-1} . The experimental results also indicate some contribution from abstraction reactions at similar temperatures, with the rate coefficient decreasing faster from 500-700 K when compared to 298-500 K, indicating non-Arrhenius behaviour with the temperature dependent trend reversing from negative to positive at ~ 780 K.

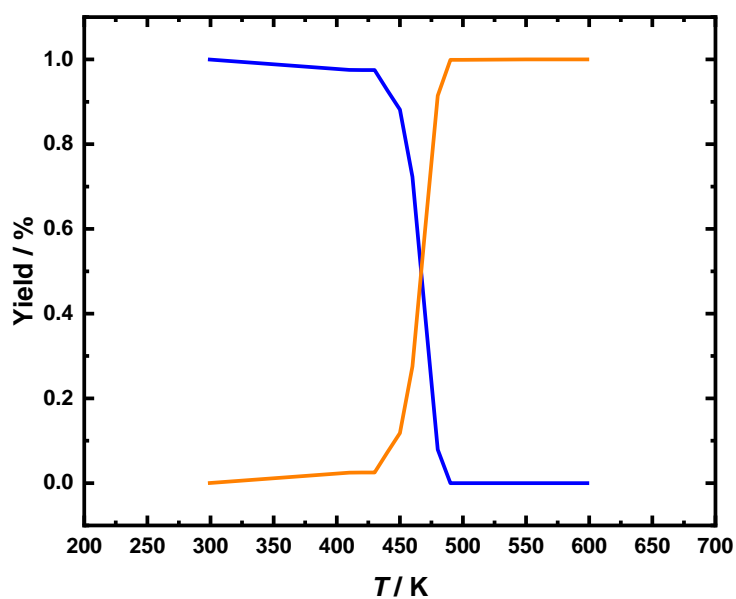


Figure 7.30 Yields for addition and abstraction channels predicted by MESMER for the reaction of OH + 2-MF at temperatures from 298 to 600 K. Blue line represents the total addition of OH to the furan ring. Orange line represents the total H atom abstraction by OH.

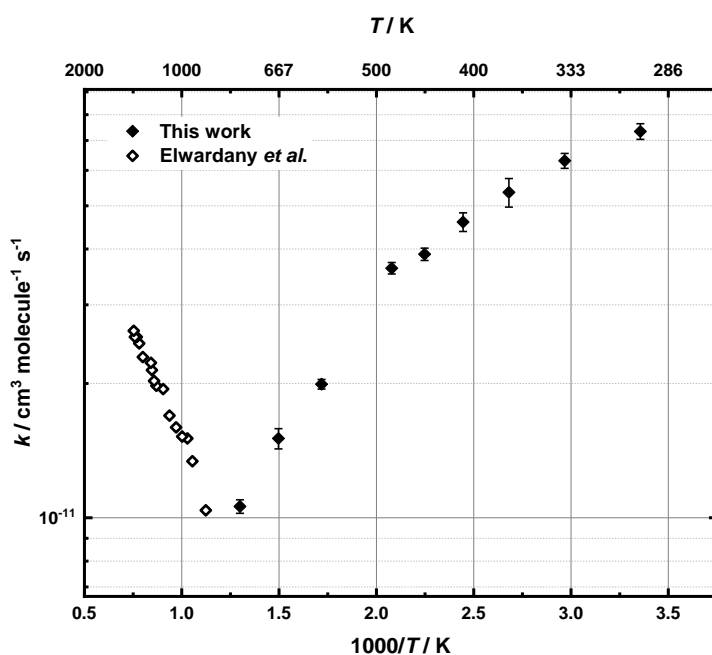


Figure 7.31 Experimental results for OH + 2-MF from this study (solid diamonds) and shock tube experiments by Elwardany *et al.*³⁵ (open diamonds). The temperature dependence of the reaction begins to turn over at ~ 780 K.

7.4.4 Master Equation Calculations of OH + 2,5-DMF

For the reactions involving 2,5-DMF, *ab initio* calculations were performed to determine the PES at the M06-2x/cc-pVTZ level of theory. The PES was used with master equation calculations to assess the kinetics of OH + 2,5-DMF over a range of temperatures and pressures and to compare with experimental observations described in Chapter 6. Master equation calculations were performed using the MESMER program.

The full surface was fit to the experimental data and showed no sensitivity towards the H abstraction channels or the OH addition to the C3 position under conditions seen experimentally, therefore, to save computational expense, the detailed fitting of the experimental data was carried out the OH addition to the C1 channel only.

The experimental data was fit to the C1 addition channels using the Levenburg Marquart fitting routine found in MESMER (E7.2). Both the barrier height to the ring-opening product P1 and the $\langle \Delta E \rangle_{\text{down}}$ were varied since the experimental results displayed both temperature and pressure dependence. From the data fitting the barrier was determined as $\text{TS1} = (-75.50 \pm 10.6) \text{ kJ mol}^{-1}$, which is within error of the *ab initio* barrier height of $-73.9 \text{ kJ mol}^{-1}$, and a $\langle \Delta E \rangle_{\text{down}}$ in N_2 of $(395 \pm 54) \text{ cm}^{-1}$. The barrierless association to the C1 adduct was treated as an ILT and also fitted to the data, resulting in a pre-exponential factor of $A = (1.07 \pm 0.09) \times 10^{-10} \text{ molecule}^{-1} \text{ cm}^3 \text{ s}^{-1}$ and a temperature exponent of $n = (-0.97 \pm 0.41)$. Figure 7.32 shows the rate coefficients calculated by MESMER against the observed rate coefficients from the experiment. The slope of the line of best fit was determined as (1.09 ± 0.04) and the intercept was determined as $(6.18 \pm 2.42) \times 10^{-12} \text{ cm}^3 \text{ molecule}^{-1} \text{ s}^{-1}$.

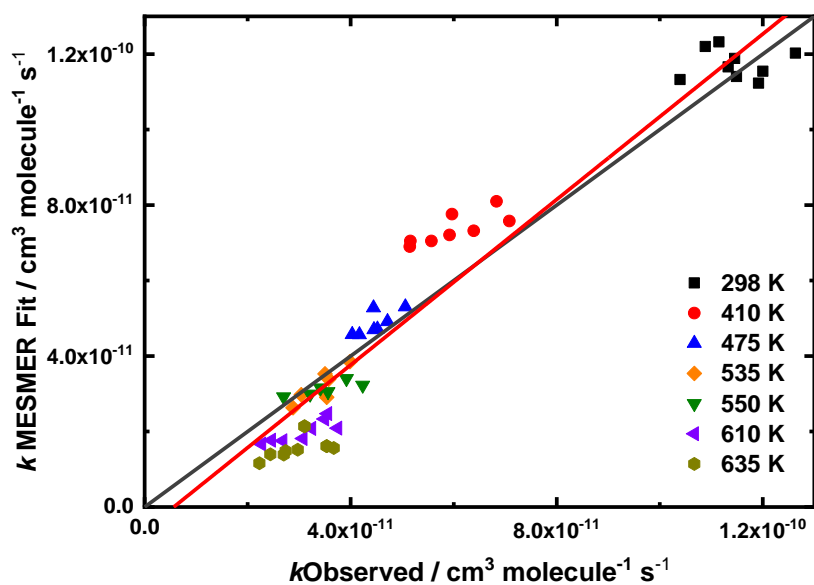


Figure 7.32 Rate coefficients for OH + 2,5-DMF calculated by MESMER against the observed rate coefficients from the experiment of Chapter 6. The grey line shows a 1:1 fit. The slope of the line of best fit was determined as 1.09 ± 0.04 and the intercept was determined as $(6.18 \pm 2.42) \times 10^{-12} \text{ cm}^3 \text{ molecule}^{-1} \text{ s}^{-1}$.

The optimised values for the TS1, $\langle \Delta E \rangle_{\text{down}}$, A and n were used to simulate rate coefficients of OH + 2,5-DMF at temperatures between 298 and 700 K and pressures from 10 to 150 Torr.

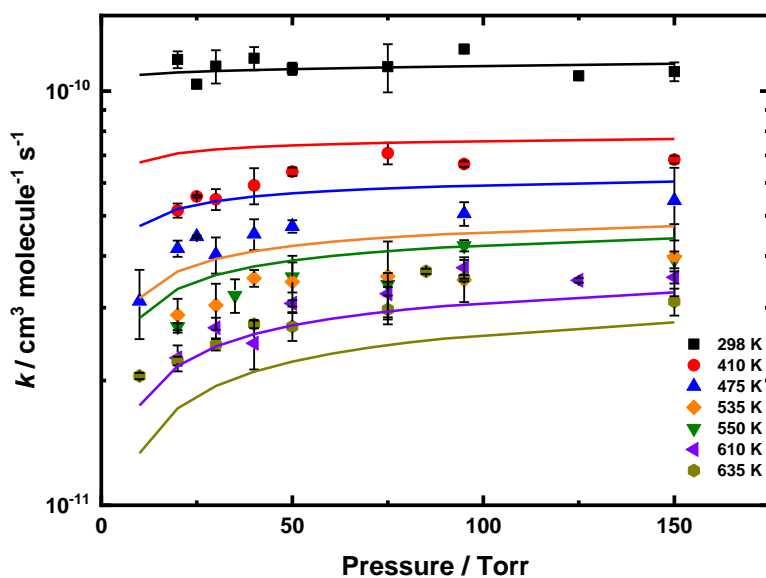


Figure 7.33 Pressure and temperature dependent results of OH + 2,5-DMF discussed in Chapter 6 (diamonds) with MESMER simulated rate coefficients (lines)

The calculated rate coefficients were parameterised using the Troe expression for broad falloff curves³⁶ (Equations 8.11-8.14) for use in kinetic models:

$$k = \frac{k_0[M]k_\infty}{k_0[M] + k_\infty} F \quad \text{E8.3}$$

$$F = \frac{\left(1 + k_0[M]/k_\infty\right)}{\left(1 + \left(k_0[M]/k_\infty\right)^n\right)^{1/n}} \quad \text{E8.4}$$

$$n = \left(\frac{\ln(2)}{\ln(2/F_c)}\right) \left((1-b) + b \left(k_0[M]/k_\infty\right)^q\right) \quad \text{E8.5}$$

$$q = \frac{(F_c - 1)}{\ln(F_c/10)} \quad \text{E8.6}$$

where $k_0(T)$ is the low-pressure and $k_\infty(T)$ is the high-pressure limiting rate coefficients, M is the total number density, and F_c is the broadening factor. The fits to the MESMER output for k are shown in Figure 7.34 and give $k_0 = 1.77 \times 10^{-24} (T/298)^{-10.8} \exp(3545/T) \text{ cm}^3 \text{ s}^{-1}$, $k_\infty = 4.70 \times 10^{-11} (T/298)^{-0.36} \exp(255/T) \text{ s}^{-1}$, $F_c = 0.049$ and $b = 0.036$.

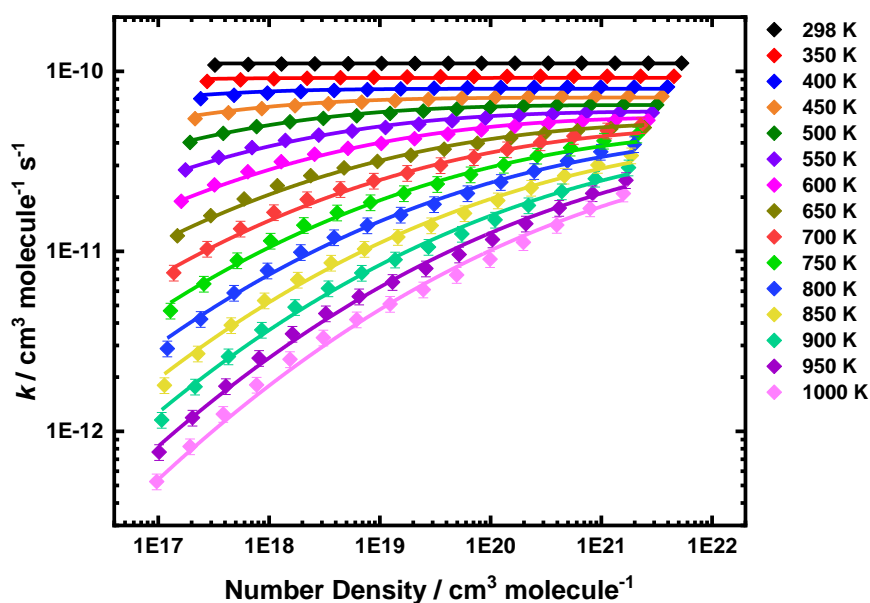


Figure 7.34 Troe fits using E8.3-E8.6 (solid lines) to MESMER simulations for kinetics of OH + 2,5-DMF (solid diamonds) using a barrier height of $-75.5 \text{ kJ mol}^{-1}$ in with $\langle \Delta E \rangle_{\text{down}} = 395 \text{ cm}^{-1}$ and $A = 1.07 \times 10^{-10} \text{ molecule}^{-1} \text{ cm}^3 \text{ s}^{-1}$.

Yields for specific reaction channels in OH + 2,5-DMF calculated by MESMER suggest the C2 addition pathway dominates at temperatures up to 1500 K. This supports the suggestion made by Bierbach *et al.* that OH radical addition to the C2 is the favoured site of attack. Addition to the C3 position is not a pathway followed in this reaction, according to MESMER. The high energy C3 addition product seen in the PES could account for this, a significant energy difference ($\sim 100 \text{ kJ mol}^{-1}$) between the two addition products results in the C2 addition as the dominant pathway. Abstraction channel pathways, where OH radicals abstract an H atom from either the C1 methyl group or from the furan ring at C3, are not significant until temperatures of 900 K and do not become the dominant channels until 1500 K, according to MESMER, as seen in Figure 7.35. This predicted behaviour reflects what has been observed experimentally (Chapter 6), where two temperature regimes dictate the chemistry of the reaction.

When compared to the OH addition and abstraction yields determined by MESMER for the channels in the OH + furan system, the 2,5-DMF abstraction channels become significant at much lower temperatures (1500 K for 2,5-DMF vs 2100 K for furan). 2,5-

DMF (C₄H₈O) has more H atoms than furan (C₄H₄O), with 6 of these in methyl groups, which have a weaker bond dissociation energy than the hydrogens bonded to the furan ring (440 kJ mol⁻¹ vs 710 kJ mol⁻¹).³⁷

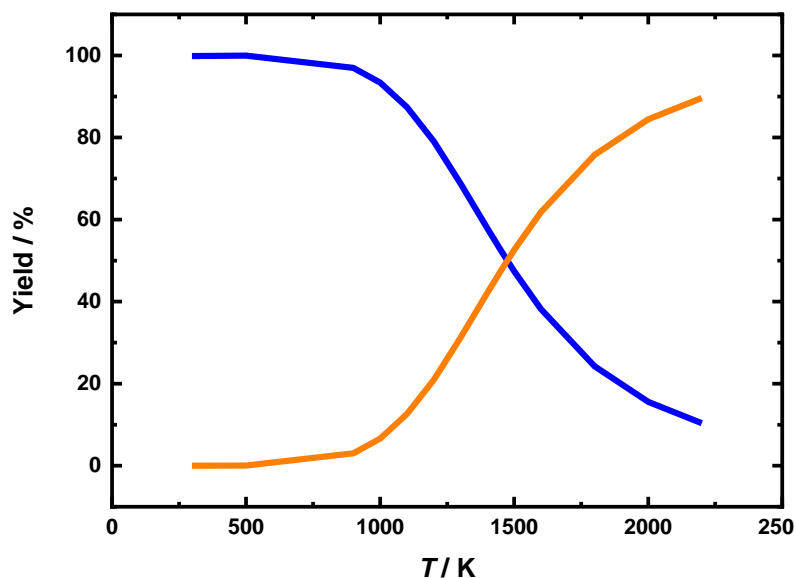


Figure 7.35 Yields for addition and abstraction channels predicted by MESMER for the reaction of OH + 2,5-DMF at temperatures from 298 to 2400 K. Blue line represents the addition of OH to the C2 position. Orange line represents abstraction of an H atom by OH at the C1 and C3 positions.

7.5 Conclusion

Master equation calculations have been performed on the experimental results described in Chapters 4-6 of this thesis. For the OH + furan system, the PES by Mousavipour *et al.* at the CCSD/6-311+G(3df,2p) level was utilised and MESMER master equation analysis was performed. MESMER calculations predicted rate coefficients that were in general agreement with the experimental results from 298 K to ~420 K. Although the simulated rate coefficients begin to diverge at higher temperatures, the MESMER rates were parameterised using the modified Arrhenius expression and the rate coefficient of $k = 2.17 \times 10^{-8} T^{1.13} \exp(171.3/RT)$ cm³ molecule⁻¹ s⁻¹ was found

to fall within the 95 % confidence limits of the unmodified Arrhenius fit to the experimental results.

For the OH + 2-MF system, *ab initio* calculations were performed at the M06-2x/cc-pVTZ level of theory and were found to be in agreement with the energies reported by Zhang *et al.* and Davis and Sarathy. Vibrational frequencies are agreement with those reported by Davis and Sarathy. MESMER analysis was performed on the C2 addition channel and simulated rate coefficients were found to be in good agreement with the experimental results of Chapter 5. The parameterisation of the simulated rate coefficients with a modified Arrhenius expression $k = 8.57 \times 10^6 T^{5.90} \exp(-14300/RT) \text{ cm}^3 \text{ molecule}^{-1} \text{ s}^{-1}$. OH addition and abstraction yields predicted by MESMER suggest abstraction channels begin to dominate at much lower temperatures than in the unsubstituted furan, which can be accounted for by the low energy barrier (4 kJ mol^{-1}) to the methyl H abstraction channel. From experiments, it is evident that the abstraction channels already have an effect at temperatures above 500 K, where the negative temperature dependent rate coefficient begins to turn over and become positive.

ab initio calculations were carried out to produce a PES of OH + 2,5-DMF at the M06-2x/cc-pVTZ level of theory. Master equation analysis gave a reasonable agreement with experimental results and MESMER simulated rate coefficients were produced for temperatures and pressures unattainable in current experiments. Simulated rate coefficients were parameterised according to the broad falloff Troe expression resulting in $k_0 = 1.77 \times 10^{-24} (T/298)^{-10.8} \exp(3545/T) \text{ cm}^3 \text{ s}^{-1}$ and $k_\infty = 4.70 \times 10^{-11} (T/298)^{-0.36} \exp(255/T) \text{ s}^{-1}$.

The focus of furan combustion models have thus far chiefly focused on the pyrolytic behaviour of furan fuels. If furans are to be employed as biofuels, models must reflect the true chemistry of the biofuels at low temperature in order to inform on engine design. Results presented in this work will provide the basis for such model calculations.

7.6 References

1. Glowacki, D.R., *et al.* MESMER: An Open-Source Master Equation Solver for Multi-Energy Well Reactions. *The Journal of Physical Chemistry A*, 2012, **116**(38), pp.9545-9560.
2. Anglada, J. The Gas Phase HO-Initiated Oxidation of Furan: A Theoretical Investigation on the Reaction Mechanism. *The Open Chemical Physics Journal*, 2008, **1**, pp.80-93.
3. M. J. Frisch, *et al.* Gaussian 09. 2009.
4. Frisch, M.J., M. Head-Gordon and J.A. Pople. A direct MP2 gradient method. *Chemical Physics Letters*, 1990, **166**(3), pp.275-280.
5. Bierbach, A., I. Barnes and K.H. Becker. Rate coefficients for the gas-phase reactions of hydroxyl radicals with furan, 2-methylfuran, 2-ethylfuran and 2,5-dimethylfuran at 300 K. *Atmospheric Environment Part a-General Topics*, 1992, **26**(5), pp.813-817.
6. Mousavipour, S.H., S. Ramazani and Z. Shahkolahi. Multichannel RRKM-TST and Direct-Dynamics VTST Study of the Reaction of Hydroxyl Radical with Furan. *The Journal of Physical Chemistry A*, 2009, **113**(12), pp.2838-2846.
7. Frisch, M., *et al.* Revision B. Gaussian. 2003.
8. Curtiss, L.A., *et al.* Gaussian-3 theory using reduced Møller-Plesset order. *The Journal of Chemical Physics*, 1999, **110**(10), pp.4703-4709.
9. Scuseria, G.E., C.L. Janssen and H.F.S. Iii. An efficient reformulation of the closed - shell coupled cluster single and double excitation (CCSD) equations. *The Journal of Chemical Physics*, 1988, **89**(12), pp.7382-7387.
10. Wine, P.H. and R.J. Thompson. Kinetics of OH reactions with furan, thiophene, and tetrahydrothiophene. *International Journal of Chemical Kinetics*, 1984, **16**(7), pp.867-878.
11. Atkinson, R. Kinetics and mechanisms of the gas-phase reactions of the hydroxyl radical with organic compounds under atmospheric conditions. *Chemical Reviews*, 1986, **86**(1), pp.69-201.
12. Tuazon, E., *et al.* A study of the atmospheric reactions of 1,3-dichloropropene and other selected organochlorine compounds. *Archives of Environmental Contamination and Toxicology*, 1984, **13**(6), pp.691-700.
13. Somers, K.P., *et al.* The pyrolysis of 2-methylfuran: a quantum chemical, statistical rate theory and kinetic modelling study. *Physical Chemistry Chemical Physics*, 2014, **16**(11), pp.5349-5367.
14. Somers, K.P., *et al.* A comprehensive experimental and detailed chemical kinetic modelling study of 2,5-dimethylfuran pyrolysis and oxidation. *Combustion and Flame*, 2013, **160**(11), pp.2291-2318.
15. Yuan, Y., *et al.* Atmospheric Oxidation of Furan and Methyl-Substituted Furans Initiated by Hydroxyl Radicals. *The Journal of Physical Chemistry A*, 2017, **121**(48), pp.9306-9319.
16. Walker, M., *et al.* Performance of M06, M06-2X, and M06-HF Density Functionals for Conformationally Flexible Anionic Clusters: M06 Functionals Perform Better than B3LYP for a Model System with Dispersion and Ionic Hydrogen-Bonding Interactions. *The Journal of Physical Chemistry A*, 2013, **117**(47), pp.12590-12600.
17. J. A. Montgomery Jr, M.J.F., J. W. Ochterski, G. A. Petersson. A complete basis set model chemistry. VII. Use of the minimum population localization method. *The Journal of Chemical Physics*, 2000, **112**(15), pp.6532-6542.
18. Atkinson, R., S.M. Aschmann and W.P.L. Carter. Kinetics of the reactions of O₃ and OH radicals with furan and thiophene at 298 ± 2 K. *International Journal of Chemical Kinetics*, 1983, **15**(1), pp.51-61.
19. Eble, J.S.R. *Ignition of oxygenated hydrocarbons: Mechanism and elementary steps*. thesis, Karlsruhe Institute of Technology (KIT), 2017.

20. Zhang, W., *et al.* Computational study on the mechanism for the reaction of OH with 2-methylfuran. *Journal of Molecular Structure: THEOCHEM*, 2008, **851**(1), pp.353-357.
21. Davis, A.C. and S.M. Sarathy. Computational Study of the Combustion and Atmospheric Decomposition of 2-Methylfuran. *The Journal of Physical Chemistry A*, 2013, **117**(33), pp.7670-7685.
22. Tsang, V.M.a.W. *ChemRate*. Gaithersburg, MD: National Institute of Standards and Technology, 2009.
23. Aschmann, S.M., *et al.* Kinetics of the Reactions of OH Radicals with 2- and 3-Methylfuran, 2,3- and 2,5-Dimethylfuran, and E- and Z-3-Hexene-2,5-dione, and Products of OH + 2,5-Dimethylfuran. *Environmental Science & Technology*, 2011, **45**(5), pp.1859-1865.
24. Simmie, J.M. and W.K. Metcalfe. Ab Initio Study of the Decomposition of 2,5-Dimethylfuran. *The Journal of Physical Chemistry A*, 2011, **115**(32), pp.8877-8888.
25. Barker, J.R. Multiple-Well, multiple-path unimolecular reaction systems. I. MultiWell computer program suite. *International Journal of Chemical Kinetics*, 2001, **33**(4), pp.232-245.
26. Cheng, Z., *et al.* Experimental and kinetic modeling study of 2,5-dimethylfuran pyrolysis at various pressures. *Combustion and Flame*, 2014, **161**(10), pp.2496-2511.
27. Togbé, C., *et al.* Combustion chemistry and flame structure of furan group biofuels using molecular-beam mass spectrometry and gas chromatography – Part III: 2,5-Dimethylfuran. *Combustion and Flame*, 2014, **161**(3), pp.780-797.
28. Somers, K.P., *et al.* A high temperature and atmospheric pressure experimental and detailed chemical kinetic modelling study of 2-methyl furan oxidation. *Proceedings of the Combustion Institute*, 2013, **34**(1), pp.225-232.
29. Tran, L.-S., *et al.* Combustion chemistry and flame structure of furan group biofuels using molecular-beam mass spectrometry and gas chromatography – Part II: 2-Methylfuran. *Combustion and Flame*, 2014, **161**(3), pp.766-779.
30. Tian, Z., *et al.* An experimental and kinetic investigation of premixed furan/oxygen/argon flames. *Combustion and Flame*, 2011, **158**(4), pp.756-773.
31. Heyberger, B., *et al.* Oxidation of small alkenes at high temperature. *International Journal of Chemical Kinetics*, 2002, **34**(12), pp.666-677.
32. Warth, V., *et al.* Computer-Aided Derivation of Gas-Phase Oxidation Mechanisms: Application to the Modeling of the Oxidation of n-Butane. *Combustion and Flame*, 1998, **114**(1), pp.81-102.
33. Liu, D., *et al.* Combustion chemistry and flame structure of furan group biofuels using molecular-beam mass spectrometry and gas chromatography – Part I: Furan. *Combustion and Flame*, 2014, **161**(3), pp.748-765.
34. Atkinson, R. and J. Arey. Atmospheric Degradation of Volatile Organic Compounds. *Chemical Reviews*, 2003, **103**(12), pp.4605-4638.
35. Elwardany, A., *et al.* A chemical kinetic study of the reaction of hydroxyl with furans. *Fuel*, 2016, **166**, pp.245-252.
36. Troe, J., V.G. Ushakov. Representation of "broad" falloff curves for dissociation and recombination reactions. *Z. Phys. Chem.*, 2014, **228**(1), pp.1-10.
37. Blanksby, S.J. and G.B. Ellison. Bond Dissociation Energies of Organic Molecules. *Accounts of Chemical Research*, 2003, **36**(4), pp.255-263.

Chapter 8 Temperature and Pressure Dependent Kinetics of QOOH Decomposition and Reaction with O₂: Experimental and Theoretical Investigations of QOOH Radicals Derived from Cl + *t*-BuOOH

8.1 Background and Previous Work

Fuel chemistry plays a central role in autoignition processes and low temperature combustion strategies designed to lower NO_x (NO_x = NO + NO₂) emissions and soot formation. This chemistry is key to the development and efficient use of alternative fuels, and is dominated by reactions involving QOOH carbon-centred radicals.^{1,2}

Fuel consumption in low temperature combustion and autoignition is initiated through hydrogen-abstraction reactions, resulting in generation of radicals, R, which undergo recombination reactions with O₂ to produce peroxy radicals, RO₂. Isomerisation reactions of RO₂ radicals, involving internal H-atom shifts, produce carbon-centred hydroperoxy radicals, QOOH, which dictate the balance between propagation and branching of the radical chain reactions. Decomposition of QOOH, producing a cyclic ether and an OH radical for alkyl hydroperoxy radicals, propagates the radical chain reactions. In competition with QOOH decomposition, addition of O₂ to the QOOH radical centre leads to the production of O₂QOOH, the decomposition of which generate a ketohydroperoxide and OH. The subsequent decomposition of the ketohydroperoxide to produce further OH gives rise to chain branching. This chemistry is summarised in Figure 8.1. Chain branching is the pivotal process in autoignition, and the QOOH radical chemistry is thus of fundamental importance in fuel combustion. In addition, the impact of auto-oxidation processes involving gas phase QOOH radicals in atmospheric oxidation processes on the formation of highly oxygenated molecules (HOMs) and aerosol particles is receiving increasing recognition.³

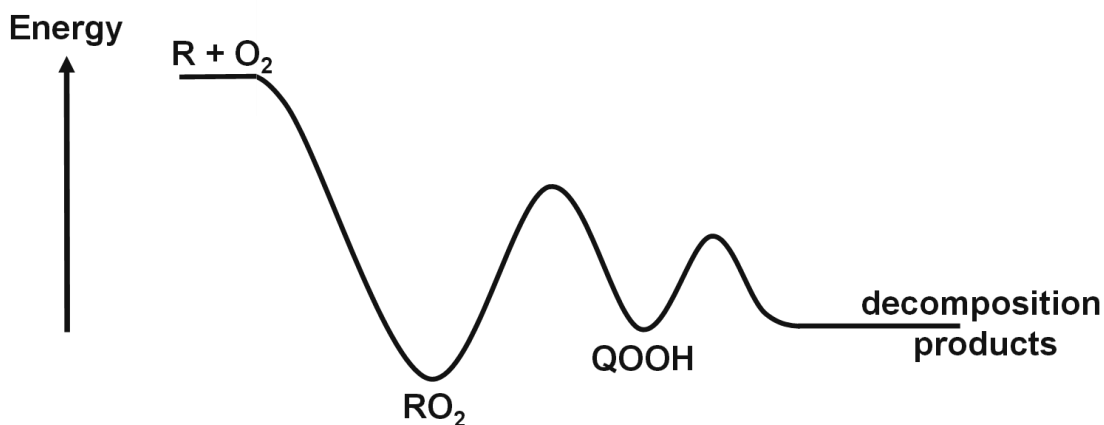
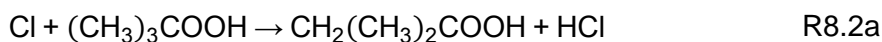
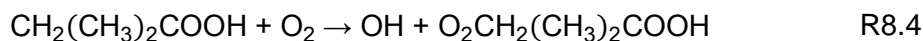
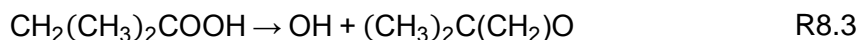


Figure 8.2 Schematic potential energy surface showing the relationship between RO_2 and QOOH.

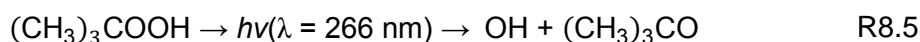
Zádor *et al.*⁸ reported the first direct measurements of any QOOH reaction kinetics. Critically, Zádor *et al.* were able to produce the $\cdot\text{CH}_2(\text{CH}_3)_2\text{COOH}$ (2-hydroperoxy-2-methylprop-1-yl) QOOH radical directly *via* abstraction of hydrogen from the C-H bonds in *t*-butyl hydroperoxide ($(\text{CH}_3)_3\text{COOH}$) by chlorine atoms (R8.1-R8.2a):



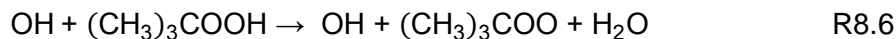
Rates of QOOH radical decomposition (R8.3) and reaction with O_2 (R8.4) were determined using infrared absorption spectroscopy to monitor the production of OH radicals:



While production of OH was observed through photolysis of $(\text{CH}_3)_3\text{COOH}$ (R8.5),⁹ the photolytic production occurred on a much shorter timescale than that through R8.3, enabling separation of the timescale of OH production from QOOH loss (R8.3 and R8.4) from the photolytic process:



Loss of OH from the system occurs through reaction with (CH₃)₃COOH (R8.6), which, in contrast to the H-atom abstraction by Cl, has been indicated by experiment⁹ and theory¹⁰ to occur exclusively at the O-H bond:⁸



Infrared absorption measurements of OH by Zádor *et al.*⁸ thus enabled determination of the kinetics of QOOH decomposition (R8.3) and QOOH + O₂ (R8.4), and the first direct kinetic measurements for any QOOH species. Moreover, experiments using the MPIMS technique were also able to identify the cyclic ether ((CH₃)₂C(CH₂)O, 2,2-dimethyloxirane, DMO) product of the QOOH decomposition (R8.3), and daughter ions of the O₂QOOH (O₂CH₂(CH₃)₂COOH) product of QOOH + O₂ (R8.4).

The unimolecular decomposition of QOOH (R8.3) was shown to be pressure dependent over the range 8 – 90 Torr in He at room temperature, with a combination of experimental data and high-level calculations giving k_3^0 (298 K) = $5.89 \times 10^{-13} \text{ cm}^3 \text{ s}^{-1}$, k_3^∞ (298 K) = $4.80 \times 10^4 \text{ s}^{-1}$ and $F_c = 0.544$ in He, with a dissociation barrier of 48.1 kJ mol⁻¹ (11.5 kcal mol⁻¹). The reaction between QOOH and O₂ (R8.4) was shown to be independent of pressure in the range 4 – 90 Torr He, with the MPIMS experiments at 4 Torr giving $k_4 = 1.1 \times 10^{-12} \text{ cm}^3 \text{ s}^{-1}$ and the OH absorption experiments between 8 and 90 Torr giving $k_4 = 8.5 \times 10^{-13} \text{ cm}^3 \text{ s}^{-1}$. Combination of the results from the two techniques gave $k_4 = (9.0 \pm 3.0) \times 10^{-13} \text{ cm}^3 \text{ s}^{-1}$ at 298 K. Theoretical investigation of the potential energy surface (PES) for the system indicated barrierless production of O₂QOOH in R8.4, with stabilisation of the O₂QOOH species resulting in no further radical production under the experimental conditions as the internal abstraction required before radical production has a significant energy barrier, making the O₂QOOH stable at 300 K, in agreement with calculations for other similar systems.¹¹

The PES reported by Zádor *et al.* can be seen in Figure 8.3, showing the fate of the *tert*-butyl radical, R. Relevant stationary points on the PES of the QOOH decomposition and

of subsequent reactions with O₂ were characterised at the CBS-QB3 level of theory, with the exception of the barrier from the QOOH radical decomposition to the DMO and OH products which was calculated at the QCISD(T)/CBS//M06-2X/6-311++G(d,p) level of theory. The CBS-QB3 and M06-2X calculations were carried out using the Gaussian09¹² program. The barrier for the QOOH decomposition to DMO + OH was found to be 12.5 kcal mol⁻¹ (52.3 kJ mol⁻¹).

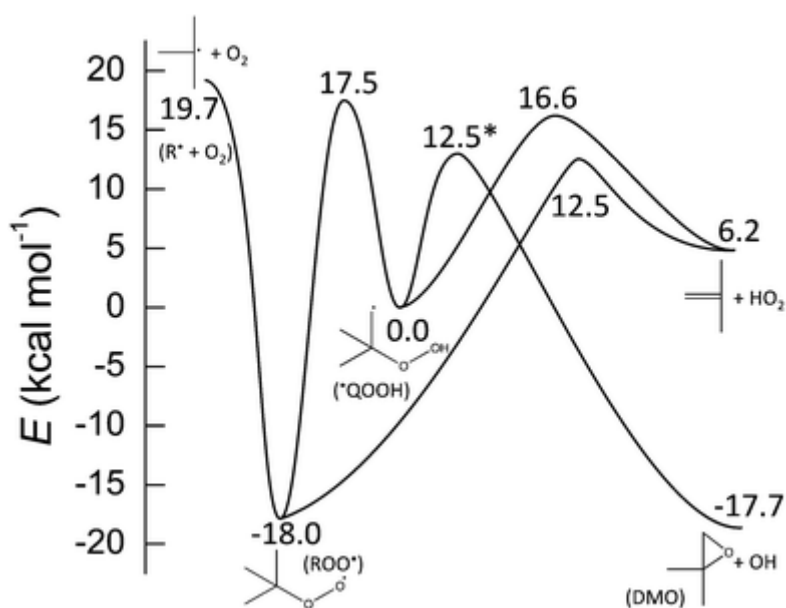


Figure 8.3 PES showing the isomerization and dissociation pathways of the QOOH from adapted from Zádor *et al.*⁸

Moore *et al.*¹³ also carried out a theoretical study into the behaviour of QOOH formed from a *t*-butyl radical in autoignition. Geometries and vibrational frequencies for the key R + O₂ and QOOH + O₂ pathways were calculated at the CCSD(T)/ANO0 level of theory and energies were calculated relative to R + O₂ to an accuracy of ± 1 kcal mol⁻¹ via extrapolation of RCCSD(T) energies. Moore *et al.* report the favoured decomposition channel for QOOH radicals leads to DMO + OH with a barrier of 12 kcal mol⁻¹ (52.3 kJ mol⁻¹) which is in agreement with the energy reported by Zádor *et al.*

For the reaction pathways of QOOH radicals with O₂ Moore *et al.* investigated three pathways: α -hydrogen abstraction, γ -hydrogen abstraction and hydrogen transfer to the

peroxy moiety, with transition state barriers of 42.0 (175.73 kJ mol⁻¹), 27.0 (112.97 kJ mol⁻¹) and 24.4 kcal mol⁻¹ (102.09 kJ mol⁻¹) barrier, respectively.

This chapter describes an investigation of the temperature and pressure dependence of the kinetics of QOOH decomposition (R8.3) and of the reaction of QOOH with O₂ (R8.4) for the QOOH radical derived from Cl + (CH₃)₃COOH (R8.2a), using laser-induced fluorescence (LIF) spectroscopy to monitor the OH radical production in the system. Treatment of the reaction system using the Master Equation Solver for Multi-Energy Well Reactions (MESMER)¹⁴ is also reported, and is used to place the experimental results in context.

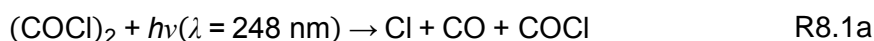
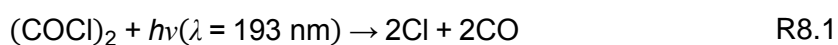
8.2 Experimental Procedure

Experiments were conducted in a slow-flow reactor described in Chapter 3 and detailed in a number of previous publications.¹⁵⁻¹⁷ Reactions were initiated by laser flash photolysis and monitored using laser-induced fluorescence (LIF) spectroscopy of OH reaction products. Precursor gas mixtures ((CH₃)₃COOH/(COCl)₂/He/O₂ or (CH₃)₃COOH/(COCl)₂/N₂/O₂) were prepared in a gas manifold and flowed into a reactor submerged in a bath. The total pressure in the reactor, monitored by a capacitance manometer, was controlled by a needle valve on the exhaust line to the pumps. The bath was filled with methanol which was cooled to the desired temperature by a refrigerated immersion probe (LabPlant Refrigerated Immersion Probe, RP-100CD), enabling control of sub-ambient reaction temperatures. Temperatures in the reactor were measured by K-type thermocouples situated close to the reaction zone.

A known flow of carrier gas (He or N₂) was passed through a bubbler containing degassed *t*-butylhydroperoxide ((CH₃)₃COOH) (Sigma Aldrich, 70 % v/v aqueous) to entrain (CH₃)₃COOH into the precursor gas flow. Oxalyl chloride ((COCl)₂, Sigma Aldrich ≥ 99 %) was prepared at a known concentration in He or N₂ and stored in a glass bulb.

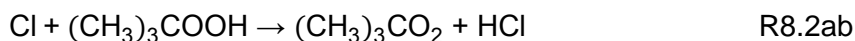
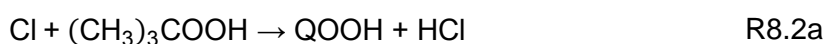
He (BOC, 99.99 %), N₂ (BOC, oxygen free, 99.99 %) and O₂ (BOC, 99.999 %) were used as supplied.

Reactions were initiated by pulsed excimer laser (Lambda Physik Compex) photolysis of (COCl)₂ at 193 nm or 248 nm. At a wavelength of 193 nm, photolysis of (COCl)₂ produces 2 Cl + 2 CO directly (R8.1), while at 248 nm the photolysis produces Cl + CO + COCl (R8.1a), which is followed by decomposition of the COCl fragment to produce CO + Cl (R8.1b):¹⁸

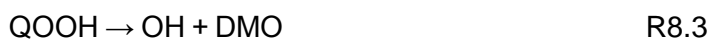


The majority of the experiments performed at a pulse repetition frequency of 10 Hz was employed, although experiments were conducted at lower repetition frequencies to ensure that there were no interferences from photolysis of reaction products.

QOOH (CH₂(CH₃)₂COOH) radicals were generated by the reaction of Cl atoms with (CH₃)₃COOH (R8.2a), with production of RO₂ radicals ((CH₃)₃CO₂, R8.2ab) through abstraction of the peroxide H-atom not contributing to observed kinetics in this work.



OH radicals, produced in the system by decomposition of QOOH radicals (R8.3) and photolysis of (CH₃)₃COOH (R8.5), were monitored by off-resonance laser-induced fluorescence (LIF) following excitation at 282 nm (A²Σ (v'=1) ← X²Π (v''=0), Q₁(1)).



Laser light at 282 nm was generated using the 532 nm output of an Nd:YAG (Continuum Powerlite 8010) to pump a dye laser (Spectra Physics PDL-3) operating on Rhodamine-6-G dye. The off-resonant OH fluorescence at ~308 nm was detected by a photomultiplier (Electron tube 9813 QB) mounted perpendicular to the plane of the photolysis and probe laser beams. The photomultiplier signal was digitized and integrated by an oscilloscope (LeCroy LT262), and passed to a computer for data analysis. The time delay between photolysis and probe laser pulses was controlled by a homebuilt digital delay generator based on National Instruments hardware and varied to enable monitoring of the OH profile as a function of time following photolysis of the gas mixture.

Experiments were performed at each temperature over a range of pressures (10 – 350 Torr) and concentrations of O₂ ($3.9 \times 10^{15} - 1.7 \times 10^{17} \text{ cm}^{-3}$). Precursor concentrations were also varied in the ranges $9.0 \times 10^{13} - 4.0 \times 10^{16} \text{ cm}^{-3}$ for (CH₃)₃COOH and $4.5 \times 10^{13} - 5.0 \times 10^{15} \text{ cm}^{-3}$ for (COCl)₂.

8.3 Analysis

The chemistry occurring within the system can be described through reactions R8.1-R8.6, and is summarised in Figure 8.4.

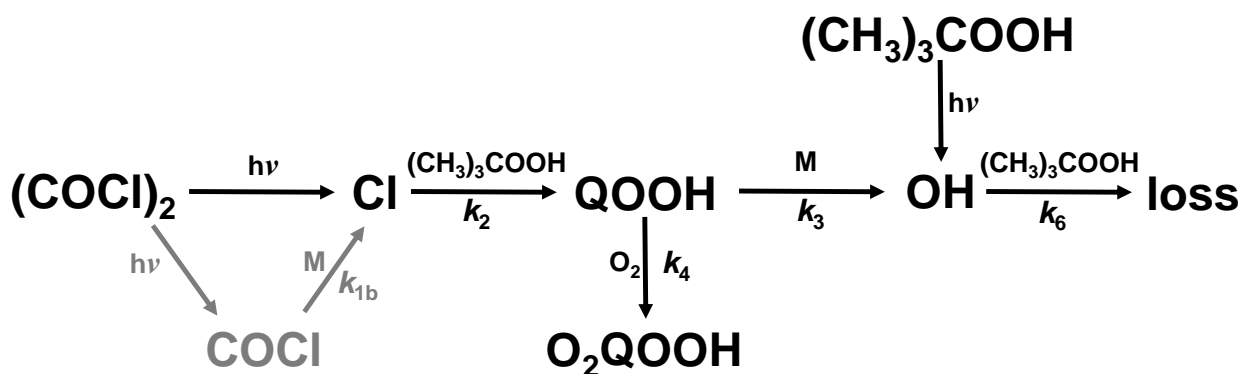


Figure 8.4 Summary of the relevant chemistry occurring within the reaction system. k_2 represents the rate coefficient for R8.2a and R8.2b, k_3 for R8.3, k_4 for R8.4 and k_6 for R8.6. Processes shown in grey occur only for photolysis at a wavelength of 248 nm.

The temporal profiles of OH can be described by the analytical expression given by E8.1:

$$S_{\text{OH}} = S_0 \exp(-k_{1b}[\text{M}]t) + S_1 \exp(-k'_2 t) + S_2 \exp(-(k_3 + k'_4) t) + S_3 \exp(-k'_6 t) \quad \text{E8.1}$$

where S_{OH} is the observed OH fluorescence signal, and is directly proportional to the OH concentration. The rate coefficient k_{1b} is that for the decomposition of COCl, which is constrained in the analysis to previous measurements,¹⁹ k'_2 is the pseudo-first-order rate coefficient for R8.2a (i.e. $k'_2 = k_2[(\text{CH}_3)_3\text{COOH}]$), k_3 is the rate coefficient for QOOH decomposition (R8.3), k'_4 is the pseudo-first-order rate coefficient for R8.4 ($k'_4 = k_4[\text{O}_2]$) since O_2 is in large excess over QOOH, and k'_6 is the pseudo-first-order rate coefficient describing the loss of OH from the system, which, although strictly includes any loss of OH through diffusion, is approximated here as being dominated by R8.6 (such that $k'_6 = k_6[(\text{CH}_3)_3\text{COOH}]$).

The coefficient S_0 is linked to the production of Cl, and subsequently OH, through the production and subsequent pressure-dependent decomposition of COCl at a photolysis wavelength of 248 nm. S_0 is given by E8.2:

$$S_0 = \frac{A_0 k_{1b} [M] k'_2 k_3}{(k'_2 - k_{1b} [M]) (k_3 + k'_4 - k_{1b} [M]) (k'_6 - k_{1b} [M])} \quad \text{E8.2}$$

where A_0 corresponds to the photolytic yield of COCl. At 193 nm, A_0 and S_0 are equal to zero and E8.1 can be simplified to E8.3:

$$S_{OH} = S_1 \exp(-k'_2 t) + S_2 \exp(-(k_3 + k'_4) t) + S_3 \exp(-k'_6 t) \quad \text{E8.3}$$

The coefficients S_1 , S_2 and S_3 in E8.1 and E8.2 are linked to the yields of OH through R8.2a, R8.3 and R8.5, respectively, through E8.4-E8.6:

$$S_1 = \frac{k'_2 k_3}{(k_3 + k'_4 - k'_2)(k'_6 - k'_2)} \left(A_1 - \frac{A_0 k_{1b} [M]}{(k'_2 - k_{1b} [M])} \right) \quad \text{E8.4}$$

$$S_2 = \frac{k'_2 k_3}{(k_3 + k'_4 - k'_2)} \left(\left(\frac{A_0 k_{1b} [M]}{(k_3 + k'_4 - k_{1b} [M])} \right) - A_1 \right) \left(\frac{1}{(k'_6 - k_3 - k'_4)} \right) \quad \text{E8.5}$$

$$S_3 = S_4 - S_0 - S_1 - S_2 \quad \text{E8.6}$$

where A_1 corresponds to the direct photolytic yield of Cl and S_4 corresponds to the photolytic signal for OH. At 193 nm, Equations E8.4-E8.6 simplify to E8.7-E8.9 since S_0 and A_0 are equal to zero:

$$S_1 = \frac{A_1 k'_2 k_3}{(k_3 + k'_4 - k'_2)(k'_6 - k'_2)} \quad \text{E8.7}$$

$$S_2 = \frac{A_1 k'_2 k_3}{(k_3 + k'_4 - k'_2)(k'_6 - k_3 - k'_4)} \quad \text{E8.8}$$

$$S_3 = S_4 - S_1 + S_2 \quad \text{E8.9}$$

Equations E8.1-E8.9 were derived by Dr Lavinia Onel by integration of the rate equations controlling OH in the system. Global fits of E8.1, with the coefficients S_1 , S_2 and S_3 described explicitly as detailed above, to experimental observations of OH LIF signals were used to determine the rate coefficients k_3 and k_4 . Experiments to determine k_3 were performed in the absence of O_2 , with several measurements performed at a single temperature and pressure as a function of the $(CH_3)_3COOH$ concentration to vary the rate of OH loss (i.e. varying k'_6) whilst maintaining the rate of QOOH decomposition between experiments. Typically, experiments were performed with five different concentrations of $(CH_3)_3COOH$, and values for k'_6 were allowed to vary in the fits for each separate dataset whilst fitting k_2 and k_3 as global parameters for each temperature and pressure. Experiments were performed to measure k_4 using both 193 nm and 248 nm photolysis under otherwise identical conditions, with no significant differences observed between the results.

In order to optimise the sensitivity of the fits to k_3 and k_4 , conditions were employed such that the formation of QOOH through reaction R8.2a was rapid compared to its subsequent decay through reactions R8.3 and R8.4, requiring high concentrations of $(CH_3)_3COOH$. Owing to the use of aqueous $(CH_3)_3COOH$ in this study and the similarity in vapour pressures between water and $(CH_3)_3COOH$,⁹ the peroxide concentrations were approximated from the vapour pressure and flow rates in the system, assuming that the peroxide contributed 55 % of the total $(CH_3)_3COOH/H_2O$ vapour pressure in keeping with the work of Baasandorj *et al.*⁹ Independent experiments were performed in the absence of $(COCl)_2$ and O_2 (i.e. using $(CH_3)_3COOH/He$ or $(CH_3)_3COOH/N_2$ gas mixtures) to determine the pseudo-first-order loss rate coefficients k'_6 ($k'_6 = k_6[(CH_3)_3COOH]$) for a range of $(CH_3)_3COOH$ concentrations at a given temperature and pressure and to verify that the resulting bimolecular rate coefficients k_6 determined were in agreement with those reported by Baasandorj *et al.*⁹

Given the complexity in the form and derivation of the analytical expression describing the temporal behaviour of OH, a series of simulations of the chemistry occurring in reactions R8.1-R8.6 were performed using the numerical integration package Kintecus,²⁰ with the simulated output for OH analysed in the same manner adopted for experimental data in order to demonstrate the fidelity of the analytical expression in describing the temporal behaviour of OH in the system, and the sensitivity of the fits to k_3 and k_4 . The rate coefficients and concentrations used in the simulations are listed in Table 8.1.

Reaction	Rate coefficient
$(\text{CH}_3)_3\text{COOH} + \text{Cl} \rightarrow \text{QOOH} + \text{HCl}$	$7.7 \times 10^{-11} \text{ cm}^3 \text{ s}^{-1}$
$\text{QOOH} \rightarrow \text{OH} + \text{DMO}$	$35,000 \text{ s}^{-1}$
$\text{QOOH} + \text{O}_2 \rightarrow \text{O}_2\text{QOOH}$	$7.5 \times 10^{-13} \text{ cm}^3 \text{ s}^{-1}$
$(\text{CH}_3)_3\text{COOH} + \text{OH} \rightarrow (\text{CH}_3)_3\text{CO}_2 + \text{H}_2\text{O}$	$3.6 \times 10^{-12} \text{ cm}^3 \text{ s}^{-1}$

Table 8.1 Reactions and rate coefficients adopted in simulations of OH used to demonstrate the fidelity and sensitivity of Equation 8.1 in determinations of k_3 and k_4 (unless otherwise shown as varying in Figures 8.6-8.9). Reactions R1 and R5 are treated as instantaneous, and thus represented by non-zero initial concentrations of Cl, COCl and OH, which were approximated from the absorption cross-sections of $(\text{COCl})_2$ ($3.10 \times 10^{-19} \text{ cm}^2$)¹⁹ and $(\text{CH}_3)_3\text{COOH}$ ($1.99 \times 10^{-20} \text{ cm}^2$)⁹ at 248 nm, typical laser fluence ($10 - 30 \text{ mJ cm}^{-2}$) and typical experimental concentrations of $(\text{COCl})_2$ and $(\text{CH}_3)_3\text{COOH}$ ($1 \times 10^{14} \text{ cm}^{-3}$ and $1 \times 10^{15} \text{ cm}^{-3}$ respectively). The reaction channel in $\text{Cl} + (\text{CH}_3)_3\text{COOH}$ in which H-abstraction occurs from one of the methyl groups (leading to production of a peroxy radical, RO_2) is not included in the simulations.

Simulations were performed in which the inputs for the rate coefficients k_3 and k'_4 ($k'_4 = k_4[\text{O}_2]$) were varied, and the output for OH analysed using E8.1 to determine the fitted values for k_3 and k'_4 . A typical simulation for OH, and the fit to the simulation using E8.1, is shown in Figure 8.5. Figure 8.6 and Figure 8.7 show the ratios of the fit output for k_3 and k'_4 to the values used as input for the simulation, respectively. Figure 8.8 shows the ratios of the fit output for k_3 and k'_4 to the input values for a range of $(\text{CH}_3)_3\text{COOH}$ concentrations. Figure 8.9 shows the sensitivity of results for k_3 and k_4 to the

decomposition rate of COCl (R8.1b) for experiments performed at a photolysis wavelength of 248 nm.

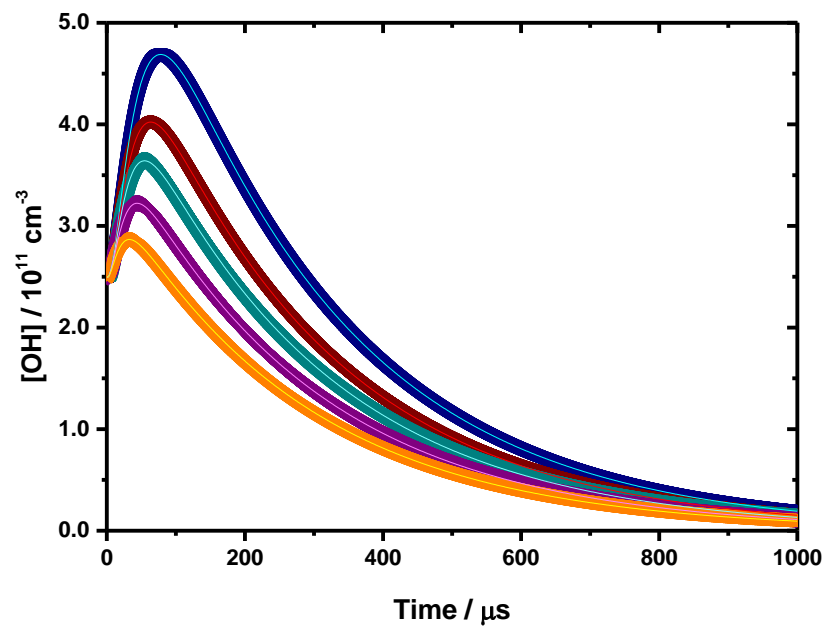


Figure 8.5 Simulated OH time-profiles (thick lines), using the reactions and rate coefficients listed in Table 8.1 for a range of O_2 concentrations, and the fit to the simulation using Equation 8.1 (thin lines).

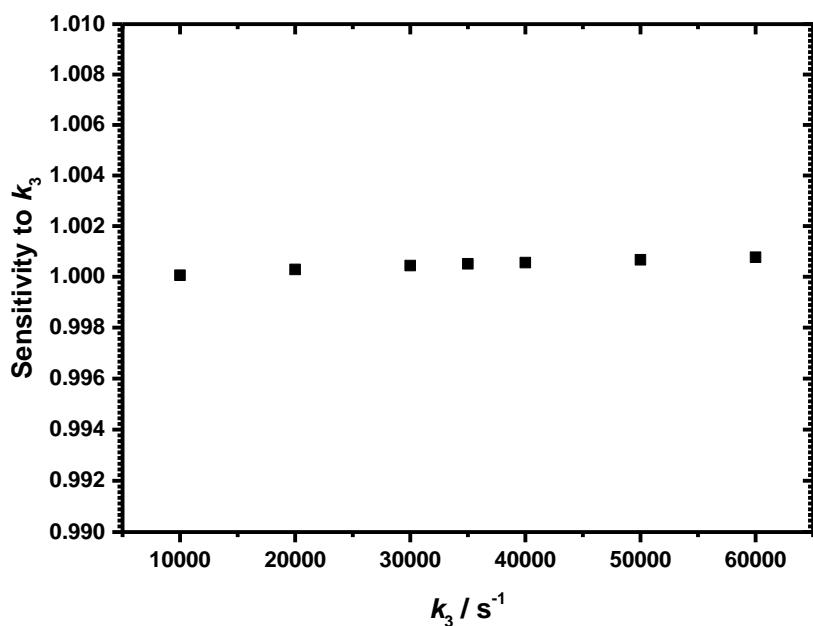


Figure 8.6 Sensitivity of fits to determine k_3 to the values for k_3 used in the model input (defined as the ratio of the value for k_3 determined by fitting Equation 1 to the output from model simulations of the temporal behaviour of OH to the corresponding value for k_3 used as input in the model).

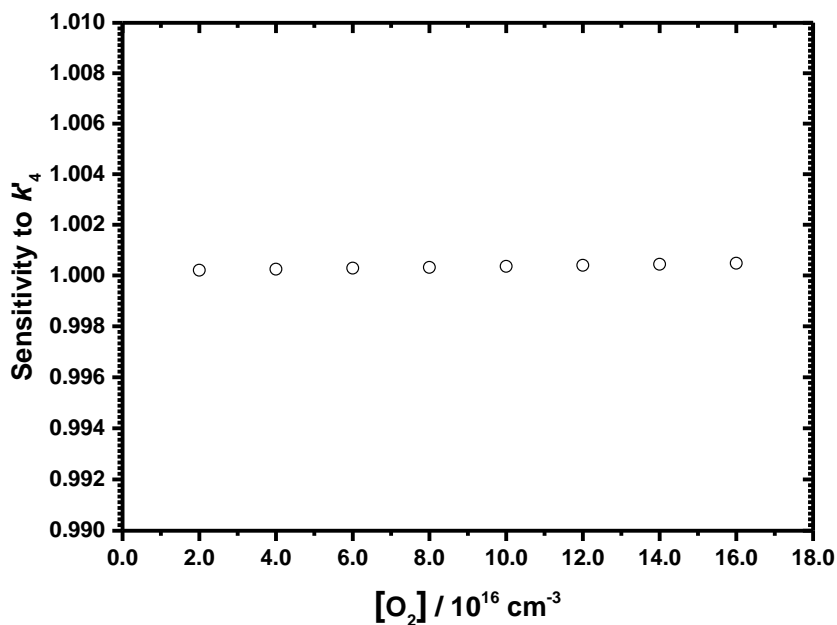


Figure 8.7 Sensitivity of fits to determine k'_4 to the concentration of O_2 used in the model input (defined as the ratio of the value for k'_4 determined by fitting Equation 8.1 to the output from model simulations of the temporal behaviour of OH to the corresponding value for k'_4 used as input in the model, where $k'_4 = k_4[O_2]$).

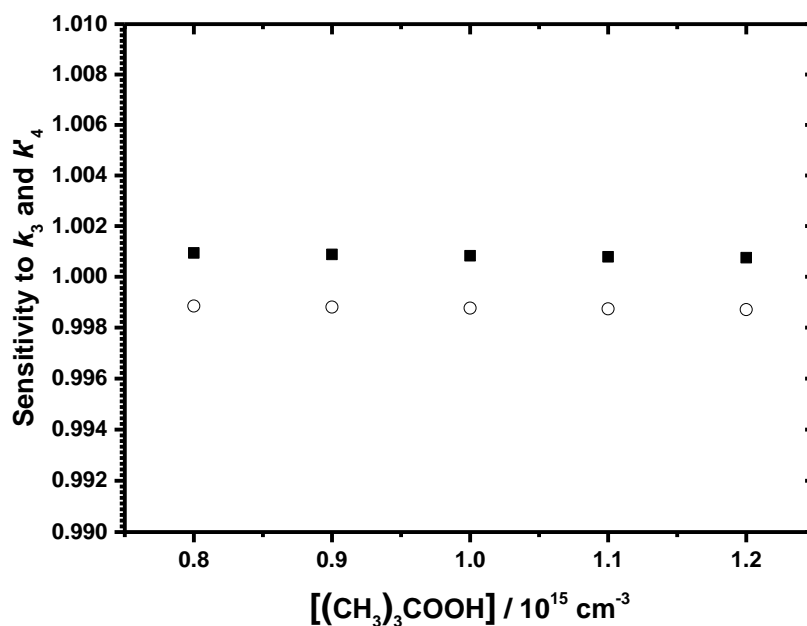


Figure 8.8 Sensitivity of fits to determine k_3 (filled squares) and k_4 (open circles) to those used as inputs for the model simulations of the temporal behaviour of OH occurring as a result of reactions R8.1-R8.6 as a function of the initial concentration of $(\text{CH}_3)_3\text{COOH}$. The sensitivities to k_3 and k_4 are as defined in Figures 8.6 and 8.7, respectively.

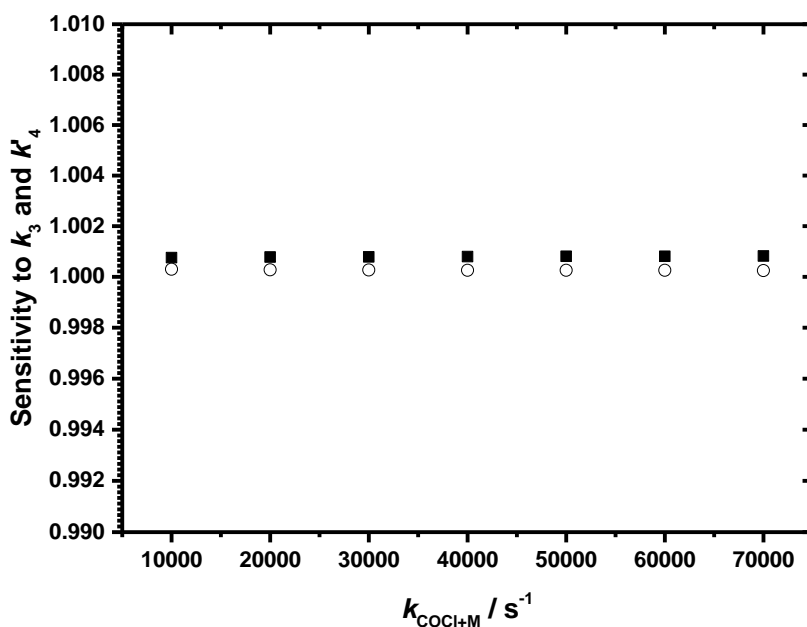


Figure 8.9 Sensitivity of fits to determine a) k_3 (filled squares) and b) k_4 (open circles) to those used as inputs for the model simulations of the temporal behaviour of OH occurring as a result of reactions R8.1-R8.6 as a function of the rate of COCl decomposition to produce Cl + CO following photolysis of $(\text{COCl})_2$ at a wavelength of 248 nm. The sensitivities to k_3 and k_4 are as defined in Figures 8.5 and 8.6, respectively.

The results of the sensitivity analysis shown in Figures 8.6-8.9 demonstrate the fidelity and sensitivity of the analytical expression, which was subsequently used to fit the experimental data. Fits to the experimental observations gave uncertainties in individual rate coefficients on the order of 5 %. While it was possible to minimise the effects of correlations between fit parameters by employing conditions to optimise the sensitivity to the kinetic parameters of interest, it was not possible to avoid correlations entirely. Uncertainties quoted for k_3 were thus determined from fits in which other kinetic parameters were fixed to ± 50 % of their values determined from global fits in which all relevant kinetic parameters were treated as variables, and are on the order of 30 %. Uncertainties reported for k_4 were determined in a similar manner and include the uncertainties associated with k_3 .

8.4 Results and Discussion

8.4.1 QOOH Decomposition Kinetics

Figure 8.10 shows typical OH fluorescence signals following initiation of chemistry within the system. Photolysis of $(\text{CH}_3)_3\text{COOH}$ results in the instantaneous OH production observed at $t = 0$, with the subsequent growth in OH, in the absence of O_2 , associated solely with QOOH decomposition. Results are summarised in Table 8.2. The initial abstraction reaction generating QOOH (R8.2a) is close to thermoneutral ($\sim -4 \text{ kJ mol}^{-1}$)²¹ hence it is expected that the decomposition of QOOH is entirely thermal, with no contribution from chemical activation. No evidence was observed in the fits to OH to suggest any influence from chemically activated processes. QOOH decomposition kinetics (k_3) were thus determined from global fits of data obtained in experiments performed in the absence of O_2 to Equation E8.1.

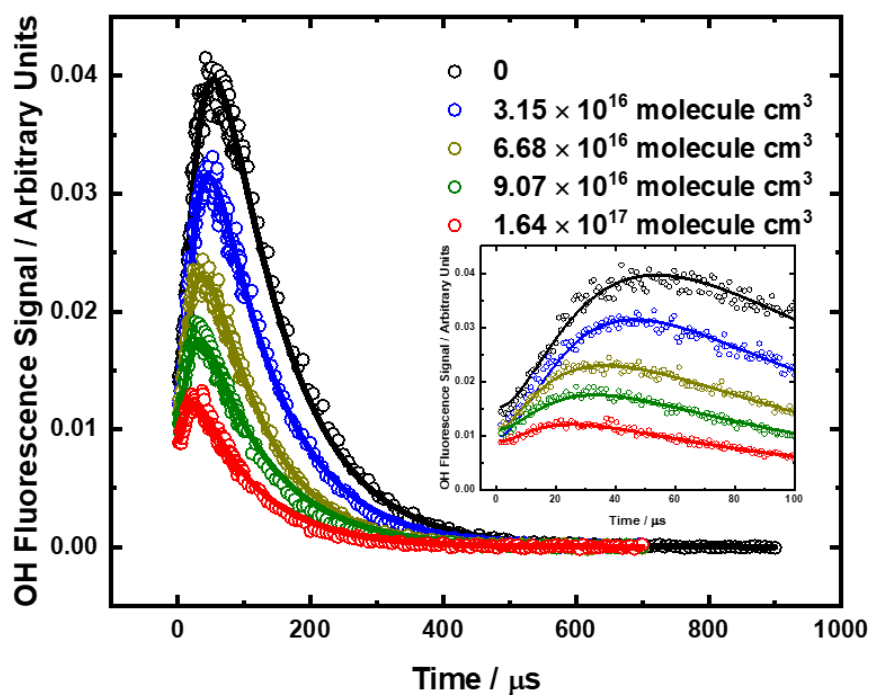


Figure 8.10 Typical OH time profiles at (10 Torr N₂, 298 K) for a range of O₂ concentrations (0 cm⁻³ (black); 3.15 × 10¹⁶ cm⁻³ (blue); 6.68 × 10¹⁶ cm⁻³ (brown); 9.07 × 10¹⁶ cm⁻³ (green); 1.64 × 10¹⁶ cm⁻³ (red)). The inset shows the first 100 μs in greater detail. Fluorescence quenching by O₂ is accounted for in E8.1.

<i>T</i> / K	<i>p</i> / Torr	Bath gas	Photolysis wavelength / nm	<i>k</i> ₃ / s ⁻¹
298	10	N ₂	248	30200 ± 9100
298	20	N ₂	248	34600 ± 10400
298	30	N ₂	248	43800 ± 13200
298	40	N ₂	248	45600 ± 13800
298	60	N ₂	248	54300 ± 16400
298	80	N ₂	248	64400 ± 19500
298	100	N ₂	248	54900 ± 16600
298	100	N ₂	248	79300 ± 24000
298	50	He	193	20100 ± 6200
298	100	He	193	53900 ± 16200
293	350	He	193	52900 ± 15900

283	40	He	193	22600 ± 6900
283	60	He	193	22100 ± 6600
283	110	He	193	34800 ± 10400
283	200	He	193	44000 ± 13200
277	10	N ₂	193	11200 ± 3400
277	20	N ₂	193	21700 ± 6500
277	50	N ₂	193	12900 ± 3900
277	50	N ₂	193	39400 ± 11900
277	110	N ₂	193	15000 ± 4500
277	190	N ₂	193	16200 ± 4900
273	25	He	193	11000 ± 3300
273	25	He	193	6400 ± 2300
273	40	He	193	14400 ± 4400
273	40	He	193	9600 ± 3200
273	80	He	193	23500 ± 7100
273	100	He	193	10900 ± 3300
273	160	He	193	32800 ± 9900
273	340	He	193	15000 ± 4500
268	170	He	193	16800 ± 5300
255	10	He	193	3000 ± 900
255	35	He	193	4500 ± 1400
255	50	He	193	4700 ± 1400
255	70	He	193	3600 ± 1100
255	185	He	193	7400 ± 2200
251	35	He	193	4200 ± 1300
251	40	He	193	5900 ± 1800
251	200	He	193	6900 ± 2100

Table 8.2 Summary of results for k_3 .

Figure 8.11 shows k_3 as a function of temperature and pressure, with the experimental data given in Table 8.2. The results at 298 K in He bath gas are in general agreement with the behaviour observed by Zádor *et al.*, although the results obtained in this work are systematically lower than those reported previously by ~30-40 %. Results at 298 K in N₂ bath gas show faster decomposition kinetics as expected for a pressure dependent reaction owing to the greater efficiency of collisional energy transfer in N₂ compared to He.

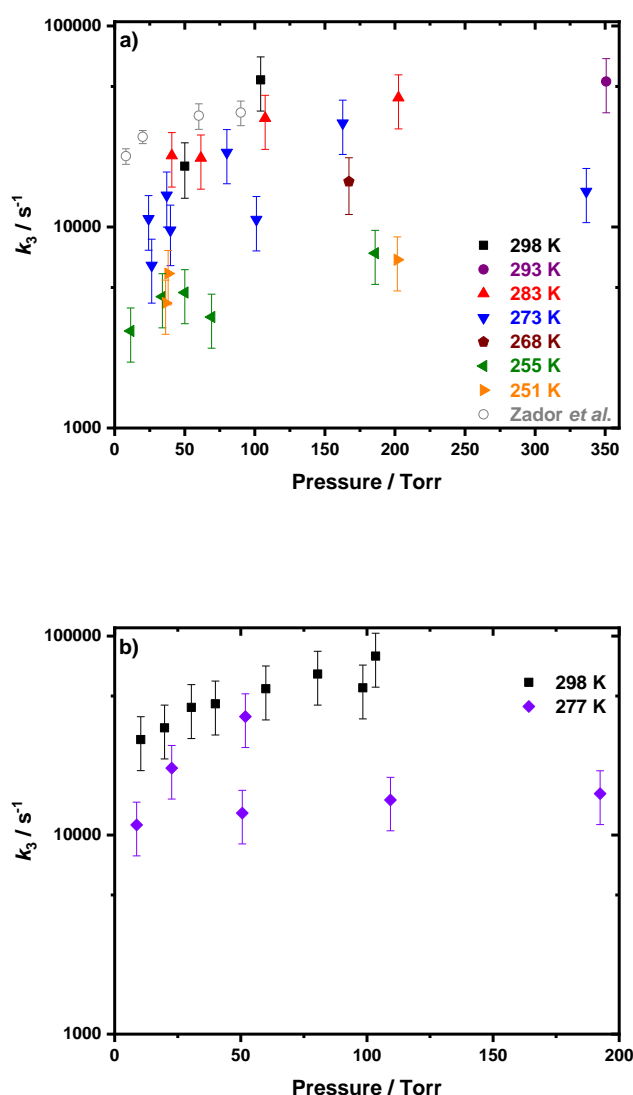


Figure 8.11 Pressure dependence of k_3 from 251 – 298 K in a) He bath gas and b) N₂ bath gas. Data reported by Zádor *et al.*⁸ for experiments at (298 ± 2) K in He bath gas are also shown (open circles).

The fits to E8.1 also give the pseudo-first-order rate coefficients k'_2 , which describes the kinetics of QOOH formation from $\text{Cl} + (\text{CH}_3)_3\text{COOH}$ (R8.2), and k'_6 , which describes the kinetics of OH loss through $\text{OH} + (\text{CH}_3)_3\text{COOH}$ (R8.6). Although the concentration of $(\text{CH}_3)_3\text{COOH}$ is only approximated from the vapour pressure and flow rates in the system, results for k'_2 and k'_6 can be used with the approximate $(\text{CH}_3)_3\text{COOH}$ concentrations to approximate the bimolecular rate coefficients k_2 and k_6 . The results are given in Table 8.3.

T / K	$k_2 / 10^{-11} \text{ cm}^3 \text{ s}^{-1}$	$k_6 / 10^{-12} \text{ cm}^3 \text{ s}^{-1}$
304	2.2 ± 0.6	2.3 ± 0.7
298	2.4 ± 0.7	2.3 ± 0.7
289	2.1 ± 0.6	2.3 ± 0.7
282	3.2 ± 1.0	1.9 ± 0.7
275	2.6 ± 0.8	2.6 ± 0.9
265	2.4 ± 0.7	2.5 ± 0.8
251	3.9 ± 1.2	3.8 ± 1.3

Table 8.3 Summary of results for k_2 ($\text{Cl} + (\text{CH}_3)_3\text{COOH}$) and k_6 ($\text{OH} + (\text{CH}_3)_3\text{COOH}$) as a function of temperature.

Results for k_2 indicate a value of $(2.4 \pm 0.7) \times 10^{-11} \text{ cm}^3 \text{ s}^{-1}$ at 298 K and a temperature dependence described by $k_2 = (2.3 \pm 2.1) \times 10^{-12} \exp[(690 \pm 250)/T] \text{ cm}^3 \text{ molecule}^{-1} \text{ s}^{-1}$ over the conditions investigated in this work, as shown in Figure 8.12.

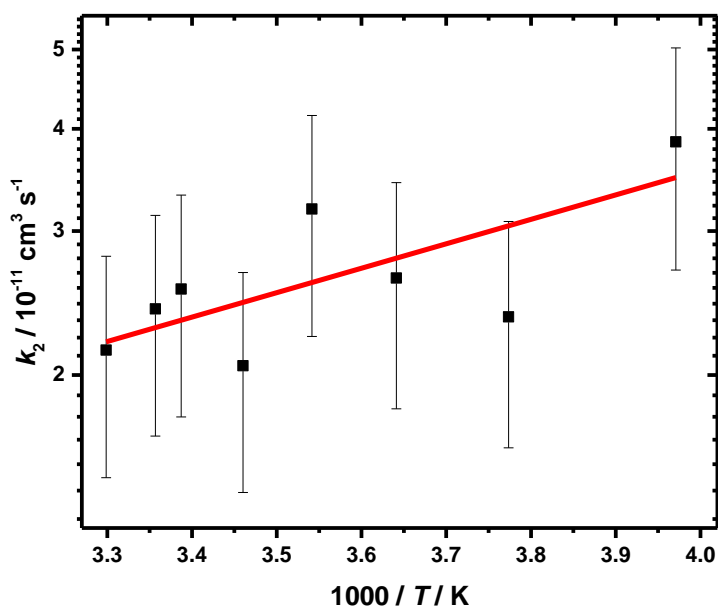


Figure 8.12 Temperature dependence of k_2 , the rate coefficient for reaction of Cl with $(\text{CH}_3)_3\text{COOH}$ observed in this work (black points) with an Arrhenius parameterisation (solid red line).

The value for k_2 determined in this work at 298 K using the approximate concentration of $(\text{CH}_3)_3\text{COOH}$ is significantly lower than the value of $7.7 \times 10^{-11} \text{ cm}^3 \text{ molecule}^{-1} \text{ s}^{-1}$ used in the analysis performed by Zádor *et al.*,⁸ which was based on the kinetics and branching ratio for the reaction between Cl and $(\text{CH}_3)_3\text{CH}^{22}$. The ratio of k_2 to k_6 determined in this work, which is independent of the absolute concentration of $(\text{CH}_3)_3\text{COOH}$, was (10.7 ± 4.8) at 298 K. Using $k_6 = (3.58 \pm 0.54) \times 10^{-12} \text{ cm}^3 \text{ s}^{-1}$ at 296 K as reported by Baasandorj *et al.*,⁹ the observed $k_2:k_6$ ratio indicates a value for k_2 of $(3.8 \pm 1.7) \times 10^{-11} \text{ cm}^3 \text{ molecule}^{-1} \text{ s}^{-1}$, which is also significantly lower than that adopted in the analysis performed by Zádor *et al.* Fits to Equation 8.1 in which k_2 was fixed to a value of $7.7 \times 10^{-11} \text{ cm}^3 \text{ molecule}^{-1} \text{ s}^{-1}$ gave values for k_3 that were 5-10 % higher than those in which k_2 was allowed to float, which may explain some of the difference in results between this work and that of Zádor *et al.* shown in Figure 8.13.

At 298 K, this work indicates $k_6 = (2.2 \pm 0.7) \times 10^{-12} \text{ cm}^3 \text{ molecule}^{-1} \text{ s}^{-1}$, with a temperature dependence described by $k_6 = (1.0 \pm 0.7) \times 10^{-13} \exp[(890 \pm 210)/T] \text{ cm}^3 \text{ molecule}^{-1} \text{ s}^{-1}$, as shown in Figure 8.13. The results of Baasandorj *et al.* gave $k_6 = (7.0 \pm 1.0) \times 10^{-13}$

$\exp[(485 \pm 20)/T]$ $\text{cm}^3 \text{ molecule}^{-1} \text{ s}^{-1}$ obtained in experiments using pulsed laser photolysis of $(\text{CH}_3)_3\text{COOH}$ at 248 nm coupled to OH detection via LIF.

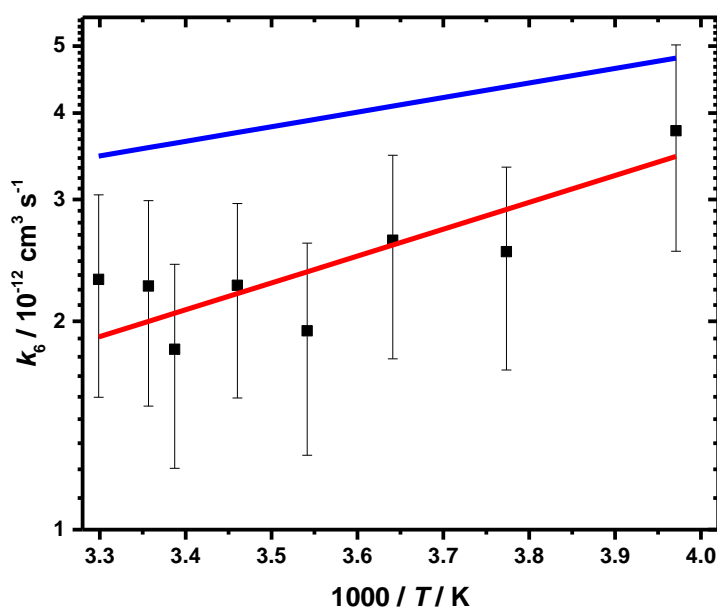


Figure 8.13 Temperature dependence of k_6 , the rate coefficient for reaction of OH with $(\text{CH}_3)_3\text{COOH}$ observed in this work (black points) with Arrhenius parameterisation (solid red line). The parameterisation for k_6 reported by Baasandorj *et al.*⁹ is also shown (solid blue line).

Reaction R8.6 has the potential to interfere with the chemistry, as abstraction from the methyl groups in $(\text{CH}_3)_3\text{COOH}$ would lead to the generation of QOOH and hence OH regeneration, with the results that the growth and decay of OH could then no longer be simply associated with reactions R8.3, R8.4, R8.6 and diffusional OH loss. While the standard experiments performed by Baasandorj *et al.* would be insensitive to fast OH regeneration from R8.3, in several experiments Baasandorj *et al.* added high concentrations of O_2 ($(2-4) \times 10^{16} \text{ cm}^{-3}$) to intercept any QOOH formed before decomposition to OH, and observed no change in the measured bimolecular rate coefficient, concluding that H-atom abstraction from the methyl groups of the molecule was insignificant. The analysis using E8.1 is based on $(\text{CH}_3)_3\text{CO}_2$ being the sole product of R8.6, consistent with theory¹⁰ and with the experimental evidence which does not indicate any growth of OH from the photolysis of $(\text{CH}_3)_3\text{COOH}$. In this scenario the

observed decay of OH following production from the decomposition of QOOH is associated with R8.6 and diffusional loss and should not vary with the concentration of O₂. No significant change in the rate coefficient describing the OH loss in the system (k_6) as a function of the O₂ concentration was observed in this work, as shown in Figure 8.14, indicating that the loss of OH is independent of O₂ and that (CH₃)₃CO₂ is the sole product of R8.6.

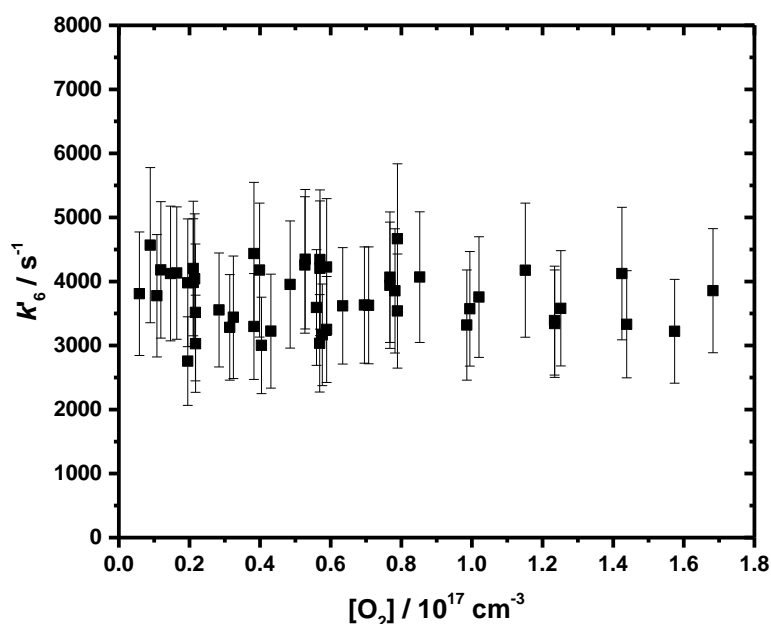


Figure 8.14 Variation of the rate coefficient describing the loss of OH in the system (k_6) as a function of the O₂ concentration for experiments performed at 298 K with similar (CH₃)₃COOH concentrations.

8.4.2 Master Equation Analysis

Statistical rate theory calculations were performed to describe the decomposition kinetics of QOOH using the master equation simulation package Master Equation Solver for Multi-Energy well Reactions (MESMER), which has been described in detail in previous work.¹⁴

The geometries, vibrational frequencies and rotational constants for the QOOH species and its transition state to decomposition were calculated at the M06-2X/cc-pVTZ level of

theory using the Gaussian 09 suite of programs¹² using the geometries reported by Zádor *et al.*⁸ as inputs. Results are summarised in Appendix D. Hindered rotation potentials were calculated by Dr Robin Shannon²³ from M06-2X/6-31+G** relaxed scans along the various dihedral co-ordinates in both the well and the transition state. Hindered rotor state densities were obtained using the methodology within MESMER which has been described previously.²⁴ Pressure dependent rate coefficients were calculated using MESMER utilising a rigid rotor-harmonic oscillator approximation for all apart from the hindered modes, which were assumed to be separable. Collisional energy transfer within the system was described by an exponential down model with the average energy transferred in a downward direction on collision with the bath gas represented by $\langle \Delta E \rangle_{\text{down}}$. An input file for the MESMER calculations is provided in Appendix.

Given the extensive experimental data, set both $\langle \Delta E \rangle_{\text{down}}$ and the barrier height to decomposition were varied in order to fit the master equation to the experimental rate coefficients. To this end, a Levenburg-Marquardt algorithm, as implemented in MESMER, was used to minimise the merit function:

$$\chi^2 = \sum_i \frac{(k_{\text{exp}}(p_i, T_i) - k_{\text{mod}}(p_i, T_i))^2}{\sigma_i^2} \quad \text{E8.10}$$

where $k_{\text{exp}}(p_i, T_i)$ and $k_{\text{mod}}(p_i, T_i)$ are the experimental and modelled rate coefficients at pressure p_i and temperature T_i , respectively, with σ_i^2 representing the appropriate experimental uncertainty.

Figure 8.15 shows the fit to the experimental data, which gave a barrier height to decomposition of 44.7 kJ mol⁻¹, $\langle \Delta E \rangle_{\text{down}} = 89$ cm⁻¹ in He, and $\langle \Delta E \rangle_{\text{down}} = 147$ cm⁻¹ in N₂. The barrier height reported in this work is lower than the value of 52.3 kJ mol⁻¹ (12.5 kcal mol⁻¹) value determined from the high level calculations (QCISD(T)/cc-pVZ//M06-2X/6-311++G(d,p)) reported by Zádor *et al.* Typical uncertainties in the high level

calculations are approximately $\pm 4 \text{ kJ mol}^{-1}$ (1 kcal mol^{-1}),⁸ but Zádor *et al.* also noted that a reduction in the barrier height to 48.1 kJ mol^{-1} ($11.5 \text{ kcal mol}^{-1}$) was required to give a better fit with their experimental data at 298 K when using $\langle \Delta E \rangle_{\text{down}} = 250 \text{ cm}^{-1}$. In addition, it was noted that value for $\langle \Delta E \rangle_{\text{down}}$ was poorly constrained, with a lower value correlating with a lower barrier height. While there is a slight inconsistency between the fitted and calculated barrier heights, there are potentially several contributing factors, and the difference reported here is significantly less than in this study on $\text{CH}_2\text{OCH}_2\text{OOH}$ decomposition.¹¹

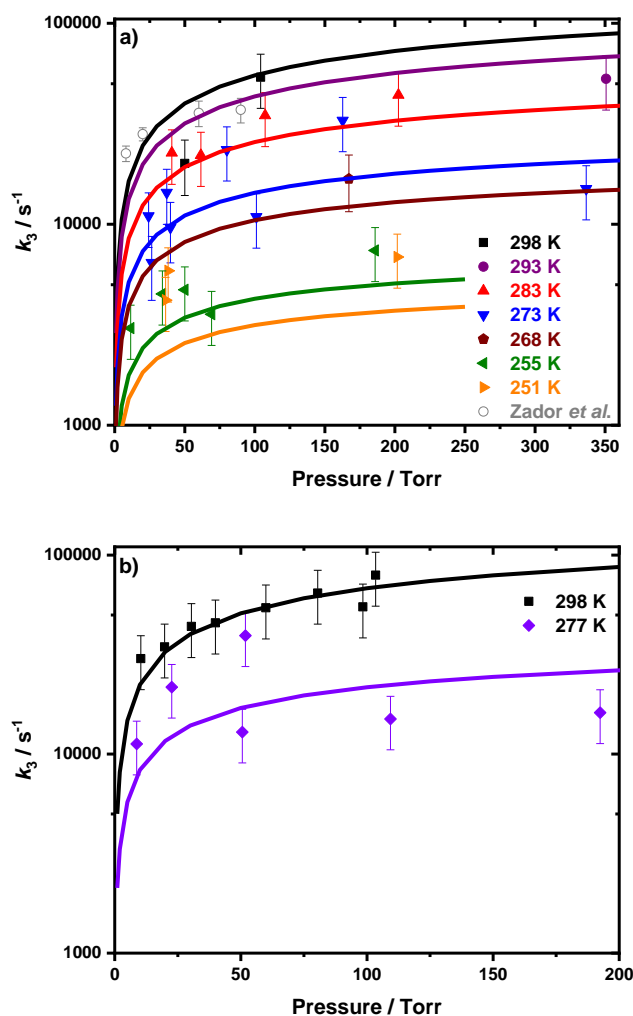


Figure 8.15 Pressure dependence of k_3 from 251 – 298 K in a) He bath gas and b) N_2 bath gas. The solid lines are the MESMER fits which give a barrier height to decomposition of 44.7 kJ mol^{-1} , with $\Delta E_{\text{down}} = 89 \text{ cm}^{-1}$ in He and $\Delta E_{\text{down}} = 147 \text{ cm}^{-1}$ in N_2 . Data reported by Zádor *et al.*⁸ for experiments at $(298 \pm 2) \text{ K}$ in He bath gas are also shown (open circles).

Simulations in MESMER constrained to the barrier height and $\langle \Delta E \rangle_{\text{down}}$ reported by Zádor *et al.* tend to underestimate the observed values for k_3 reported in this work and those by Zádor *et al.*, as shown in Figure 14. However, fitting the results of Zádor *et al.* using MESMER gave poorly defined results when both the barrier height and $\langle \Delta E \rangle_{\text{down}}$ were varied together owing to correlations between the parameters which are difficult to characterise using data obtained at a single temperature. Fits to the results of Zádor *et al.* in which the barrier height was constrained to 48.1 kJ mol^{-1} required a value for $\langle \Delta E \rangle_{\text{down}}$ in excess of 650 cm^{-1} , while fits constrained to the barrier of 44.7 kJ mol^{-1} determined in this work gave an optimum $\langle \Delta E \rangle_{\text{down}}$ of 94 cm^{-1} . Conversely, fits constrained to $\langle \Delta E \rangle_{\text{down}} = 250 \text{ cm}^{-1}$ used in the work of Zádor *et al.* gave an optimum barrier height of 47.1 kJ mol^{-1} , while fits constrained to $\langle \Delta E \rangle_{\text{down}} = 89 \text{ cm}^{-1}$, as determined in this work, gave an optimum barrier height of 44.8 kJ mol^{-1} . These results are shown in Figure 8.16.

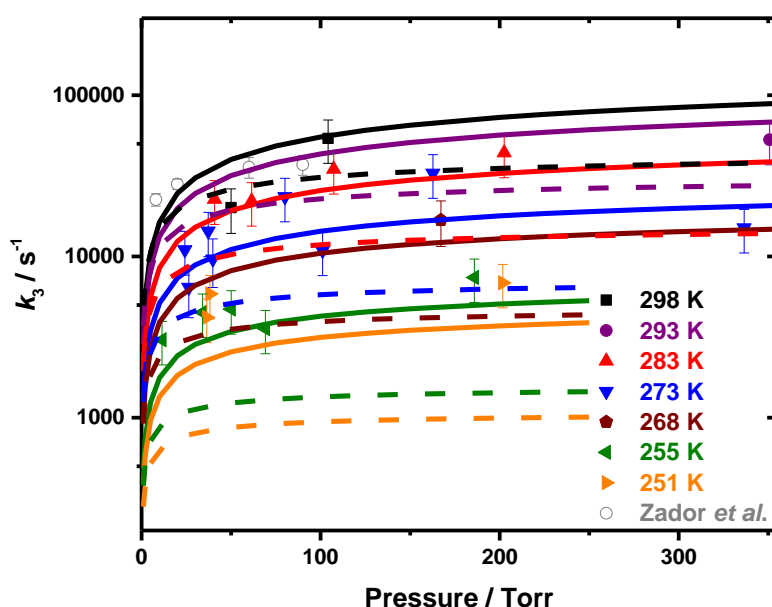


Figure 8.16 Pressure dependence of k_3 from in He bath gas observed in this work (filled data points) and by Zádor *et al.* (open data points). Solid lines are the MESMER fits to the observations made in this work, which gave a barrier height to decomposition of 44.7 kJ mol^{-1} and $\Delta E_{\text{down}} = 89 \text{ cm}^{-1}$ in He. Broken lines are MESMER simulations using a barrier height of 48.1 kJ mol^{-1} and $\Delta E_{\text{down}} = 250 \text{ cm}^{-1}$, as reported by Zádor *et al.* at 298 K.⁸

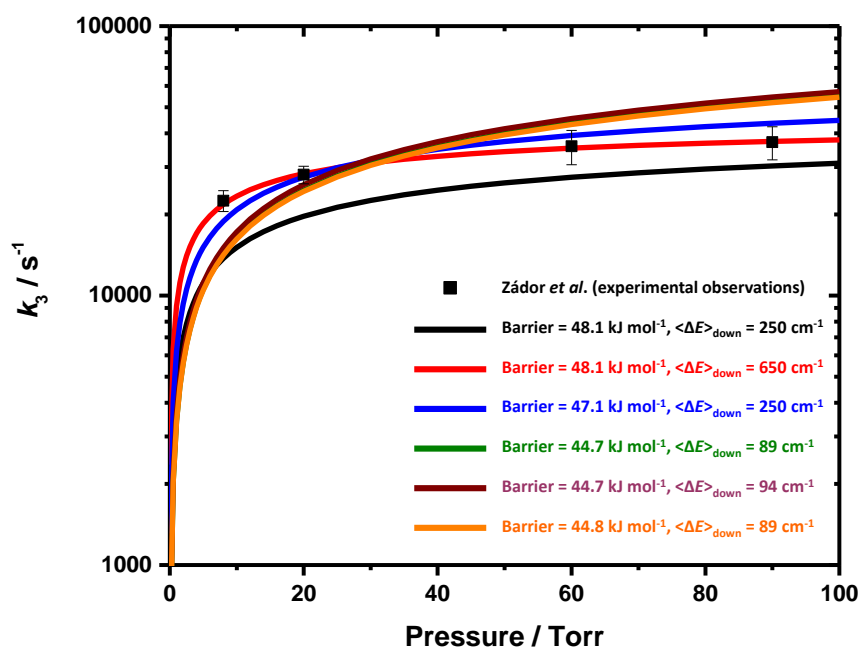


Figure 8.17 Results for k_3 at 298 K reported by Zádor *et al.*⁸ and corresponding output from MESMER for simulations (black line, barrier to decomposition of 48.1 kJ mol^{-1} and $\langle \Delta E \rangle_{\text{down}} = 250 \text{ cm}^{-1}$) and fits to the results of Zádor *et al.* (coloured lines).

The optimised values for the barrier height and $\langle \Delta E \rangle_{\text{down}}$ were used in MESMER simulations to determine k_3 at temperatures between 200 and 800 K and pressures between 1 and 10^6 Torr in He and N_2 . The calculated rate coefficients were parameterised using the Troe expression for broad falloff curves²⁵ (Equations 8.11-8.14) for use in kinetic models to assess the competition between chain propagation and chain branching reactions:

$$k = \frac{k_0[M]k_\infty}{k_0[M] + k_\infty} F \quad \text{E8.11}$$

$$F = \frac{\left(1 + k_0[M]/k_\infty\right)}{\left(1 + \left(k_0[M]/k_\infty\right)^n\right)^{1/n}} \quad \text{E8.12}$$

$$n = \left(\frac{\ln(2)}{\ln(2/F_c)} \right) \left((1-b) + b \left(k_0[M]/k_\infty \right)^q \right) \quad \text{E8.13}$$

$$q = \frac{(F_c - 1)}{\ln(F_c/10)} \quad \text{E8.14}$$

where $k_{3,0}(T)$ is the low-pressure and $k_{3,\infty}(T)$ is the high-pressure limiting rate coefficient for QOOH decomposition, M is the total number density, and F_c is the broadening factor. The fits to the MESMER output for k_3 are shown in Figure 8.18 and give $k_{3,0} = 3.27 \times 10^{-7} (T/298)^{-6.675} \exp(-4746/T) \text{ cm}^3 \text{ s}^{-1}$, $k_{3,\infty} = 1.57 \times 10^{13} (T/298)^{0.344} \exp(-5457/T) \text{ s}^{-1}$, $F_c = 0.212$ and $b = 0.213$ in He bath gas and $k_{3,0} = 6.06 \times 10^{-6} (T/298)^{-6.649} \exp(-4762/T) \text{ cm}^3 \text{ s}^{-1}$, $k_{3,\infty} = 1.54 \times 10^{13} (T/298)^{0.355} \exp(-5452/T) \text{ s}^{-1}$, $F_c = 0.206$ and $b = 0.215$ in N_2 .

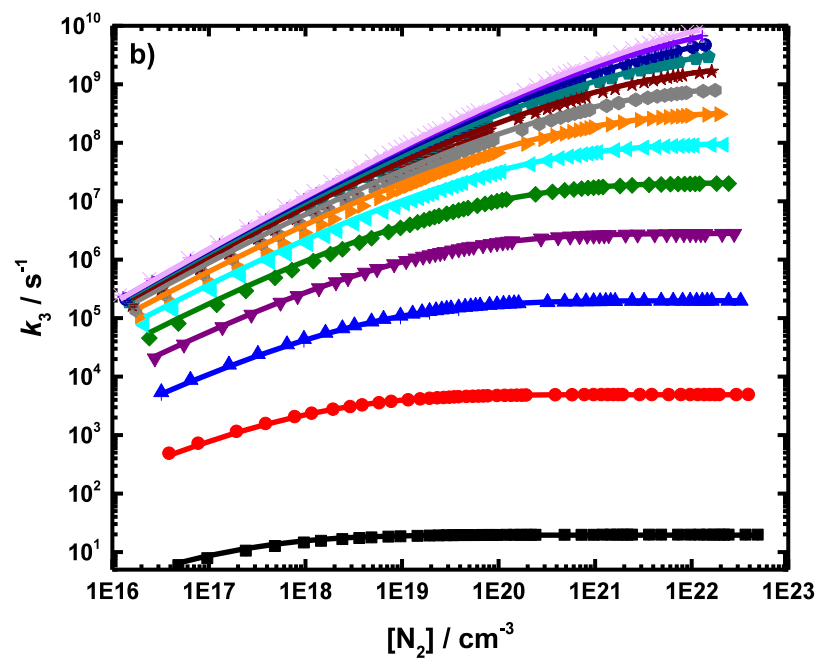
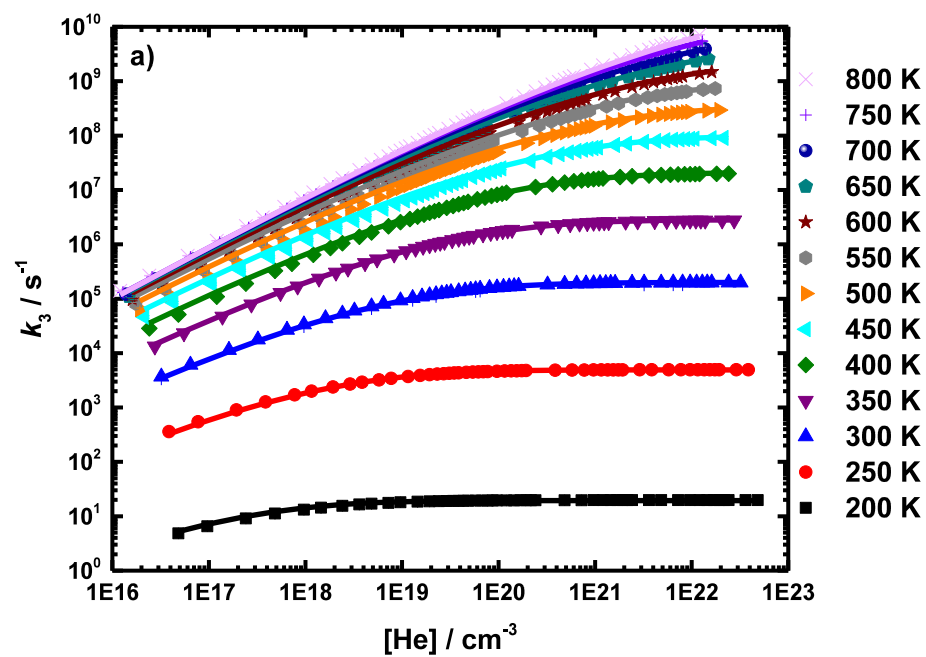


Figure 8.18 Troe fits using Equations E8.3-E8.6 (solid lines) to MESMER simulations (filled data points) using a barrier height of 44.7 kJ mol^{-1} in a) He, with $\langle \Delta E \rangle_{\text{down}} = 89 \text{ cm}^{-1}$ and b) N_2 , with $\langle \Delta E \rangle_{\text{down}} = 147 \text{ cm}^{-1}$.

8.4.3 Kinetics of QOOH + O₂

Figure 8.10 (above) shows temporal profiles for OH recorded in the presence of varying amounts of O₂. In the presence of O₂, the yield of OH produced *via* QOOH decomposition is reduced owing to competition between the decomposition process and QOOH + O₂ (R8.4), and the rate of the non-photolytic production of OH is increased owing to the increased rate of QOOH consumption. Measurements were made at pressures between 10 and 100 Torr at temperatures between 251 and 304 K to determine k_4 , the rate coefficient for O₂ addition to QOOH. Fits to Equation 8.1 were performed with kinetics for R8.1-8.3 constrained to the values reported above for each temperature and pressure, with k_4 determined from the pseudo-first-order rate coefficient k'_4 ($k'_4 = k_4[\text{O}_2]$). Values for k_4 determined from fits in which k_4 was treated as a global parameter at each temperature, with the O₂ concentration constrained for each experiment, were typically within 10 % of those obtained from fits in which k'_4 ($k'_4 = k_4[\text{O}_2]$) was treated as a local parameter for each experiment, with results at one temperature (282 K) within 25 % and associated with larger uncertainties.

At 298 K, results from this work indicate $k_4 = (5.6 \pm 1.7) \times 10^{-13} \text{ cm}^3 \text{ molecule}^{-1} \text{ s}^{-1}$, compared to the previous measurement⁸ of $(9.0 \pm 3.0) \times 10^{-13} \text{ cm}^3 \text{ molecule}^{-1} \text{ s}^{-1}$ and the calculated value of $12.5 \times 10^{-13} \text{ cm}^3 \text{ molecule}^{-1} \text{ s}^{-1}$.⁸ Owing to the complexity of the mechanism controlling OH in the system, the sensitivity of the fits to k_4 was investigated by performing fits to the data in which k_4 was fixed to a range of values while k_2 and k_6 were allowed to float. The variation in χ^2 for fits performed with different fixed values of k_4 for temperatures between 251 and 298 K indicate that, at each temperature, the minimum in the χ^2 , which indicates the best fit to the data, corresponds to the value of k_4 determined by the unconstrained fits to Equation 8.1, giving confidence in the results for k_4 . However, as shown in Figure 8.19 it can also be observed that k_4 is better defined at low temperatures than at 298 K, with fits at lower temperatures displaying a steeper change in χ^2 around the minimum value than the fit at 298 K.

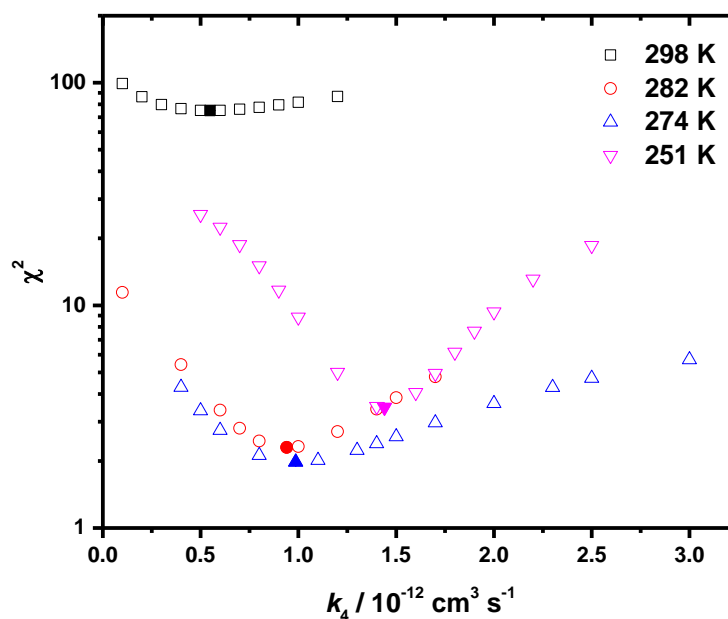


Figure 8.19 Variation in χ^2 for fits fixed to k_4 for data at 298 K, 282 K, 274 K and 251 K. In each case, the minimum in the χ^2 for the fit, indicating the best fit to the data, corresponds to the value of k_4 determined by the unconstrained fit (shown by filled symbols).

No significant dependence of k_4 on pressure was observed, consistent with the results of Zádor *et al.* over the range of 4 – 90 Torr He at room temperature, and with other measurements of R + O₂ reactions, where, for >C₃ alkyl radicals, the reactions appear to be at their high pressure limits at room temperature.²⁶ Effects of pressure were investigated in the range 10-100 Torr at 298 K, with fits to individual pressures giving $k_4 = (4.9 \pm 1.5) \times 10^{-13} \text{ cm}^3 \text{ s}^{-1}$ at 10 Torr, $k_4 = (6.4 \pm 2.2) \times 10^{-13} \text{ cm}^3 \text{ molecule}^{-1} \text{ s}^{-1}$ at 60 Torr, and $k_4 = (5.5 \pm 2.1) \times 10^{-13} \text{ cm}^3 \text{ molecule}^{-1} \text{ s}^{-1}$ at 100 Torr. Experiments were also performed at 298 K using photolysis wavelengths of 193 nm and 248 nm, under otherwise identical conditions, to assess the impact of the production and subsequent decomposition of COCl (R8.1a and R8.1b) on the observed kinetics. For experiments at 193 nm, the S₀ term in Equation 1 is equal to zero, while for those experiments performed at 248 nm the S₀ term is included, with k_{1b} constrained to the previous measurements of Ghosh *et al.*¹⁹ No significant differences were observed between values for k_4 determined from experiments using 193 nm photolysis ($k_4 = (5.3 \pm 1.7) \times 10^{-13} \text{ cm}^3 \text{ molecule}^{-1} \text{ s}^{-1}$)

compared to those using 248 nm ($k_4 = (5.5 \pm 2.1) \times 10^{-13} \text{ cm}^3 \text{ molecule}^{-1} \text{ s}^{-1}$). The result given for k_4 at 298 K is the average of all experiments at 298 K.

Figure 8.20 shows the temperature dependence of k_4 , which can be described by the Arrhenius parameters $A = (7.3 \pm 6.8) \times 10^{-14} \text{ cm}^3 \text{ molecule}^{-1} \text{ s}^{-1}$ and $E_a = -(5.4 \pm 2.1) \text{ kJ mol}^{-1}$. Results are summarised in Table 8.4. The observed behaviour is consistent with that that expected for a barrierless potential energy surface for the reaction between $\text{CH}_2(\text{CH}_3)_2\text{COOH}$ and O_2 as predicted by the calculations of Zádor *et al.*

T / K	$k_4 / 10^{-13} \text{ cm}^3 \text{ s}^{-1}$
304	7.2 ± 2.5
298	5.6 ± 1.7
289	5.9 ± 2.1
282	9.6 ± 3.0
277	6.8 ± 2.2
274	7.1 ± 2.4
262	8.7 ± 2.7
251	9.9 ± 3.5

Table 8.4 Summary of results for k_4 .

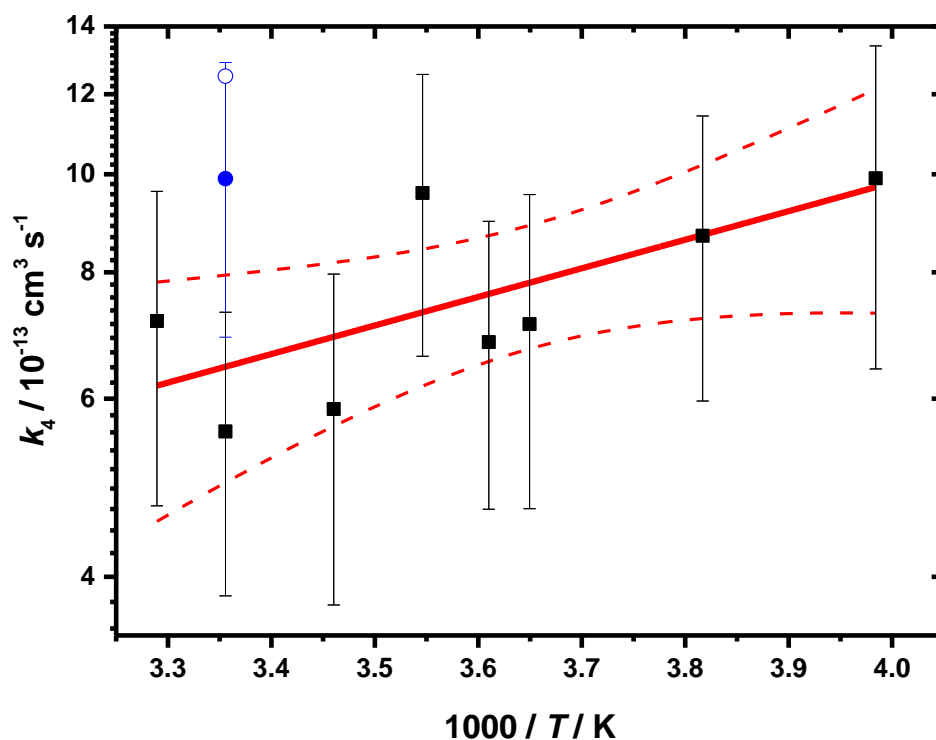


Figure 8.20 Experimental results for k_4 as a function of temperature (black points) with an Arrhenius fit to the data (red solid line), giving $A = (7.3 \pm 6.8) \times 10^{-14} \text{ cm}^3 \text{ s}^{-1}$ and $E_a = -(5.4 \pm 2.1) \text{ kJ mol}^{-1}$. Confidence intervals (95 %) for the Arrhenius fit are given by the red broken lines. Also shown are the measured (blue filled circle) and calculated (blue open circle) results for k_4 at room temperature reported by Zádor *et al.*⁸

8.5 Conclusions

Observations of OH radical production and decay following H-atom abstraction from $(\text{CH}_3)_3\text{COOH}$ by Cl atoms to produce QOOH ($\text{CH}_2(\text{CH}_3)_2\text{COOH}$) radicals have been used to determine the kinetics of QOOH decomposition and the reaction between QOOH and O_2 as a function of temperature and pressure. The decomposition of QOOH radicals was observed to display a pressure dependence between 10 and 350 Torr. Master equation analysis, using MESMER, was used to investigate the decomposition reaction and to fit the barrier height for decomposition to the experimental data, yielding a barrier height of 44.7 kJ mol^{-1} , compared to a value of 52.3 kJ mol^{-1} determined previously by high level calculations,⁸ and collisional energy transfer parameters of $\Delta E_{\text{down}} = 89 \text{ cm}^{-1}$ in He bath gas and $\Delta E_{\text{down}} = 147 \text{ cm}^{-1}$ in N_2 bath gas. The rate coefficient for the reaction between QOOH and O_2 was determined to be $(5.6 \pm 0.5) \times 10^{-13} \text{ cm}^3 \text{ molecule}^{-1} \text{ s}^{-1}$ at 298 K, and

was shown to be independent of pressure in the range 10 to 100 Torr. Kinetics of QOOH + O₂ were also investigated as a function of temperature between 251 and 304 K, for the first time, and can be described by the Arrhenius parameters $A = (7.3 \pm 6.8) \times 10^{-14} \text{ cm}^3 \text{ molecule}^{-1} \text{ s}^{-1}$ and $E_a = -(5.4 \pm 2.1) \text{ kJ mol}^{-1}$.

8.6 References

1. Zador, J., C.A. Taatjes and R.X. Fernandes. Kinetics of elementary reactions in low-temperature autoignition chemistry. *Progress in Energy and Combustion Science*, 2011, **37**(4), pp.371-421.
2. Pilling, M.J., S.H. Robertson and P.W. Seakins. Elementary Radical Reactions and Autoignition. *Journal of the Chemical Society-Faraday Transactions*, 1995, **91**(23), pp.4179-4188.
3. Praske, E., *et al.* Atmospheric autoxidation is increasingly important in urban and suburban North America. *Proceedings of the National Academy of Sciences of the United States of America*, 2018, **115**(1), pp.64-69.
4. Scheer, A.M., *et al.* Low-temperature combustion chemistry of novel biofuels: resonance-stabilized QOOH in the oxidation of diethyl ketone. *Physical Chemistry Chemical Physics*, 2014, **16**(26), pp.13027-13040.
5. Welz, O., *et al.* Unconventional Peroxy Chemistry in Alcohol Oxidation: The Water Elimination Pathway. *Journal of Physical Chemistry Letters*, 2013, **4**(3), pp.350-354.
6. Koritzke, A.L., *et al.* QOOH-mediated reactions in cyclohexene oxidation. *Proceedings of the Combustion Institute*, 2019, **37**(1), pp.323-335.
7. Savee, J.D., *et al.* Direct observation and kinetics of a hydroperoxyalkyl radical (QOOH). *Science*, 2015, **347**(6222), pp.643-646.
8. Zador, J., *et al.* Directly measuring reaction kinetics of QOOH - a crucial but elusive intermediate in hydrocarbon autoignition. *Physical Chemistry Chemical Physics*, 2013, **15**(26), pp.10753-10760.
9. Baasandorj, M., *et al.* (CH₃)₃COOH (tert-butyl hydroperoxide): OH reaction rate coefficients between 206 and 375 K and the OH photolysis quantum yield at 248 nm. *Physical Chemistry Chemical Physics*, 2010, **12**(38), pp.12101-12111.
10. Ren, H., *et al.* Theoretical Studies on the Mechanisms and Dynamics of OH Radical with (CH₃)₃COOH and (CH₃)₂CHOOH. *Journal of Physical Chemistry A*, 2012, **116**(44), pp.10647-10655.
11. Eskola, A.J., *et al.* Analysis of the Kinetics and Yields of OH Radical Production from the CH₃OCH₂ + O₂ Reaction in the Temperature Range 195-650 K: An Experimental and Computational study. *Journal of Physical Chemistry A*, 2014, **118**(34), pp.6773-6788.
- 12.
13. Moore, K.B., J.M. Turney and H.F. Schaefer. The fate of the tert-butyl radical in low-temperature autoignition reactions. *Journal of Chemical Physics*, 2017, **146**(19).
14. Glowacki, D.R., *et al.* MESMER: An Open-Source Master Equation Solver for Multi-Energy Well Reactions. *The Journal of Physical Chemistry A*, 2012, **116**(38), pp.9545-9560.
15. Glowacki, D.R., *et al.* Interception of Excited Vibrational Quantum States by O₂ in Atmospheric Association Reactions. *Science*, 2012, **337**(6098), pp.1066-1069.

16. Carr, S.A., *et al.* OH yields from the CH₃CO+O₂ reaction using an internal standard *Chemical Physics Letters*, 2007, pp.108-112.
17. Baeza-Romero, M.T., *et al.* A combined experimental and theoretical study of the reaction between methylglyoxal and OH/OD radical: OH regeneration. *Physical Chemistry Chemical Physics*, 2007, **9**(31), pp.4114-4128.
18. Baklanov, A.V. and L.N. Krasnoperov. Oxalyl Chloride A Clean Source of Chlorine Atoms for Kinetic Studies. *The Journal of Physical Chemistry A*, 2001, **105**(1), pp.97-103.
19. Ghosh, B., D.K. Papanastasiou and J.B. Burkholder. Oxalyl chloride, (COCl)₂: UV/vis spectrum and Cl atom photolysis quantum yields at 193, 248, and 351 nm. *The Journal of Chemical Physics*, 2012, **137**(16), p.164315.
20. Ianni, J.C. *Kintecus, Windows Version 2.80*, www.kintecus.com, 2002.
21. D F Mcmillen, A. and D.M. Golden. Hydrocarbon Bond Dissociation Energies. 1982, **33**(1), pp.493-532.
22. Choi, N., *et al.* Studies of site selective hydrogen atom abstractions by Cl atoms from isobutane and propane by laser flash photolysis/IR diode laser spectroscopy. *Physical Chemistry Chemical Physics*, 2006, **8**(18), pp.2172-2178.
23. Shannon, R.
24. Shannon, R.J., *et al.* Bimolecular reactions of activated species: An analysis of problematic HC(O)C(O) chemistry. *Chemical Physics Letters*, 2016, **661**, pp.58-64.
25. Troe, J., V.G. Ushakov. Representation of "broad" falloff curves for dissociation and recombination reactions. *Z. Phys. Chem.*, 2014, **228**(1), pp.1-10.
26. Lightfoot, P.D., *et al.* Organic Peroxy-Radicals - Kinetics, Spectroscopy and Tropospheric Chemistry. *Atmos. Environ. A*, 1992, **26**(10), pp.1805-1961.

Summary and Future Work

The use and development of biofuels offers the potential to mitigate issues such as poor air quality and climate change, but requires improved understanding of the fundamental chemistry governing their combustion. In particular, the use of biofuels under low temperature combustion conditions is of interest, with combustion models for such systems requiring knowledge of the kinetics of fuel oxidation processes such as OH + fuel and OH chain branching reactions which govern ignition delay times. This work has investigated the kinetics of OH radical reactions with the potential biofuels furan and its alkylated derivatives 2-MF and 2,5-DMF, and the kinetics of QOOH radical reactions involved in chain propagation vs chain branching in autoignition processes.

The rate coefficients for the reaction between OH and furan and its alkylated derivatives, 2-MF and 2,5-DMF, have been measured as a function of temperature and pressure using the LPF-LIF technique. The work of OH + furan has extended the temperature range reported in the literature by Wine and Thompson¹ from 254-425 K to 298-595 K. Measurements of OH + 2-MF and OH + 2,5-DMF at 298-770 K and 298-640 K, respectively, relevant to low temperature combustion have been made in this work for which there are currently no reports in the literature for these reactions at these temperatures. Experimental results are complemented by master equation calculations using MESMER.

For the OH + furan system the measured room temperature rate coefficient, $k = (3.34 \pm 0.48) \times 10^{-11} \text{ cm}^3 \text{ molecule}^{-1} \text{ s}^{-1}$, was found to be within experimental uncertainties of the rate coefficients report by Atkinson *et al.*², Wine and Thompson, Tuazon *et al.*³ and Eble⁴. Over the temperature range investigated the reaction appears to be at, or close to, the high-pressure limit. Results demonstrate a negative temperature dependence for the reaction of OH + furan over temperatures between 298 K and 595

K, with $-E_a/R = (510 \pm 71)$ K. This temperature dependence is consistent with the behaviour observed in previous studies by Wine and Thompson and Eble.

This work has been analysed in combination with the low temperature kinetic data provided from Eble's thesis and the shock tube data obtained by Elwardany *et al.*⁵ in order to assess the kinetics of the reaction over a wide temperature range. The data were fit to a double modified Arrhenius to obtain Arrhenius parameters that describe the low and high temperature kinetics of the OH + furan system.

A PES was available in the literature for the OH + furan reaction, by Mousavipour *et al.*⁶, which was utilised for master equation calculations. The results from MESMER⁷ supported the experimental results seen in this work, suggesting the addition to the C1 carbon is the dominant reaction pathway up to temperature of ~2100 K. This is in agreement with the results of master equation calculations performed by Mousavipour *et al.* on the PES.

Average room temperature kinetics of the OH + 2-MF reaction were measured as $k = (7.38 \pm 0.37) \times 10^{-11} \text{ cm}^3 \text{ molecule}^{-1} \text{ s}^{-1}$ and were in agreement with the previous studies by Aschmann *et al.*⁸ and Eble. Rate coefficients measured over the experimental temperature range of 298 K to 770 K showed no pressure dependence from between 18 and 150 Torr. A negative temperature dependence was observed up to 770 K.

As with furan, the rate coefficients were analysed in combination with the high pressure work by Eble and shock tube work by Elwardany *et al.* A double modified Arrhenius was fit to the work to parameterise over a wide temperature range.

ab initio calculations were performed at the M06-2x/cc-pVTZ level using Gaussian 09⁹ and compared to the work by Zhang *et al.*¹⁰ at the G3MP2 level and Davis and Sarathy¹¹ at the CBS-QB3 and G4 levels. Relative energies were found to be in agreement with both studies and vibrational frequencies were in agreement with those reported by Davis and Sarathy. MESMER analysis of the *ab initio* PES demonstrate that the abstraction

channels begin to dominate at much lower temperatures than in the unsubstituted furan, which can be accounted for by the low energy barrier (4 kJ mol^{-1}) to the methyl H abstraction channel. From experiments, it is evident that the abstraction channels already have an effect at temperatures above 500 K, where the negative temperature dependent rate coefficient begins to turn over and become positive.

The OH + 2,5-DMF system was also found to be independent of pressure at room temperature, where the average rate coefficient at 298 K was measured as $k = (1.14 \pm 0.11) \times 10^{-10} \text{ cm}^3 \text{ molecule}^{-1} \text{ s}^{-1}$, which is within the experimental uncertainties of the rate coefficients reported by Bierbach *et al.* and Aschmann *et al.* However, in contrast to the results observed in the furan and 2-MF systems, the results are not in agreement with the work by Eble, who found $k = (9.20 \pm 0.40) \times 10^{-11} \text{ cm}^3 \text{ molecule}^{-1} \text{ s}^{-1}$.

At room temperature, the average rate coefficient for this work is at, or close to, the high-pressure limit. Results show a clear pressure dependence for reactions carried out at 410 K and above, that can be described well by a Troe¹² expression.

A PES for the reaction of OH + 2,5-DMF was calculated at the M06-2x/cc-pVTZ level. Master equation analysis by MESMER was found to be supportive of the proposed mechanism. Addition to the C2 carbon of 2,5-DMF was determined as the dominant pathway for the reaction with OH up to temperatures of 1500 K.

This work has extended the temperature range of the oxidation of furans in the low temperature region, however, there is still scope to extend temperatures up to those of the shock tube data reported by Elwardany *et al.* in order to obtain a complete temperature range.

The MESMER analysis performed in this work can be developed to include the analysis of the high-temperature shock tube data to give a more accurate examination of the reaction channels populated during the addition and abstraction processes.

Further computational assessment could be carried out by employing the parameters determined in this work in a combustion model to evaluate the impact on yields and ignition delay times.

Other species in the furan group, such as 3-methylfuran, 2-ethylfuran and 2,3-dimethylfuran, could be studied in order to build a full understanding of the heterocyclic group and their implications on combustion and the environment.

This work also reports decomposition kinetics of the QOOH radical $\text{CH}_2(\text{CH}_3)_2\text{COOH}$, generated from H-atom abstraction from $(\text{CH}_3)_3\text{COOH}$ by Cl atoms. Observations of OH radical production and decay have been used to determine the kinetics of QOOH decomposition and the reaction between QOOH and O_2 as a function of temperature and pressure. The decomposition of QOOH radicals was observed to display a pressure dependence between 10 and 350 Torr. Master equation analysis, using MESMER, was used to investigate the decomposition reaction and to fit the barrier height for decomposition to the experimental data, yielding a barrier height of 44.7 kJ mol^{-1} , compared to a value of 52.3 kJ mol^{-1} determined previously by high level calculations,¹³ and collisional energy transfer parameters of $\Delta E_{\text{down}} = 89 \text{ cm}^{-1}$ in He bath gas and $\Delta E_{\text{down}} = 147 \text{ cm}^{-1}$ in N_2 bath gas. The rate coefficient for the reaction between QOOH and O_2 was determined to be $(5.6 \pm 0.5) \times 10^{-13} \text{ cm}^3 \text{ s}^{-1}$ at 298 K, and was shown to be independent of pressure in the range 10 to 100 Torr. Kinetics of $\text{QOOH} + \text{O}_2$ were also investigated as a function of temperature between 251 and 304 K, and can be described by the Arrhenius parameters $A = (7.3 \pm 6.8) \times 10^{-14} \text{ cm}^3 \text{ s}^{-1}$ and $E_a = -(5.4 \pm 2.1) \text{ kJ mol}^{-1}$. These results represent the first temperature dependent measurements of the kinetics for any QOOH radical reaction and will provide key input data for combustion models. Measurements made in this work could be extended to other temperature and pressure ranges, and to other QOOH species. Calculations for the QOOH system investigated in this work indicate the potential to perform direct measurements of the $\text{CH}_2(\text{CH}_3)_2\text{COOH}$

QOOH radical by infrared (IR) spectroscopy using the IR Quantum Cascade Laser recently developed at the University of Leeds.

Results obtained in this work will provide valuable kinetic data for use in combustion models used to investigate the feasibility of furan, and furan derivatives, for use as novel fuels and to determine optimum engine conditions, while those for QOOH can be applied to a wide range of combustion systems.

References

1. Wine, P.H. and R.J. Thompson. Kinetics of OH reactions with furan, thiophene, and tetrahydrothiophene. *International Journal of Chemical Kinetics*, 1984, **16**(7), pp.867-878.
2. Atkinson, R., S.M. Aschmann and W.P.L. Carter. Kinetics of the reactions of O₃ and OH radicals with furan and thiophene at 298 ± 2 K. *International Journal of Chemical Kinetics*, 1983, **15**(1), pp.51-61.
3. Tuazon, E., *et al.* A study of the atmospheric reactions of 1,3-dichloropropene and other selected organochlorine compounds. *Archives of Environmental Contamination and Toxicology*, 1984, **13**(6), pp.691-700.
4. Eble, J.S.R. *Ignition of oxygenated hydrocarbons: Mechanism and elementary steps*. thesis, Karlsruhe Institute of Technology (KIT), 2017.
5. Elwardany, A., *et al.* A chemical kinetic study of the reaction of hydroxyl with furans. *Fuel*, 2016, **166**, pp.245-252.
6. Mousavipour, S.H., S. Ramazani and Z. Shahkolahi. Multichannel RRKM-TST and Direct-Dynamics VTST Study of the Reaction of Hydroxyl Radical with Furan. *The Journal of Physical Chemistry A*, 2009, **113**(12), pp.2838-2846.
7. Glowacki, D.R., *et al.* MESMER: An Open-Source Master Equation Solver for Multi-Energy Well Reactions. *The Journal of Physical Chemistry A*, 2012, **116**(38), pp.9545-9560.
8. Aschmann, S.M., *et al.* Kinetics of the Reactions of OH Radicals with 2- and 3-Methylfuran, 2,3- and 2,5-Dimethylfuran, and E- and Z-3-Hexene-2,5-dione, and Products of OH + 2,5-Dimethylfuran. *Environmental Science & Technology*, 2011, **45**(5), pp.1859-1865.
9. M. J. Frisch, *et al.* Gaussian 09. 2009.
10. Zhang, W., *et al.* Computational study on the mechanism for the reaction of OH with 2-methylfuran. *Journal of Molecular Structure: THEOCHEM*, 2008, **851**(1), pp.353-357.
11. Davis, A.C. and S.M. Sarathy. Computational Study of the Combustion and Atmospheric Decomposition of 2-Methylfuran. *The Journal of Physical Chemistry A*, 2013, **117**(33), pp.7670-7685.
12. Troe, J. Theory of thermal unimolecular reactions at low pressures. I. Solutions of the master equation. *The Journal of Chemical Physics*, 1977, **66**(11), pp.4745-4757.
13. Zador, J., *et al.* Directly measuring reaction kinetics of (center dot)QOOH - a crucial but elusive intermediate in hydrocarbon autoignition. *Physical Chemistry Chemical Physics*, 2013, **15**(26), pp.10753-10760.

Appendix

OH + Furan

Temperature / K	Pressure / Torr	$k / 10^{11} \text{ cm}^3 \text{ molecule}^{-1} \text{ s}^{-1}$
298	50	3.36 ± 0.06
298	95	3.30 ± 0.05
298	20	3.65 ± 0.06
298	50	3.69 ± 0.11
298	50	3.09 ± 0.10
298	50	2.94 ± 0.02
298	50	3.17 ± 0.07
298	50	3.38 ± 0.05
298	50	3.69 ± 0.08
298	50	3.22 ± 0.07
294	20	3.41 ± 0.04
294	14	3.42 ± 0.02
294	4	3.40 ± 0.04
298	37	3.00 ± 0.26
340	50	3.21 ± 0.09
340	50	2.75 ± 0.05
340	50	2.94 ± 0.13
383	50	2.74 ± 0.06
380	25	2.31 ± 0.06
380	95	2.62 ± 0.05
380	50	2.80 ± 0.04
380	50	2.60 ± 0.14
423	50	2.44 ± 0.04
420	50	2.36 ± 0.04
463	50	1.88 ± 0.04
460	50	2.06 ± 0.03
457	50	1.01 ± 0.06
457	50	1.47 ± 0.09
457	50	1.55 ± 0.05
457	70	1.38 ± 0.05
457	5	1.89 ± 0.06
457	100	1.59 ± 0.37
500	50	2.06 ± 0.04
500	50	1.99 ± 0.05
548	45	1.60 ± 0.05
548	20	1.54 ± 0.06
548	95	1.36 ± 0.06
548	90	1.38 ± 0.06
594	40	1.18 ± 0.07

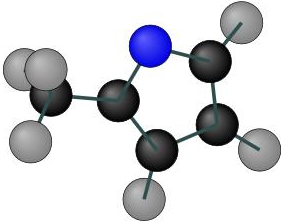
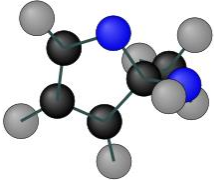
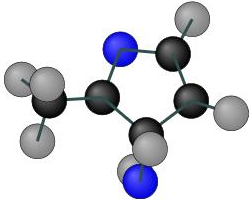
594	10	1.23 ± 0.06
595	90	1.23 ± 0.05
595	20	1.43 ± 0.07

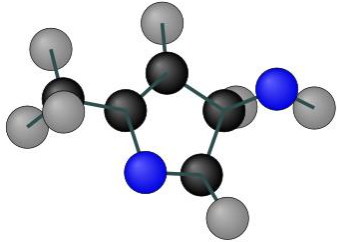
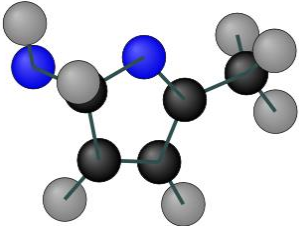
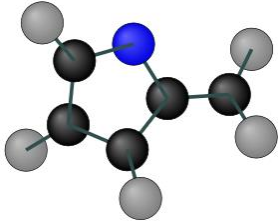
Table 1 Bimolecular rate coefficients for OH + furan in N₂ obtained using the LFP-LIF technique.

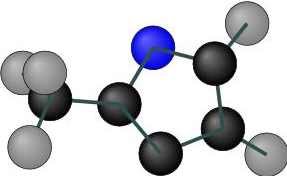
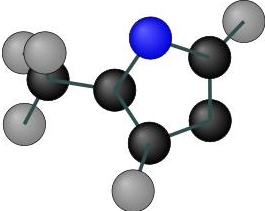
OH + 2-Methylfuran

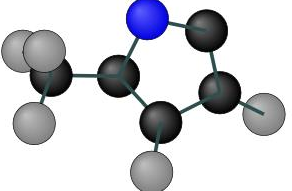
Temperature / K	Pressure / Torr	$k / 10^{11} \text{ cm}^3 \text{ molecule}^{-1} \text{ s}^{-1}$
298	50	7.15 ± 0.23
298	50	7.60 ± 0.32
298	50	7.36 ± 0.22
298	50	7.14 ± 0.18
298	20	7.82 ± 0.23
298	20	7.46 ± 0.19
298	95	7.12 ± 0.51
298	95	7.64 ± 0.15
298	50	7.27 ± 0.12
298	50	6.84 ± 0.27
340	50	6.34 ± 0.24
340	50	6.29 ± 0.19
340	50	6.05 ± 0.15
340	50	5.80 ± 0.27
380	50	5.23 ± 0.08
380	50	5.53 ± 0.19
380	50	4.80 ± 0.15
380	50	5.14 ± 0.14
420	50	4.74 ± 0.18
420	50	4.69 ± 0.06
420	50	4.38 ± 0.80
460	50	3.86 ± 0.07
460	50	4.08 ± 0.16
460	50	3.90 ± 0.13
500	50	3.60 ± 0.05
500	50	3.50 ± 0.08
500	50	4.16 ± 0.15
580	58	1.99 ± 0.05
668	18	1.56 ± 0.07
668	150	1.45 ± 0.05
668	56	1.67 ± 0.05
770	58	1.06 ± 0.04

Table 2 Bimolecular rate coefficients for OH + 2-MF in N₂ obtained using the LFP-LIF technique.

Species	Structure	Energy kJ mol ⁻¹	Rotational constants cm ⁻¹	Vibrational frequencies cm ⁻¹
MF		0	0.297 0.119 0.086	100.91 245.24 333.41 624.93 655.43 668.16 770.48 836.21 906.80 907.06 956.05 998.00 1033.36 1070.67 1134.36 1198.49 1251.94 1281.65 1411.88 1434.88 1473.38 1498.50 1572.42 1674.19 3055.64 3117.42 3147.23 3261.10 3271.66 3289.09
OH		0	18.527	3695.80
C2 Adduct		-159.20	0.156 0.084 0.080	124.89 240.39 290.28 376.33 409.12 450.87 536.77 550.31 657.49 665.70 700.18 799.63 840.18 908.98 946.19 987.44 1028.19 1075.05 1132.17 1150.95 1225.71 1243.49 1335.82 1391.58 1398.13 1427.16 1485.02 1491.59 1525.49 3067.52 3150.31 3162.14 3241.88 3254.27 3279.08 3863.47
C3 Adduct		-87.999	0.115 0.108 0.061	115.05 154.00 187.86 255.33 356.81 409.93 488.20 563.71 639.72 764.32 816.15 854.58 939.65 944.26 1007.46 1020.63 1050.82 1114.91 1183.01 1231.91 1245.86 1271.85 1369.62 1384.53 1418.88 1431.59 1474.83 1492.37 1680.72 3006.92 3028.85 3097.36 3145.36 3248.24 3272.64 3841.77

C4 Adduct		-80.164	0.199	0.069	0.057	122.08 165.76 204.49 212.32 299.01 320.36 422.03 520.08 599.88 654.89 779.08 824.01 921.90 944.24 1005.10 1027.29 1036.49 1071.52 1166.85 1208.78 1233.54 1273.09 1345.66 1372.31 1415.99 1429.73 1476.91 1491.37 1751.18 3025.17 3065.51 3128.78 3163.37 3257.46 3264.93 3883.90
C5 Adduct		-157.72	0.186	0.074	0.058	105.27 117.02 227.26 293.80 367.08 416.64 538.84 564.43 615.95 663.49 813.06 892.77 922.91 946.15 983.55 1017.00 1025.01 1065.12 1146.66 1221.36 1258.24 1306.41 1365.82 1402.70 1431.51 1445.41 1456.15 1467.51 1559.83 3037.60 3046.59 3110.70 3162.89 3264.45 3288.38 3828.26
Methyl Abstraction		-121.03	0.299	0.130	0.091	250.63 357.39 521.91 598.86 675.85 707.09 734.88 751.28 798.57 894.14 909.40 924.53 963.14 1029.67 1137.40 1209.66 1259.71 1329.30 1370.55 1445.69 1509.46 1560.99 3187.71 3256.07 3269.02 3281.33 3298.88
Methyl Abstraction TS		3.9427	0.168	0.057	0.049	54.57 73.33 220.03 251.63 303.01 324.51 619.04 635.86 670.04 775.53 782.68 846.50 901.76 916.14 929.78 964.88 1016.04 1037.28 1114.56 1168.01 1204.94 1262.51 1276.33 1364.71 1436.98 1450.67 1552.18 1618.96 1687.69 3094.54 3170.67 3261.66 3272.86 3288.48 3765.06

C3 Abstraction		5.699	0.332 0.118 0.088	97.82 235.32 329.22 606.87 633.20 664.26 749.15 886.09 891.64 945.97 990.42 1067.68 1108.84 1179.69 1196.14 1252.24 1393.24 1416.59 1473.63 1493.56 1549.63 1662.59 3056.30 3118.85 3150.51 3264.57 3286.10
C3 Abstraction TS		33.81355195	0.124 0.072 0.046	80.17 118.90 135.16 213.56 240.17 337.72 386.41 606.54 638.65 673.53 749.70 756.98 890.91 893.90 942.91 974.13 1038.69 1069.68 1124.71 1186.11 1200.95 1269.58 1345.85 1403.18 1428.32 1481.34 1490.98 1563.70 1674.31 3057.12 3118.64 3158.03 3268.18 3289.44 3814.63
TS4		54.261	0.234 0.065 0.053	133.10 191.93 280.48 293.91 350.34 413.20 504.99 566.50 618.63 650.30 689.53 755.91 782.83 837.53 941.74 996.15 1028.18 1070.29 1162.33 1194.36 1210.60 1289.75 1326.12 1395.04 1423.66 1477.74 1493.88 1595.10 1688.21 3059.87 3123.16 3155.92 3268.44 3274.38 3855.16
C4 Abstraction		5.452	0.303 0.125 0.090	143.85 253.33 342.19 568.51 653.02 662.79 755.05 813.75 890.77 950.54 1006.12 1072.30 1094.40 1150.65 1222.53 1257.33 1389.85 1419.20 1476.96 1496.08 1556.02 1636.67 3063.43 3126.80 3152.50 3274.89 3276.89
C4 Abstraction TS		37.124	0.238 0.047 0.040	77.10 98.57 135.10 202.06 251.75 335.64 386.70 590.44 650.94 669.51 746.69 804.54 832.42 911.42 935.19 954.82 1012.53 1068.91 1111.54 1177.45

					1232.38 1256.42 1351.54 1396.60 1418.96 1476.94 1494.71 1581.09 1656.12 3059.26 3120.93 3157.47 3272.94 3285.30 3814.73
C5 Abstraction TS		40.2	0.190 0.052 0.042		76.95 86.45 119.41 169.52 244.51 338.90 381.49 572.38 649.70 665.49 753.08 816.35 876.69 923.74 933.84 996.02 1014.37 1040.36 1070.71 1159.52 1234.07 1240.68 1346.84 1397.51 1420.16 1475.88 1493.86 1551.75 1674.14 3059.61 3120.83 3154.33 3261.57 3284.92 3819.13
C5 Abstraction		4.752	0.312 0.123 0.089		120.53 239.16 333.24 559.33 642.25 662.40 784.14 858.28 888.12 949.76 992.86 1026.15 1066.73 1150.78 1227.54 1240.25 1370.04 1418.14 1473.41 1494.03 1525.10 1683.49 3053.97 3114.59 3150.46 3260.61 3278.93
H		0			

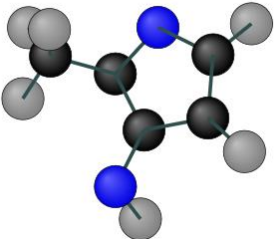
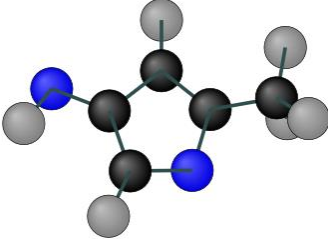
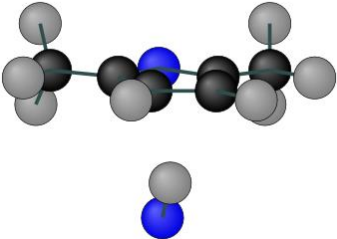
P3		28.567	0.123	0.113	0.060	127.54 184.01 226.55 253.03 328.48 441.88 627.22 646.17 681.05 741.93 751.63 867.30 913.17 974.53 1075.33 1081.59 1106.17 1205.26 1273.80 1305.06 1326.66 1419.39 1485.76 1487.22 1503.14 1573.23 1751.90 3062.21 3119.15 3158.68 3245.58 3288.03 3912.23
P4		27.152	0.247	0.067	0.053	104.72 199.18 268.22 284.23 372.73 436.59 600.51 615.13 668.09 718.23 743.05 827.35 956.44 1001.96 1035.95 1069.55 1152.81 1173.65 1211.15 1280.05 1354.10 1420.67 1479.70 1482.99 1508.12 1627.14 1708.81 3055.05 3115.70 3154.44 3267.22 3272.41 3895.53
Pre-reactive Complex		0	0.082	0.054	0.047	399.68 453.47 623.80 643.21 661.16 705.93 811.27 857.54 958.38 990.24 1013.90 1045.71 1050.67 1071.17 1077.68 1226.19 1261.58 1285.17 1399.24 1417.53 1428.87 1481.15 1482.37 1497.14 1504.94 1638.10 1682.48 3064.05 3064.32 3124.99 3125.16 3160.48 3160.49 3248.90 3260.88 3704.29
water		0	27.527	14.469	9.484	1623.90 3876.71 3980.08

Table 3 *ab initio* calculations of the OH + 2-MF reaction, structures, relative energies, rotational constant and vibrational frequencies are shown.

OH + 2,5-Dimethylfuran

Pressure / Torr	Temperature / K	$k / 10^{-11} \text{cm}^3 \text{molecule}^{-1} \text{s}^{-1}$	Number of Experiments
20	298	11.90 ± 0.60	3
25	298	10.40 ± 0.20	2
30	298	11.50 ± 1.10	2
40	298	12.00 ± 0.80	2
50	298	11.30 ± 0.40	9
75	298	11.50 ± 1.50	2
95	298	12.60 ± 0.20	2
125	298	10.90 ± 0.30	1
150	298	11.10 ± 0.60	2
20	410	5.20 ± 0.20	4
25	410	5.60 ± 0.10	2
30	410	5.50 ± 0.30	2
40	410	5.90 ± 0.60	2
50	410	6.40 ± 0.20	4
75	410	7.10 ± 0.40	1
95	410	6.70 ± 0.10	2
150	410	6.80 ± 0.10	2
20	475	4.20 ± 0.20	3
25	475	4.50 ± 0.10	1
30	475	4.00 ± 0.40	2
40	475	4.50 ± 0.40	2
50	475	4.70 ± 0.20	7
95	475	5.10 ± 0.30	3
150	475	5.40 ± 0.20	2
20	535	2.90 ± 0.30	2
30	535	3.00 ± 0.40	2
40	535	3.50 ± 0.20	2
50	535	3.50 ± 0.50	3
75	535	3.60 ± 0.80	2
95	535	3.50 ± 0.40	2
150	535	4.00 ± 0.80	2
20	550	2.70 ± 0.10	2
35	550	3.20 ± 0.30	2
50	550	3.60 ± 0.30	2
75	550	3.40 ± 0.10	2
95	550	4.20 ± 0.10	2
150	550	3.90 ± 0.20	2
20	610	2.30 ± 0.20	2
30	610	2.70 ± 0.20	2
40	610	2.50 ± 0.30	3
50	610	3.10 ± 0.10	4
75	610	3.20 ± 0.40	2
95	610	3.80 ± 0.20	2
125	610	3.50 ± 0.10	2
150	610	3.60 ± 0.10	2
20	635	2.20 ± 0.10	2
30	635	2.40 ± 0.10	2
40	635	2.70 ± 0.10	2
50	635	2.70 ± 0.20	4
75	635	3.00 ± 0.20	3

85	635	3.70 ± 0.10	1
95	635	3.50 ± 0.10	2
150	635	3.10 ± 0.20	2

Table 4 Bimolecular rate coefficients for OH + 2,5-DMF in N₂ obtained using the LFP-LIF technique.

Name	Energy kJ mol ⁻¹	Rotational constants cm ⁻¹	Vibrational frequencies cm ⁻¹
DMF	0	0.208 0.072 0.054	29.83 64.76 186.93 252.02 285.10 393.90 623.69 641.01 656.43 706.77 825.53 874.36 948.99 989.30 1016.73 1039.06 1050.70 1060.45 1067.87 1231.47 1262.55 1287.55 1396.81 1409.36 1421.72 1472.04 1472.57 1490.14 1498.19 1645.34 1694.70 3046.35 3046.90 3105.76 3106.04 3141.81 3141.84 3263.88 3276.38
OH	0.0	19.2438	3722.0
Int1	-156.43	0.130 0.054 0.049	94.12 174.40 226.07 245.35 286.78 320.16 365.70 391.12 472.37 539.34 571.22 617.35 636.08 691.23 839.34 882.57 920.68 959.41 986.12 1018.57 1038.91 1041.91 1097.49 1154.52 1218.24 1298.22 1336.82 1386.72 1417.22 1425.07 1444.97 1473.69 1479.63 1485.91 1492.92 1553.07 3045.77 3069.81 3095.89 3155.35 3160.11 3161.21 3234.08 3252.15 3861.95
Int2	-116.39	0.214 0.076 0.056	26.71 183.18 268.61 288.62 407.29 550.36 625.84 633.23 673.33 730.76 734.93 780.22 888.70 925.24 963.31 997.75 1030.19 1040.53 1050.41 1230.97 1291.01 1334.87 1390.81 1413.80 1427.70 1466.70 1488.24 1524.75 1613.15 3042.09 3099.48 3144.12 3194.51 3259.66 3276.24 3300.15
Int3	-76.85	0.113 0.059 0.042	113.51 141.57 168.70 173.32 217.38 221.61 272.39 352.71 453.48 532.35 597.64 605.47 695.25 802.80 854.75 929.47 989.70 1008.75 1026.97 1033.11 1034.78 1075.79 1176.87 1225.15 1265.86 1280.02 1335.49 1368.57 1395.82 1418.06 1435.59 1474.90 1480.24 1492.01 1496.40 1750.88 3012.15 3032.55 3070.39 3096.89 3133.60 3138.90 3165.42 3270.78 3880.43
Int4	13.48	0.222 0.072 0.055	97.38 184.49 248.90 275.12 397.26 603.55 616.11 648.77 705.99 809.03 940.21 983.64 1027.97 1035.99 1056.11 1065.85 1132.67 1246.38 1259.89 1365.39 1407.43 1414.52 1471.27 1474.91 1487.18 1492.61 1633.95 1671.17 3046.74 3052.69 3106.65 3113.58 3144.98 3146.45 3271.05
P1	-139.68	0.161 0.037 0.030	33.29 73.83 122.20 136.33 193.91 247.98 324.01 352.87 471.10 484.17 503.37 560.01 598.81 739.95 748.63 781.94 922.76 922.97 990.18 1034.37 1038.24 1054.41 1181.72 1220.32 1284.72 1318.78 1386.21 1399.50 1461.23 1468.29 1485.77 1486.51 1491.03 1534.20 1596.86 1733.32 3048.05 3060.91 3101.59 3108.12 3123.72 3163.47 3182.08 3219.19 3853.17
P3	36.46	0.120 0.058 0.040	72.38 132.26 137.23 177.38 236.98 237.37 279.90 367.08 481.74 601.16 650.03 651.27 682.52 797.16 813.46 951.89 1026.11 1038.87 1061.23 1074.15 1106.55 1182.04 1268.97 1302.99 1348.33 1413.93 1421.29 1474.12 1475.19 1475.79

					1494.12 1507.54 1650.71 1762.68 3048.99 3060.39 3106.23 3121.93 3140.75 3149.43 3254.94 3914.44
TS1	-73.94	0.135	0.049	0.045	112.06 126.93 224.30 248.51 315.33 354.99 363.29 436.83 506.30 571.20 594.27 627.00 669.42 709.91 829.33 865.08 967.65 1014.74 1025.69 1044.69 1045.47 1102.85 1177.09 1254.01 1347.58 1384.06 1400.19 1439.94 1442.74 1468.48 1474.21 1480.74 1504.96 1531.49 1551.40 3056.69 3059.87 3127.18 3137.52 3150.36 3174.10 3177.42 3226.96 3834.55
TS2	10.98	0.104	0.045	0.035	46.29 67.64 114.32 182.71 223.79 249.96 297.17 315.32 393.77 615.76 638.76 651.54 702.86 779.86 820.27 876.58 921.41 968.76 1001.11 1025.34 1040.31 1054.24 1067.74 1155.07 1249.89 1271.07 1275.41 1373.21 1410.70 1426.33 1455.94 1477.33 1495.86 1597.11 1673.31 1713.32 3053.05 3096.49 3111.81 3153.61 3177.32 3261.95 3274.62 3761.75
TS3	54.22	0.117	0.057	0.040	134.70 146.03 170.76 214.10 235.68 247.33 282.53 351.82 446.96 510.06 574.19 629.84 649.11 707.94 714.89 822.12 829.69 948.15 1021.74 1035.55 1053.49 1075.32 1133.06 1162.98 1271.00 1298.02 1314.96 1396.79 1420.81 1451.09 1477.55 1479.40 1485.53 1498.39 1636.93 1693.22 3044.65 3061.70 3106.04 3124.47 3155.42 3161.33 3273.12 3849.15
TS4	41.19	0.114	0.044	0.032	73.75 96.59 136.28 157.75 199.24 229.26 250.31 276.71 382.43 406.29 613.95 619.16 652.01 703.43 771.54 820.46 948.55 953.49 1023.68 1035.77 1062.46 1066.04 1072.22 1157.30 1252.91 1269.48 1345.36 1387.79 1414.97 1420.91 1477.55 1479.06 1491.78 1496.72 1642.59 1684.88 3054.53 3055.80 3114.87 3115.55 3154.78 3155.14 3273.04 3816.72
water	0	27.547	14.469	9.487	1623.34 3878.44 3981.96

Table 5 Table 4 ab initio calculations of the OH + 2,5-DMF reaction, relative energies, rotational constant and vibrational frequencies are shown.

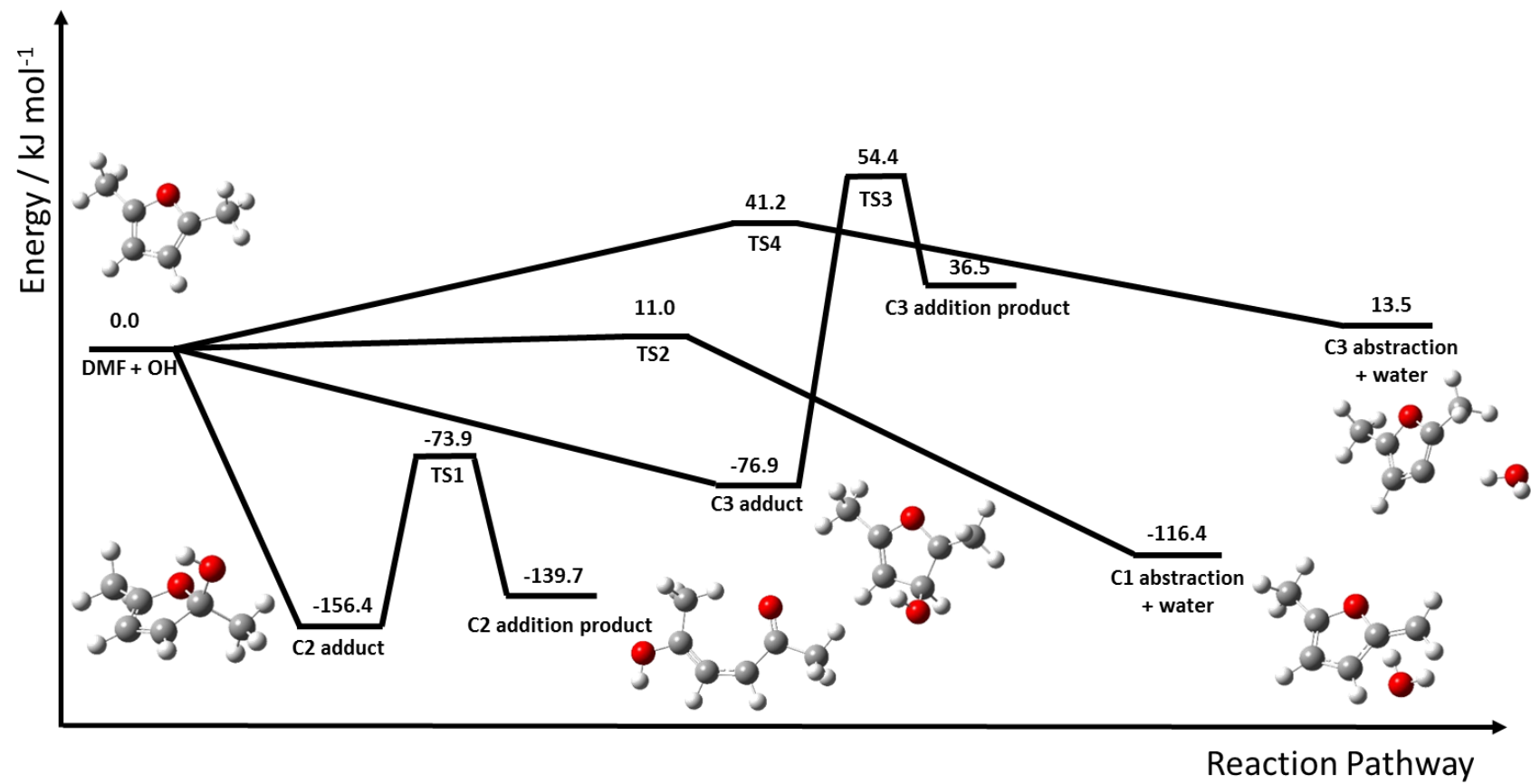


Figure 1 PES for the 2,5-DMF + OH reaction calculated at the M06-2x/cc-PVTZ level of theory using Gaussia 09 program.

QOOH Decomposition

<i>T</i> / K	<i>p</i> / Torr	Bath gas	Photolysis wavelength / nm	<i>k</i> ₃ / s ⁻¹
298	10	N ₂	248	30200 ± 9100
298	20	N ₂	248	34600 ± 10400
298	30	N ₂	248	43800 ± 13200
298	40	N ₂	248	45600 ± 13800
298	60	N ₂	248	54300 ± 16400
298	80	N ₂	248	64400 ± 19500
298	100	N ₂	248	54900 ± 16600
298	100	N ₂	248	79300 ± 24000
298	50	He	193	20100 ± 6200
298	100	He	193	53900 ± 16200
293	350	He	193	52900 ± 15900
283	40	He	193	22600 ± 6900
283	60	He	193	22100 ± 6600
283	110	He	193	34800 ± 10400
283	200	He	193	44000 ± 13200
277	10	N ₂	193	11200 ± 3400
277	20	N ₂	193	21700 ± 6500
277	50	N ₂	193	12900 ± 3900
277	50	N ₂	193	39400 ± 11900
277	110	N ₂	193	15000 ± 4500
277	190	N ₂	193	16200 ± 4900
273	25	He	193	11000 ± 3300
273	25	He	193	6400 ± 2300

273	40	He	193	14400 ± 4400
273	40	He	193	9600 ± 3200
273	80	He	193	23500 ± 7100
273	100	He	193	10900 ± 3300
273	160	He	193	32800 ± 9900
273	340	He	193	15000 ± 4500
268	170	He	193	16800 ± 5300
255	10	He	193	3000 ± 900
255	35	He	193	4500 ± 1400
255	50	He	193	4700 ± 1400
255	70	He	193	3600 ± 1100
255	185	He	193	7400 ± 2200
251	35	He	193	4200 ± 1300
251	40	He	193	5900 ± 1800
251	200	He	193	6900 ± 2100

Table 6 Summary of results for the rate of decomposition of QOOH radical.

<i>T</i> / K	<i>k</i> ₄ / 10 ⁻¹³ cm ³ s ⁻¹
304	7.2 ± 2.5
298	5.6 ± 1.7
289	5.9 ± 2.1
282	9.6 ± 3.0
277	6.8 ± 2.2
274	7.1 ± 2.4
262	8.7 ± 2.7
251	9.9 ± 3.5

Table 8.7 Summary of results for QOOH + O₂.

Name	Energy kJ mol ⁻¹	Rotational constants cm ⁻¹	Vibrational frequencies cm ⁻¹
QOOH	0	0.154 0.097 0.095	151.15 204.75 223.18 260.91 273.84 289.77 340.21 367.13 406.70 461.57 511.19 592.62 792.63 888.39 927.23 958.11 995.65 1023.90 1043.11 1183.35 1288.38 1292.55 1397.46 1402.16 1413.08 1459.63 1477.85 1489.86 1497.24 1516.82 3055.26 3058.91 3133.14 3142.04 3145.21 3153.30 3155.51 3270.46 3834.85
TS	44.7371	0.157 0.096 0.094	120.96 187.90 206.23 222.56 250.41 349.71 352.74 403.28 425.95 482.00 571.49 773.34 785.20 916.18 923.60 961.31 1017.66 1030.30 1064.78 1180.49 1288.84 1357.16 1408.23 1417.74 1470.30 1476.63 1488.50 1508.66 1514.61 3054.91 3061.51 3137.03 3142.69 3146.06 3152.20 3178.78 3300.59 3856.67
DMO	-74.51	0.219 0.186 0.131	189.40 231.31 358.14 369.56 407.26 420.62 729.81 864.22 918.96 964.50 969.77 1022.98 1094.62 1144.94 1162.31 1181.05 1303.79 1405.54 1422.64 1438.09 1479.20 1493.93 1500.02 1516.33 1556.44 3055.32 3058.99 3116.68 3127.26 3131.24 3148.40 3149.96 3208.99
OH	0.0	19.2438	3722.0

Table 8 *ab initio* calculations of the QOOH decomposition reaction, structures, relative energies, rotational constant and vibrational frequencies are shown.